

Series on Bioengineering & Biomedical Engineering – Vol. 1

# DYNAMICS of the VASCULAR SYSTEM

John K-J Li



**DYNAMICS of the  
VASCULAR SYSTEM**

## **SERIES ON BIOENGINEERING AND BIOMEDICAL ENGINEERING**

**Series Editor:** John K-J Li (*Department of Biomedical Engineering,  
Rutgers University, USA*)

---

- Vol. 1: Dynamics of the Vascular System  
by John K-J Li (*Department of Biomedical Engineering, Rutgers University, USA*)
- Vol. 2: Neuroprosthetics  
Theory and Practice  
eds. Kenneth W Horch and Gurpreet S Dhillon (*Department of Bioengineering,  
University of Utah, USA*)
- Vol. 3: Cerebral Hemodynamics & Metabolism Using Magnetic Resonance Imaging &  
Spectroscopy  
by Weili Lin (*Department of Radiology, University of North Carolina, USA*),  
Chung Y Hsu and Williams Power (*Department of Neurology, Washington University  
School of Medicine, USA*)

Series on Bioengineering & Biomedical Engineering – Vol. 1

# DYNAMICS of the VASCULAR SYSTEM



John K-J Li  
Rutgers University, USA

 **World Scientific**

NEW JERSEY • LONDON • SINGAPORE • SHANGHAI • HONG KONG • TAIPEI • CHENNAI

*Published by*

World Scientific Publishing Co. Pte. Ltd.

5 Toh Tuck Link, Singapore 596224

*USA office:* Suite 202, 1060 Main Street, River Edge, NJ 07661

*UK office:* 57 Shelton Street, Covent Garden, London WC2H 9HE

**British Library Cataloguing-in-Publication Data**

A catalogue record for this book is available from the British Library.

**DYNAMICS OF VASCULAR SYSTEM**

**Series on Bioengineering & Biomedical Engineering — Vol. 1**

Copyright © 2004 by World Scientific Publishing Co. Pte. Ltd.

*All rights reserved. This book, or parts thereof, may not be reproduced in any form or by any means, electronic or mechanical, including photocopying, recording or any information storage and retrieval system now known or to be invented, without written permission from the Publisher.*

For photocopying of material in this volume, please pay a copying fee through the Copyright Clearance Center, Inc., 222 Rosewood Drive, Danvers, MA 01923, USA. In this case permission to photocopy is not required from the publisher.

ISBN 981-02-4907-1

## Author Biography

John K-J. Li received his Ph.D. in bioengineering in 1978 from the University of Pennsylvania. He was Head of Biomedical Engineering at Presbyterian-University of Pennsylvania Medical Center from 1977-1979 prior to joining Rutgers University where he is currently a Professor II (distinguished) of Biomedical Engineering. He has been a Director of Joint Graduate Program of Rutgers and UMDNJ-Robert Wood Johnson Medical School and has supervised more than 60 Ph.D. and M.S. theses projects. Dr. Li is a Fellow of the American Institute for Medical and Biological Engineering, the American College of Cardiology and the American College of Angiology. He is a recipient of IEEE Millennium Medal award and of research grants from the National Institutes of Health, the National Science Foundation, DOD and the American Heart Association on cardiovascular function, computer modeling, controlled drug delivery (with U.S. patents) and biomedical sensors. He has served as a member of NIH special study sections, a reviewer for NSF and the International Science Foundation. He is Editor-in-chief of *Cardiovascular Engineering: an International Journal* and has been an Associate Editor of *IEEE Transactions on Biomedical Engineering* and a number of other biomedical engineering journals. Dr. Li is a frequently invited speaker and scientific session chair on cardiovascular dynamics, biomedical instrumentation and their clinical applications. He has more than 350 publications and *Dynamics of the Vascular System* is his fifth book. Dr. Li is the Editor of World Scientific *Bioengineering and Biomedical Engineering* Book Series.

This page intentionally left blank

## Preface

This book is the first volume of the Bioengineering and Biomedical Engineering Book Series. As the Series Editor, and to set a good example, I have taken the task of writing yet another book on the cardiovascular system.

The contents of this book extends from "*Arterial System Dynamics*", my first book published some fifteen years ago, to distinctly different regimes of the microcirculation and the venous system, as well as the assisted circulation.

The vascular system is indeed so vast, that a binocular vision is often needed to unravel the mystery of the many concurrent interactions occurring at different sites of the vascular tree. This becomes more challenging with the imposition of studying its dynamic phenomena. "*The Dynamics of the Vascular System*" is written employing mathematical techniques to formulate the physical principles involved in the structural and functional correlates of the underlying physiology. The intriguing control and geometric perspectives are also included wherever possible. The book also serves as a companion text to "*The Arterial Circulation: Physical Principles and Clinical Applications*".

Selected topics and references are provided, so that I and the readers are not overwhelmed by the otherwise exhaustive presentations of the many observed phenomena and the subsequent diverse interpretations of their origins and mechanisms.

I hope professionals and students in the field of bioengineering and biomedical engineering, biomathematics, biophysics, cardiovascular physiology and medicine will find this book a relevant source of

reference. Much of the work is the culmination of my three decades of learning, experimenting and investigation. I am aware that there are other works of notable items and newer advances which I have not yet included in this book. I will continue to learn more of them. Finally, I like to thank those who have contributed to the completion of this book, especially Dr. Ying Zhu.

*John K-J. Li*  
*New Jersey*

# Contents

Preface .....	vii
1. Historical Backgrounds and Book Contents	
1.1 Discoveries of the Circulation.....	1
1.2 Importance of the Vascular System .....	7
1.3 Modern Concepts .....	8
1.4 Book Contents.....	9
2. Vascular Biology, Structure and Function	
2.1 Anatomical Organization of the Vasculature .....	14
2.1.1 The Circulatory System .....	14
2.1.2 The Heart .....	14
2.1.3 The Arteries .....	18
2.1.4 The Veins.....	18
2.1.5 The Microvasculature .....	19
2.2 Mechanical Properties of Blood Vessels.....	20
2.2.1 Some Geometric Aspects of Blood Vessels.....	20
2.2.2 Vascular Stiffness and Elastic Properties.....	25
2.3 Functional Properties of Blood .....	30
2.3.1 Blood Plasma and Blood Gas.....	30
2.3.2 Oxygen Saturation Curves and Hemoglobin.....	31
2.3.3 Red Blood Cells, Hematocrit and Blood Volume .....	33
2.4 Control Aspects of the Vascular System.....	35
2.4.1 Control of the Central Cardiovascular System.....	36
2.4.2 Functions of the Baroreceptors .....	37
2.4.3 Arterial Chemoreceptors .....	39
3. Physical Concepts and Basic Fluid Mechanics	
3.1 Basic Mechanics and Dimensional Analysis .....	41
3.1.1 Mass, Length and Time System and the Pi-Theorem of Buckingham .....	41

3.1.2	Dimensional Matrix .....	43
3.1.3	Dynamic Similitude in Vascular Biology .....	44
3.1.4	Elastic and Viscoelastic Properties of Blood Vessels .....	46
3.2	Frequency Domain and Fourier Analysis .....	54
3.2.1	Periodic Functions .....	54
3.2.2	Trigonometric Fourier Series .....	55
3.2.3	Complex Form of Fourier Series .....	58
3.2.4	Other Aspects of Frequency Domain Analysis .....	60
3.2.4.1	Dirichlet Conditions .....	60
3.2.4.2	Line Spectrum and Nyquist Criterion .....	61
3.2.4.3	Correlation, Coherence and Power Spectrum .....	61
3.3	Fluid Mechanics and Rheology .....	63
3.3.1	Steady Flow and Poiseuille Equation .....	63
3.3.2	Bernoulli's Equation and Narrowing Vessel Lumen .....	67
3.3.3	Orifice Flow and Torricelli's Equation .....	68
3.3.4	The Gorlin Equation .....	69
3.3.5	Flow and Flow Acceleration .....	69
3.3.6	Newtonian Fluid, No-Slip, Boundary Conditions and Entry Length .....	72
3.3.6.1	Newtonian Fluid .....	72
3.3.6.2	No-Slip Boundary Conditions .....	73
3.3.6.3	Laminar and Turbulent Flow .....	73
3.3.6.4	Entry Length .....	75
4.	Hemodynamics of Large Arteries	
4.1	Ventricular Outflow and the Aorta .....	76
4.1.1	Ventricular Ejection .....	76
4.1.2	Cardiac Muscle Contraction and Force-Length-Velocity Relation .....	78
4.1.3	The Pressure-Volume Curve and Contractility of the Heart .....	81
4.1.4	Ejection Fraction, Cardiac Performance, Preload and Afterload .....	82
4.1.5	Coupling of the Ventricle and the Arterial System .....	83
4.1.6	Dynamic of Heart-Arterial System Interactions .....	87
4.2	Pressure-Flow Relations and Vascular Impedance .....	89
4.2.1	Pressure and Flow Waveforms in Large and Small Arteries .....	89
4.2.2	Vascular Impedance to Blood Flow .....	94
4.3	Wave Propagation Phenomena .....	99
4.3.1	The Propagation Constant .....	99
4.3.2	Foot-to-Foot Velocity .....	100
4.3.3	Apparent Propagation Constant and Transfer Function .....	103
4.3.4	Determination of the Propagation Constant .....	107

4.4	Wave Reflection Phenomena .....	110
4.4.1	Influence of Wave Reflections on Pressure and Flow Waveforms .....	110
4.4.2	The Reflection Coefficients .....	116
4.4.3	Augmentation Index .....	118
4.4.4	Wave Reflection Sites .....	119
4.5	Modeling Aspects of the Arterial System .....	120
4.5.1	Mathematical Formulations .....	120
4.5.2	Linear Theories of Oscillatory Blood Flow in Arteries .....	124
4.5.3	The Lumped Model of the Arterial System: The Windkessel .....	130
4.5.4	Nonlinear Aspects and Pressure-Dependent Arterial Compliance .....	136
5.	Vascular Branching .....	
5.1	Branching Geometry .....	142
5.1.1	Complexity of Vascular Branching .....	142
5.1.2	Nonuniform Branching and 3-D Branching Structure .....	144
5.1.3	Space-Filling Properties and Modeling .....	146
5.2	Fluid Mechanics of Vascular Branching .....	148
5.2.1	Branching Geometry and Fluid Dynamic Considerations .....	148
5.2.2	Fluid Mechanics Associated with Atherosclerosis and Stenosis .....	154
5.3	Pulse Transmission Characteristics at Vascular Branching .....	157
5.3.1	Impedance Matching and Wave Reflections .....	157
5.3.2	Area Ratio Concept .....	160
5.3.3	Minimum Local Reflections at Vascular Branching Junctions .....	164
5.4	Optimization Aspects Applicable to Vascular Branching .....	166
5.4.1	Optimizing Vessel Radius and the Cube Law .....	166
5.4.2	Optimizing Branching Radii and Angles .....	170
6.	The Venous System .....	
6.1	The Reservoir Properties and Venous Return .....	172
6.1.1	Venous Compliance and Reservoir Characteristics .....	172
6.1.2	Structural Properties of Veins .....	174
6.1.3	Venous Return .....	175
6.2	Pressure and Flow Waveforms in Vein .....	176
6.2.1	The Normal Pressure and Flow Waveforms in Veins .....	176
6.2.2	Respiration Effects on Venous Pressure and Flow Waveforms .....	178
6.2.3	Abnormal Venous Pressure and Flow Waveforms .....	180
6.3	Modeling and Collapsible Vessel Properties .....	182
6.3.1	Steady Flow in Collapsible Tubes .....	182
6.3.2	Flow Limitation and Model Experiments .....	184
6.3.3	Pulse Wave Transmission Characteristics in Veins .....	188

7. The Microcirculation	
7.1 Structure of the Microcirculation .....	192
7.1.1 Functional Organization of the Microvasculature .....	192
7.1.2 The Capillary Circulation.....	196
7.2 Pressure-Flow Relation and Microcirculatory Mechanics .....	200
7.2.1 Flow-Related Mechanical Characteristics of the Microcirculation.....	200
7.2.2 Some Pressure-Related Mechanical Characteristics .....	202
7.3 Pulse Transmission and Modeling Aspects.....	206
7.3.1 Pressure and Flow Waveforms in Arterioles and Capillaries.....	206
7.3.2 Pulse Transmission Characteristics in the Microcirculation .....	208
7.3.3 Modeling Aspects of the Microcirculation.....	210
8. Hemodynamic Measurements and Dynamics of the Assisted Circulation	
8.1 Pressure, Flow and Dimension Measurements .....	214
8.1.1 Invasive Blood Pressure Measurements.....	214
8.1.1.1 The Needle-Pressure Transducer System.....	214
8.1.1.2 The Catheter-Pressure Transducer Systems .....	217
8.1.2 Noninvasive Blood Pressure Measurements .....	222
8.1.2.1 Auscultatory Measurement of Blood Pressure .....	222
8.1.2.2 Blood Pressure Measurement with the Oscillometric Method .....	224
8.1.2.3 Noninvasive Blood Pressure Monitoring with Tonometer .....	225
8.1.3 Blood Flow Measurement.....	226
8.1.3.1 Electromagnetic Flowmeter .....	226
8.1.3.2 Ultrasound Doppler Velocimeters.....	227
8.1.3.3 Indicator Dilution Methods and Thermodilution .....	229
8.1.4 Measurement of Vascular Dimensions .....	233
8.2 The Assisted Circulation and the Intra-Aortic Balloon Pump.....	234
8.2.1 Mechanical Assist Devices and the Assisted Circulation .....	234
Bibliography .....	245
Index .....	253

## Chapter 1

# Historical Background and Book Contents

### 1.1 Discoveries of the Circulation

That “blood moves in closed circle” was apparently known in the Far East, several millennia ago, about 2,650 B.C., as recorded in the book by the Yellow Emperor of China written in the Canon of Medicine (Nei Ching). Ancient Chinese practitioners customarily felt palpable wrist artery (radial artery) pulsations as a means of diagnosing the cardiac states of their patients. In this approach, the practitioners were able to obtain both the strength of the pulsation to infer the vigor of contraction of the heart, and the interval duration of the pulses, hence heart rate. This seemingly indicates that the importance of the rate-pressure product, now a popular clinical index of myocardial oxygen consumption, might even have been considered pertinent at that time. The supply and demand of oxygenation, as well as its proper utilization in terms of energy balance, or ying-yang, is center to achieving body harmony. Thus, this suggestion of an intrinsic transfer of the energy (Chi) generated by the heart to the peripheral arteries may have been known since antiquity, although the theoretical foundation was not established until much later.

In the West, the observation that man must inspire air to sustain life led ancient scientists and philosophers to toy with the idea that arteries contained air rather than blood. This was the notion originally attributed to Erasistratus in the third century B.C., following the teaching of Aristotle. Aristotle and later Herophilus performed numerous anatomical studies and the latter discovered the connecting arteries to the contracting heart. That arteries themselves contract and relax thus was known in Aristotle's time. Galen's (130-200) description of the ebb and flow of blood in arteries, though lasted for centuries, was grossly inaccurate.

Additionally, in the Galenic view, blood was passed from the right side of the heart to the left side through pores, which was later shown to be incorrect as they do not exist within the ventricular septum, as demonstrated by Columbus (1516-1559), a Belgian anatomist. Columbus, during his many dissections, confirmed that venous blood of the right ventricle passed into the left ventricle through the lungs. This was concluded a few years earlier by Servetus (1511-1553), a Spanish theologian and physician. Thus, the open-circuit interpretation of the circulation by Galen cannot accurately describe the "circulation of blood".

In his many teachings, though some aspects were later known to be erroneous, Galen was the first to recognize that the walls of arteries are thicker than those of the veins and that arteries were connected to veins. It was the Persian physician Ibn an-Nafis (1210-1288) who claimed that venous blood of the right ventricle is carried by the artery-like vein into the lungs, where it mixes with the air and then into the left ventricle through vein-like artery.

Galilei (1564-1642) in his "Dialogue of the Two Sciences", which appeared in 1637, suggested the circulation of blood in a closed system. Centuries later today, the idea of the circulation of blood was credited to William Harvey (1578-1657), a contemporary of Galilei, in his now famous "De Motu Cordis and De Circulatione Sanguinis" (1628) presented to King Charles. He described in his "Anatomical Exercises" that "blood does continually passes through the heart" and that "blood flow continually out the arteries and into the veins". Harvey's work indicated the pulsatile nature of blood as a consequence of intermittent inflow, during roughly one-third of the heart cycle, now known as systole, in combination with essentially steady outflow through the periphery during the remaining cardiac period, the diastole.

Harvey's work was completed before Malpighi who worked with the aid of a compound microscope. He reported in 1661 the discovery of the capillaries linking the arterial circulation to the venous circulation, while he was working with the microscopic anatomy of the pulmonary parenchyma in the frog, a uni-ventricular amphibian. Dutch anatomist Van Leeuwenhoek (1632-1723) confirmed the capillaries in different organs of several animal species and established the concept of the

capillary bed. Bypassing the capillaries are the arterio-venous anastomoses, which are now known to perform the function of controlling blood flow.

German anatomist Henle discovered the smooth muscle cells in small arteries in 1841. Thus, this provided the first evidence that smooth muscle contributes to arterial contraction. But it is not until 1937 that Zweifach showed that active contractility of the microvessels is confined to those vessels with smooth muscle cells.

In the investigation of the microcirculation, credit was given to Hall, an English physiologist, first to differentiate the capillaries from arterioles. The fact that capillaries transfer water and water-soluble substances from the blood stream to surrounding tissues, was shown by Starling and is now known as the Starling's hypothesis. The measurement of capillary blood pressure by cannulation was first performed in 1930, by Landis, in the nail microvascular bed (Mayrovitz, 1998). The ultra-structure of the microcirculation has now been established from electron microscope studies.

French physiologist Claude Bernard in 1852 showed that stimulation of sympathetic nerves induces vasoconstriction and the concept of controlling blood flow by vasomotor nerves. Neural control of the circulation is an important aspect of assessing vascular function.

Fascinated by anatomic structure of the vascular tree, as an art, Leonardo da Vinci (1452-1519) made many detailed drawings of the constituent parts of the circulatory system. He apparently already knew that both the contraction and resting periods are necessary for the heart to function with a normal rhythm. His anatomic drawings of the heart and the perfusing arteries are, to a large extent, amazingly accurate. This includes drawings of the heart and the great vessels, together with the main, anterior descending and circumflex coronary arteries and their major branches. Several drawings of the heart valves, demonstrating how well the leaflets are arranged when the valves are closed, as well as the detailed anatomic drawing of the neck arteries in man with its branching morphology were also shown (Li, 2000). In these, both the length and angle of branching arteries are incredibly accurate. Vesalius (1514-1564), an anatomist, later provided a detailed drawing of the entire human vascular tree (Fig. 1.1.1).

DE HVMANI CORPORIS FABRICA LIBER III. 295  
INTEGRAE TORSIONIS  
ARTERIAE AB  
tribus liberis delineatio, duobus  
bus communis.  
TIVS MAGNAE  
OMNIBVS PARTIBVS  
proxime sequentibus Capiti

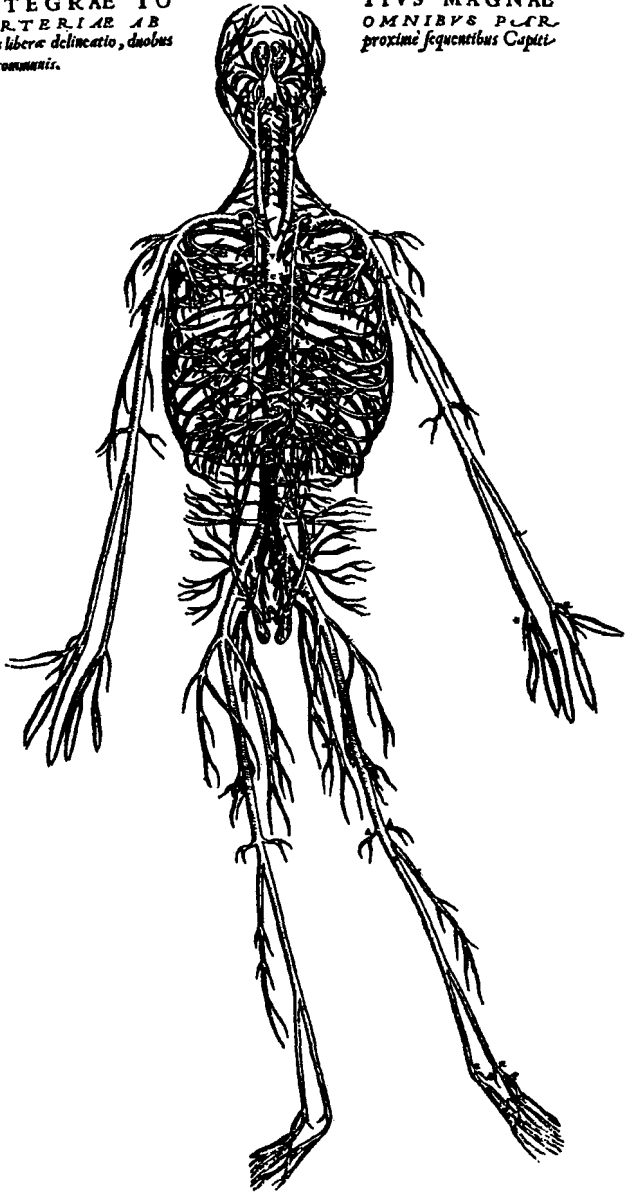


Fig. 1.1.1: Anatomic drawings by Vesalius. The extensiveness of the vascular tree is well appreciated.

Italian physician Caesalpinus apparently identified the pulmonary circulation and its two types of blood vessels: vena cava and pulmonary vein and pulmonary artery and aorta. Hooke (1635-1703; of Hooke's law of elasticity), an assistant of the English chemist Boyle (1627-1692; of Boyle's law of gases), recognized that respiration was necessary. But it was the English physiologist Lower (1631-1691) who continued the investigation to show the importance of ventilation-perfusion, i.e. exchange of gases between the lung and blood. Gas transport in blood was reported by Magnus in 1837. He demonstrated that there was greater oxygen content in arterial blood and greater carbon dioxide content in the venous blood. Other formed elements, such as hemoglobin were discovered by Funke in 1851 and has been shown as an oxygen transporter. Neural effect was shown by Haldane, that carbon dioxide is a normal physiologic stimulus for the respiratory centers. The Haldane effect is now well appreciated in respiratory function.

Lack of instrumentation, the measurements of the magnitudes of blood pressure and flow took considerably longer than the interpretation of the circulatory function. Hales in 1733 had incidentally already registered the magnitude of the blood pressure level about which blood oscillates. His initial measurement of blood pressure with a glass tube in a hare has been well illustrated in many publications. Thus, the magnitude of the mean arterial pressure and the amplitude of oscillation, or pulse pressure, were already known at that time. Hales' measurements however, did not induce recognition of the great importance of blood pressure magnitude for many decades. We now know that the increased magnitudes of mean blood pressure and pulse pressure are major contributors to hypertension and many forms of cardiovascular diseases.

The shape of the pressure pulse became known only in the 19th century when Ludwig came up with the kymograph which inscribed blood pressure waveforms. His instrument provided information within a single beat which was a truly a technological advance. Its accuracy was not comparable to present day instrument, although not an issue at the time. Blood pressure recording with the sphygmographs by Marey and his contemporary Mahomed has led to the clinical assessment of arterial diseases, such as hypertension. Incidentally, Chaveau and Marey (1863) also recorded cardiac chamber pressures. Both, shortly later, measured blood flow with an instrument they developed, now known as the bristle flowmeter.

Modern understanding of pressure-flow relationships came with the inventions of fluid-filled catheter-manometer system and the electromagnetic flowmeter. The simultaneous measurements of blood pressure and flow have led to considerable advancement of the studies of blood flow or hemodynamics. The catheter was introduced in man by Forssmann in 1929, and later advanced for catheterization of right heart for pressure measurement by Cournand and Range in 1941 (Li et al., 1976). Cournand and Forssmann shared the Nobel prize for medicine in 1956 for the invention leading to the advancement of modern day catheterization for visualization of blood pressure waveforms in various anatomical sites throughout the circulation. The electromagnetic flowmeter was introduced by Kolin in 1936. But ultrasonic transit-time and Doppler flow velocity probes have taken center stage in modern research and routine clinical measurements.

In an attempt to understand the function of the arterial system as a whole, Hales (1733) concluded that in order for the arteries to accept the large amount of blood ejected, or the stroke volume, the arteries must behave like a temporary storage reservoir. Since the size of the aorta is considerably smaller than that of the ventricle, the receiving aorta must be elastic in order to perform the function as a reservoir. This interpretation of the reservoir function of arteries became known later as the windkessel theory which was vigorously pursued a century later by a German physician Frank towards the end of the 19<sup>th</sup> century. The emphasis on the storage properties of the arteries modeled by Frank as a single elastic tube implied that all pressure fluctuations in the arterial tree should occur synchronously. In other words, the blood pressure pulse should propagate with infinite velocity. The peripheral vessels, on the other hand, are assumed rigid as stiff tubes. This gives rise to the lumped compliance-resistance model of the arterial circulation. This windkessel model lacks the description of the propagation characteristics of the pressure pulse.

Blood pressure pulse propagation with finite wave velocity in a blood vessel was considered over two centuries ago by Euler in 1775. He attempted to develop a formula for its calculation. The well-known physicist Young in 1816, and also the Weber brothers in 1866, apparently solved for the propagation velocity in an elastic tube

(Noordergraaf, 1969). Incorporating the elastic properties and geometry of the blood vessel, Moens (1878) and Korteweg (1878) separately developed what is now known as the Moens-Korteweg formula for the pulse wave velocity:

$$c_0 = \sqrt{\frac{Eh}{2r\rho}} \quad (1.1.1)$$

where  $E$  is, appropriately at the time, defined as the Young's modulus of elasticity of the blood vessel,  $h$  and  $r$  are the wall thickness and inner radius of the uniform cylindrical vessel, respectively, and  $\rho$  is the density of blood. Pulse propagation velocity is seen related to the mechanical and geometrical properties of the blood vessel.

## 1.2 Importance of the Vascular System

In terms of the dynamics of the vascular system, the function of the heart is to provide energy and perfuse organ vascular beds. For the heart to accomplish this efficiently, the vascular system plays a central role as the distributing conduits. Both the distributing arteries and the peripheral vascular beds present the load to the pumping heart. Peripheral resistance has been popularly viewed in the clinical setting as the vascular load to the heart. This applies mainly to steady flow conditions. This description is naturally inadequate, because of the pulsatile nature of blood flow which remains throughout the microcirculation. Pulsatility implies that there is an oscillatory or pulsatile contribution to the vascular load to the heart. The importance of pulsatility, though still under much debate, is nevertheless necessary in terms of synchronicity and efficiency.

The vascular system provides a seamless illustration of an efficient transport system. This can be seen from the function of, for instances, the coronary circulation in perfusing the heart, the renal circulation in perfusing the kidneys, the cerebral circulation in perfusing the brain and the pulmonary circulation in perfusing the lungs. By virtue of the distributing arterial trees, oxygen, humoral agents, and nutrients be transported to the vital parts of the body, and at the same time, removal of biological waste materials is also accomplished.

### 1.3 Modern Concepts

Modern development of the theory related to blood flow in the vascular system has included multi-faceted aspects, such as, fluid mechanics, fluid-vessel interface, vascular tissue engineering, pulse wave transmission and mathematical modeling.

The mathematical formulations of blood flow through viscoelastic arteries have been well established and documented in many texts (e.g. Noordergraaf, 1978; Li, 1987; Nichols and O'Rourke, 1998; Li, 2000). These texts also provided experimental measurement methods and quantitative approaches to the assessments of the state of the arterial circulation. There are also several texts in describing the microcirculation (e.g. Lee and Skalak, 1989; Fung, 1997)

In the application to clinical situations, the interpretation of the morphology of blood pressure and flow waveforms in relation to underlying diseased conditions has attracted the most attention. The introduction of new groups of drugs beyond vasodilators, beta adrenergic blockers, calcium channel blockers and angiotensin-converting enzyme inhibitors that includes local targeted vascular drug delivery, as well the beginning stages of gene therapy, to improve vascular perfusion and in the treatment of diseases, have become more *avant garde*.

Not only the arteries, the microcirculatory vessels are no longer viewed as resistance vessels, but are compliant with viscoelastic properties that vary with frequency. The classical elastic description of blood vessels has been modified to include viscosity of the blood and the vessel wall. The viscosity causes energy dissipation. Thus, the energy utilization and dissipation in relation to blood flow is now considered pertinent. Regarding  $\chi$ , or energy, the amount of the work that the heart has to generate during each beat has generated considerable attention. This included the steady energy dissipation through peripheral resistance vessels in different parts of the body, as well as energy required to overcome pulsations which persist even in the microcirculation.

Clinical applications of modern development of dynamics of the vascular system have initiated both invasive and noninvasive technological development and improvement in the accuracy of assessing

the vascular structure and function. These include laser-Doppler velocimeter, multi-sensor pressure-velocity catheter, magnetic resonance imaging and intravascular ultrasonic imaging. There are also advancements in the development of interventional devices, such as local drug delivery catheter, laser- or balloon-angioplasty catheter, vascular stents and grafts. Many of these have been used for the assessment and treatment of vascular hypertrophy, stenosis and aneurysm, hypertension and atherosclerosis.

#### **1.4 Book Contents**

This book deals primarily with the dynamic behavior of the components of the vascular system and methods and techniques for their quantitative measurements. The book was written applying fundamental physical principles in conjunction with physiological measurements to the analysis of the structural and functional aspects of the vascular tree that includes the arterial circulation, the venous circulation, and the microcirculation, inclusive of arterioles, capillaries and venules. In addition, the constituent components, such as collagen, elastin, smooth muscle, and endothelial and red blood cells as well as transport phenomena are also discussed. Quantitative approaches are emphasized in the overall treatment.

In Chapter 2, modern concepts of vascular biology are illustrated. This begins with the anatomical organization of the vascular tree. Major branches of the aorta and some arteries at similar anatomic sites in some mammalian species, such as human, dog and rats, are described. These latter are common mammalian species where experimental measurements and data are most frequently collected. Geometric nonuniformities in terms of tapering and branching of the vessels are quantified. The fractal nature of the vascular tree can be well appreciated from some of the illustrations. The distributing channels and networking environment are illustrated.

Examination of structural properties allows us to differentiate the mechanical and functional characteristics of various vessels. This includes the nonuniformities in elasticity reflected in the content and organization of the walls of the various blood vessels. Constituent

structural components of the arterial and venous wall are examined in rheological terms. In particular, the physical properties of elastin, collagen, and smooth muscle. The relative contents of the wall materials differentiate arteries from veins, arterioles and capillaries.

Oxygen is perhaps the most important component to be transported in the blood. The formed elements of blood are dealt with, that includes hemoglobin, red blood cells and plasma. Functional properties of blood are therefore included in this chapter. Some aspects of the circulating catecholamines and hormones, as well as neural control of the vascular system are equally important.

Chapter 3 deals with some fundamental concepts for analysis of the vascular system. The differences in their mechanical properties in large and small arteries and veins are examined. Their collective contributions to the overall function are analyzed. The arterial wall does not merely behave as an elastic vessel, therefore viscoelastic behavior becomes important. In this context, the viscous and elastic behavior of the composite, i.e., the arterial wall, is discussed. This includes the characteristics of a viscoelastic material, i.e. creep phenomenon, stress relaxation, and hysteresis. These aspects are also applied to veins, except the differences in distending pressures and collapsibility come into play.

Fundamental principles of fluid mechanics that includes classical laws and governing equations are provided. This includes Poiseuille's equation, Bernoulli's equation and the determining laminar and turbulent behavior in terms of Reynolds number. This is examined in terms of the rheology of blood flow to the containing vessel properties.

Engineering methods of basic analysis in the time domain, the Fourier analysis in the frequency domain are also included with examples that apply to the vascular system.

Chapter 4 deals with the hemodynamics of large arteries. Aorta is the largest artery whose distensibility and great compliance facilitates ventricular ejection in systole. The manner how ventricle and aorta interact will be explained, as well as the initial impulse aspect of ventricular ejection. The pulsatile wave transmission characteristics of blood pressure and flow and simplified mathematical description, and fundamentals of modeling are included. The description classic of the windkessel model of the arterial system is first introduced. The

windkessel is the mostly used lumped model and its analysis is elaborated in terms of total arterial system compliance and peripheral resistance. Extension of this model to more sophisticated later models include those that vary from a linear rigid tube model to a freely moving or constrained thin- or thick-walled, viscoelastic tube model. Some of these utilize Navier-Stokes equations describing fluid motion, Navier equations describing wall movement, and the equation of continuity describing the incompressibility of the blood. Experimental deviations from linear models are compared to nonlinear theories, so as to identify the regimes of nonlinearities.

Distributed model provide more precise descriptions of the pressure and flow behavior under varied conditions. However, they are generally complex and time-consuming in identify individual parameters, and less useful in daily clinical settings. Reduced models that are useful for practical and clinical applications are discussed. A recently introduced model to analyze the arterial wall behavior subject to varying pressure amplitudes in terms of pressure-dependent compliance is elaborated. This helps to explain the cyclical stress placed on the arterial wall and how the arterial wall adjust to rapidly changing pressure amplitudes.

Once models of the arterial system have been developed, it is necessary to verify the validity and limitations of these models. Such verifications depend often critically on the specific design of the experiments for measuring relevant hemodynamic parameters. For all practical purposes, these are pressure, flow, velocity, and vessel dimensions.

Pulsatile pressure and flow and their transmission characteristics are also the centerpoints of this chapter. Here, the peculiarities and features associated with pressure and flow waveforms measured in their respective anatomical sites are explained. How the vascular beds present as load to impede blood flow is quantitatively described in terms of the vascular impedance concept. Impedance, unlike resistance, which remains constant, is complex with its magnitude changes with frequency. Its usefulness is in its ability to include alterations in compliance, resistance and inertance. This provides a useful description of the changing arterial tree and individual vascular bed behavior. The manner

by which pressure and flow pulses propagate and reflect can also be quantified.

Chapter 5 addresses the vascular branching aspects of the circulation, whether of arterial, venous or capillary, except the latter two are dealt in more detail in subsequent chapters. Branching geometry is examined in terms of morphological measurements. The basic fluid mechanic aspects of vascular branching in terms of pressure and flow transmission, shear stresses are explained, best with illustrations and mathematical formulations.

How efficient the pressure and flow pulses transmit depends on the propagation and reflection characteristics through different arteries and vascular branching junctions. Pulse wave velocity, a popularly used index to describe the vascular stiffness, is dependent on the geometric and elastic properties of the local arterial wall. Its measurement is therefore, elaborated.

With differing vascular impedances, wave reflections arise, because of the mismatching in impedances. The large peripheral resistances in the arterioles are the principal sites contributing to reflections. Increased wave reflection increases blood pressure amplitude and thus decreases flow. This reduces the pulse transmission efficiency for the propagating pulse. Pulse transmission through vascular branching junctions is dictated by the local blood vessel properties. For forward traveling wave, it is practically impedance-matched, resulting in optimal transmission. For the backward traveling wave towards the heart, it is greatly attenuated at the vascular branching. Thus, the design of the arterial tree is to facilitate pulse transmission to vascular beds. How this is optimized is explained.

Chapter 6 deals with the less studied aspects of the venous circulation, because of its low pressure and collapsibility and less life-threatening behavior. Blood volume is the highest at rest in the venous circulation, giving rise to its reservoir-like properties. The functional aspects of collapsibility and venous valves are also discussed, in terms of pressure-flow relations and the waterfall hypothesis. Modeling aspect is given in terms of mathematical descriptions and hydrodynamic set-ups.

Chapter 7 deals with the microcirculation. The greatest drop in mean blood pressure is found in the arterioles, hence justifying the vascular

waterfall interpretation. How the contributions of the microcirculation to total peripheral resistance in its control of cardiac output are explained. The capillary circulation, for its vast networking and exchange environment is of utmost importance in terms of meeting the metabolic demand of the supplying tissues. The aspects of diffusion and cellular transports are of critical importance.

Thus, the design of the arterial tree is to facilitate pulse transmission to vascular beds. These latter are discussed in detail for their importance in both basic and clinical situations. Pulse pressure and flow remain pulsatile even in the microcirculation, albeit to a much more reduced amplitudes. The pulsatility facilitates capillary exchanges.

The final chapter deals with aspects of experimental methods, instrumentation and devices that are widely used for hemodynamic measurements. Clinically useful methods and instruments for invasive and noninvasive determination of blood pressure flow, and vessel dimensions are first described. This begins with the commonly used noninvasive methods, such as auscultatory method, the sphygmomanometer cuff method and tonometry. Invasive blood pressure measurement system such as catheter-pressure transducer combination is also evaluated in terms of its frequency response.

Blood flow measurement with both electromagnetic flowmeter and Doppler ultrasonic method are described, as well as the technique of thermodilution measurement of cardiac output. The combination of Doppler echocardiography and intravascular imaging devices now afford simultaneous flow velocity and lumen diameter measurements.

The aspect of cardiac assist device to aid the failing heart is well appreciated with the introduction of the intra-aortic balloon pump. Our experience with this in-series cardiac assist device is illustrated in terms of hemodynamic function. The dynamics of the assisted circulation is examined in terms of different modes of mechanical assistance.

The overall function of the dynamics of the vascular system depends not only on the anatomical structure of the individual vessels, but also on their multi-faceted functional interaction with neighboring and distant vessels. This will become apparent to the readers from the contents of this book.

## Chapter 2

# Vascular Biology, Structure and Function

### 2.1 Anatomical Organization of the Vasculature

#### 2.1.1 *The Circulatory System*

The heart, the arterial systems, the venous systems and the microcirculatory systems, coupled with neuro-humoral influences form the entire circulation. Each is an important functional complement that the circulatory system cannot be effectively described by one part alone. By virtue of the distributing vascular trees, oxygen, humoral agents, and nutrients are transported to the vital parts of the body and the waste products are removed. The heart provides the necessary energy.

In terms of the general structure components, Fig. 2.1.1 suffices to provide an overview of the connectivity of the circulation.

#### 2.1.2 *The Heart*

The heart in mammalian species has four chambers, the left ventricle, the right ventricle, left and right atria. The left ventricle pumps blood into the aorta and perfuse the systemic arterial system and the right ventricle pumps into the main pulmonary trunk and perfuse the pulmonary arterial tree.

The shape of the left ventricle is in-between conical and semi-ellipsoidal with its narrow end forming the apex of the heart. These shapes, as well as cylinder and sphere, have been used in ventricular modeling. The left ventricular wall is about three times as thick as the right ventricle, thus is able to develop a much higher pressure. The thick interventricular septum, separating the left and right ventricles, is more

closely associated with the pumping action of the left ventricle. The ventricle also contracts much more in the short-axis or circumferential direction than the long-axis or base-to-apex direction. The ventricles are made up of muscular fibers. This so-called "myocardium" can be further divided transmurally into the inner endocardium and the outer epicardium.

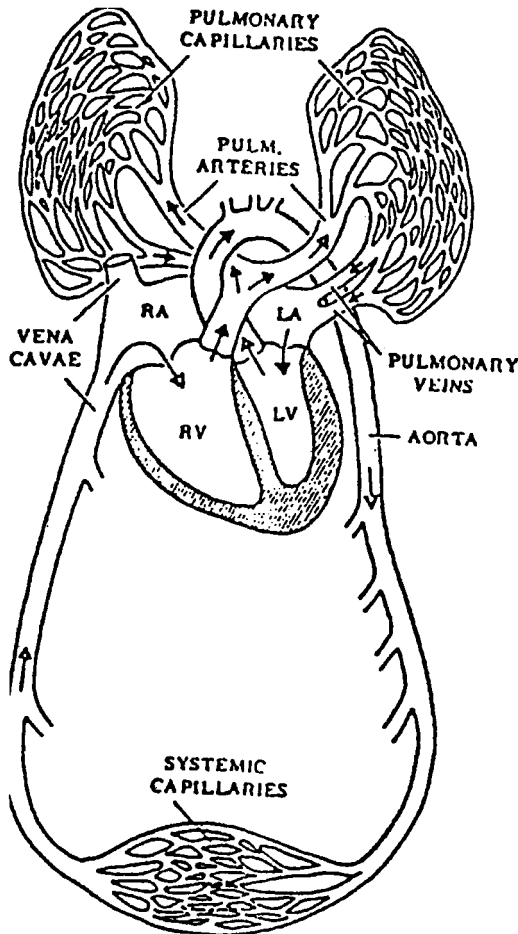


Fig. 2.1.1: Diagram illustrating the overall circulation. The four cardiac chambers (LV = left ventricle, LA = left atrium, RV = right ventricle, RA = right atrium) and systemic and pulmonary circulations are shown. Arrows indicate directions of blood flow.

There are four heart valves involved in the filling and pumping action of the heart. The mitral valve situates between the left atrium and the left ventricle. It controls the flow between these two chambers, but is a one-way valve. The tricuspid valve as the name implies has three cusps. These are the posterior, the septal, and the anterior. The cusps have similar geometric shapes. The right ventricle and the low-pressure pulmonary arterial system on the other hand, is separated by the pulmonary valve. The aortic valve separates the left ventricle from the ascending aorta leading to the high pressure systemic arterial system. These valves are tricuspid valves whose leaflets are of similar shape.

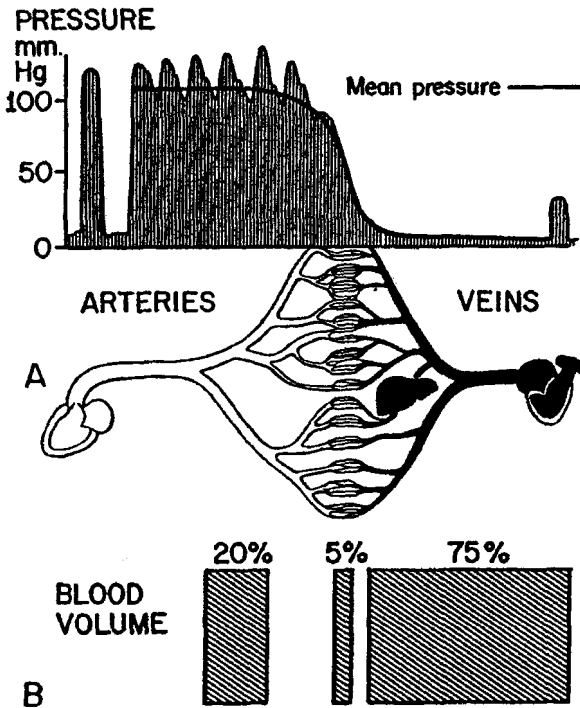


Fig. 2.1.2: Blood pressure and blood volume distribution of the systemic circulation. Notice the largest pressure drop occurs in the arterioles and the largest amount of blood volume reside in the veins which serve as reservoirs. From Rushmer (1972).

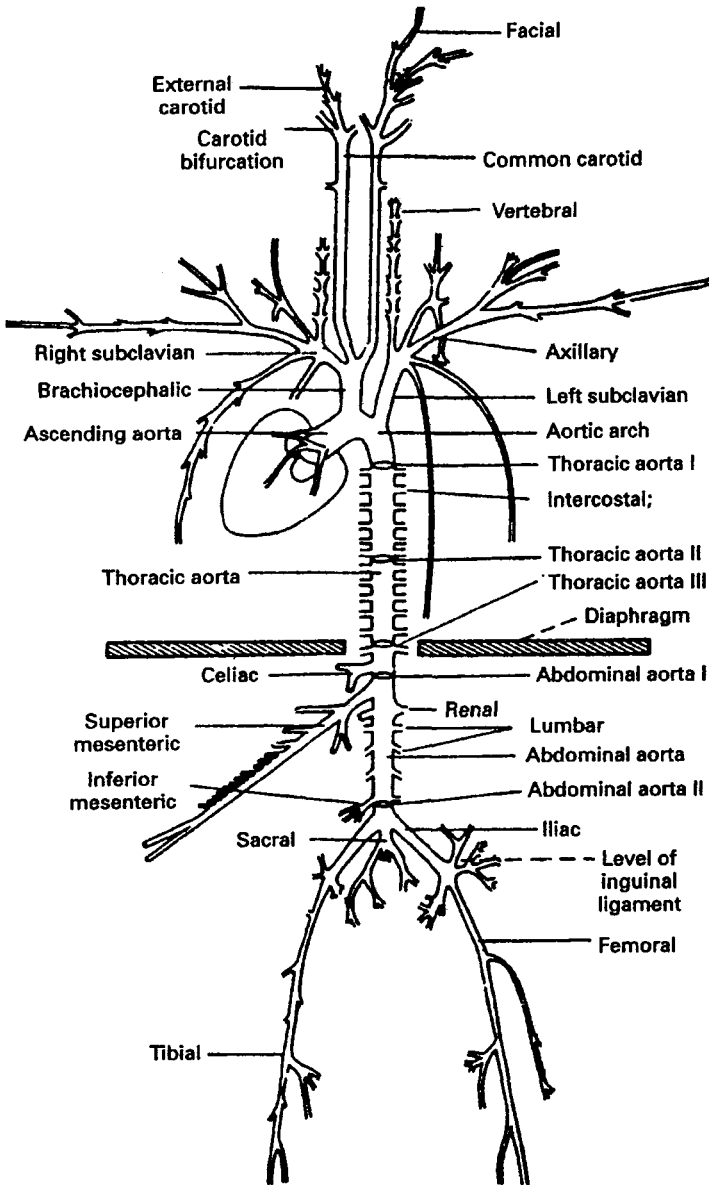


Fig. 2.1.3: Schematic representation of the arterial tree of a dog. Anatomic structures reveal geometric tapering and branching characteristics of the arterial system. From Nichols and O'Rourke (1998).

### ***2.1.3 The Arteries***

Anatomical descriptions of the human and other mammalian vascular trees can be found in many textbooks. For the purpose of illustrating the blood perfusion and pressure pulse transmission path, the major branches of the arterial tree are shown in Fig. 2.1.3.

There are considerable similarities among the corresponding anatomical sites of the mammalian arterial circulation (Li, 1996). The root of the aorta begins immediately at the aortic valve. The outlet of the valve sits the ascending aorta having the largest diameter. The first branching off the aorta are the left and right main coronary arteries. The aortic arch junction is formed by the ascending aorta, the brachiocephalic artery, the left subclavian artery, and the descending thoracic aorta.

There are numerous branches come off the descending aorta at right angles, renal arteries which perfuse the kidneys are such examples. The distal end of the descending aorta is the abdominal aorta which forms the aorto-iliac junction with left and right iliac arteries and its continuation. In the human, it is a bifurcation. The femoral artery, a well-known peripheral artery, because of its accessibility, continues from the iliac artery. These are the arteries perfusing the upper thighs, with the tibial arteries peruse the lower legs. The aorta has, comparatively speaking, the greatest geometric taper, with its diameter decreasing with increasing distance away from the ventricle. The common carotid arteries are the longest, relatively uniform vessels, with the least geometrical tapering. The brachial arteries perfusing the upper arms lead to distal radial arteries. Both brachial and radial arteries are the most common sites for noninvasive blood pressure monitoring.

### ***2.1.4 The Veins***

Arteries deliver blood from the ventricles to vascular beds, while veins return it to the atria. Veins, unlike arteries are generally thin-walled and have low distending pressures. They are collapsible even under normal conditions of blood pressure pulsation.

The inferior vena cava is the main trunk vein. The superior vena cava feeds into the right atrium and the main pulmonary vein leads into the left atrium with oxygen-enriched blood.

Veins have a greater total number than arteries and thus the venous system has a much larger cross-sectional area. This results in a much larger volume available for blood storage. Indeed, veins are known as low pressure storage reservoirs of blood. Under normal physiological conditions, the venous system contains about 75% of the total blood volume in the systemic circulation with the systemic arterial system constitutes some 15%. For this reason, veins are often referred to as capacitance vessels. Venous return is an important determinant of cardiac output. The pulmonary circulation contains about one quarter the blood volume of the systemic circulation.

Veins have much thinner walls and less elastins than arteries. Because of this, veins are stiffer than arteries. However, the low operating pressure and collapsibility allows veins to increase their volume by several times under a small increase of distending pressure.

There are bicuspid valves in veins. These valves permit unidirectional flow, thus preventing retrograde blood flow to tissues due to high hydrostatic pressures. These valves are notably present in the muscular lower limbs.

### ***2.1.5 The Microvasculature***

As stated previously, the function of the cardiovascular system is to provide a homeostatic environment for the cells of the organism. The exchange of the essential nutrients and gaseous materials occurs in the microcirculation at the level of the capillaries. These microvessels are of extreme importance for the maintenance of a balanced constant cellular environment. Capillaries and venules are known as exchange vessels where the interchange between the contents in these walls and the interstitial space occur across their walls.

The microcirculation can be described in terms of a network such as that shown in Fig. 7.1.1. It consists of an arteriole and its major branches, the metarterioles. The metarterioles lead to the true capillaries via a precapillary sphincter. The capillaries gather to form small venules, which in turn become the collecting venules. There can be vessels going directly from the metarterioles to the venules without supplying capillary beds. These vessels form arteriovenous (A-V) shunts

and are called arteriovenous capillaries. The capillary and venule have very thin walls. The capillary as mentioned before, lacks smooth muscle and only has a layer of endothelium. The smooth muscle and elastic tissue are present in greater amounts in vessels having vasoactive capabilities, such as arterioles. This is also the site of greatest drop in mean blood pressure. For this reason, arterioles are the principal contributors to peripheral vascular resistance that can effectively alter cardiac output.

The structural components of the microcirculation are classified into resistance, exchange, shunt, and capacitance vessels. The resistance vessels, comprising the arterioles, metarterioles, and precapillary sphincters, serve primarily to decrease the arterial pressure to the levels of the capillaries to facilitate effective exchange.

## **2.2 Mechanical Properties of Blood Vessels**

### ***2.2.1 Some Geometric Aspects of Blood Vessels***

The arterial system is a tapered branching system. Changes in lumen size are often associated with branching and appropriate tapering. In the normal arterial system, the branched daughter vessels are always narrower than the mother vessel, but with slightly larger total cross-sectional areas. This means that the branching area ratio, or the ratio of the total cross-sectional area of the daughter vessels to that of the mother vessel, is slightly greater than one. This has significance in terms of pulsatile energy transmission.

Arterial diameters and lumen areas of the vascular tree can be determined from postmortem cast or angio-radiography. Arteries in man and in dog retract some 25 to 40 percent when removed. It is therefore necessary that in-vivo lengths are restored and corresponding pressures are given. Under normal conditions, a higher distending pressure lead to greater lumen diameter. Arterial vessel dimensions have been provided for the dog (McDonald, 1974) and man (Westerhof et al., 1969). The latter were used for constructing the analog model of the human systemic arterial tree.

There are several branching junctions before the pulse reaches the vascular beds. In relation to this, the number of generations of blood vessels are given by Green (1950) and Iberall (1967).

Experimental data by Li (1987) gives typical values of internal diameters in a 20 kg dog: ascending aorta, 15 mm; abdominal aorta, 8 mm; femoral artery, 3 mm; small artery, 0.1 mm. These values reveal an appreciable "geometric taper" in the aorta from the root to the aortoiliac junction. Together with branching, it contributes to the "geometric nonuniformity, observed throughout the arterial system.

The term "geometrical taper" is appropriate when applied to a single continuous conduit, such as the aorta. The area change of the aortic cross section is close to an exponential form and can be expressed as:

$$A(z) = A(0)e^{-kz/r} \quad (2.2.1)$$

where:

$z$  = distance in the longitudinal axial direction along the vessel

$r$  = vessel lumen radius in cm

$k$  = taper factor, dimensionless

$A(0)$  = the cross-sectional area at the entrance of the vessel in  $\text{cm}^2$

$A(z)$  = the cross-sectional at distance  $z$  along the vessel in  $\text{cm}^2$

The vessel area is calculated, assuming a circular cross-section,

$$A = \pi r^2 \quad (2.2.2)$$

The taper factor  $k$ , can be readily obtained as

$$k = \frac{r}{z} \ln \frac{A(o)}{A(z)} \quad (2.2.3)$$

Taper factor,  $k$ , for the aorta has been reported to be in the range of 0.0314-0.0367 for 20-30 Kg dogs (Li, 2000). Geometric taper factor can change substantially during varied vasoactive conditions and in disease conditions. When vasoactive drugs are administered which have

differential effects on large and small arteries, changes in taper factors from normal can be quite pronounced.

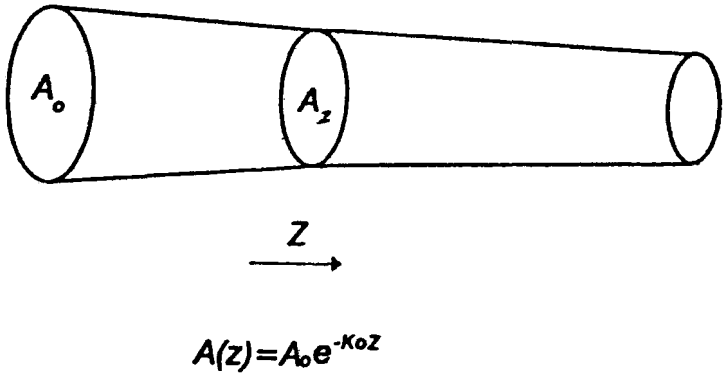


Fig. 2.2.1: Schematic diagram illustrating a blood vessel with geometric taper. The vessel diameter narrows with increasing distance ( $z$ ) away from the origin. Geometric taper, an exponential function of distance, is normally calculated from the change in cross-sectional areas ( $A$ ) as shown.

Alternative formula to calculate taper factor per unit length, or  $k_0$ , is expressed as follows:

$$A(z) = A(0)e^{-k_0 z} \quad (2.2.4)$$

The reported values of  $k_0$  obtained for the abdominal aorta, the iliac, femoral and carotid arteries are shown in Table 2.2.1. These are measured in vivo at a mean arterial pressure of about 90 mmHg. The average body weights of dogs used are about 20 kg. It is obvious from these data that the taper factor is smaller for smaller vessels. Carotid arteries have the least taper. They are thus the best approximation to a geometrically uniform cylindrical vessel.

Area ratios calculated for vascular branching junctions were about 1.08 at the aortic arch, and 1.05 at the aorto-iliac junction (Li et al., 1984). These values are slightly larger than 1.0. The hemodynamic consequences of these are discussed in Chapter 5.

Table 2.2.1: External diameters and taper factors.

	d (cm)	$k_o$ (cm <sup>-1</sup> )
Abdominal aorta	0.777	0.027±0.007
Iliac artery	0.413	0.021±0.005
Femoral artery	0.342	0.018±0.007
Carotid artery	0.378	0.008±0.004

In the broadest sense, the arterial wall (Fig. 2.2.2) consists of elastin, collagen, and smooth muscle embedded in a mucopolysaccharide ground substance. A cross section reveals the tunica intima, which is the innermost layer consisting of a thin layer (0.5-1  $\mu\text{m}$ ) of endothelial cells, connective tissue, and basement membrane. The next layer is the thick tunica media, separated from the intima by a prominent layer of elastic tissue, the internal lamina. The media contains elastin, smooth muscle, and collagen. The difference in their composition divides arteries into elastic and muscular vessels.

The relative content of these in different vessels is shown in Fig. 2.2.3. All vessels, including the capillary, have endothelium. The capillary does not have smooth muscle content and has only a single layer of endothelial cells. The outermost layer is the adventitia which is made up mostly of stiff collagenous fibers.

Elastic laminae are concentrically distributed and attached by smooth muscle cells and connective tissue. Longitudinally, we find that the number of elastic laminae decreases with increasing distance from the aorta, but the amount of smooth muscle increases and the relative wall thickness increases. Thus, the wall thickness to radius ratio, or  $h/r$  is increased. The net stiffness is also increased, accounting for the increase in pulse wave velocity towards the periphery. The mechanical behavior of peripheral vessels is largely influenced by the behavior of the smooth muscle, particularly by its degree of activation.

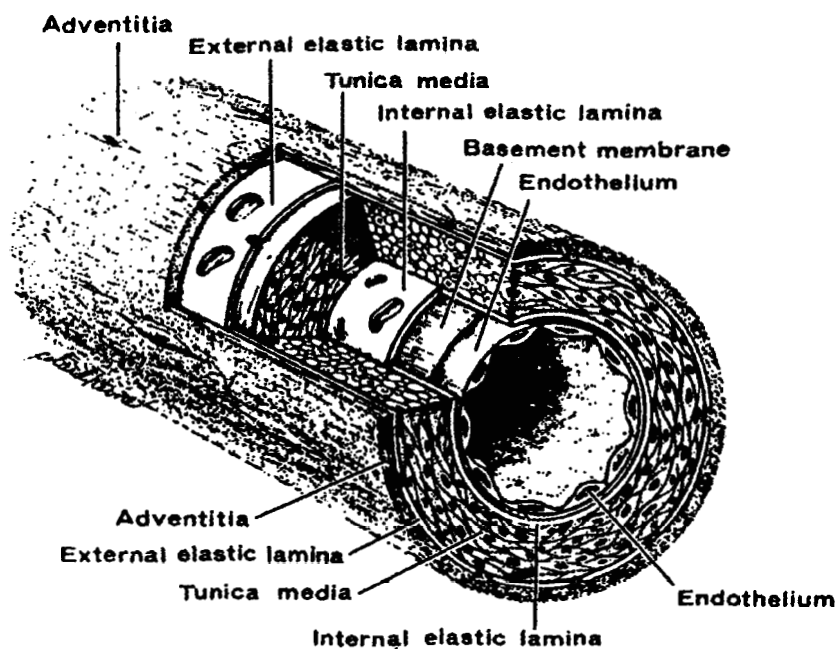


Fig. 2.2.2: Cross sections of the artery reveal three distinctive layers: the innermost tunica intima, the thick tunica media, and the outermost adventitia. From Fawcett (1994).

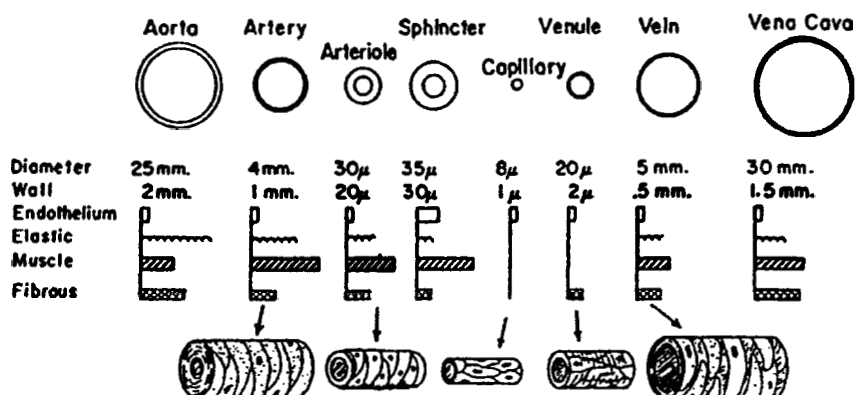


Fig. 2.2.3: Relative contents of endothelium, elastic and fibrous tissues, and smooth muscle in different vessels. Large arteries have more elastic and fibrous tissues while smaller arteries have more smooth muscle in the tunica media. From Rushmer (1972).

### 2.2.2 Vascular Stiffness and Elastic Properties

Vascular stiffness is traditionally expressed in terms of Young's modulus of elasticity, which gives a simple description of the elasticity of the arterial wall. Young's modulus of elasticity ( $E$ ) is defined by the ratio of tensile stress ( $\sigma_t$ ) to tensile strain ( $\epsilon_t$ ). When the relationship between stress and strain is a linear one, then the material is said to be Hookian, or simply, it obeys Hooke's law of elasticity. This normally applies to a purely elastic material. It is only valid for application to a cylindrical blood vessel when the radial and longitudinal deformations are small compared to the respective lumen diameter or length of the arterial segment.

For the following analysis of the physical aspect of an artery, we shall consider a segment of the artery represented by a uniform isotropic cylinder with radius  $r$ , wall thickness  $h$ , and segment length  $l$ . Isotropy implies the uniform physical properties of the content of the arterial wall. The arterial wall is actually anisotropic, consisting of various components discussed above, and the assumption of isotropy can not be exactly true. Although a gross approximation, this assumption allows simple descriptions of the mechanical properties of the arterial wall to be obtained.

Young's modulus of elasticity in terms of tensile stress and tensile strain is:

$$E = \frac{\sigma_t}{\epsilon_t} \quad (2.2.5)$$

Stress has the dimension of pressure, or force ( $F$ ) per unit area ( $A$ ),

$$\sigma_t = \frac{F}{A} = P \quad (2.2.6)$$

where  $P$  is pressure, in mmHg or dynes/cm<sup>2</sup>. Thus, stress has the dimension of mmHg or dynes/cm<sup>2</sup> in cm-gm-sec or CGS units. The conversion of mmHg to dynes/cm<sup>2</sup> follows the formula that expresses the hydrostatic pressure above atmospheric pressure:

$$P = h \rho g \quad (2.2.7)$$

where  $h$  is the height in terms of the mercury column,  $\rho$  is the density of mercury, or  $13.6 \text{ gm/cm}^3$ , and  $g$  is the gravitational acceleration. Hence  $100 \text{ mmHg}$ , or  $10 \text{ cmHg}$ , is equivalent to

$$P = 100 \text{ mmHg} = 10 \times 13.6 \times 980 = 133,280 \text{ dynes/cm}^2 \text{ or about } 1.33 \times 10^5 \text{ dynes/cm}^2. \quad (2.2.8)$$

Strain in the longitudinal direction, or along the length of the blood vessel is expressed as the ratio of extension per unit length, or the ratio of the amount stretched longitudinally to the length of the original vessel segment,

$$\varepsilon_l = \frac{\Delta l}{l} \quad (2.2.9)$$

Strain in the radial direction, or perpendicular to the vessel segment length, is the fraction of distention of the vessel lumen radius or diameter. It is given by :

$$\varepsilon_r = \frac{\Delta r}{r} \quad (2.2.10)$$

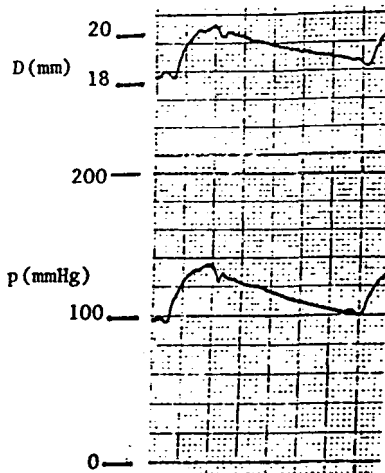


Fig. 2.2.4: Ultrasonic dimension gages recorded diameter of the aorta, together with aortic blood pressure. Calculation of radial strain can be obtained from the fractional change in diameter,  $\Delta D/D$ .

As an example, the radial strain calculated from an ultrasonic dimension gage recording of the aortic diameter shown in Fig. 2.2.4 is

$$\varepsilon_r = \frac{1.93}{19.3} = 0.1 \quad (2.2.11)$$

In this case, the fractional change in diameter, or  $\Delta D/D$ , represents the radial strain.

For a blood vessel considered to be purely elastic, Hooke's law applies. To find the tension ( $T$ ) exerted on the vessel wall due to intraluminal blood pressure distention, Laplace's law is useful. Laplace's law describes the tension exerted on a curved membrane with a radius of curvature. In the case of blood vessel, there are two radii of curvature, one that is infinite in the longitudinal direction along the blood vessel axis and the other is in the radial direction. Thus, Laplace's law for an artery can be written as:

$$T = p \cdot r \quad (2.2.12)$$

This assumes the vessel has a thin wall or that the ratio of vessel wall thickness ( $h$ ) to vessel lumen radius ( $r$ ) is small, or  $h/r \leq 1/10$ . Here  $p$  is the intramural-extramural pressure difference, or the transmural pressure. When the vessel wall thickness is taken into account, the Lamé equation becomes relevant:

$$\sigma_t = \frac{pr}{h} \quad (2.2.13)$$

Arteries have been assumed to be incompressible. Although not exactly so, this is in general a good approximation. To assess the compressibility of a material, the Poisson ratio is defined. It is the ratio of radial strain to longitudinal strain. We obtain from the above definitions, the Poisson ratio as:

$$\sigma = \frac{\varepsilon_r}{\varepsilon_l} = \frac{\Delta r / r}{\Delta l / l} \quad (2.2.14)$$

When radial strain is half that of longitudinal strain, or when  $\sigma = 0.5$ , the material is said to be incompressible. This means that when a cylindrical material is stretched, its volume remains unchanged. Or, in the case of an artery, when it is stretched, its lumen volume remains unchanged. Experimental measurements to obtain the Poisson ratio for arteries have shown  $\sigma$  to be close to 0.5. Arteries, therefore, can be considered to be close to being incompressible.

The above analysis assumes an isotropic arterial wall. The non-isotropy, or anisotropy is seen in the various differences in the relative content and physical properties of the arterial wall. Collagen is the stiffest wall component, with an elastic modulus of  $10^8 - 10^9$  dynes/cm<sup>2</sup>. This is some two orders of magnitude larger than those of elastin,  $1-6 \times 10^6$  dynes/cm<sup>2</sup>, and smooth muscle,  $0.1-2.5 \times 10^6$  dynes/cm<sup>2</sup>.

Elastin is relatively extensible, but is not a purely Hookean material. Collagen on the other hand is relatively inextensible, because of its high stiffness. Much more is known about vascular smooth muscle. Mechanical properties of arterial vessel walls can also be altered by neural mechanisms and by circulating catecholamines, such as norepinephrine. The composite of the arterial wall components operates in such a manner that at low pressures, elastin dominates the composite behavior. At high pressures, collagen becomes more important. Elastic modulus is a nonlinear function of pressure. The pressure dependence of the mechanical properties of arteries has been reported by several investigators (e.g., Cox, 1975; Wezsacker and Pascal, 1982; Drzewiecki et al, 1997). Fig. 2.2.5 illustrates how arterial lumen diameter and compliance vary with changing transmural pressure. With increasing positive transmural pressure, arterial vessel diameter is distended (Wezsacker and Pascal, 1982), as expected, the corresponding compliance however, declines. With negative transmural pressure, the arterial area compliance decreases as the artery is under collapse. The decrease in compliance with increasing transmural pressure follows a negative exponential function.

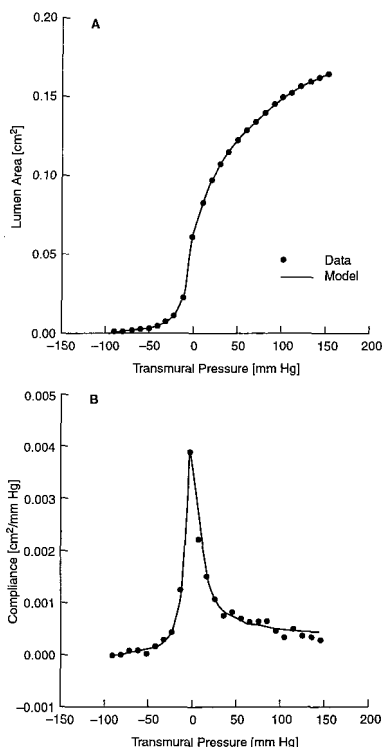


Fig. 2.2.5: Pressure dependence of mechanical properties of arteries is demonstrated in these figures. A. Lumen diameter increases with transmural pressure, following an S-shape. B. Area compliance plotted as a function of both positive and negative transmural pressures. Compliance decreases with increasing pressure when the transmural pressure is positive and when the vessel is collapsing with negative transmural pressure. From Drzewiecki et al. (1997).

Along the arterial tree, longitudinally, we find that the number of elastic laminae decreases with increasing distance from the aorta, but the amount of smooth muscle increases and the wall thickness to radius ratio increases. The stiffness is thus increased. This latter phenomenon accounts for the large increase in pulse wave velocity (Chapter 4). The mechanical properties are largely influenced by the behavior of the smooth muscle. Its elastic properties and activation have attracted considerable interests. A longitudinal section also reveals a helical organization of the collagen fiber network. It is this network that contributes mostly to the anisotropic properties of the arterial wall.

## 2.3 Functional Properties of Blood

Blood is the principal vehicle and medium that serves to provide nutrients and remove waste products throughout the complex multi-cellular constituents of the body organs. It consists of a plasma fluid with a number of formed elements.

### 2.3.1 Blood Plasma and Blood Gas

Blood plasma is about 90-95% water and contains numerous dissolved materials that include proteins, lipids, carbohydrates, electrolytes, hormones and pigments. It is the proteins that dominant the characteristics of the plasma, which has a specific gravity (SG) of plasma, which is about 1.028.. These are albumin, globulin and fibrinogen. The principal concentration by weight through fractionation electrophoresis shows that albumin which has the lowest molecular weight (69,000) exhibits the highest concentration of some 55%, followed by globulin (80,000-200,000) of about 38% and largest molecular weighted fibrinogen (350,000-400,000) of just 7%.

These proteins play an important functional role in viscosity, osmotic pressure and suspension characteristics of the plasma. Gases, such as oxygen and carbon dioxide are dissolved in the blood plasma. Their partial pressures can be derived from gas laws. We know that for an ideal gas, the pressure, volume and temperature are related by the gas law:

$$PV = nkT \quad (2.3.1)$$

where P is the pressure, V is the volume, n is the number of gas molecules, k is Boltzmann's constant, and T is absolute temperature in Kelvin. The concentration,  $C_c$ , is normally expressed in terms of moles per unit volume,

$$C_c = \frac{n}{N_A V} \quad (2.3.2)$$

where  $N_A$  is the Avogadro's number. Substitute for the universal gas constant  $R=kN_A$  we have

$$P = C_c RT \quad (2.3.3)$$

The partial pressure of a gas mixture,  $p_i$ , can be calculated knowing the molar fraction of the gas,  $f_i$ , and the total pressure,  $P$ , i.e.

$$p_i = f_i P \quad (2.3.4)$$

When a gas with partial pressure  $p_i$  is in contact with a liquid, some of the gas will be dissolved in the liquid. Here we can define the solubility which is related to the concentration  $c_i$  of the gas, and its partial pressure:

$$S_i = \frac{c_i}{p_i} = \frac{n}{p_i V} \quad (2.3.5)$$

Solubility in general is dependent on the total pressure above the liquid and temperature. Solubility of some gases in blood plasma is shown in Table 2.3.1.

Table 2.3.1 Solubility of gases in blood plasma.

Gas	Solubility in Molar/mmHg
O <sub>2</sub>	1.4 x 10 <sup>-6</sup>
CO <sub>2</sub>	3.3 x 10 <sup>-5</sup>
CO	1.2 x 10 <sup>-6</sup>
N <sub>2</sub>	7 x 10 <sup>-7</sup>
He	4.8 x 10 <sup>-7</sup>

### 2.3.2 Oxygen Saturation Curves and Hemoglobin

The binding of oxygen with hemoglobin provides an efficient transport system to deliver and maintain a desirable amount of tissue and organ oxygenation. The oxygen saturation curve follows an S-shape as shown in Fig. 2.3.1. At a partial pressure of 100 mmHg, typical in the lungs and in arteries, hemoglobin is about 97% saturated. In veins and some tissues, the partial pressure of oxygen is about 40 mmHg, here the saturation decreases to 75% or so. Since the slope of the curve changes greatly at this level, hemoglobin can easily give up its carrying oxygen readily when the metabolic need arises. This is accompanied by a drop

in the partial pressure of oxygen, hence a reduced saturation of hemoglobin. Thus, the oxygen transport system is ideally designed to perform the tasks of on-demand metabolic adjustments. This is even better illustrated when oxygen is transferred from hemoglobin to myoglobin during greater muscle tissue demand. The affinity of myoglobin for oxygen is significantly greater than that of hemoglobin.

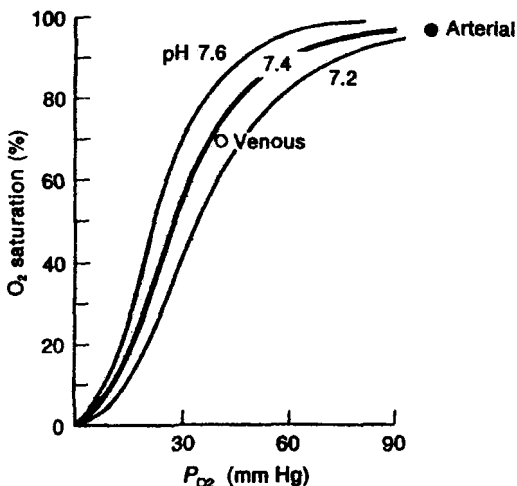


Fig. 2.3.1: Oxygen saturation curve displaying its S-shaped characteristics. Normal arterial and venous blood  $O_2$  saturations are also indicated.

The oxygen affinity decreases with decreasing pH. This is termed the Bohr effect by which changes in blood  $PCO_2$  which affects blood pH, indirectly also influence hemoglobin-oxygen affinity.

Hemoglobin consists of four polypeptide chains or globins and four disc-shaped molecular ring or *heme* groups, allowing binding of four oxygen molecules. Once bound with oxygen, the iron atoms in hemoglobin gives it the red color. Optical absorptions of hemoglobin and oxy-hemoglobin (Fig. 2.3.2) can be readily monitored by near-infrared spectroscopy. The isobestic point, when the two absorptions are equal which can be used as a reference, is at 805 nm.

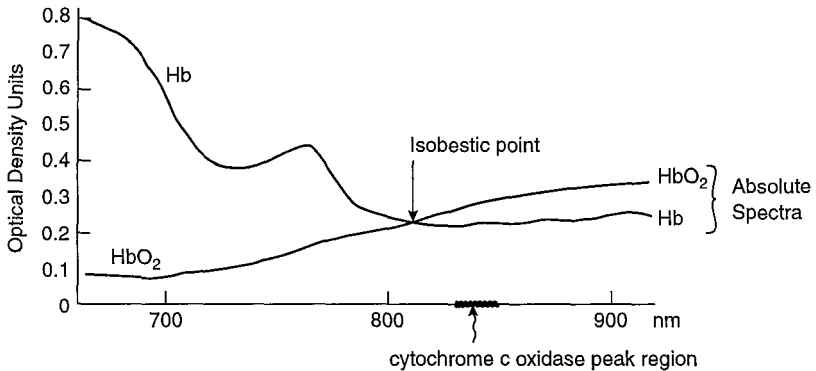


Fig. 2.3.2: Optical absorptions of hemoglobin and oxy-hemoglobin. The isobestic point is at 805 nm. Cytochrome c oxidase absorption region is also indicated.

### 2.3.3 Red Blood Cells, Hematocrit and Blood Volume

The principal formed elements are erythrocytes or red blood cells (RBC or rbc), leukocytes or white blood cells and thrombocytes.

The principal function of the red blood cell is in the transport of oxygen (O<sub>2</sub>) and carbon dioxide (CO<sub>2</sub>). The concentration of hydrogen ion (pH) determines the acidity/alkalinity. These three quantities (pO<sub>2</sub>, pCO<sub>2</sub> and pH) are the principal components involved in the blood gas analysis. Some of the definitions from blood sample analysis are shown below:

$$pH = \frac{1}{\log[H^+]} \quad (2.3.6)$$

$$\text{Hematocrit, or Hct(\%)} = \frac{\text{Red Blood Cells}}{\text{Blood}} \times 100 \quad (2.3.7)$$

$$Fcr = \frac{\text{Hct}(\text{totalbody})}{\text{Hct}(\text{venous})} \quad (2.3.8)$$

Mean corpuscular volume is defined as

$$MCV = \frac{\text{HematocritRatio} \times 10^3}{\text{RBCcount}(10^6 / \text{mm}^3)} \quad (2.3.9)$$

Mean corpuscular hemoglobin is defined as

$$MCH = \frac{\text{Hemoglobin}(g/L)}{\text{RBCcount}(10^6 / \text{mm}^3)} \quad (2.3.10)$$

Blood volume is normally determined by the sum of the red blood cell volume ( $V_{rbc}$ ) and the plasma volume ( $V_p$ ):

$$V_B = V_{rbc} + V_p \quad (2.3.11)$$

The total blood volume in a normal 70 Kg adult is about 5 liters. This value is not constant and changes according to properties of the vascular system and activity.

Although total blood volume (TBV) can be obtained from dilution techniques, an estimate of the total blood volume can be obtained from a single determination of red blood cell volume or plasma volume and corrected venous hematocrit from the following expressions:

$$BV = \frac{V_p}{(100 - Hct) \times Fcr} \quad (2.3.12)$$

$$BV = \frac{V_{rbc}}{Hct \times Fcr} \quad (2.3.13)$$

Indicator dilution techniques, are commonly employed in the determination of blood volume. For instance, for the determination of plasma volume, small amount (5 microcurie) of radioactively isodinated ( $I^{125}$ ) serum albumin (RISA) is injected into the circulation and its concentration sampled. For determination of red blood cell volume, radioactive labeling (e.g. chromium  $^{51}\text{Cr}$ ) of red blood cells have been used and again, concentration of injected sample determined for a prescribed intervals.

Data from Altman and Dittmer (1961) have shown that in more than one hundred mammalian species, the red blood cells are of similar size. If we compare the size of red cells from various mammals, we find the perhaps surprising fact that their diameters seem to be rather uniform and independent of mammalian body size (Table 2.3.2).

Table 2.3.2: Diameters of red blood cells (RBC) of some mammalian species.

Species	Body weight (kg)	RBC Diameter (um)
Shrew	.01	7.5
Mouse	.20	6.6
Rat	.50	6.8
Dog	20	7.1
Man	70	7.5
Cattle	300	5.9
Horse	400	5.5
Elephant	2000	9.2

## 2.4 Control Aspects of the Vascular System

Homeostasis and overall control of the circulation hinge on the regulation and control of blood pressure and maintaining adequate perfusion to vital organ vascular beds. In addition, the delivery of oxygen and nutrients and the removal of carbon dioxide and metabolic waste products are also important considerations. Controlling blood pressure is necessary to ensure adequate and on-demand supply of blood to the heart and the brain and, also, to the rest of the body organs. Control of capillary pressure is necessary to maintain tissue volume and the composition of the interstitial fluid within desirable ranges

Various receptors of the body are anatomically structured to sense and monitor the state of the heart and the vascular system. In response to sensory inputs from these receptors, either individually or in an integrated manner, both neural and chemical signals induce adjustments to maintain arterial pressure, blood flow and other hemodynamic variables.

### ***2.4.1 Control of the Central Cardiovascular System***

Arterial baroreceptors sense and monitor blood pressure at various sites in the cardiovascular system. They are principally located at the aortic arch and the carotid sinus. Responses from these baroreceptors, together with those of chemoreceptors are transmitted to the brain. The chemoreceptors which monitor the  $\text{CO}_2$ ,  $\text{O}_2$ , and pH of the blood are located principally at the aortic body and the carotid body.

There are also mechanoreceptors in the heart (i.e. atrial mechanoreceptive afferent fibers), as well as thermoregulatory receptors, that initiate appropriate reflex effects on the overall cardiovascular system. Additionally, skeletal muscle contraction or changes in the composition of the extracellular fluid of tissues can activate afferent fibers which are embedded in the muscle or tissue to cause changes in the cardiovascular system.

Sensory inputs are temporally and spatially integrated at regions that contain neurons in the brain occupying space known as the cardiovascular center. This region is located at the medulla oblongata and pons. The medullary cardiovascular center also receives inputs from other regions of the brain, including the medullary respiratory center, hypothalamus, and cerebral cortex. The output from the medullary cardiovascular center feeds into sympathetic and parasympathetic autonomic motor neurons that innervate the heart and the smooth muscle of arterioles and veins, as well as to other brain neurons.

The autonomic nervous system consists of two principal trunks: the sympathetic nervous system and the parasympathetic system. Stimulation of sympathetic nerves increases the rate and force of contraction of the heart and causes vasoconstriction which increases arterial blood pressure. The stimulation of parasympathetic nerves, causes a decrease in arterial blood pressure. The opposing effects of these two systems on blood pressure are sensed by two functionally different regions of the medullary cardiovascular center. These are known as the pressor and depressor regions. Stimulation of the pressor center results in sympathetic activation and an increase in blood pressure. Stimulation of the depressor center results in parasympathetic activation and a decrease

in blood pressure. Figure 2.4.1 presents one scheme that summarizes the overall central cardiovascular system control.

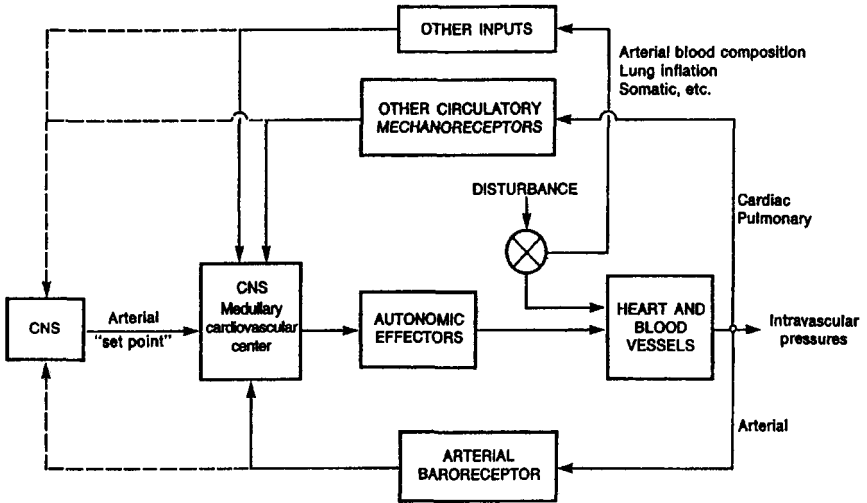


Fig. 2.4.1: A schematic illustration of the cardiovascular control system. A number of negative feedback loops are seen. Various receptors monitor changes in the state of the cardiovascular system, sending inputs to medullary cardiovascular center. From Randall et al. (1997).

### 2.4.2 Functions of the Baroreceptors

Baroreceptors are located in the carotid sinus and the aortic arch. There are two types of baroreceptors. The unmyelinated baroreceptors are localized in the central cardiovascular system and respond to pressures above normal and initiate reflexes to reduce arterial blood pressure. The myelinated baroreceptors respond to blood pressures below normal and thus protecting the cardiovascular system from prolonged reduction in blood pressure. The carotid sinus and aortic arch perform similar functions and differ only slightly in terms of structure.

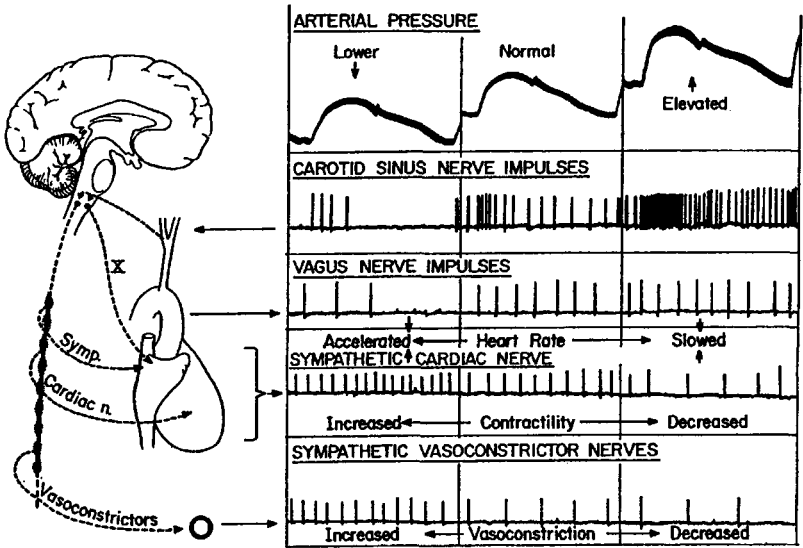


Fig. 2.4.2: Discharge frequencies of carotid sinus stretch receptors in the control of blood pressure, via sympathetic and vagal stimulations. From Rushmore (1972).

A perturbation that gives rise to an increase in blood pressure stretches the wall of the carotid sinus. This in turn causes an increase in discharge frequency from the baroreceptors (Fig. 2.4.2). When the pressure is low, the pressor-receptor impulse frequency decreases, the vagus nerve impulses diminish and sympathetic cardiac nerve impulses increase to accelerate the heart rate. This is accompanied by increased activation of sympathetic vasoconstrictor fibers. The result is an increase in peripheral resistance, hence an increase in blood pressure towards normal level. With an increase in blood pressure the carotid sinus impulse frequency decreases, reducing the sympathetic discharge and increasing the vagal discharge. The accompanied slowing in heart rate and peripheral vasodilation restores blood pressure to normal level.

A sigmoidal relationship between blood pressure and baroreceptor impulse frequency has been found and the system is most sensitive over the physiological range of blood pressures. It has been shown that the baroreceptor discharge frequency is higher when pressure is pulsatile

than when it is steady and that the carotid sinus baroreceptors are most sensitive to frequencies of pressure oscillation between 1 and 10 Hz.

An increase in blood pressure sensed by baroreceptors is signaled to the medullary cardiovascular center, which in turn, through autonomic motor neurons, initiates a reflex reduction in both cardiac output and peripheral vascular resistance. The reduction in cardiac output results from both a decreased heart rate and a reduced force of cardiac contraction results in a decrease in arterial blood pressure. Thus the baroreceptor reflex of the carotid sinus is a negative feedback loop that tends to stabilize arterial blood pressure at a particular set point. This set point concept has been instrumental in understanding many physiological control mechanisms.

### *2.4.3 Arterial Chemoreceptors*

Chemoreceptors are located in the carotid and aortic bodies. These chemoreceptors respond with an increase in discharge frequency to an increase in  $\text{CO}_2$  or to decreases in  $\text{O}_2$  and reduced pH of the blood perfusing the carotid and aortic bodies. Because  $\text{CO}_2$  and  $\text{O}_2$  are intimately related to the ventilation-perfusion process, chemoreceptors are particularly important in regulating ventilation.

An increase in discharge frequency of the chemoreceptor results in peripheral vasoconstriction and a slowing of the heart rate. Vasoconstriction can result in an increase in blood pressure, which in turn can stimulate the baroreceptor to cause a reflex decrease in blood pressure. Thus, chemoreceptors have a direct effect on heart rate and an indirect effect on blood pressure.

Smooth muscle can exert influence on large vessels such as the aorta. Its activity in smaller arteries is greater, because of the increased wall thickness to radius ratio. With varied vasoactivity, arterial lumen can be modulated to regulate perfusion. Fig. 2.4.3 illustrates this. Considerable variations in the constituent wall components, collagen, elastin and smooth muscle can be observed. Geometric change, such as the increased wall thickness to radius ratio is clearly visible.

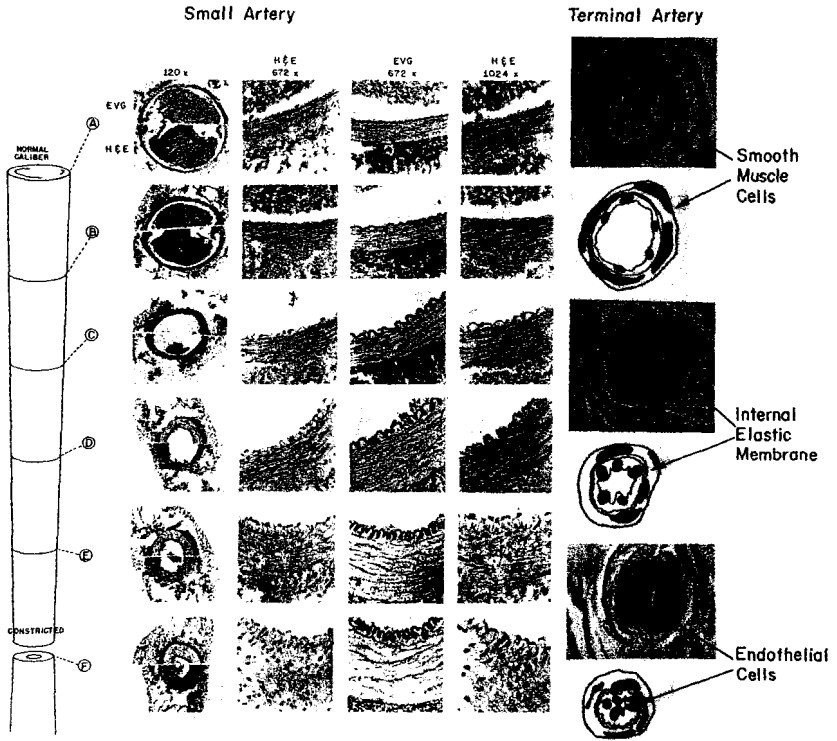


Fig. 2.4.3: Effects of vasoactivity on arterial lumen diameters. With vasoconstriction the lumen size decreases significantly (A through F) with corresponding increase in wall thickness. The relative changes in constituent components are also shown on the right panels. From Rushmer (1972).

## Chapter 3

# Physical Concepts and Basic Fluid Mechanics

### 3.1 Basic Mechanics and Dimensional Analysis

#### *3.1.1 Mass, Length and Time System and the Pi-Theorem of Buckingham*

Description of physical quantities requires the use of dimensions. The mass (M), length (L) and time (T) representation of a physical variable or parameter, or the so-called the MLT system is the most common. Dimensional analysis has its well-founded place in the physical sciences and engineering.

We must differentiate between physical quantities and physical constants. The former always possess units, while the latter are not always dimensionless (e.g. Planck's constant). The use of Buckingham's Pi-theorem for dimensional analysis requires all physical quantities be expressed in M (mass), L (length) and T (time). The theorem has wide applications, as will be shown later.

Dimensional homogeneity, another requirement in order to use the Pi-theorem, was first proposed by Fourier in 1882, who stated that any equation applied to physical phenomena or involving physical measurements must be dimensionally homogeneous. Its usefulness can be found in the Navier-Stokes equations describing incompressible fluid flow in the longitudinal direction, for instance, (in cylindrical coordinates). Every term in the equation has the dimension of a pressure gradient, or  $M^1L^{-2}T^{-2}$ .

Many dimensionless numbers have found their way through the use of the dimensional matrix. The matrix comprises columns representing physical quantities, while rows are filled with basic units (M, L, T). To

form a dimensional matrix, a priori knowledge of pertinent physical parameters is necessary. For instance, if 8 physical quantities are important for the description of blood flow in arteries, and there are 3 basic units (M, L, T) to represent them, then we are able to obtain  $8 - 3 = 5$  dimensionless Pi-numbers. In general, the number of dimensionless Pi-numbers are determined by the number of physical quantities minus the rank of the dimensional matrix.

To use the MLT system, one needs to first express explicitly any variable in its physical units, either using the CGS (cm,g,s) or the MKS (m,Kg,s) system or SI units of representation. For instance, blood pressure is commonly measured in mmHg and must be converted to  $\text{g/cm s}^2$ . Thus, pressure (p) is given as force per unit area,

$$p = \frac{F}{A} = [M][L]^{-1}[T]^{-2} \quad (3.1.1)$$

where A has the dimension of  $\text{cm}^2$ , or  $[L]^2$ , and force is mass times acceleration,

$$F = m \cdot a = [M][L]/[T]^2 \quad (3.1.2)$$

where a is the acceleration in  $\text{cm/s/s} = \text{cm/s}^2$ .

The left ventricular volume V, has the unit of ml or  $\text{cm}^3$ , and a dimension of

$$V = [L]^3 \quad (3.1.3)$$

The aortic flow Q, as a rate of change of ventricular volume, has the unit of ml/s, or

$$Q = \frac{dV}{dt} = [L]^3/[T] \quad (3.1.4)$$

Linear flow velocity has the dimension of

$$v = \frac{dz}{dt} = [L]/[T] \quad (3.1.5)$$

or with a physical unit of cm/sec;  $z$  is along the axis of the direction of blood flow.

Heart rate in beats per minute or second has the dimension of

$$f_h = [T]^{-1} \quad (3.1.6)$$

### 3.1.2 Dimensional Matrix

When formulating a dimensional matrix, it is necessary to identify the parameters that are considered pertinent to the problem at hand. These parameters need to be expressed in terms of  $[M]$   $[L]$  and  $[T]$ . For example, given arterial blood pressure ( $P$ ), flow ( $Q$ ) and heart rate ( $f_h$ ), a dimensional matrix can be formed

$$\begin{array}{cccc} & P & Q & f_h \\ M & 1 & 0 & 0 \\ L & -1 & 3 & 0 \\ T & -2 & -1 & -1 \end{array} \quad (3.1.7)$$

This is therefore, a  $3 \times 3$  matrix, or a square matrix.

As another example, suppose that one wishes to examine the relationship between left ventricular wall tension ( $T$ ) and left ventricular diameter or radius ( $r$ ) and left ventricular pressure (knowingly, this is the Laplace's law), then a dimensional matrix can be formed in terms of the three parameters, prior to the application of Buckingham's Pi-theorem. This dimensional matrix is:

$$\begin{array}{cccc} & T & P & r \\ M & 1 & 1 & 0 \\ L & 0 & -1 & 1 \\ T & -2 & -2 & 0 \end{array} \quad (3.1.8)$$

Again, this is a  $3 \times 3$  square matrix.

### 3.1.3 Dynamics Similitude in Vascular Biology

Dimensionless numbers provide useful scaling laws, particularly in modeling and similarity transformation. Dimensional analysis is a powerful tool, not limited to just mathematics, physics and modeling, but has immense applicability to many biological phenomena.

Despite its many useful applications, dimensional analysis is not without shortfalls. For a given set of physical quantities and basic units, we can generate new dimensionless numbers, which are not necessarily always invariant for a given system. They cannot therefore, be regarded as similarity criteria. The definition of dimensionless numbers as similarity criteria (Stahl, 1963), is therefore inadequate.

Let us consider blood flow in vessels and see how similarity criteria are obtained. A dimensional matrix is first formed by incorporating parameters that are pertinent to the analysis. These are the fluid density ( $\rho$ ) and viscosity ( $\eta$ ), diameter (D) of the blood vessel, velocities of the flowing blood ( $v$ ) and of the pulse wave ( $c$ ). In terms of the dimensioning mass (M), length (L) and time (T) system, we can write down the following dimensional matrix,

	$\rho$	$c$	D	$\eta$	$v$
	(g/cm <sup>3</sup> )	(cm/s)	(cm)	(poise)	(cm/s)
M	1	0	0	1	0
L	-3	1	1	-1	1
T	0	-1	0	-1	-1
	$k_1$	$k_2$	$k_3$	$k_4$	$k_5$

(3.1.9)

where  $k_n$ 's are Rayleigh indices referring to the exponents of the parameters. According to Buckingham's Pi-theorem (Li, 1983, 1986), two dimensionless pi-numbers ( $5-3 = 2$ ) can be deduced.

Mathematically, we have

$$\pi_i = p^{k_1} c^{k_2} D^{k_3} \rho^{k_4} v^{k_5} \quad (3.1.10)$$

or in terms of M, L and T, then

$$\pi_i = (M^{k_1} L^{-3k_1} T^0) (M^0 L^{k_2} T^{-k_2}) (M^0 L^{k_3} T^0) \\ (M^0 M^{k_4} L^{-k_4} T^{-k_4}) (L^{k_5} T^{-k_5}) \quad (3.1.11)$$

Since pi-numbers are dimensionless, this means the exponent needs to be zero. Equating the exponents of M, L and T to zero and solve, we obtain two pi numbers or similarity criteria (Li, 1983):

$$\pi_1 = \frac{\rho v D}{\eta} = Re \quad \text{and} \quad \pi_2 = \frac{c}{v} = \frac{1}{Ma} \quad (3.1.12)$$

The first pi-number is clearly identified as the Reynolds number, Re. The second is the inverse of the Mach number, Ma. The Mach number is the ratio of flow speed to the local sonic speed, or in this case the ratio of flow velocity to the pulse wave velocity. It is also termed the velocity fluctuation ratio (VFR). Recalling that to assume linearity of the arterial system, the flow velocity should be small as compared to the pulse wave velocity, or that VFR should be small.

The requirements for dynamic similarity (Rosen, 1978) are that two flows must possess both geometric and kinematic similarity. Thus the effects of, for instance, viscous forces, pressure forces, surface tension, (Li, 1996) need to be considered. Here we have only the ratio of inertial forces to viscous forces i.e. Reynolds number, and the ratio of inertial forces to compressibility forces i.e. Mach's number or velocity fluctuation ratio. For a truly incompressible fluid,  $c \gg v$  such that  $Ma = 0$ . For the analysis of blood flow in arteries, both blood and arterial walls are normally assumed to be incompressible. The Poisson ratio ( $\sigma_p$ ) for the aorta is about 0.48 close to an incompressible material ( $\sigma_p=0.5$ ). The assumptions of linearity and linear system analysis applied to hemodynamic studies often require the ratio  $v/c \ll 1$ , or that the

diameter of the blood vessel is small as compared to the pulse propagation wavelength. This is justified during the large part of the cardiac cycle. At peak flow rates in early systole however, the ratio of  $v/c$  is large (but not exceeding 1), turbulence may ensue to produce nonlinear effects.

Reynolds number from eqn. (3.1.12) is seen to vary with body length dimensions, or the diameter of the aorta. One question immediately arises is that the resulting Reynolds numbers calculated for large mammals, such as the horse, show that turbulence may occur for a large portion of the systole in the aorta. But this may not necessarily be the case. It has been well documented that turbulence may not exist even for Reynolds number greatly exceeding the critical value of 2,000. It is only established that for Reynolds number under 2,000, turbulence does not normally occur. Again, this value was established under steady flow conditions in rigid tubes.

The arterial blood flow exhibits pulsatile characteristics and peripheral outflow occurs mostly in diastole. In systole during ventricular ejection, the aorta distends as a reservoir to accommodate the flow as described by the classic windkessel model of the arterial system. In concert with the pulsation, this compliance of the aorta acts to protect the peripheral vascular beds from sudden surges in pressure and flow. The compliance, defined as the ratio of change in volume due to a change in pressure,

$$C = dV/dP \quad (3.1.13)$$

is proportional to body weight. A larger volume change occurs in the aorta of a larger mammal and the longer effective length of the aorta and a much slower heart rate, all help to reduce the tendency of turbulence to reside in too large a portion of systole.

### ***3.1.4 Elastic and Viscoelastic Properties of Blood Vessels***

Many investigators have examined elastic properties of arteries. It is found that the stress-strain or length-tension relationship is nonlinear and thus does not obey Hooke's law. Arterial elasticity increases with extension and

the length-tension relation is curvilinear. Many experiments, however, were done in-vitro situations, having the advantage of well-controlled experimental conditions, but the disadvantage of extending the results to equate with in-vivo parametric changes.

A material that obeys Young's modulus of elasticity in terms of tensile stress and tensile strain is:

$$E = \frac{\sigma_t}{\varepsilon_t} \quad (3.1.14)$$

Stress has the dimension of pressure, or force (F) per unit area (A),

$$\sigma_t = \frac{F}{A} = P \quad (3.1.15)$$

where P is pressure, in mmHg or dynes/cm<sup>2</sup>. Thus, stress has the dimension of mmHg or dynes/cm<sup>2</sup> in cm-gm-sec or CGS units.

Strain in the longitudinal direction, or along the length of the blood vessel is expressed as the ratio of extension per unit length, or the ratio of the amount stretched longitudinally to the length of the original vessel segment,

$$\varepsilon_t = \frac{\Delta l}{l} \quad (3.1.16)$$

Strain in the radial direction, or perpendicular to the vessel segment length, is the fraction of distention of the vessel lumen radius or diameter. It is given by

$$\varepsilon_r = \frac{\Delta r}{r} \quad (3.1.17)$$

For a blood vessel considered to be purely elastic, Hooke's law applies. To find the tension (T) exerted on the arterial wall due to intraluminal blood pressure distention, Laplace's law is useful. Laplace's law describes the tension exerted on a curved membrane with a radius of curvature. In the case of blood vessel, there are two radii of curvature,

one that is infinite in the longitudinal direction along the blood vessel axis and the other is in the radial direction. Thus, Laplace's law for an artery can be written as:

$$T = p \cdot r \quad (3.1.18)$$

This assumes the artery has a thin-wall or that the ratio of arterial wall thickness ( $h$ ) to arterial lumen radius ( $r$ ) is small, or  $h/r \leq 1/10$ . Here  $p$  is the intramural-extramural pressure difference, or the transmural pressure. When the arterial wall thickness is taken into account, the Lamé equation becomes relevant:

$$\sigma_t = \frac{pr}{h} \quad (3.1.19)$$

Arteries have been assumed to be incompressible. Although not exactly so, this is in general a good approximation. To assess the compressibility of a material, the Poisson ratio is defined. It is the ratio of radial strain to longitudinal strain. We obtain from the above definitions, the Poisson ratio as:

$$\sigma = \frac{\varepsilon_r}{\varepsilon_l} = \frac{\Delta r / r}{\Delta l / l} \quad (3.1.20)$$

When radial strain is half that of longitudinal strain, or when  $\sigma = 0.5$ , the material is said to be incompressible. This means that when a cylindrical material is stretched, its volume remains unchanged. Or, in the case of an artery, when it is stretched, its luminal volume remains unchanged. Experimental measurements to obtain the Poisson ratio for arteries have shown  $\sigma$  to be close to 0.5. Arteries, therefore, can be considered to be close to being incompressible.

A purely elastic material differs from a viscoelastic material. The former depends only on strain (eqns. 3.1.16 and 3.1.17) while the latter depends on the rate of change of strain, or strain rate ( $d\varepsilon/dt$ ) also. The artery as a viscoelastic material exhibits stress-relaxation, creep, and hysteresis phenomena (Fig. 3.1.1).

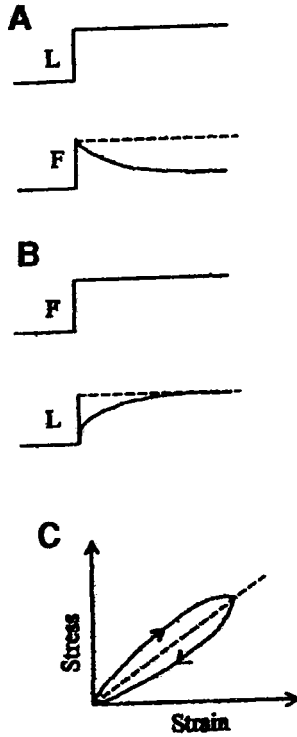


Fig. 3.1.1: Diagram illustrating the characteristics of a viscoelastic material such as the arterial wall: (a) stress relaxation: a step increase in length,  $L$ , or diameter results in an increase in force or tension which declines over time to a lower level, (b) creep phenomenon: with a step increment in applied force, the arterial length or diameter increases, but gradually and (c) hysteresis; with increase in stress, strain increases, but when the stress is removed, the strain follows a different path, resulting in a "hysteresis loop" indicating energy loss.

If a strip of artery is subjected to a step change in length, it will result in an initial increase in stress, and then decays to a lower value. This is known as stress-relaxation. There is a finite amount of time the vessel takes to relax. This is described by a time constant, which differs in different arteries. When an artery is subjected to a stepwise change in stress, its length will gradually increase to a constant value. This is the so-called, "creep phenomenon". As with stress relaxation, the increase in length or diameter, also takes a finite amount of time and is also

subscribed to a time constant. These properties allow arteries to respond to rapid transient changes in transmural blood pressures.

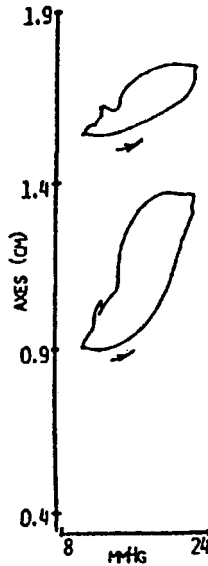


Fig. 3.1.2: Pressure-diameter relation of the main pulmonary artery showing hysteresis loops. Top tracing: major axis. Bottom tracing: minor axis.

Hysteresis develops when the vessel is subjected to sinusoidal or cyclic changes. If the artery is purely elastic, there will be no phase shift between the applied pressure and the resulting change in diameter. The viscoelastic behavior of the artery leads to phase shifts in its pressure-diameter relation. A hysteresis loop is observed, reflecting viscous losses. In other words, energy is dissipated in stretching the artery and allowing it to return to its control value. If the artery were purely elastic, there would be no energy loss and the artery would return to its control value along the exact path during stretching.

Examples of experimentally measured pressure-diameter relations are shown in Fig. 3.1.2 for the pulmonary aorta. Since the pulmonary aorta is normally oval, there are two different diameters, namely, the major axis diameter and the minor axis diameter. When the major and minor axes diameters are plotted against pressure, the hysteresis loops are

clearly seen. It is also clear that the pulmonary aorta is stiffer (less diameter distention with increasing pressure) along the major axis than the minor axis. In small peripheral vessels the viscous modulus is larger and the phase shift becomes more pronounced. This can be seen in the simultaneously measured pressure-diameter relation obtained for the femoral artery, for instance.

The static modulus of elasticity differs from the dynamic elastic value. Measurement of dynamic elasticity has gained considerable attention, mainly because of its applicability to pulsatile conditions. The approach employs the measurement of pressure-diameter relations, and the subsequent calculations of the incremental elastic modulus ( $E_{inc}$ ) which is complex ( $E_c$ ):

$$E_{inc} = E_{dyn} + \eta\omega \quad (3.1.21)$$

When an elastic modulus is complex, it implies frequency-dependence. The in-phase component defines the dynamic elastic modulus,

$$E_{dyn} = |E_c| \cos\phi \quad (3.1.22)$$

and the viscous modulus is defined by

$$\eta\omega = |E_c| \sin\phi \quad (3.1.23)$$

where  $\phi$  is the phase lag, generally between pressure ( $p$ ) and diameter ( $d$ ). In the case that pressure leads diameter, or that the diameter distention delays after the arrival of the pressure pulse,  $\phi$  is positive. When considering the artery as purely elastic, i.e. no viscosity damping is present, then the arterial lumen diameter change instantaneous with the distending pressure pulse. In this case,  $\phi$  is zero and the viscous term  $\eta\omega$  disappears.

A similar form of complex elastic modulus was given by Cox (1975), accounting for arterial wall thickness:

$$E(\omega) = \frac{4a^2b}{b^2 - a^2} \frac{P(\omega)}{D(\omega)} \quad (3.1.24)$$

where  $a$  and  $b$  are inner and outer arterial diameters, respectively.  $P(\omega)$  and  $D(\omega)$  are frequency domain pressure and diameter, respectively.

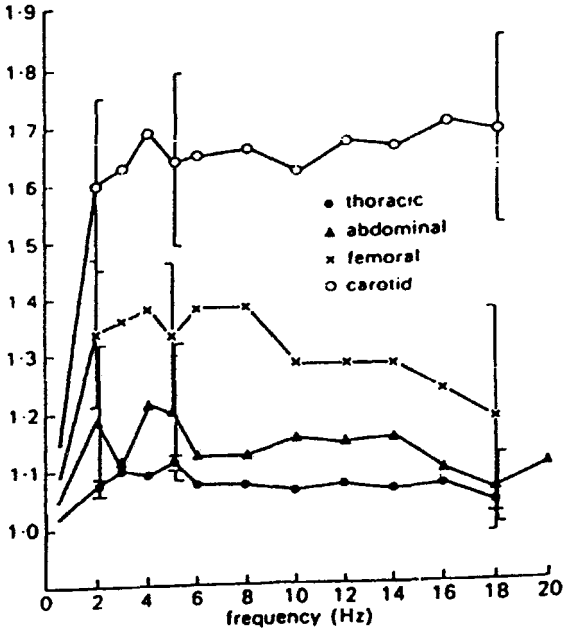


Fig. 3.1.3: Dynamic elastic modulus ( $E_{\text{dyn}}$ ) plotted as a function of frequency for the thoracic aorta, abdominal aorta, femoral and carotid arteries. Notice the  $E_{\text{dyn}}$  is essentially unchanged above 2 Hz.

Experimental results show that the viscous modulus is small compared with the elastic modulus (Li et al., 1981; Li, 1987; Nichols and O'Rourke, 1998). It is of the order of 10%. The dynamic modulus has also been found to be essentially constant above 2 Hz (Li, 2000).

A complex Young's modulus was considered by Westerhof and Noordergraaf (1970) to describe arterial wall viscoelasticity and also utilized frequency dependent parameters. They define the complex elastic modulus as the ratio of complex stress to complex strain:

$$Ec(\omega) = \frac{\sigma(\omega)}{\varepsilon(\omega)} \quad (3.1.25)$$

$$Ec(\omega) = \frac{F(\omega) / A}{\Delta l(\omega) / l(\omega)} \quad (3.1.26)$$

It is clear that at  $\omega = 0$ , or when the elastic modulus is frequency-independent, eqn. (3.1.25) reduces to eqn. (3.1.14).  $l(\omega)$  is the length,  $F(\omega)$  is the sinusoidally applied force, and  $\Delta l(\omega)$  is the change in length. In Laplace notation, they showed that if a unit change in length in the form of a step function is applied to the Voigt model (Fig. 3.1.3), its force development (stress relaxation) is unbounded. When a unit change in force is applied to the Maxwell model (Fig. 3.1.3), its change in length (creep phenomenon) is unbounded. Thus, both models fail to represent adequately the physical properties of blood vessels. This indicates that a single time constant alone is not sufficient to describe either the stress-relaxation or the creep phenomenon.

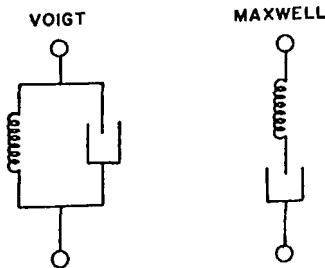


Fig. 3.1.3: Mechanical models of viscoelastic arteries. The spring-dashpot models are subjected to step changes in force, and step changes in length. In a Maxwell model (right), creep is unbounded; in a Voigt model (left), stress relaxation is unbounded.

## 3.2 Frequency Domain and Fourier Analysis

### 3.2.1 Periodic Functions

A periodic function with a period  $T$ , is defined by=

$$f(t) = f(t+T) \quad (3.2.1)$$

and it follows that:

$$f(t) = f(t+nT), n = 0, \pm 1, \pm 2, \dots \quad (3.2.2)$$

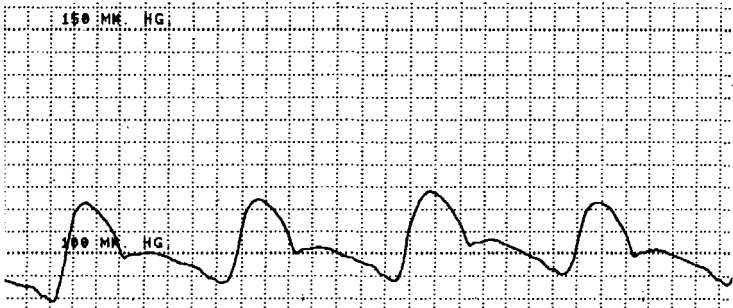


Fig. 3.2.1: Measured aortic blood pressure waveforms showing periodicity. Oscillations within systolic and diastolic pressure levels are slightly modulated by respiratory effects.

Figure 3.2-1 illustrates the periodic blood pressure waveforms oscillating within systolic and diastolic pressure levels with cardiac period  $T$ . There is in general a slight change in pressure waveform amplitudes due to the influence of respiration, i.e. inspiration and expiration. In this case, we have for the pulsatile pressure waveforms:

$$p(t) = p(t+nT), n = 0, \pm 1, \pm 2, \dots \quad (3.2.3)$$

It is clear that any periodic signal satisfying the Dirichlet conditions (convergence conditions) can be expressed by the Fourier series. To

apply the Fourier series, periodicity and linearity need to be satisfied. Periodicity is often observed, because cardiac period is varies little from beat to beat during a short interval.

### 3.2.2 Trigonometric Fourier Series

A periodic function can be expressed in terms of its sine and cosine components:

$$f(t) = a_0 + a_1 \cos \omega_0 t + a_2 \cos 2\omega_0 t + \dots + b_1 \sin \omega_0 t + b_2 \sin 2\omega_0 t + \dots \quad (3.2.4)$$

which is

$$f(t) = a_0 + \sum_{n=1}^N [(a_n \cos(n\omega_0 t) + b_n \sin(n\omega_0 t))] \quad (3.2.5)$$

where the Fourier coefficients are:

$$a_0 = \frac{1}{T} \int_0^T f(t) dt \quad (3.2.6)$$

$$a_n = \frac{2}{T} \int_0^T f(t) \cos(n\omega_0 t) dt \quad (3.2.7)$$

$$b_n = \frac{2}{T} \int_0^T f(t) \sin(n\omega_0 t) dt \quad (3.2.8)$$

$$\omega_0 = 2\pi f = \frac{2\pi}{T} \quad (3.2.9)$$

where  $\omega_0$  is the angular frequency,  $f_0$  is the fundamental frequency and  $T$  is the period,  $n$  is the  $n$ th number of harmonics and  $N$  is the total number of harmonics in the Fourier series summation.

The trigonometric representations of the above series give the following:

$$f(t) = c_0 + \sum_{n=1}^N c_n \cos(n\omega_0 t - \theta_n) \quad (3.2.10)$$

where the harmonic magnitude and phase are represented by

$$c_n = \sqrt{a_n^2 + b_n^2} \quad (3.2.11)$$

and

$$\theta_n = \tan^{-1} \frac{b_n}{a_n} \quad (3.2.12)$$

In terms of pulsatile pressure waveforms, the Fourier series can be written as:

$$p(t) = \bar{p} + \sum_{n=1}^N p_n \cos(n\omega t - \phi_n) \quad (3.2.13)$$

Thus, Fourier series representation of a periodic pressure waveform is the summation of a mean pressure component and its sinusoidal or cosinusoidal harmonic components.

A similar Fourier series representation can be written for the flow waveform:

$$Q(t) = \bar{Q} + \sum_{n=1}^N Q_n \cos(n\omega t - \varphi_n) \quad (3.2.14)$$

Figure 3.2.2 gives an example of the summation of Fourier components that provides the re-synthesis of the aortic pressure waveform. For the aortic pressure waveform, 10 harmonics are sufficient to accurately reconstruct the waveform.

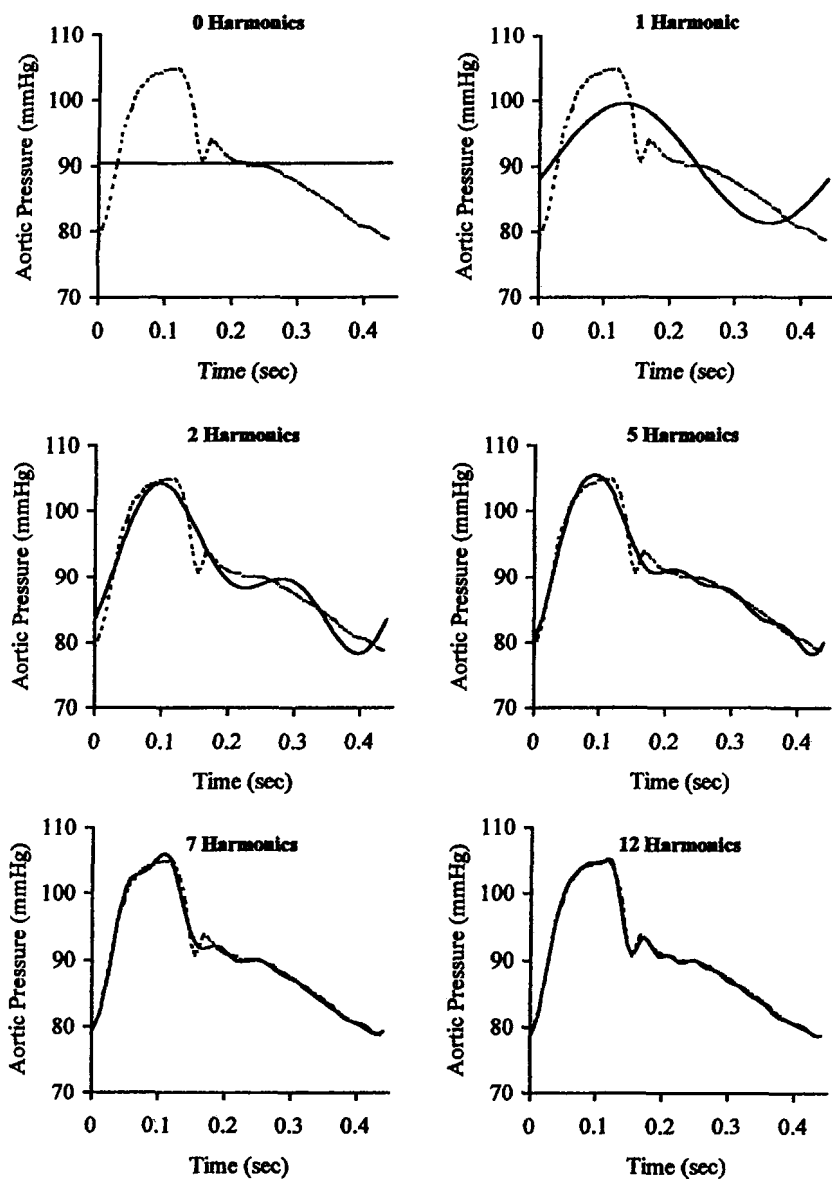


Fig. 3.2.2: Re-synthesis of aortic pressure waveform by summation of the first 10 harmonic components.

### 3.2.3 Complex Form of Fourier Series

By expressing sine and cosine in terms of exponentials, we have

$$\cos(n\omega_0 t) = \frac{1}{2}(e^{jn\omega_0 t} + e^{-jn\omega_0 t}) \quad (3.2.15)$$

$$\sin(n\omega_0 t) = \frac{1}{2j}(e^{jn\omega_0 t} - e^{-jn\omega_0 t}) \quad (3.2.16)$$

and substituting into

$$f(t) = a_0 + \sum_{n=1}^N [(a_n \cos(n\omega_0 t) + b_n \sin(n\omega_0 t))] \quad (3.2.17)$$

we have

$$f(t) = \frac{1}{2}a_0 + \sum_{n=1}^N \left[ \frac{1}{2}(a_n - jb_n)e^{jn\omega_0 t} + \frac{1}{2}(a_n + jb_n)e^{-jn\omega_0 t} \right] \quad (3.2.18)$$

or simply:

$$f(t) = c_0 + \sum_{n=1}^N (c_n e^{jn\omega_0 t} + c_{-n} e^{-jn\omega_0 t}) \quad (3.2.19)$$

where

$$c_0 = \frac{1}{2}a_0 = \frac{1}{T} \int_0^T f(t) dt \quad (3.2.20)$$

$$c_n = \frac{1}{2}(a_n - jb_n) = \frac{1}{T} \int_0^T f(t) e^{-jn\omega_0 t} dt \quad (3.2.21)$$

$$c_{-n} = \frac{1}{2}(a_n + jb_n) = \frac{1}{T} \int_0^T f(t) e^{jn\omega_0 t} dt \quad (3.2.22)$$

For real  $f(t)$ , then  $c_{-n}$  is  $c_n$ 's complex conjugate, and if phase is considered, then:

$$c_n = |c_n| e^{j(n\omega_0 t - \theta_n)} \quad (3.2.23)$$

where

$$|c_n| = \frac{1}{2} \sqrt{a_n^2 + b_n^2} \quad (3.2.24)$$

and

$$\theta_n = \tan^{-1} \left( \frac{-b_n}{a_n} \right) \quad (3.2.25)$$

In terms of pulsatile blood pressure waveforms  $p(t)$ , we have for mean pressure:

$$\bar{p} = \frac{1}{T} \int_0^T p(t) dt \quad (3.2.26)$$

and for the  $n$ th harmonic of the pressure waveform:

$$P_n(\omega) = |P_n(\omega)| e^{j(n\omega_0 t - \phi_n)} \quad (3.2.27)$$

For the corresponding flow waveform harmonic component, we have

$$Q_n(\omega) = |Q_n(\omega)| e^{j(n\omega_0 t - \varphi_n)} \quad (3.2.28)$$

Vascular impedance, expressed as the harmonic ratios of pressure to flow, is:

$$Z_n(\omega) = |Z_n(\omega)| e^{j\theta_n} \quad (3.2.29)$$

From which, it is clear that the magnitude and phase for the corresponding harmonics are

$$|Z_n| = \frac{|P_n|}{|Q_n|} \quad \text{and} \quad \theta_n = \phi_n - \varphi_n \quad (3.2.30)$$

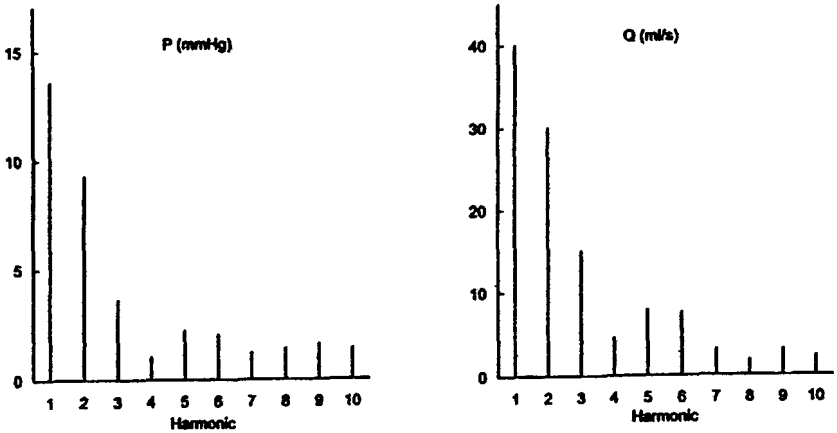


Fig. 3.2.3: Harmonic magnitudes of an aortic pressure pulse and an aortic flow pulse.

### 3.2.4 Other Aspects of Frequency Domain Analysis

#### 3.2.4.1 Dirichlet Conditions

We have assumed that in the forgoing discussions that the periodic function, and the pressure and flow waveforms can be represented by the Fourier series. In general, there is a convergence requirement that is known as the Dirichlet Conditions, under which a Fourier series representation of a function  $f(t)$  is possible. The Dirichlet conditions are as follows:

- (1) the function  $f(t)$  has a finite number of discontinuities in one period
- (2) the function  $f(t)$  has a finite number of maxima and minima in one period
- (3) the function  $f(t)$  is absolutely integrable over a period.

The function is said to be piecewise continuous in the finite interval  $T$  if conditions (1) and (2) are satisfied.

### 3.2.4.2 Line Spectrum and Nyquist Criterion

The harmonic magnitudes of a typical aortic pressure pulse and aortic flow pulse are shown in Fig. 3.2.3. The magnitudes are small and negligible beyond the tenth harmonic component. The Nyquist criterion requires sampling frequency of at least twice the highest frequency content in order to reconstruct the original waveform accurately. In the present example, the tenth harmonic would be  $1.5 \times 10$  or 15 Hz. The minimal sampling frequency required is therefore 30 Hz. In most cases, sampling frequency applied is much higher than this and typically at 100Hz. In other words, the pressure waveform is digitized at 10 msec intervals.

### 3.2.4.3 Correlation, Coherence and Power Spectrum

Autocorrelation for a periodic function  $f(t)$  can be defined by

$$\frac{1}{T} \int_0^T f_1(t) f_1(t + \tau) dt = \sum_0^{\infty} |F(n\omega)|^2 e^{jn\omega\tau} \quad (3.2.31)$$

where  $\tau$  represents the time delay. Its power spectrum is given as

$$\Phi_{11}(n\omega) = |F_1(n\omega)|^2 \quad (3.2.32)$$

$$\phi_{11}(\tau) = \sum_0^{\infty} \Phi_{11}(n\omega) e^{jn\omega\tau} \quad (3.2.33)$$

and inversely,

$$\Phi_{11}(n\omega) = \frac{1}{T} \int_0^T \phi_{11}(\tau) e^{-jn\omega\tau} \quad (3.2.34)$$

Similarly, the cross-correlation for two functions  $f_1(t)$  and  $f_2(t)$  can be defined as:

$$\phi_{12}(\tau) = \frac{1}{T} \int_0^T f_1(t) f_2(t + \tau) dt = \sum_0^{\infty} |F_{12}(n\omega)|^2 e^{jn\omega\tau} \quad (3.2.35)$$

$$\phi_{12}(\tau) = \sum_0^{\infty} \Phi_{12}(n\omega) e^{jn\omega\tau} \quad (3.2.36)$$

and

$$\Phi_{12}(n\omega) = \frac{1}{T} \int_0^T \phi_{12}(\tau) e^{-jn\omega\tau} \quad (3.2.37)$$

which has a co-spectral of  $C_{12}$  and quadrature term,  $Q_{12}$ .

As an example, given that pressure and flow can be represented by  $f_1(t)$  and  $f_2(t)$ , we have for impedance:

$$Z = |Z| e^{-j\theta} \quad (3.2.38)$$

which can be written as

$$|Z| = \sqrt{\frac{\Phi_{11}}{\Phi_{12}}} \quad (3.2.39)$$

with a phase

$$\theta = \tan^{-1} \frac{Q_{12}}{C_{12}} \quad (3.2.40)$$

The coherence observed is given by

$$C_{oe} = \frac{(C_{12}^2 + Q_{12}^2)}{\sqrt{\Phi_{11} \cdot \Phi_{12}}} \quad (3.2.41)$$

### 3.3 Fluid Mechanics and Rheology

#### 3.3.1 Steady Flow and Poiseuille Equation

The flow of viscous blood in a relatively cylindrical elastic arterial vessel has borrowed much of the quantitative treatment from fluid mechanics. Navier-Stokes equations are the fundamental equations describing fluid motion. Poiseuille equation is a special case of the general solution of the Navier-Stokes equations.

Steady pressure-flow relations are commonly described by the Poiseuille's equation:

$$Q = \frac{\pi r^4 \Delta p}{8\eta l} \quad (3.3.1)$$

where  $Q$  is the mean or steady flow in ml/s,  $r$  is the inner radius of the vessel,  $l$  is the length through which blood flows and  $\eta$  is the viscosity of the fluid, in this case, blood (0.03 poise or 3 centi-poise) and  $\Delta p$  is the pressure drop across the vessel. Thus, the amount of flow is critically dependent on the size of the lumen radius and is proportional to its fourth power. This equation has also been used to determine fluid viscosity, by measuring flow and pressure drop over a known geometry of the tube.

The force opposing the flow of a viscous fluid with surface area  $A$ , is proportional to the viscosity and the velocity gradient ( $v/d$ ) across the fluid layers with separation  $d$ . This defines the fluid viscosity as,

$$\eta = \frac{F/A}{v/d} \quad (3.3.2)$$

It is clear that the numerator is the applied pressure and the denominator, velocity gradient. Thus, the more viscous the fluid, the greater amount of pressure is needed to apply to the fluid to generate the same amount of velocity gradient.

For a constant vessel geometry and fluid viscosity, it can be seen that the pressure gradient governs the flow. From Fig. 3.3.1, it is clear that the pressure gradient is

$$\frac{dp}{dz} \approx \frac{\Delta p}{\Delta z} \approx \frac{(p_1 - p_2)}{l} \quad (3.3.3)$$

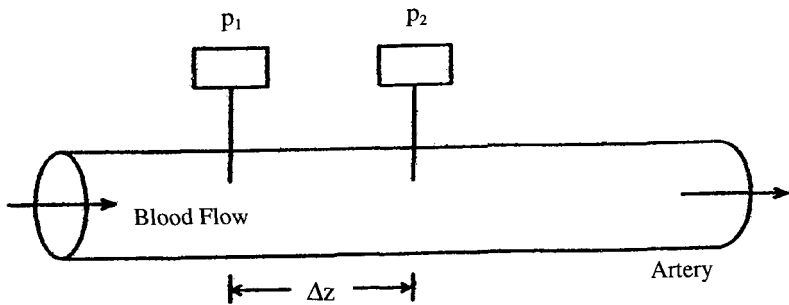


Fig. 3.3.1: A cylindrical tube containing steady flow of a fluid with viscosity  $\eta$ .

For pulsatile flow, this pressure gradient changes with time. In fact, before the advent of electromagnetic and ultrasonic flow transducers, derivation of flow from pressure gradient was common. This latter was applied to obtain pulsatile flow information, rather the steady or mean flow.

The velocity profile for a steady, laminar flow is based on the general derivation of Poiseuille's equation. Consider a cylindrical vessel with internal radius  $r_i$  and length  $l$ , the viscous force exerted on the cylindrical unit of fluid is

$$F_p = (p_1 - p_2)\pi r^2 \quad (3.3.4)$$

The viscous force retarding the motion of the cylindrical volume of flow, is, from (3.3.2), the product of cross-sectional area and viscosity, multiplied by the velocity gradient,

$$F_\eta = 2\pi r l \eta \frac{dv}{dr} \quad (3.3.5)$$

Under equilibrium, these forces balance each other, i.e. equal and opposite,

$$(p_1 - p_2)\pi r^2 = -2\pi r l \eta \frac{dv}{dr} \quad (3.3.6)$$

The velocity gradient for the particular laminar layer of fluid is therefore,

$$\frac{dv}{dr} = -\frac{(p_1 - p_2)}{2\eta l} \quad (3.3.7)$$

Substituting for the pressure gradient from equation (3.3.3), we have the relation between the velocity gradient and pressure gradient,

$$\frac{dv}{dr} = -\frac{1}{2\eta} \frac{dp}{dz} \quad (3.3.8)$$

Notice that the velocity gradient is in the radial direction, i.e. across the vessel, whereas the pressure gradient is in the longitudinal direction, i.e. along the vessel axis. Velocity at radius  $r$  across the vessel can be readily obtained by integration of (3.3.7)

$$v = -\frac{(p_1 - p_2)r^2}{4\eta l} + k \quad (3.3.9)$$

where  $k$  is the constant of integration, obtainable by applying the boundary condition that the velocity of fluid at the vessel wall ( $r=r_i$ ) is zero, i.e.  $v(r=r_i) = 0$ . We have,

$$v = \frac{1}{4\eta} \frac{(p_1 - p_2)}{l} (r_i^2 - r^2) \quad (3.3.10)$$

Thus, velocity is maximum, or  $v_{\max}$ , when  $r=0$ , or along the axis,

$$v_{\max} = \frac{(p_1 - p_2)r_i^2}{4\eta l} \quad (3.3.11)$$

This is sometimes referred to as the centerline velocity or axial velocity. The velocity is zero at the vessel wall, when  $r=r_i$ .

Equation (3.3.10) is that of a parabola, hence the velocity profile across the vessel wall is known as a parabolic velocity profile. This is shown in Fig. 3.3.2.

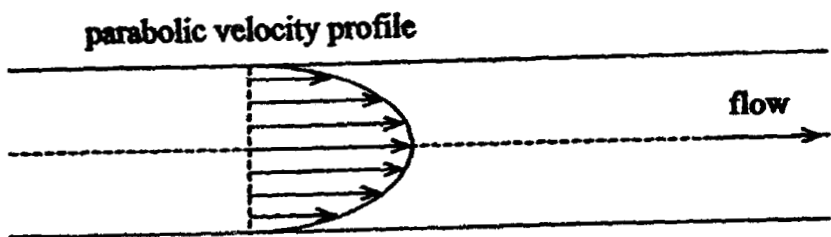


Fig. 3.3.2: Illustration of the parabolic velocity profile. The velocity is maximal at the centerline and decreases progressively towards the vessel wall in a parabolic fashion.

The amount of flow, or volume flow, is obtained as,

$$Q = \int_0^{r_i} 2\pi r v dr \quad (3.3.12)$$

which results in the well-known Poiseuille equation

$$Q = \frac{\pi r_i^4 (p_1 - p_2)}{8\eta l} \quad (3.3.13)$$

The average velocity across the velocity profile is simply the amount of flow divide by the cross-sectional area of the vessel lumen,  $\pi r_i^2$ ,

$$v_{av} = \frac{r^2}{8\eta l} (p_1 - p_2) \quad (3.3.14)$$

### 3.3.2 Bernoulli's Equation and Narrowing Vessel Lumen

For a vessel with a narrowed segment or stenosis, as shown in Fig. 3.3.3, the total volume flow through all segments must be the same, by the conservation of mass. The flow is given by the product of the cross-sectional area and the flow velocity:

$$Q = A_1v_1 = A_2v_2 = A_3v_3 \quad (3.3.15)$$

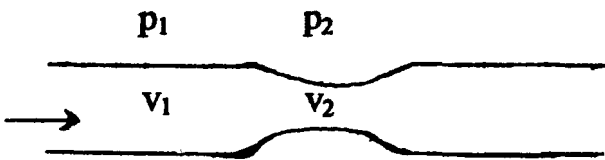


Fig. 3.3.3: A cylindrical vessel with a narrowed segment or stenosis.

The familiar kinetic energy equation is given as

$$K.E. = \frac{1}{2}mv^2 \quad (3.3.16)$$

and the corresponding potential energy is

$$P.E. = pQ \quad (3.3.17)$$

The total energy is their sum:

$$W = P.E. + K.E. \quad (3.3.18)$$

This gives rise to

$$W_1 = (h\rho g)(A_1v_1) + \frac{1}{2}(\rho A_1v_1)v_1^2 \quad (3.3.19)$$

associated with the pre-stenotic section, with  $p=h\rho g$  due to gravity or static pressure difference.

We have also, for the stenotic section:

$$W_2 = (h\rho g)(A_2 v_2) + \frac{1}{2}(\rho A_2 v_2)v_2^2 \quad (3.3.20)$$

From the conservation of energy, equating these 2 equations, we have

$$(p_1 - p_2) + \frac{1}{2}\rho(v_1^2 - v_2^2) + \rho g(h_1 - h_2) = k \quad (3.3.21)$$

For the case when gravity is ignored or when  $h_1=h_2$ , we have the familiar Bernoulli equation

$$p_1 = p_2 + \frac{1}{2}\rho(v_1^2 - v_2^2) \quad (3.3.22)$$

The commonly known phrase that the faster the flow velocity, the lower the pressure, i.e.  $v_2 > v_1$ , then  $p_2 < p_1$ . This is clearly seen from the illustration in the figure. The well-known Bernoulli equation described above is for a steady, inviscid (non-viscous) and incompressible fluid flow.

### 3.3.3 Orifice Flow and Torricelli's Equation

The problem of flow through an orifice small in dimension compared with the reservoir was considered by Torricelli in the 17<sup>th</sup> century. The pressure and velocity at the surface of the reservoir are  $p_1$  and  $v_1$  and those at the orifice are  $p_2$  and  $v_2$ , respectively. We have for the velocities,

$$v_2^2 - v_1^2 = \frac{2}{\rho}(p_1 - p_2) + 2g(h_1 - h_2) \quad (3.3.23)$$

From continuity equation that flow entering equals flow leaving, we have

$$v_1 A_1 = v_2 A_2 \quad (3.3.24)$$

In general,  $A_1 \gg A_2$  and  $v_1 \ll v_2$  and assume  $p_1 = p_2$ , we have

$$v_2^2 = 2g(h_1 - h_2) \quad (3.3.25)$$

This results in the Torricelli's equation describing the velocity speed of flow leaving the orifice. Substituting  $v = v_2$ , we obtain

$$v = \sqrt{2g(h_1 - h_2)} \quad (3.3.26)$$

The amount of flow leaving the orifice with circular cross section of radius  $r$  is therefore,

$$Q = \pi r^2 v = \pi r^2 \sqrt{2g(h_1 - h_2)} \quad (3.3.27)$$

### 3.3.4 The Gorlin Equation

A popular equation that has been used in the clinical applications is the Gorlin equation describing the orifice cross-section area. The equation is used in calculating valvular cross-sectional area, particularly during valvular stenotic conditions. The orifice cross-sectional area is given by:

$$A = \frac{Q}{\sqrt{2g(p_1 - p_2)}} \frac{1}{\pi K_c} \quad (3.3.28)$$

where  $K_c$  is the contraction coefficient or the ratio of the cross-sectional area of orifice flow jet to the actual opening of the orifice

$$K_c = A_o / A \quad (3.3.29)$$

### 3.3.5 Flow and Flow Acceleration

The Cartesian coordinates in three dimensions, in the x-axis, y-axis and z-axis together with time is usually represented as:

$$f = f(x, y, z, t) \quad (3.3.30)$$

The cylindrical polar coordinates representation, one has

$$f = f(z, r, \theta, t) \quad (3.3.31)$$

Thus for velocities,  $u$ ,  $v$ ,  $w$ , we have

$$\begin{aligned} u &= u(z, r, \theta, t) \\ v &= v(z, r, \theta, t) \\ w &= w(z, r, \theta, t) \end{aligned} \quad (3.3.32)$$

along the direction of flow  $z$  in a cylindrical blood vessel, along its radius ( $r$ ) or radial component, and the rotational component associated with an angular component ( $\theta$ ). This representation identifies position within the blood vessel at any given time  $t$ . This coordinates system was originated by Euler, and is sometimes referred to as the Eulerian velocities.

Thus, it is clear that when the positions are time-dependent, i.e. the fluid element moves from one position to another with changing time, then we have, for the velocities:

$$\begin{aligned} u &= \frac{dz}{dt} \\ v &= \frac{dr}{dt} \\ w &= r \frac{d\theta}{dt} \end{aligned} \quad (3.3.33)$$

Velocity is clearly here defined as the rate of change of distance or position. In the case of irrotational flow, or that the rotational flow component is negligible, one remains with  $u$  and  $v$ . In the case of one-dimensional flow, i.e. along the longitudinal  $z$ -axis of the vessel then only  $u$  exists.

The rate of change of flow velocity is the acceleration. Faster rate of change in velocity gives rise to a greater acceleration in flow. Such acceleration can be either positive, i.e. when the velocity is increasing or negative, i.e. when the velocity is reducing.

This can be appreciated from the flow velocity recording of aortic velocity and its derivative. Fig. 3.3.4 shows the aortic flow and the flow acceleration.

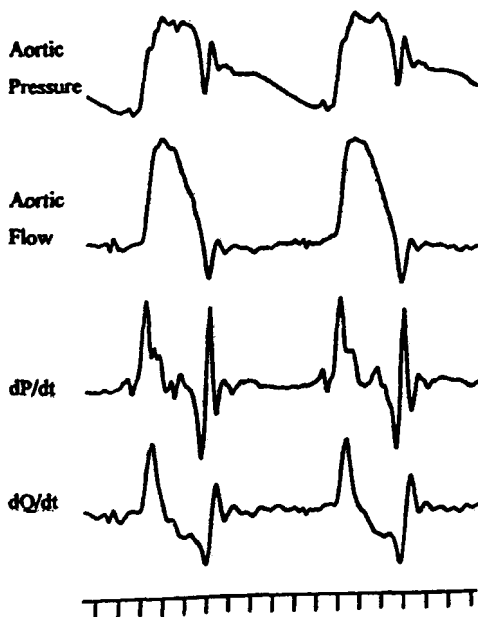


Fig. 3.3.4: Aortic flow and its first derivative, the flow acceleration ( $dQ/dt$ ). Aortic pressure and rate of its pressure change ( $dP/dt$ ) is also shown.

Thus acceleration is the rate of change of velocity. We have for the accelerations associated with the longitudinal, radial and rotational velocities (Zamir, 2000):

$$a_z = \frac{\partial u}{\partial t} + u \frac{\partial u}{\partial z} + v \frac{\partial u}{\partial r} + \frac{w}{r} \frac{\partial u}{\partial \theta}$$

$$a_r = \frac{\partial v}{\partial t} + u \frac{\partial v}{\partial z} + v \frac{\partial v}{\partial r} + \frac{w}{r} \frac{\partial v}{\partial \theta} - \frac{w}{r^2} \quad (3.3.34)$$

$$a_\theta = \frac{\partial w}{\partial t} + u \frac{\partial w}{\partial z} + v \frac{\partial w}{\partial r} + \frac{w}{r} \frac{\partial w}{\partial \theta} + \frac{vw}{r}$$

These partial derivatives of velocities other than the first terms are sometimes known as convective accelerations. Notice that acceleration at a particular instant in time when  $z$ ,  $r$  and  $\theta$ , are kept constant (i.e. velocities do not change with  $z$ ,  $r$  and  $\theta$ ), one obtains the familiar equations for acceleration:

$$a_z = \frac{\partial u}{\partial t}$$

$$a_r = \frac{\partial v}{\partial t} \quad (3.3.35)$$

$$a_\theta = \frac{\partial w}{\partial t}$$

### 3.3.6 Newtonian Fluid, No-Slip, Boundary Conditions and Entry Length

#### 3.3.6.1 Newtonian Fluid

The coefficient of viscosity of blood as we have shown earlier, is defined as the ratio of applied pressure to the velocity gradient. In other words, it is the shear stress that represents the resisting force of the fluid deformation along the direction of flow:

$$\tau_s = \eta \frac{dv}{dz} \quad (3.3.36)$$

Fluid that behaves in this manner is known as the Newtonian fluid, attributed to its originator, Newton. This assumes that the rate of

deformation, or the velocity gradient is small. And for a cylindrical vessel with velocity  $v$ , and diameter  $d$ , this becomes:

$$\eta = \frac{F/A}{v/d} \quad (3.3.37)$$

Blood has plasma, blood cells and other formed elements. In most common analysis of blood flow in vessels, the assumption of blood as a Newtonian fluid seems to work well. Except in the case of very small vessels, such as the small arterioles capillaries where red blood cell size actually approaches that of the vessel lumen diameter, one needs to be concerned, not only of fluid shear, but also of shear stress on the flowing red blood cell and of the differential velocity gradients generated by the formed elements.

### 3.3.6.2 No-Slip Boundary Conditions

The “no-slip” condition refers to the assumption that concerns the fluid-solid interface or blood-vessel wall interface. No-slip boundary condition refers to the condition when the flow velocity at the tube wall is the same as the wall velocity, such that there is no “jump” or a step change in velocity to cause discontinuity. The general assumption is that the fluid in contact with the wall does not move at all. This assumption is generally true for the large vessels. In small vessels, plasma dominates as fluid and this no-slip condition generally applies to the plasma in contact with the wall, rather than red blood cells or the formed elements in blood.

### 3.3.6.3 Laminar and Turbulent Flow

Reynolds apparently was the first to use dye of visible color to investigate the manner in which fluid flows in a tube and provided a quantitative relation between the viscosity of the fluid and the mass of the fluid. Reynolds number as it is called, and as we derived earlier is given by

$$R_e = \frac{\rho v d}{\eta} \quad (3.3.38)$$

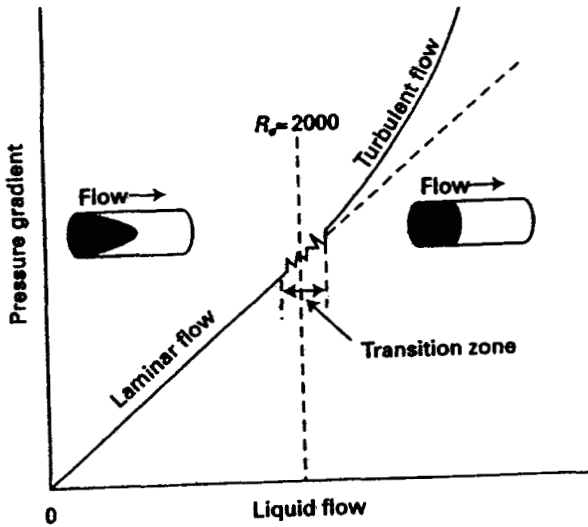


Fig. 3.3.5: Illustration of laminar to turbulent flow transition as a function of Reynolds number. Velocity transition from a parabolic profile to a blunt profile is also seen. From Nichols and O'Rourke (1998).

The most important observation and quantification made by Reynolds is in the differentiation of turbulent flow from laminar flow. This means that the turbulence depends not only on the average velocity  $v$  of the fluid, but also depending on the fluid property and the lumen diameter  $d$ .

The laminar to turbulent flow transition is shown in Fig. 3.3.5. Reynolds number of 2000 is assumed when turbulence begins. The Mach number is invariant among mammalian blood vessels, but the Reynolds number is dependent on body size (Li, 2000). Turbulence that normally occurs with high Reynolds number is somewhat constrained in a larger mammal's aorta by the larger compliance (Li, 1988).

### 3.3.6.4 Entry Length

Entry length is defined as the distance from the entrance or inlet of a vessel at which point the flow is fully developed. In the case of Poiseuille flow, this means that the centerline velocity reaches its maximum with the velocity profile becomes fully parabolic. But Poiseuille flow assumes a tube that is long enough for such flow to occur. However, under pulsatile flow conditions, flow does not fully develop and hence the accuracy in the determination of entry length becomes an issue. This is normally circumvented by assuming that the flow is almost fully developed in analyzing flow in blood vessels. A common criterion that is used assumes that the centerline velocity is within 1 or 2% of the centerline velocity according to Poiseuille's flow, i.e. 98% or 99%.

The determined entry length is of course determined also by the manner in which flow enters the vessel. A general rule of thumb used follows the following formulation:

$$\frac{l_e}{d} = 0.04R_e \quad (3.3.39)$$

This assumes that the entry length  $l_e$  in a vessel of diameter  $d$  as a flow with uniform velocity  $v$ .  $R_e$  is Reynolds number, as defined above.

Because of the finite geometry of the vascular segments, i.e. finite length and diameter, there are situation where the entry length requirement for an almost fully developed flow is not met. Thus, flow is frequently accepted as partially developed. A lower Reynolds number, such as those occurring at smaller vessels, with much smaller lumen diameters, the requirement of the entry length becomes much less stringent.

## CHAPTER 4

# Hemodynamics of Large Arteries

### 4.1 Ventricular Outflow and the Aorta

#### 4.1.1 Ventricular Ejection

Cardiac contraction which results in ventricular ejection of blood flow into the aorta occurs in systole. This corresponds to the ejection period during which the aortic valve is open (Fig. 4.1.1). This is preceded by an isovolumic contraction period when the cardiac muscles develop force and generate pressure, while the ventricular volume stays constant. Only when the ventricular pressure exceeds the aortic pressure, the aortic valve opens and ejection begins. Ventricular outflow is a function of the rate of change of ventricular volume, i.e.

$$Q = \frac{dV}{dt} \quad (4.1.1)$$

Aorta is the principal receiving conduit and thus its properties play a dominating role in ventricular ejection. Ventricular outflow is pulsatile, due to the contractile apparatus of the ventricle. This pulsatility is preserved due to the distensibility of the aorta and its branching arteries. This pulsatility also implies that there is an oscillatory or pulsatile contribution to the vascular load of the heart. Components of this load are the resistance (R), compliance (C) and inertance (L) associated with blood flow and vessel wall properties. It is recognized that aorta contributes largely to the overall arterial system compliance. The greater mass of blood ejected during systole, contributes to inertia, hence greater overall inertance. To facilitate ventricular ejection, the aorta presents the

least amount of resistance. Thus, the aorta is principally responsible for overall arterial system compliance and inertance, but less so for total resistance.

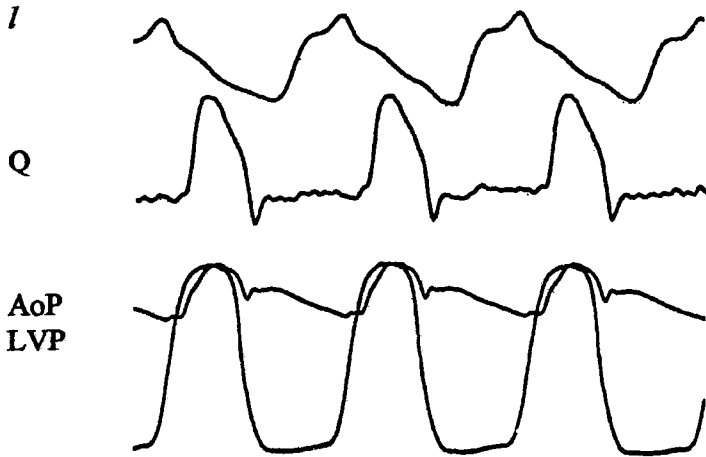


Fig. 4.1.1: Simultaneously measured cardiac muscle segment length (top tracing), left ventricular pressure (LVP), aortic pressure (AoP) and aortic flow (Q). Ejection begins when LVP exceeds AoP and ends with aortic valve closure. Cardiac muscle shortening from end-diastole to end-systole is clearly shown.

It is important to know about the function of the heart as an energetic mechanical pump. To this end, it suffices to understand the global pressure-volume behavior in relation to cardiac muscle shortening and force generation. This section first looks at factors that give rise to ventricular ejection and then examines the factors that can modify this ejection by the aorta and the rest of the arterial system. To accomplish these, we begin with the dynamics of cardiac muscle contraction to overall ventricular pumping mechanism, and the timing and duration of the ejection. We will then look at the corresponding dynamic changes that take place in the aorta and how these changes can significantly modify ventricular outflow.

### 4.1.2 Dynamics of Cardiac Muscle Contraction and Force-Length-Velocity Relations

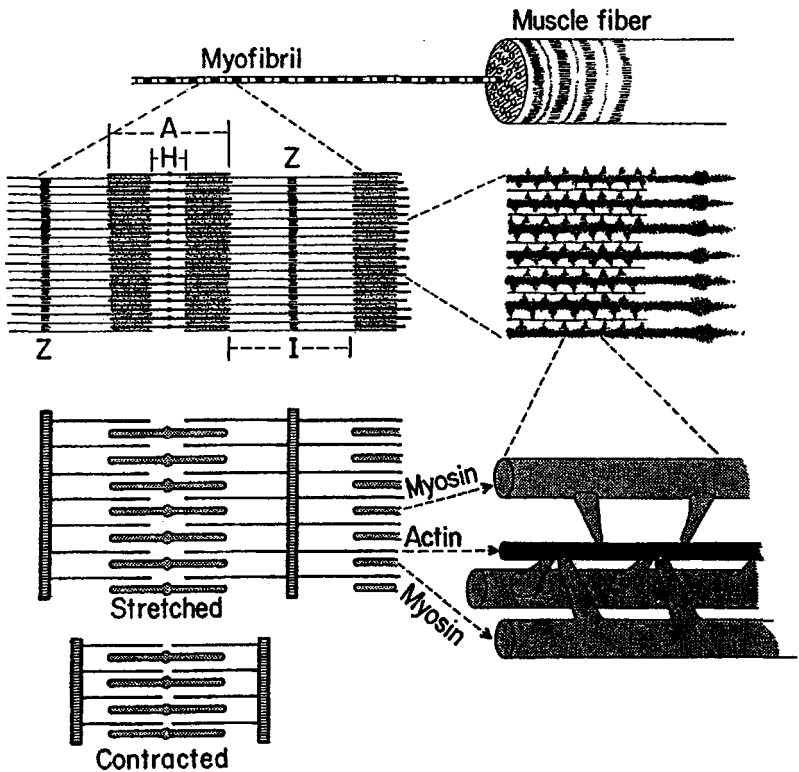


Fig. 4.1.2: Illustration of the role of the sliding filament hypothesis. The overlap of actin and myosin gives rise to contraction. A-band, H-zone and Z-line are shown. From Rushmer (1972).

Sarcomeres are the fundamental building blocks of the myocardium. They exhibit the ability to change length, generate force and govern overall ventricular contraction. Within the sarcomere, there are thick and thin filaments. These are the actin and myosin molecules. The overlapping and relative positions of these filaments determine the changes in force development. The "sliding filament hypothesis" as it is called formed the original basis for the understanding of the contraction process in striated muscle. The tension initially increases with increasing

length of the fiber, until the sarcomere reaches a length of about  $2.2 \mu\text{m}$ , the tension reaches a maximum and then declines as the length is increased further. The extent of the overlapping filaments determines the amount of force generation. This scheme is illustrated in Fig. 4.1.2.

The sarcomere tension-length relationship has been translated to the intact global heart in terms of left ventricular developed pressure (LVP) and end-diastolic volume (EDV). The former is related to the developed tension or force, while the latter is related to the initial muscle fiber length ( $l_0$ ) or "preload".

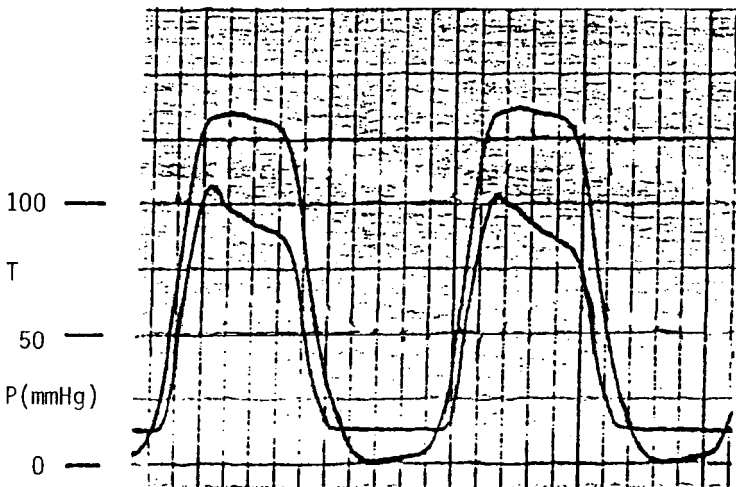


Fig. 4.1.3: Simultaneously measured regional tension and global ventricular in a dog left ventricle. Notice the parallel relationship in the isovolumic phases.

The relation between sarcomere length ( $l$ ) and left ventricular volume ( $V$ ) however, is not a linear one. This is expected, as the left ventricle is non-cubical in shape. Thus, the percentage change in cardiac muscle fiber length cannot be interpreted as a corresponding percentage in left ventricular cavity volume. Even in the isovolumic ejection phase, when the ventricular volume remains constant, cardiac muscle fibers at different part of the ventricle may still be changing their lengths. Thus, isovolumic (constant volume) contraction does not exactly correspond to

isometric (constant length) contraction. The regional tension and global ventricular pressure relationship is seen to be parallel however, only during this phase (Fig. 4.1.3, Li, 1987). The anisotropic properties and differential epicardial and endocardial segmental contraction due to their fiber orientations complicate the direct translation of mechanics from the muscle level to the global ventricular level.

Much of the biomechanics of muscle contraction can be traced back to Hill, who was concerned about the mechanical efficiency, in terms of work and speed, of human muscles. Although the concept of mechanical spring as an energy storage element was introduced to model muscle behavior before him, Hill accounted for the energy dissipation through the introduction of a viscoelastic model. This leads to the expression:

$$k(l - l_0) - \beta_0 \frac{dl}{dt} = F \quad (4.1.2)$$

where  $k$  and  $\beta_0$  are constants,  $l$  and  $l_0$  are the instantaneous and the initial muscle lengths, respectively.  $F$  is the applied force. The velocity of shortening is represented by the rate of change of fiber length

$$v = \frac{dl}{dt} \quad (4.1.3)$$

This velocity term thus gives rise to the viscous effect. At any given muscle length  $l$ , a larger load  $F$  is lifted with a lower velocity than a smaller load. Thus, the ability to generate force and the extent of velocity of shortening of the contractile element has an inverse relationship.

Hill's two element model, consisting of a passive series elastic element and a contractile element has become popular and follows the general expression:

$$(F + a)(v + b) = k_0 \quad (4.1.4)$$

where  $k_0$  is a constant. The velocity of shortening is a function of initial length of the muscle fiber. Combined with the earlier force-length

relation, the force-velocity-length ( $f-v-l$ ) relation has been suggested to be able to completely describe the physical behavior of the muscle.

#### 4.1.3 The Pressure-Volume Curve and Contractility of the Heart

The Frank-Starling mechanism, or better known as the “Starling’s Law of the Heart”, has classically been regarded as a fundamental property of the ventricle to regulate its cardiac output. The larger the volume before the onset of contraction or preload, the higher is its output under otherwise identical conditions. In this context, the preload has been identified as the end-diastolic volume.

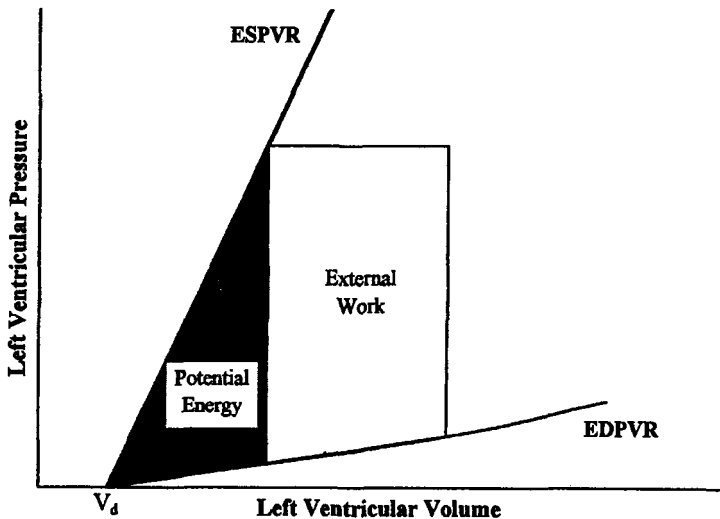


Fig. 4.1.4 Pressure-volume (P-V) diagram of the left ventricle defining ventricular elastance and  $V_d$ . The end-systolic pressure-volume line is drawn as tangent to the P-V loop at end-systole. Its slope represents the maximum elastance of the left ventricle, or  $E_{max}$ .

The pressure-volume relation has been popular because it provides the inter-relationships between stroke volume (SV), end-diastolic volume (EDV), end-systolic volume (ESV) and ejection fraction on a single diagram. The pressure-volume diagram (Fig. 4.1.4) is constructed from the instantaneous recordings of left ventricular pressure and volume. In

addition, it has been suggested that the separation of cardiac mechanical pump function and contractile state can be obtained. Pump function is related to loading conditions whereas contractility or inotropic state depends only on the intrinsic properties of the contracting muscle fibers or the myocardium.

The importance of P-V loop or pressure-diameter (P-D) loops of the ventricle has been frequently emphasized. This diagram points to the ESV as one of the functional determinants of this representation of ventricular pump function. Preload is indicated by the EDV and

$$SV = EDV - ESV \quad (4.1.5)$$

is the stroke volume.

#### ***4.1.4 Ejection Fraction, Cardiac Performance, Preload and Afterload***

The amount of blood ejected out of the ventricle per beat or the stroke volume is dependent not only on the operating Starling mechanism, or the preload, it is also dependent on afterload, contractility and heart rate. Starling's law can be expressed in terms of the ratio of the volume that is ejected to the total resting volume. This ejection fraction is defined as:

$$EF = SV / EDV \quad (4.1.6)$$

The normal mammalian heart has an ejection fraction of 0.5 to 0.7. Table 4.1.1 provides some of the reported values of ejection fraction in different species of mammals.

Table 4.1.1: Ejection fractions in some mammalian species

Man	0.67
Dog	0.65
Cat	0.64
Rabbit	0.61

Together with cardiac output, the product of stroke volume and heart rate,

$$CO = SV \times HR \quad (4.1.7)$$

ejection fraction has been widely used in the clinical setting as an index of LV performance. It is clear that the pressure-volume relationship provides a gross assessment of the global mechanical performance of the heart.

Another important aspect of the pressure-volume curve is the area under the loop which represents the mechanical work performed by the ventricle to overcome its vascular load. For this reason, it is often termed the *external work of the heart* and the area under the P-V loop is also known as the "work loop". This loop area is approximately the product of mean aortic pressure and the stroke volume, viz.

$$EW \approx \bar{p} \times SV \quad (4.1.8)$$

As a general definition, afterload can be considered as the forces that resist ejection of the ventricular outflow. The dynamics of the vascular system thus plays a vital role in determining this outflow.

#### *4.1.5 Coupling of the Ventricle and the Arterial System*

In assessing the coupling and the interaction of the heart and the arterial system several methods have been proposed. To simplify the analysis, approaches have mostly been based on models with lumped parameters. One such method the arterial system is represented by an effective arterial elastance ( $E_a$ ), although  $E_a$  does not directly reflect the physical elastic properties of the arteries. Elastance defined here, reflects only a system property, i.e. it does not equal the elastic properties of arteries. It is derived from the three-element windkessel model and based on the assumption that the arterial system behaves linearly. As such, it is a steady-state parameter that incorporates peripheral resistance, arterial compliance and characteristic impedance of the aorta, and systolic and diastolic intervals,

$$E_a = \frac{R_s}{[t_s + \tau(1 - e^{-t_d/\tau})]} \quad (4.1.9)$$

where  $t_s$  and  $t_d$  are systolic and diastolic periods, respectively. The diastolic pressure decay time constant is shown as before,

$$\tau = R_s C \quad (4.1.10)$$

$E_a$  has been approximated by the ratio of end-systolic pressure to stroke volume (SV or  $V_s$ ), or

$$E_a \approx P_{es} / SV \quad (4.1.11)$$

When the mean arterial pressure is used to approximate  $P_{es}$ , then  $E_a$  can be easily estimated from

$$E_a = \bar{P} / V_s \quad (4.1.12)$$

Approximation of mean pressure to  $P_{es}$  is good under normal physiological conditions, but poor during strong vasoactive conditions.

Cardiac output is the product of stroke volume and heart rate, as defined before,

$$CO = V_z \cdot f_h \quad (4.1.13)$$

where

$$f_h = \frac{1}{T} \quad (4.1.14)$$

$T$  is cardiac period. The effective arterial elastance can be rewritten as

$$E_a \approx \frac{R_s}{T} \quad (4.1.15)$$

since  $R_s$  is simply the ratio of mean arterial pressure divided by cardiac output.

Alternatively, when the diastolic aortic pressure decay time constant is long compared with the diastolic period, or  $\tau \gg t_d$ , the denominator of equation (4.1.9) reduces to

$$t_s - \tau (1 - 1 - t_d/\tau) = t_s + t_d = T \quad (4.1.16)$$

where Taylor expansion is applied to the exponential term. When the assumption that the peripheral resistance is much larger than the characteristic impedance of the aorta, or  $R_s \gg Z_o$ , is also made, then the effective arterial elastance becomes, again,

$$E_a \approx \frac{R_s}{T} \quad (4.1.17)$$

The effective arterial system elastance obtained in this manner is only dependent on the peripheral resistance and the cardiac period. It is totally independent of the elastic properties of the arterial system.

In terms of ventricular function, a popular index used to describe its contractility is the maximal elastance ( $E_{\max}$ ) of the ventricle. It is derived from the ventricular pressure-volume relation (Suga et al., 1973). In this context, the ventricle is modeled with a time-varying compliance,  $C_v(t)$ , the inverse of which is the time-varying elastance,  $E(t)$ . The concept of using  $E_{\max}$  as an "index of cardiac contractility" is more clearly demonstrated when interventions that alter pumping ability of the heart are imposed. For instance, with epinephrine infusion, the slope increased and hence an increase in contractility. Fig. 4.1.4 gives a schematic drawing of left ventricular pressure plotted against left ventricular volume. The pressure-volume loop, or P-V loop, follows an anti-clockwise direction. It can be seen that the end-systolic points of the P-V loops lie on a straight line. This line intercepts the volume axis at  $V_d$ . At end-systole, the elastance ( $E(t)$ ) slope is at its maximum and this defines  $E_{\max}$ :

$$E_{\max} = \frac{P_{es}}{V_{es} - V_0} \quad (4.1.18)$$

where  $E_{\max}$  is the maximum elastance of the ventricle,  $V_{es}$  is the end-systolic volume and  $V_0$  is the dead volume, or the volume at which the

ventricle no longer has the ability to develop pressure. Neglect  $V_o$  results in a simplified relation

$$E_{es} = P_{cs} / V_{es} \quad (4.1.19)$$

Despite its obvious limitations, the simple ratio of  $E_a/E_{es}$  has been used extensively to characterize the interaction of the heart and the arterial system (e.g. Kelly et al., 1992; Starling, 1993). Fig. 4.1.5 illustrates the steady state coupling of the ventricle and the arterial system using the ratio of  $E_a/E_{es}$  (Sunagawa et al., 1983).

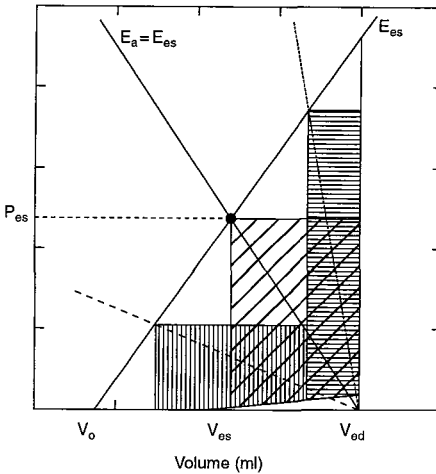


Fig. 4.1.5: Diagram defining the effective arterial elastance  $E_a$ , showing its relation to the ventricular elastance,  $E_{es}$ .

It has been shown by that the use of peripheral vasoactive agents such as the potent vasoconstrictor methoxamine and vasodilator nitroprusside (Li and Zhu, 1994), do not alter the slope of the end-systolic pressure-volume line, or  $E_{cs}$  (Starling, 1993). But the slope of  $E_a$  is increased with methoxamine and decreased with nitroprusside, as expected. As a result, the ratio of  $E_a/E_{es}$  is altered, indicates changes in ventricle-arterial system coupling. With dobutamine, on the other hand,  $E_a$  stays unaltered, while

$E_{es}$  is increased, indicating changing cardiac contractility (Fig. 4.1.6). Thus, the coupling ratio  $E_a/E_{es}$  can be altered by either change in cardiac contractility or arterial load.

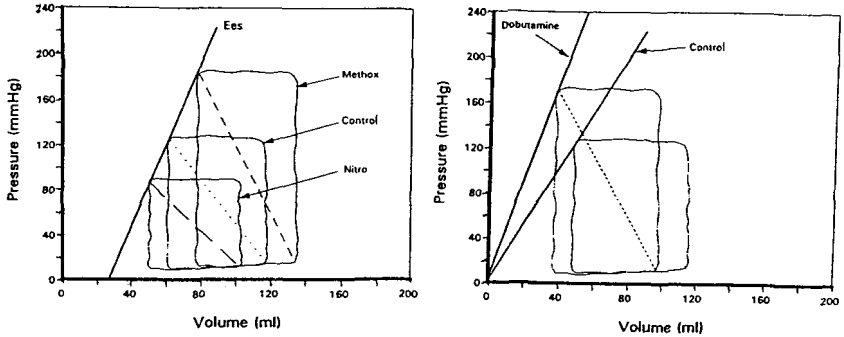


Fig. 4.1.6: Pressure-volume diagrams of the ventricle illustrating the steady state coupling of the ventricle and the arterial system using the ratio of  $E_a/E_{es}$ . With methoxamine and nitroprusside infusions, the slope of  $E_{es}$  is unchanged, while  $E_a$  is altered. With dobutamine infusion,  $E_{es}$  is increased, while  $E_a$  is unchanged. From Starling (1993).

The effects of alterations of windkessel model parameters on the ventricular pressure-volume relation under steady state conditions have been investigated (Maughan et al., 1984). The changes in arterial compliance and peripheral resistance have little effects on the slope of the end-systolic pressure-volume relation. However, the shape and the trajectory of left ventricular elastance are significantly altered.

It should be noted here that there are other indices to cardiac performance, such as the pump function curve proposed by Van den Horn et al. (1984), the maximum velocity of cardiac muscle shortening concept suggested by Brutsaert (1974) based on force-velocity-length relations.

#### 4.1.6 Dynamic Heart-Arterial System Interactions

Blood pressure varies during the cardiac cycle. Thus, vascular compliance is also expected to vary continuously. This dynamic time-varying, pressure-dependent compliance property is incorporated in a

nonlinear model of the systemic arterial system (see Section 4.5). A model incorporating this property to investigate the dynamic heart-arterial system interaction is shown in Fig. 4.1.7. The left ventricle is represented by a time-varying compliance and a systolic resistance. The time-varying compliance is the inverse of time-varying elastance. Both time-varying compliance of the left ventricle and the pressure-dependent compliance of the arterial system exhibit temporal dependence, hence they are dynamic in nature.

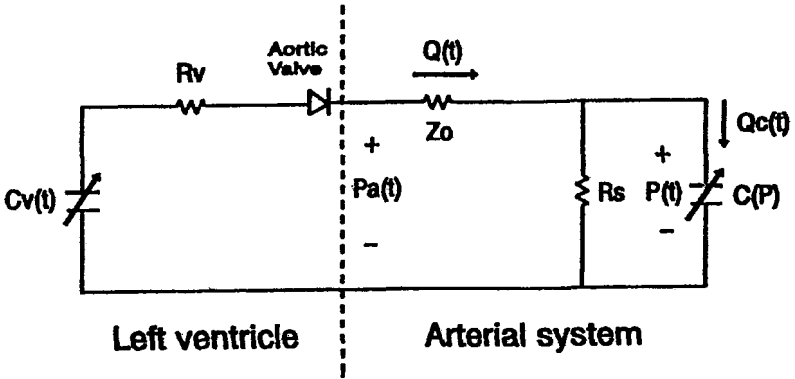


Fig. 4.1.7: Nonlinear model of the arterial system coupled to the left ventricle.  $C_v(t)$  =time-varying left ventricular compliance,  $R_v$  =systolic ventricular resistance,  $Z_o$  = aortic characteristic impedance,  $R_s$  =peripheral resistance,  $C(P)$  =pressure-dependent or dynamic arterial compliance.  $P_a(t)$  and  $Q(t)$  are aortic pressure and flow, respectively. Provided by Dr. Ying Zhu.

This model predicted changes have particular implications in terms of global heart-arterial system interaction. For instance, the pressure-dependent arterial compliance ( $C(P)$ ) increases during the early systole to facilitate ventricular ejection, but reaches a minimum at about end-systole (Fig. 4.1.8). The dynamic elastance of the arterial system represented as the inverse of the pressure-dependent arterial system compliance is:

$$E_{as}(t) = 1 / C(P) \quad (4.1.20)$$

At end-systole, is when both time-varying arterial elastance and ventricular elastance are at their respective maximum ( $E_{max}$ , also Berger

and Li, 1992). The developing arterial elastance at systole reflects the time-varying compliance characteristics that are associated with active tension development of the arterial wall, as established for the ventricular muscle. This also demonstrates that the interaction of the heart and the arterial system is a dynamic one, particularly in systole. The arterial compliance thus bears a temporal, hence dynamic, relation to left ventricular function.

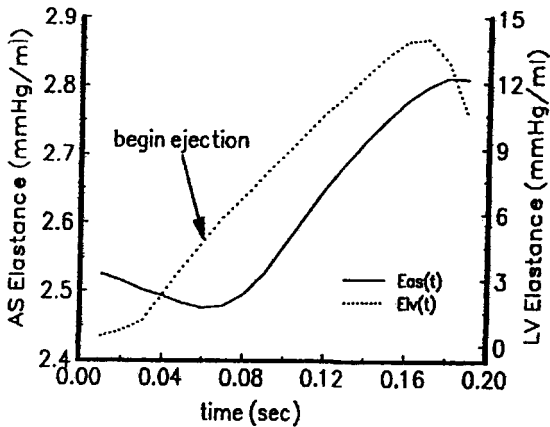


Fig. 4.1.8: Temporal relation of time-varying left ventricular and arterial system elastances, demonstrating the dynamic interaction during systole. Arterial system elastance is obtained from the pressure-dependent compliance ( $E_{as}(t) = 1/C(P)$ ).

## 4.2 Pressure-Flow Relations and Vascular Impedance

### 4.2.1 Pressure and Flow Waveforms in Large and Small Arteries

Pressure and flow waveforms in different anatomic locations in the vascular system owe to their structural and geometric nonuniformities, as well as central and peripheral interactions. Simultaneous recordings of pressure and flow waveforms in different parts of the vascular tree have shown some distinct features as the pulse travels away from the heart.

First, the pressure pulse increases and the flow pulse decreases in amplitude progressively. The mean blood pressure declines slowly in arteries, but dramatically so in the arteriolar beds. Secondly, the rate of rise of the pressure ( $dp/dt$ ) in early systole increases and the wavefront becomes steeper, while that of the flow wave behaves in just the opposite manner. Thirdly, the incisura, or dirotic notch, due to aortic valve closure, is more rounded as the pressure wave propagates towards the periphery and the diastolic pressure wave becomes more accentuated. These features are seen from Fig. 4.2.1. These observed changes are related to the functional aspects of the arterial system. Consequently, considerable diagnostic information can be derived from the accurate measurements and analysis of pressure and flow pulse contours.

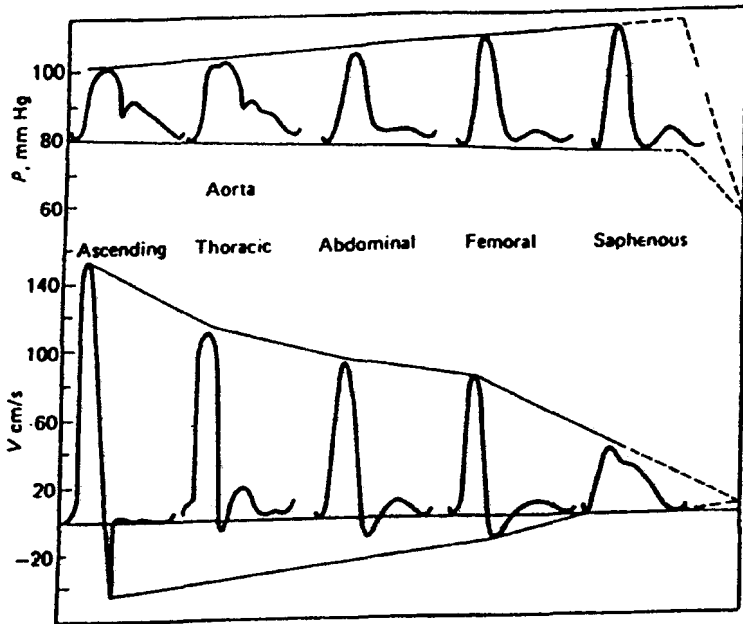


Fig. 4.2.1: Pressure and flow waveforms in the ascending, thoracic and abdominal aortas, as well as the femoral and saphenous arteries. The progressive increases in pulse pressure and decreases in pulsatile flow magnitudes are seen. From Nichols and O'Rourke (1998).

Multi-sensor catheter has been used for simultaneous recordings of pressure and flow waveforms at several sites along the pulse propagation path. This allows extraction of pulse transmission information, and in the interpretation of hemodynamic alterations in diseased conditions.

Simultaneous recording of pressure and flow velocity waveforms in man can be achieved in the clinical setting with catheter tip pressure and velocity sensors. In general, pressure and flow waveforms are similar at corresponding anatomic sites among many mammalian species (Li, 1996).

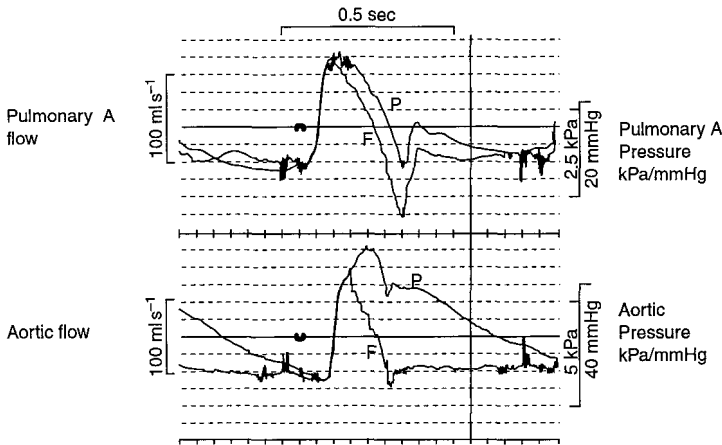


Fig. 4.2.2: Simultaneously recorded pressure and flow waveforms in the pulmonary aorta (top tracings) and in the ascending aorta (bottom tracings). Notice the pressure and flow waveforms are more similar in the more compliant pulmonary arterial system.

At the onset of systole, left ventricular pressure (LVP or  $P_v$ ) develops rapidly during the cardiac isometric contraction period. When LVP exceeds the aortic pressure (AoP or  $P_a$ ), ventricular ejection begins. The ventricular outflow is large and rapid at the onset of ejection, becomes more gradual and then declines towards end-systole. At aortic valve closure, there is backflow, followed by small oscillations. In diastole, the aortic flow reaches zero. The diastolic aortic pressure decays precipitously towards end-diastole. In the windkessel approximation, this decay follows a mono-exponential pattern. In actuality, there are

oscillations superimposed on the diastolic pressure and the decay is not necessarily mono-exponential.

The right ventricle and the pulmonary arterial system is known as the “low pressure” system and the left ventricle and the systemic arterial system is known as the “high pressure” system. This implies that pulmonary aorta has a much lower pressure amplitude than that of the aorta. The stroke volume is the same, therefore, the flow magnitudes are similar, although their waveforms can be quite different. Fig. 4.2.2 illustrates the differences. The pulmonary aorta is much more compliant than the aorta and the pressure waveform tends to be more closer in morphology to the flow waveform (Van den Bos et al. , 1982). This has been attributed to the comparatively smaller amount of wave reflections in the pulmonary system. This is due to the spatial distribution of compliances that are greater in the pulmonary arteries than the stiffer systemic arteries. Major reflections do not reach the proximal aortas in early ejection phase. Thus, the time courses of pressure and flow waveforms are similar during this interval.

Blood pressure waveforms are periodical, as illustrated in Fig. 4.2.3 which displays pressure waveforms recorded in the ascending aorta, descending thoracic aorta, the abdominal aorta and the iliac artery, when the catheter-tip pressure transducer is slowly withdrawn away from the heart. The progressive increases in pulse pressure amplitudes with increasing systolic pressure and decreasing diastolic pressure can be observed. The electrocardiogram (ECG) is normally recorded as timing reference and for the calculation of cardiac period ( $T$ ). The bottom tracing is the ascending aortic flow measured with an electromagnetic flow probe. The waveforms are reproducible following each heart beat. This is normally true under steady state conditions.

Respiratory influence on the pressure waveforms is easily observed when consecutive beats are recorded over a respiratory cycle. The normal ratio of heart frequency to respiratory frequency is about 4:1. The changes induced by respiration are usually small, except in some pathological conditions, such as in pulsus paradoxus where blood pressure change is excessive during both inspiration and expiration.

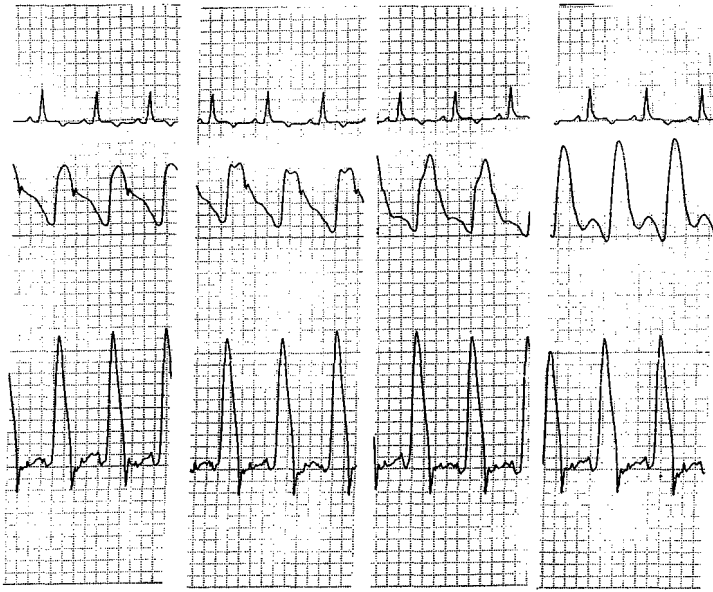


Fig. 4.2.3: Simultaneously recorded electrocardiogram (top panel), blood pressure (middle panel) and ascending aortic flow (bottom panel) waveforms. Pressure waveforms in the ascending aorta (first left), descending thoracic aorta (second left), the abdominal aorta (second right) and the iliac artery (first right) are shown.

The more distal the pressure pulse away from the heart, the larger is its amplitude. This is attributed to the larger amplitudes of peripheral wave reflections. Such reflections have been suggested as a closed-end type, with the principal sites of reflections in the arterioles. Structural and geometric changes along a vessel also give rise to reflections, but are of smaller magnitudes. Reflections, in general, have opposite effects on pressure and flow.

Geometric nonuniformities constitutes the second factor that influences the pulse waveforms. These may be tapering or vascular branching. The many aspects of vascular branching is the subject of the following chapter.

The third influential factor is elastic nonuniformity. The vascular wall becomes progressively stiffer toward the periphery owing to

increased elastic moduli, and accounts for the dispersion of wave velocity.

Finally, the wall and fluid viscosities attenuate the pulse wave. The extent of attenuation, or the degree of damping, is greater at higher frequencies. For instance, the pulse at the femoral artery no longer exhibits the characteristic high frequency features of the aortic pulse. Instead, a smooth waveform is seen. The pulse reaching the arterioles is normally so damped that its waveform appears sinusoidal.

In summary, pressure and flow pulses are modified as they travel away from the heart due to (1) wave reflections, (2) geometric nonuniformity, (3) elastic nonuniformity, and (4) damping.

#### ***4.2.2 Vascular Impedance to Blood Flow***

The impedance of the total systemic vascular tree, or the input impedance to the arterial system, is defined as the complex ratio by harmonic of pressure to flow. This is so defined when the pressure and flow waveforms are measured at the entrance to the arterial system, namely, at the root or the aorta or ascending aorta. Impedance can also be measured at different parts of the circulation. For instances, when pressure and flow are measured at the femoral artery, then the vascular impedance so obtained represents that of the impedance of the femoral arterial vascular bed.

Vascular impedance has both a magnitude and a phase for each harmonic. Since pressure and flow are generally not in phase, the impedance possesses a phase angle within  $90^\circ$ . This is attributed to the time delayed arrival between the pressure pulse and the flow pulse. When the particular pressure harmonic leads the flow harmonic, then the phase angle between them is positive. Conversely, when the pressure harmonic lags behind the corresponding flow harmonic, then the phase is negative. Phase difference in the frequency domain, therefore, refers to time delay in the time domain.

The harmonic contents of pressure and flow waveforms can be obtained through Fourier analysis, as shown in Chapter 3. Pulsatile blood pressure waveform can be considered an oscillatory part with sinusoidal components oscillating at different harmonic frequencies,  $n\omega$ ,

and phase,  $\phi_n$ , superimposed on a DC component or mean blood pressure:

$$p(t) = \bar{p} + \sum_{n=1}^N P_n \sin(n\omega t + \phi_n) \quad (4.2.1)$$

$$\omega = 2\pi f \quad (4.2.2)$$

where  $f$  (Hz) is the number of heart beats per second. Similar equations can be written for the flow waveform.

The relations for the pressure and flow pulse waveforms expressed as magnitude and phase are, for the  $n$ th harmonic:

$$P_n = |P_n| e^{j(\omega t + \phi_n)} \quad (4.2.3)$$

$$Q = |Q_n| e^{j(\omega t + \phi_n)} \quad (4.2.4)$$

The ratio of pressure to flow is, therefore,

$$\frac{P}{Q} = \frac{|P_n| e^{j(\omega t + \phi_n)}}{|Q_n| e^{j(\omega t + \phi_n)}} \quad (4.2.5)$$

The vascular impedance obtained for the  $n$ th harmonic is therefore

$$Z_n = |Z_n| e^{j\theta_n} \quad (4.2.6)$$

where the magnitude of impedance is simply the ratio of the pressure amplitude to the flow amplitude for the  $n$ th harmonic:

$$|Z_n| = \frac{|P_n|}{|Q_n|} \quad (4.2.7)$$

and the phase lag

$$\theta_n = \phi_n - \varphi_n \quad (4.2.8)$$

Pressure and flow waveforms do not necessarily contain the exact number of significant harmonics. When the flow harmonic becomes very small, the ratio of pressure to flow or the impedance modulus for that harmonic component obtained can be erroneous.

Input impedance of the systemic arterial tree have been obtained in the systemic pulmonary and coronary arterial circulations. Vascular impedances have been measured in man, dog and other mammalian species. Fig. 4.2.4 gives an example of the modulus and phase of the vascular impedance measured at the ascending aorta or the input impedance of the systemic arterial tree in normal adults.

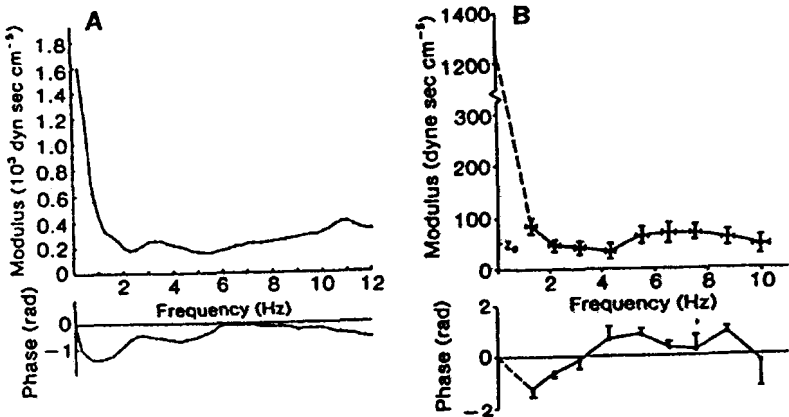


Fig. 4.2.4: Modulus and phase of the impedance measured at the ascending aorta or input impedance of the systemic arterial tree in a normal adult (A) and the average obtained in five adults (B).  $Z_0$  indicates characteristic impedance of the proximal aorta. From Nichols and O'Rourke (1998).

Input impedance shows a large decrease in magnitude at very low frequencies ( $<2$  Hz), then oscillates, exhibiting maxima and minima, and eventually reaches a somewhat constant level-low compared to its zero frequency (DC) value, at higher frequencies ( $>5$  Hz). The input impedance ( $Z$ ) approaches the characteristic impedance ( $Z_0$ ) of the proximal aorta at these high frequencies. The phase of the impedance is initially negative, becoming progressively more positive and crossing zero at about 3-5 Hz, and remains positive but close to zero thereafter.

The characteristic maxima and minima associated with the input impedance spectrum is closely related to reflections in the arterial system.

The initial large decrease in impedance modulus accompanying a negative phase indicates that the load facing the left ventricle at low frequencies is capacitive in nature, while at high frequencies it is inductive. The viscous losses in the proximal aorta are small, but are more appreciable elsewhere in the arterial system (Li, 2000). Hence, approximating characteristic impedance by the high frequency values of the input impedance is more accurate in the proximal aorta than in other vessels.

$$Z_o \approx \overline{Z}(\omega)_{HF} \quad (4.2.9)$$

Values of characteristic impedance of the aorta estimated from high frequency average of the input impedance spectrum have been variable, mostly due to the frequency range used for the estimation and the body size. In the dog,  $Z_o$  has been found to be 200-300 dyn.s.cm<sup>5</sup> when a typical high frequency range used for taking the average is 3-10 Hz.

In the time domain, a simple method to approximate characteristic impedance of the aorta is to utilize the fact that in early ejection, reflected waves cannot reach the proximate aorta. In this case,  $Z_o$  can be obtained, simply from the ratio of instantaneous aortic pressure and flow above their end-diastolic levels (Li, 1986):

$$Z_o = \frac{p(t) - p_d}{Q(t)} \quad (4.2.10)$$

This method is valid for the first 60-80 ms of ejection.

Another method, also with the assumption that reflected waves do not influence the measurement, is the classic water-hammer formula:

$$Z_o = \frac{\rho c}{\pi r^2} \quad (4.2.11)$$

where  $c$  is pulse wave velocity,  $r$  is radius and  $\rho$  is blood density,  $1.06 \text{ g/cm}^3$ . This method can be applied clinically where the cross-section area can be obtained with ultrasound echocardiograph and the foot-to-foot pulse wave velocity with a dual-sensor catheter.

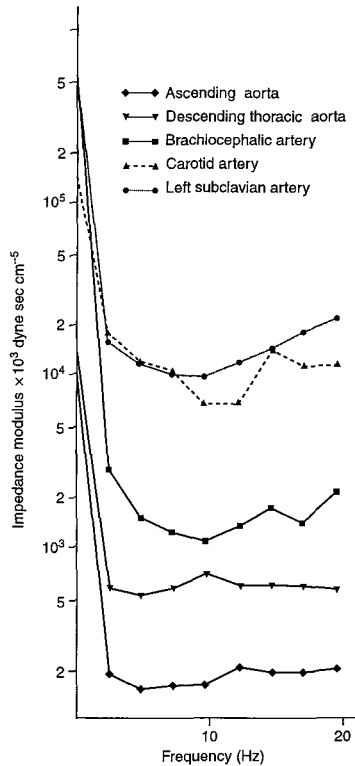


Fig. 4.2.5: Vascular impedances measured in several systemic arteries at aortic arch. Notice that impedance modulus increases dramatically in smaller arteries. From Cox and Pace (1975).

Both the input impedance and characteristic impedance moduli increase as the measurement site becomes further away from the heart. In addition, zero crossing of the phase occurs at a much higher frequency. Since only harmonic components can appear in the spectrum, extended information can often be obtained by imposing cardiac pacing at different frequencies. The Vascular impedances obtained by Cox and

Pace (1975) at aortic arch junction suffice to illustrate these (Fig. 4.2.5). It is clear from these impedance spectra that ascending aorta has the lowest impedance modulus and the impedance modulus is higher through descending thoracic aorta, the left subclavian, the brachiocephalic and the carotid arteries. The characteristic impedances are also higher in smaller arteries due to their increased stiffness and reduced lumen diameter. Resistance of vascular beds that are perfused by smaller arteries is also higher.

Ventricular afterload is defined as all external factors that oppose ventricular ejection. For this reason arterial input impedance has been suggested as being afterload. It is important to note that both the ability of the left ventricle to do work (myocardial performance) and the properties of the arterial system are important in determining the power generated by the ventricle.

In general, input impedance as predicted by the three-element windkessel model gives a reasonable overall estimate of experimentally measured input impedance. This is more so in moduli than in phase. With vasoconstriction, the impedance modulus is increased and its first minimum is shifted to a higher frequency. With vasodilation, the impedance modulus decreases and its first minimum is shifted to a lower frequency. The corresponding zero-phase crossing also applies. This indicates that wave reflections arrive earlier due to a closer effective reflection site in the case of vasoconstriction.

## 4.3 Wave Propagation Phenomena

### 4.3.1 The Propagation Constant

For a pressure pulse wave propagating along a uniform artery without the influence of wave reflections, the pressures measured simultaneously at any two sites along the vessel are related by:

$$p_2 = p_1 e^{-\alpha z} \quad (4.3.1)$$

where  $p_2$  is the distal pressure,  $p_1$  is the proximal pressure,  $\gamma$  is the propagation constant and  $z$  is along the longitudinal axis of the artery in the direction of pulse propagation. The propagation constant obtained under such circumstances, is known as the “true” propagation constant, since it is not influenced by wave reflections. It is a complex variable, thus has both magnitude and phase. It encompasses both the attenuation coefficient,  $\alpha$ , and the phase constant,  $\beta$ :

$$\gamma = \alpha + j\beta \quad (4.3.2)$$

The attenuation coefficient dictates the amount of damping imposed on the propagating pressure pulse due to both viscosity of the blood and viscosity of the arterial walls.

The phase constant arises because of the finite pulse wave velocity,  $c$ . In other words, the pressure pulse travels at finite velocity and therefore, takes finite amount of time to go through each arterial segment. Pulse wave velocity at any given frequency is given by:

$$c = \frac{\omega}{\beta} \quad (4.3.3)$$

Thus, pulse wave velocity varies with frequency. This arises, because different harmonic component travels at different velocity, known as harmonic dispersion. Li et al. (1981) have shown that that true phase velocity increases at low frequencies and reach a somewhat constant value at high frequencies, usually beyond the third harmonic. Anliker et al. (1968) utilized high frequency artificial waves, essentially unaffected by reflections, to obtain phase velocity and attenuation in the dog aorta.

#### ***4.3.2 Foot-to-Foot Velocity***

Pulse wave velocity has been popularly approximated by the so-called “foot-to-foot” velocity. Here, one simply estimates the pulse wave velocity from the transit time delay ( $\Delta t$ ) of the “onset” or the “foot” between two pressure pulses measured at two different sites along an artery or the pulse propagation path. This requires again, the

simultaneous measurements of two pressures separated by a finite distance,  $\Delta z$ , normally 4-6 cm apart. A double-lumen catheter with two pressure ports connected to two pressure transducers or a Millar catheter with dual pressure sensors suffice for such measurement. Thus, the foot-to-foot velocity,  $c_f$  is calculated from:

$$c_f = \frac{\Delta z}{\Delta t} \quad (4.3.4)$$

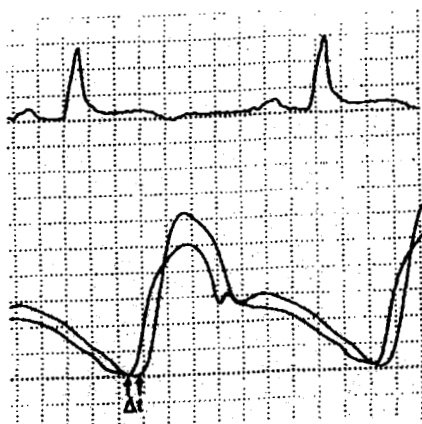


Fig. 4.3.1: Diagram illustrating how foot-to-foot velocity is calculated given pressure measurements at different sites separated by a known distance  $\Delta z$ . Here the foot-to-foot velocity is given by  $c_f = \Delta z / \Delta t$ .  $\Delta t$  is pulse transit time delay. Notice the peak-to-peak transit time is different from that of the foot-to-foot.

This method assumes that reflected waves do not interfere with the onset of the propagating pulse. As an example, referring to Fig. 4.3.1, the distance between the two pressure measurement sites is 5 cm and the calculated time delay,  $\Delta t$ , is 60 msec, or 0.06 sec, then the foot-to-foot velocity is

$$c_f = \frac{5}{0.06} = 833 \text{ cm/s} \quad (4.3.5)$$

or 8.33 m/s.

Fig. 4.3.2 shows the foot-to-foot velocity measured in different arteries (Nichols and McDonald, 1972). Wave velocity increased from

about 5 m/s in the ascending aorta to about 10 m/s in the femoral artery, higher in the tibial artery.

Pulse wave velocity estimated from the peaks, or the peak-to-peak velocity, can give considerable errors, although the peak of the pulse is frequently easier to identify than that the foot. This stems from the fact that the peak of the pressure pulse is often contaminated with reflected waves, since it allows sufficient time for reflected waves to arrive at the measurement sites.

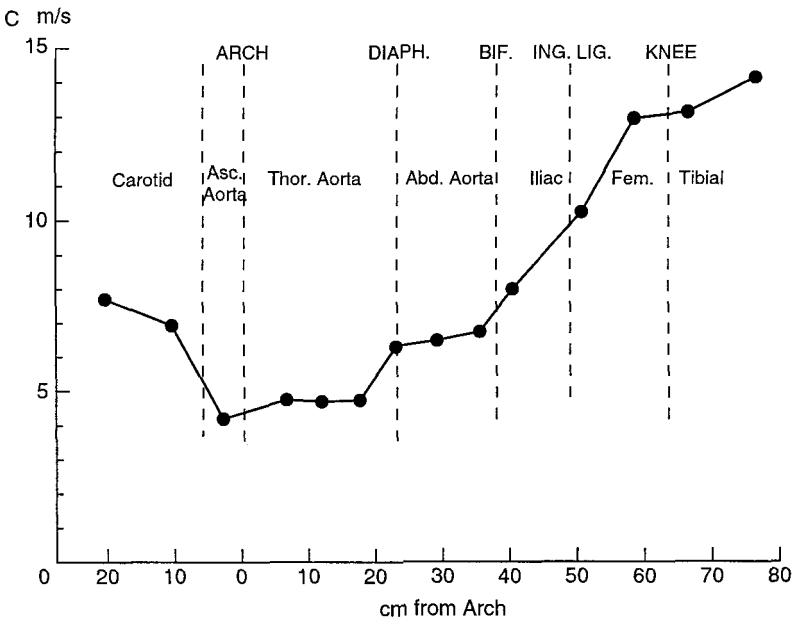


Fig. 4.3.2: Pulse wave velocity recorded as foot-to-foot velocity measured in different arteries. Higher wave velocity in smaller arteries are seen. From Nichols and McDonald, (1972).

With changing geometry and elastic properties away from the ascending aorta, the pulse wave velocity also changes. This is seen from the Moens-Korteweg formula for estimating pulse wave velocity:

$$c_o = \sqrt{\frac{Eh}{2\rho r}} \quad (4.3.6)$$

where  $E$  is the elastic modulus of the artery,  $h$  and  $r$  are the wall thickness and radius of the artery and  $\rho$  is the density of blood. This formula is applicable to a single vessel, while foot-to-foot velocity has been obtained either for a single artery or over the pulse propagation path, e.g. over several arteries.

#### 4.3.3 Apparent Propagation Constant and Transfer Function

Vascular tree structure and neuro-humoral influences, there are considerable differences in the amount of wave reflections that arise in different parts of the circulation. In the presence of reflected waves, one can define an apparent propagation constant where

$$p_2 = p_1 e^{-\gamma_{app} z} \quad (4.3.7)$$

$$\frac{p_2}{p_1} = e^{-\gamma_{app} z} \quad (4.3.8)$$

and

$$\gamma_{app} = \frac{1}{\Delta z} \ln \frac{p_1}{p_2} \quad (4.3.9)$$

The apparent propagation constant so defined is dependent on wave reflections and reflects local propagation characteristics. In this case, the separation ( $\Delta z$ ) between  $p_2$  and  $p_1$  needs to be small, so that  $c_{app}$  is more representative of the underlying artery. When the separation is large, say from the ascending aorta to the abdominal aorta, the apparent wave velocity obtained may contain interactions resulting from branching vessels with their vascular beds. On the other hand, the larger the distance of separation, gives much better accuracy or resolution of the attenuation and phase shift.

The apparent propagation constant at any point along the vessel is defined by:

$$\gamma_{app} = \alpha_{app} + j\beta_{app} \quad (4.3.10)$$

and  $\alpha_{app}$ , the apparent attenuation coefficient, is obtained from:

$$\alpha_{app} = \frac{1}{\Delta z} \ln \frac{|p_1|}{|p_2|} \quad (4.3.11)$$

where  $|p_1|$  and  $|p_2|$  are the harmonic moduli of  $p$ , and  $p_2$ , respectively. It is clear that  $\alpha_{app}$ , describes the degree of damping or the attenuation of the pressure pulse as it propagates between the two arterial sites.

The apparent phase constant  $\beta_{app}$  is obtained from:

$$\beta_{app} = (\phi_1 - \phi_2) / \Delta z \quad (4.3.12)$$

where  $\phi_1$  and  $\phi_2$  are the harmonic phases of  $p$ , and  $p_2$ , respectively. The apparent phase velocity of propagation is calculated from:

$$c_{app} = \frac{\omega}{\beta_{app}} \quad (4.3.13)$$

or more explicitly

$$c_{app} = \frac{2\pi f \cdot \Delta z}{\phi - \phi_2} \quad (4.3.14)$$

$c_{app}$  is also known as the measured velocity. This apparent phase velocity is significantly affected by the presence of wave reflections, in the similar manner as vascular impedance.

The true and apparent propagation constants can be related to characteristic and input impedances as:

$$\frac{\gamma_{app}}{\gamma} = \frac{Z_o}{Z} \quad (4.3.15)$$

This formula also provides a new method for obtaining true propagation constant from measured input impedance and apparent propagation constant (Li, 1987).

Because the apparent phase velocity,  $c_{app}$ , is influenced by wave reflections in the same manner that input impedance is affected, its frequency spectrum is similar to that of input impedance. Thus,  $\gamma_{app}$  is also influenced by wave reflections. An example of the frequency dependence of apparent propagation constant calculated for the femoral arterial bed is shown in Fig. 4.3.3. They are both dependent on the magnitude and phase of the global reflection coefficient.  $\gamma$ , on the other hand, is, by definition, independent of reflections, and the manner it varies with frequency has been quantified by Li et al. (1980, 1981). It can be deduced that, in the absence of reflected waves,  $\Gamma=0$  and  $\beta_{app}=\beta$ , i.e., apparent phase velocity equals true phase velocity. This is easily seen from Fig. 4.3.4 from data obtained by Li et al. (1980) in a viscoelastic tube.

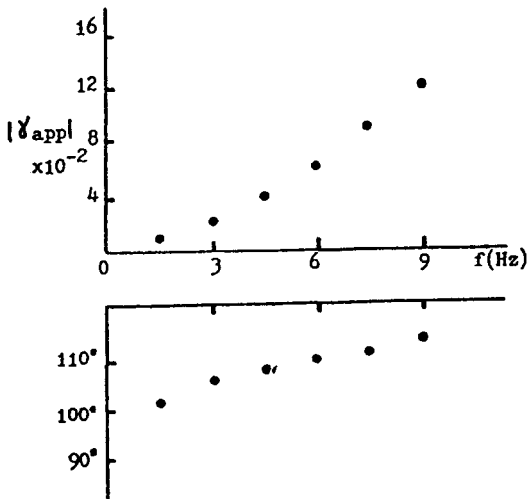


Fig. 4.3.3: Apparent propagation constant obtained as a function of frequency for the femoral arterial bed. From Li (1980).

Apparent phase velocities have been obtained noninvasively with tonometers. One such example is shown in Fig. 4.3.5. The pressure

waveforms were first obtained and the apparent phase velocity spectra calculated between the carotid and radial arterial sites for normal and hypertensive adults (Li et al., 1996). It must be stated that estimation of  $c_{app}$  over a long propagation path usually subject to more random summation and cancellation of reflected waves within the path.

The definition of apparent propagation constant,  $\gamma_{app}$ , by equation (4.3.9) also represents what is popularly known as the “pressure transfer function”, or simply transfer function. Thus, knowing the transfer function of two arterial sites, one can obtain one blood pressure waveform from the other. This follows from the definition of apparent propagation constant (equations (4.3.7) and (4.3.9)). For, instant, one can obtain the central aortic pressure waveform from carotid pressure pulse measurement, if the apparent propagation constant or the transfer function is known. Since carotid pulse, radial pulse and brachial pulse can be readily obtained noninvasively, this transfer function method has attracted clinical interest in recent years. The goal is to obtain central aortic pressure from noninvasive peripheral arterial pulse measurement. The transfer function obtained takes the similar form as the propagation constant defined above.

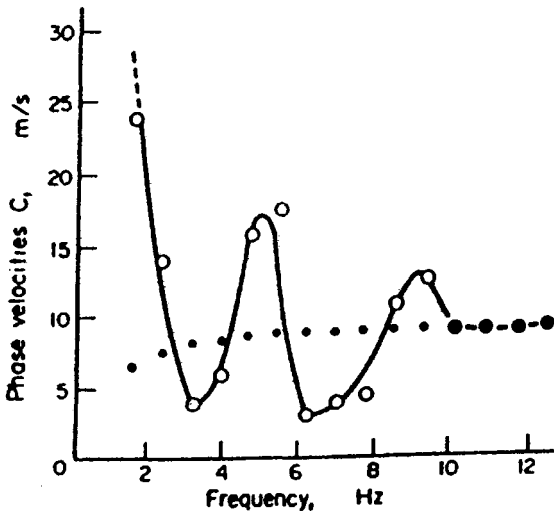


Fig. 4.3.4: Apparent phase velocity compared to true phase velocity in a viscoelastic tube. The influence of wave reflections on apparent phase velocity at low frequencies is clearly seen. At high frequencies the two velocities approach a somewhat constant value. (From Li et al. (1980).

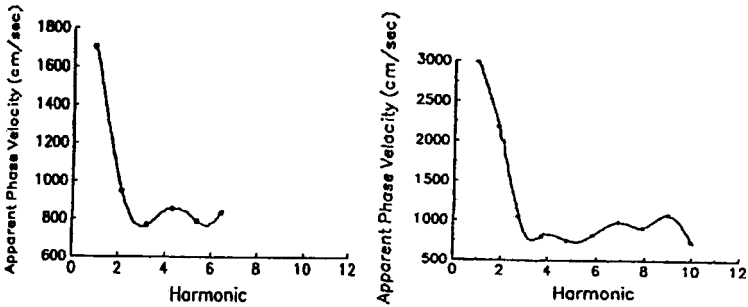


Fig. 4.3.5: Apparent phase velocities obtained by noninvasive pressure measurements with tonometers at the carotid and radial arterial sites in normal and hypertensive adults. (From Li et al. (1996). Larger low frequency amplitudes and greater oscillations at higher frequencies can be seen.

#### 4.3.4 Determination of the Propagation Constant

Experimental determination of the apparent propagation constant is simpler than that of the true propagation constant. The former can be determined by simultaneously measuring either two pressures for the pressure pulse, or two flows for the flow pulse. Determination of the true propagation constant which is independent of wave reflections, in the presence of reflections, however, requires simultaneous measurement of three variables.

Several methods are available to determine the true propagation constant, all of which are based on linear transmission theory. From the definition of the propagation constant as it relates to longitudinal ( $Z_l$ ) and transverse ( $Z_t$ ) impedances:

$$\gamma = \sqrt{Z_l / Z_t} \quad (4.3.16)$$

where

$$Z_l = \frac{-\partial p / \partial z}{Q} \quad (4.3.17)$$

$$Z_i = \frac{-p}{\partial Q / \partial z} \quad (4.3.18)$$

Knowing these relationships, the measurement of pressure and flow together with their gradients permit determination of the propagation constant. Thus, one can apply this method by measuring two pressures and two flows, or by measuring two pressures, a few centimeters apart, a flow midway between them, and the pulsatile change in diameter. Alternatively, the transverse impedance, which is related to vessel wall properties, can be obtained from the dynamic pressure-area relationship.

If two pressures and flows are measured simultaneously at two sites along a uniform vessel, the propagation constant can be obtained from:

$$\gamma = \frac{1}{\Delta z} \cosh^{-1} \left[ \frac{p_1 Q + p_2 Q_2}{p_2 Q + p_1 Q_2} \right] \quad (4.3.19)$$

where  $\Delta z$  denotes the distance between the two sites. Subscript <sub>1</sub> refers to the upstream site and <sub>2</sub>, the downstream site.

Another method utilizes the simultaneous recording of three pressures along a uniform vessel. The propagation constant is obtained as:

$$\gamma = \frac{1}{\Delta z} \cosh^{-1} \left[ \frac{\Delta p_1 + \Delta p_3}{2 p_2} \right] \quad (4.3.20)$$

when differential pressures are measured,  $\Delta p_1 = p_1 - p_2$ ;  $\Delta p_3 = p_3 - p_2$ . The three pressures  $p_1$ ,  $p_2$ ,  $p_3$ , are simultaneously measured at an equal distance ( $\Delta z$ ) apart.

The three-point pressure method was extensively evaluated by Li et al. (1980) in a hydrodynamic model. Subsequently, this method was applied to investigate pulse wave propagation in dogs (Li et al., 1981) with respect to contributions by vascular wall elastic and geometric properties, vessel wall and blood viscosity, and nonlinearities in system parameters and in the equations of motion. Discrepancies in results obtained with different experimental methods and theory were discussed and resolved. Measurements were obtained from the abdominal aorta, as

well as the carotid, iliac, and femoral arteries of dogs. The components of the propagation constant, i.e., attenuation coefficient and phase velocity, were obtained for each of the vessels investigated (Fig. 4.3.6, Fig. 4.3.7). Results were presented along a continuous path of transmission (abdominal aorta, iliac, femoral) and it was shown that variations in phase velocity can be explained entirely by the geometric variation of these vessels. Phase velocities were shown to be frequency independent at  $\geq 4$  Hz, while attenuation increases progressively for higher frequencies. The three-point method was also applied by Wells et al. (1998) to infer the contributions of collagen and elastin to overall viscoelastic properties of sheep thoracic aorta.

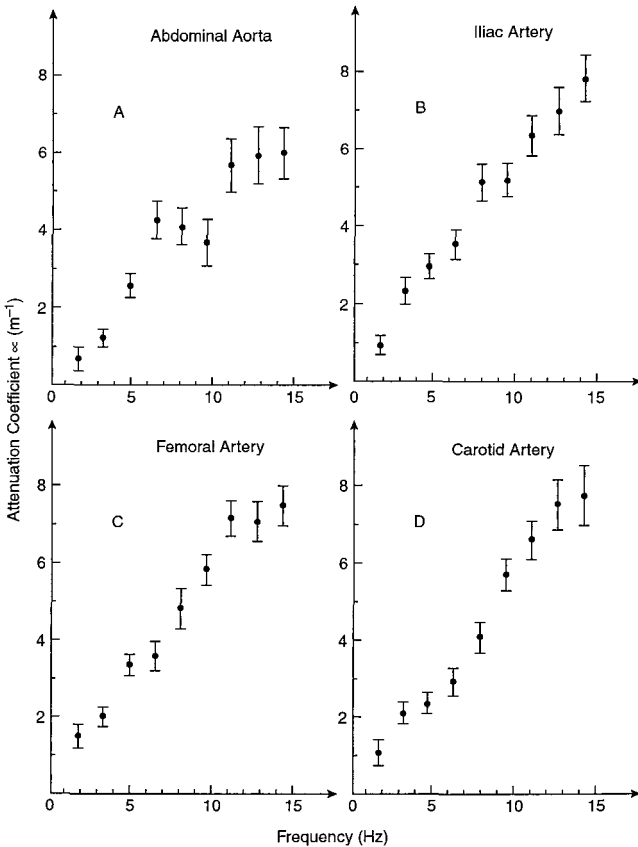


Fig. 4.3.6: Attenuation coefficients obtained for the lower abdominal aorta (a), iliac artery (b), femoral artery (c), and carotid artery (d). Mean  $\pm$  SEM. From Li et al. (1981).

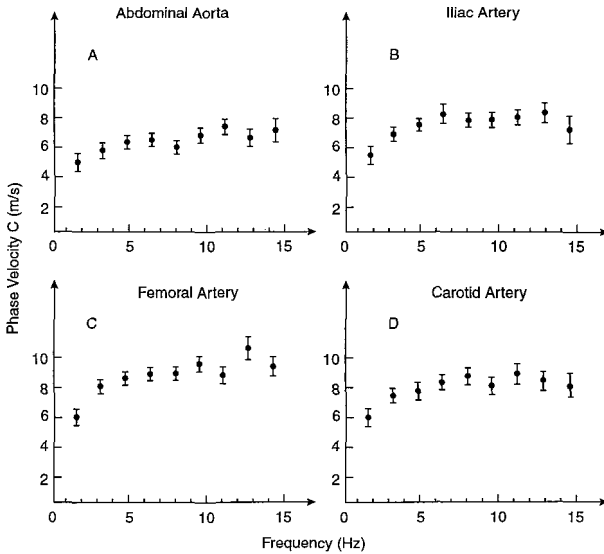


Fig. 4.3.7: Phase velocities obtained in the (a) lower abdominal aorta, (b) iliac artery, (c) femoral artery, and (d) carotid artery. From Li et al. (1981).

## 4.4 Wave Reflection Phenomena

### 4.4.1 Influence of Wave Reflections on Pressure and Flow Waveforms

The amplification of pressure pulses has been attributed to the in-phase summation of reflected waves arising from structural and geometric nonuniformities. The microvascular beds have been recognized as the principal reflection sites. Thus, pulsatile pressure and flow waveforms contain information about the heart as well as the vascular system. Reflection in the vascular system has been suggested as a closed-end

type, with arterioles being the major reflection site. Reflected pressure and flow waves are  $180^\circ$  out of phase. This means an increase in reflection increases pressure amplitude, but decreases flow amplitude.

Measured pressure ( $P$ ) and flow ( $Q$ ) waveforms measured at any site in the vascular system can be considered as the summation of a forward, or antegrade, traveling wave and a reflected, or retrograde, traveling wave:

$$P = P_f + P_r \quad (4.4.1)$$

$$Q = Q_f + Q_r \quad (4.4.2)$$

The forward and reflected pressure components can be resolved by means of the following set of equations:

$$P_f = (P + Q \cdot Z_o) / 2 \quad (4.4.3)$$

$$P_r = (P - Q \cdot Z_o) / 2 \quad (4.4.4)$$

where  $Z_o$  is the characteristic impedance, defined as the ratio of forward pressure to forward flow, or in other words, independent of wave reflections:

$$Z_o = \frac{P_f}{Q_f} = -\frac{P_r}{Q_r} \quad (4.4.5)$$

$Z_o$  can be obtained from the water-hammer formula:

$$Z_o = \frac{\rho c}{\pi r^2} \quad (4.4.6)$$

where  $\rho$  is the density of blood ( $1.06 \text{ g/cm}^3$ ),  $c$  is pulse wave velocity,  $\pi r^2$  is the cross-sectional area of the artery. With the characteristic impedance determined by a time domain method, forward and reflected waves can also be resolved in the time domain (Li, 1986).

Similarly, resolution of flow into its forward and reflected components can be obtained from a set of two equations:

$$Q_f = (Q + P/Z_o)/2 \quad (4.4.7)$$

$$Q_r = (Q - P/Z_o)/2 \quad (4.4.8)$$

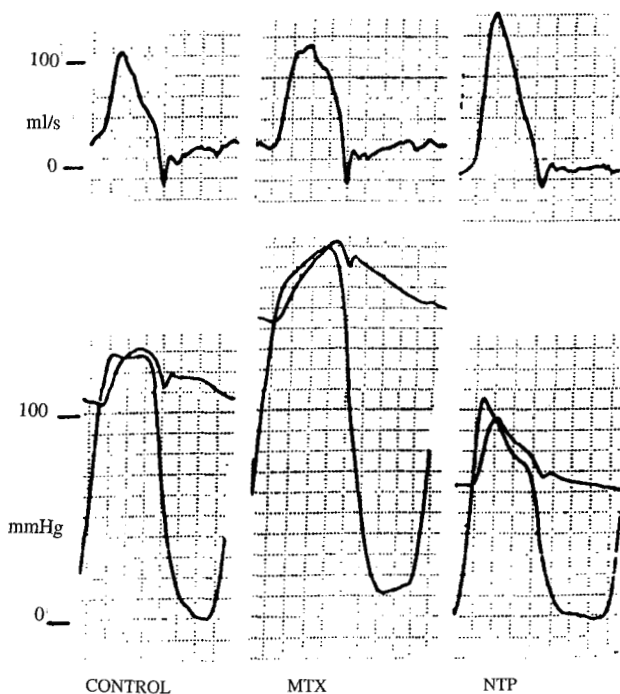


Fig. 4.4.1: Simultaneously recorded ascending aortic pressure and flow waveforms during control (left), methoximaine induced vasoconstriction (middle) and nitroprusside induced vasodilation (right).

From the above equations, it can be seen that wave reflection has opposite effects on pressure and flow. An increase in wave reflection increases the pressure amplitude, but decreases the flow amplitude. This is particularly evident during different vasoactive states. Fig. 4.4.1 illustrates the pressure and flow waveforms recorded during control,

vasoconstriction and vasodilation conditions. Vasoconstriction is induced by intravenous infusion of methoxamine, a potent vasoconstrictor. Its primary effect is in increasing peripheral vascular resistance and has little cardiac effect. Vasodilation is induced by intravenous infusion of nitroprusside. This is a common vasodilator that can profoundly decrease peripheral vascular resistance and increase arterial compliance. It can be seen that the pressure waveform during strong vasodilation more closely resembles that of the flow waveform.

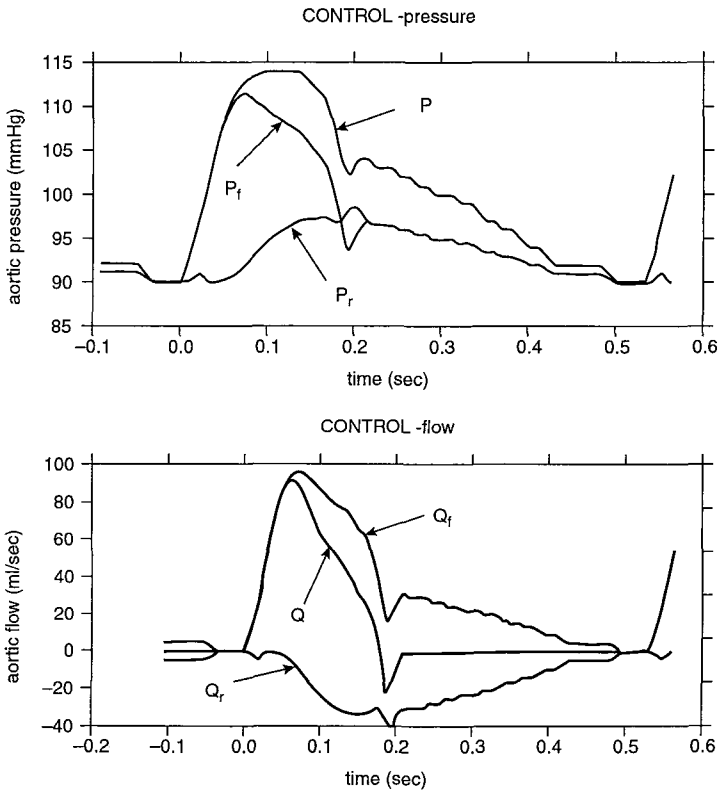


Fig. 4.4.2: Ascending aortic pressure (top) and flow (bottom) waveforms resolved into their respective forward ( $P_f$ ,  $Q_f$ ) or antegrade, and reflected ( $P_r$ ,  $Q_r$ ) or retrograde components. Notice that wave reflection exerts opposite effects on pressure and flow waveforms, as seen from  $Q_r$  and  $P_r$ . Provided by Dr. Ying Zhu.

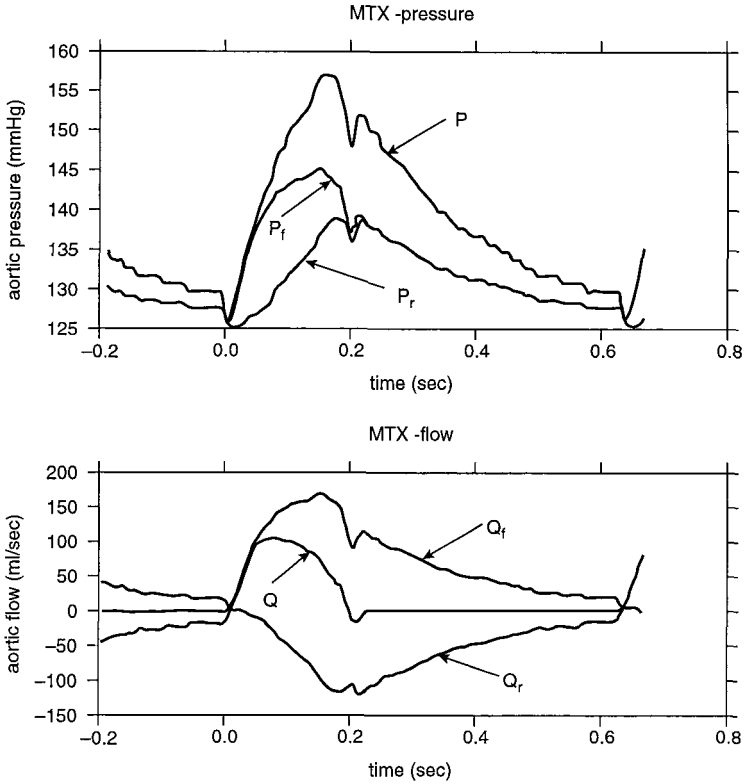


Fig. 4.4.3: Ascending aortic pressure and flow waveforms resolved into their respective forward and reflected components during vasoconstriction induced by intravenous infusion of methoxamine. Notice the significantly increased reflected pressure component.

Aortic pressure (top) and flow (bottom) waveforms resolved into their respective forward ( $P_f$ ,  $Q_f$ ) or antegrade, and reflected ( $P_r$ ,  $Q_r$ ) or retrograde components are shown in Fig. 4.4.2. It is clear that wave reflection exerts opposite effects on pressure and flow waveforms. The increased reflected pressure component adds to the forward wave to result in the measured pressure waveform. Reflected wave has a more significant effect in mid- to late systole to impede ventricular ejection. Wave reflection decreases the flow, as the reflected component of flow is mostly negative. With an increased amount of wave reflection, the

pressure amplitude is increased. This is seen in the case of strong vasoconstriction shown in Fig. 4.4.3. Here reflected waves arrive earlier and with greater magnitudes. As a consequence, the pulse pressure is significantly increased with a concurrent decrease in flow amplitude. The time that takes for forward pressure to reach its peak is not too different from that of the reflected component. With profound vasodilation (Fig. 4.4.4), the measured pressure and flow waveforms resemble each other and both peak at about the same time. The reflected wave is largely abolished. Thus, both pressure and flow waves are transmitted with maximal efficiency.

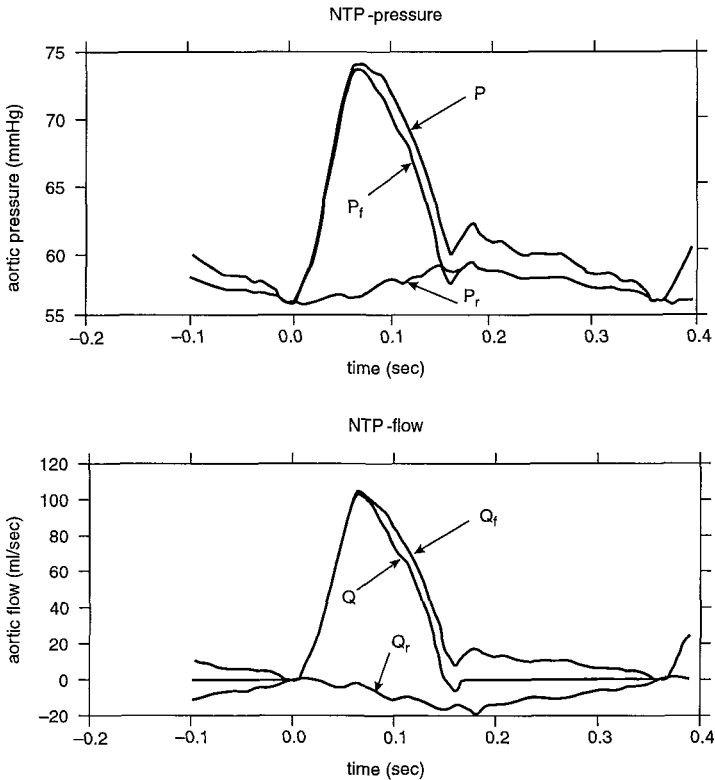


Fig. 4.4.4: Ascending aortic pressure and flow waveforms resolved into their respective forward and reflected components during vasodilation induced by intravenous infusion of nitroprusside. Notice the similarity between the pressure and flow waveforms and that the reflected components are small.

### 4.4.2 The Reflection Coefficients

The reflection coefficient is defined as the harmonic ratio of reflected wave to the forward wave in the frequency domain:

$$\Gamma = \frac{P_r}{P_f} \quad (4.4.9)$$

It has both a modulus and a phase, and varies with frequency:

$$\Gamma = |\Gamma| \angle \phi_r \quad (4.4.10)$$

Reflection coefficients calculated for the normal, vasoconstricted and vasodilated conditions obtained from canine experiments are shown in Fig. 4.4.5. For the fundamental harmonic, the mean value of the reflection coefficient at control is about 0.45. This is increased to 0.65 during vasoconstriction and decreased to about 0.15 during vasodilation. The reflection coefficient remains low for higher frequencies during vasodilation.

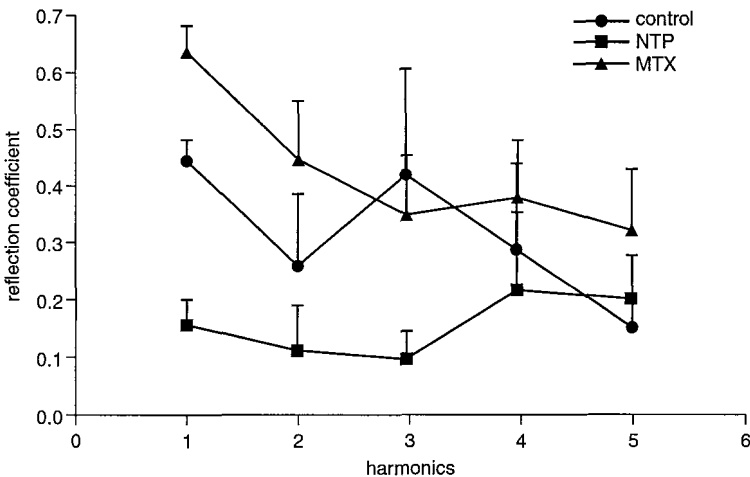


Fig. 4.4.5: Global reflection coefficients obtained during control (circle), vasoconstriction (triangle) and vasodilation (square) conditions.

Reflection coefficient can also be defined in terms of vascular impedances. For a vessel with characteristic impedance  $Z_0$  and terminated with vascular load impedance  $Z$ , the reflection coefficient  $\Gamma$  is given by:

$$\Gamma = \frac{Z - Z_0}{Z + Z_0} \quad (4.4.11)$$

The reflection coefficient so obtained is therefore a complex quantity with modulus  $\Gamma$  and phase  $\phi_\Gamma$  varying with frequency, as before.

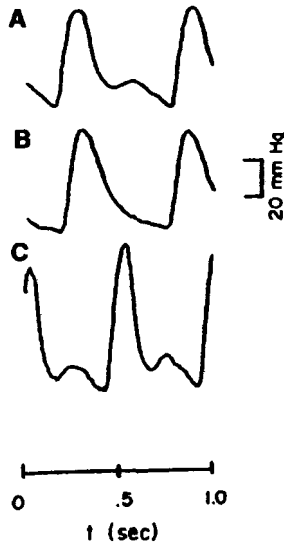


Fig. 4.4.6: Pressure waveforms measured in the femoral artery during control (A), acetylcholine induced vasodilated (B), and norepinephrine induced vasoconstricted (C) states. From Li et al. (1984).

The reflection coefficient can also be defined for a particular vascular bed. For instance, Li et al. (1984) utilized a three-point pressure method to measure the amount of reflections arising from the femoral arterial bed during (a) control, (b) acetylcholine-induced vasodilation, and (c) norepinephrine-induced vasoconstriction states (Fig. 4.4.6). Notice that

the diastolic pressure wave is abolished during acetylcholine-induced vasodilation and accentuated during norepinephrine-induced vasoconstriction.

Reflection coefficients obtained for the femoral vascular bed are shown in Fig. 4.4.7. For the control data (circle), the magnitude of the reflection coefficient ranged from 0.42 at 1.6 Hz, to 0.22 at 9.6 Hz. During vasoconstriction, the reflection coefficient increased to about 0.65 at 1.6 Hz and 0.32 at 9.6 Hz. Vasodilation (triangles) decreased the reflection coefficient to a value less than 0.1 for all frequencies, essentially abolishing the reflected waves.

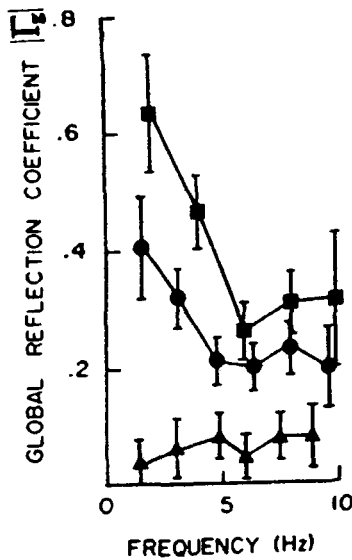


Fig. 4.4.7: Reflections arising from the femoral vascular bed during control (circle), vasoconstriction (square) and vasodilation (triangle). Reflection coefficients were computed from the three-point method. From Li et al. (1984).

#### 4.4.3 Augmentation Index

A simplified index to interpret wave reflection in the aorta, in the time domain, was introduced by Murgo et al. (1980). Ascending aortic

pressure waveforms were defined in terms of their morphological differences and separated into different types. Peak systolic pressure ( $P_s$  or  $P_{pk}$ ), diastolic pressure ( $P_d$ ), pulse pressure (PP), pressure at inflection point ( $P_i$ ) and the augmented pressure,  $\Delta P$  are defined. Systolic pressure augmentation is given by

$$\Delta P = P_s - P_i \quad (4.4.12)$$

and the corresponding augmentation index is given by

$$AI = \frac{\Delta P}{PP} = \frac{P_s - P_i}{P_s - P_d} \quad (4.4.13)$$

Although the augmentation index has been used to represent the reflection ratio, it is not equivalent to the reflection coefficient. Augmentation index is merely a single number and does not represent the frequency content of the reflected wave.

#### **4.4.4 Wave Reflection Sites**

Wave reflection sites exist all over the systemic arterial tree, due to geometric and elastic nonuniformities, branching, and impedance mismatching at arterial terminations. Therefore, reflections cannot originate from one site only. Indeed, there is no agreement on the location of reflecting sites. Some suggest that the major reflection site as seen from the proximal aorta, appears to be in the region of the pelvis or the aorto-iliac branching junction. Others, however, suggest that the first major potential reflecting site is at the aortic arch. Although there is no major agreement on the reflecting sites, the arterioles are recognized as being the principal sites for wave reflection, and the reflection coefficient as being high. There are multiple reflection sites and the effects of repeated reflections on pressure and flow waveforms have been investigated (Berger et al., 1993). The model-based analysis showed how the forward and reflected waves are actually the summations of repeated antegrade and retrograde waves. The dispersion of such multiple reflections make direct measurement and quantification of their

individual contributions to global reflection phenomenon a demanding task.

Reflection sites have generally been determined from the first impedance minimum, and subsequent calculation:

$$\lambda_{\min} = \frac{c}{f_{\min}} \quad (4.4.14)$$

and

$$L_R = \frac{\lambda_{\min}}{4} \quad (4.4.15)$$

$\lambda_{\min}$  and  $f_{\min}$  are the wavelength and frequency corresponding to the impedance minimum.  $L_R$  is the distance of the effective reflection site from the point of measurement. Some investigators have used the zero-phase crossing of impedance for the calculation of effective reflection sites.

## 4.5 Modeling Aspects of the Arterial System

### 4.5.1 Mathematical Formulations

There are three equations generally thought to be sufficient to characterize the propagation of the pulse wave. The first of these equations describes fluid motion,

$$-\frac{\partial v_z}{\partial t} = \frac{1}{\rho} \frac{\partial p}{\partial z} \quad (4.5.1)$$

where  $v_z$  is the blood velocity in the longitudinal  $z$  direction or along the blood vessel from proximal to distal locations,  $p$  is pressure and  $\rho$  is the density of blood. The left side of the equation represents the rate of change of velocity, or flow acceleration. This equation implies that blood flow acceleration is proportional to the pressure gradient. For this

reason, this formula has been used to obtain blood flow from the measurement of pressure gradient.

The second is the equation of continuity to describe the incompressibility of the fluid:

$$-\frac{\partial v_z}{\partial z} = \frac{1}{A} \frac{\partial A}{\partial t} = \frac{2}{r} \frac{\partial r}{\partial t} \quad (4.5.2)$$

or that blood flow velocity gradient is related to the rate of change in cross-sectional area of the blood vessel. In a cylindrical blood vessel, the cross-sectional area  $A$ , is related to its inner lumen radius  $r$ , as

The third equation is the equation of state to describe the elastic properties of the vessel wall

$$\frac{dr}{dp} = k \quad (4.5.3)$$

where  $k$  is a constant.

From this set of equations, the wave equation is obtained as:

$$\frac{\partial^2 v_z}{\partial t^2} = \frac{r}{2k\rho} \frac{\partial^2 v_z}{\partial z^2} \quad (4.5.4)$$

Which gives the wave velocity

$$c_o = \left(\frac{r}{2k\rho}\right)^{\frac{1}{2}} = \left(\frac{r}{2\rho} \frac{dp}{dr}\right)^{\frac{1}{2}} \quad (4.5.5)$$

This equation also provides a means to obtain pulse wave velocity from the simultaneous measurements of pressure and diameter. Define Young's modulus of elasticity as:

$$E = \frac{\sigma_t}{\epsilon_t} \quad (4.5.6)$$

Using the Lamé equation for stress

$$\sigma_t = \frac{pr}{h} \quad (4.5.7)$$

and write strain as:

$$\varepsilon_t = \frac{dr}{r} \quad (4.5.8)$$

we obtain a similar wave equation:

$$\frac{\partial^2 v_z}{\partial t^2} = \frac{Eh}{2r\rho} \frac{\partial^2 v_z}{\partial z^2} \quad (4.5.9)$$

which gives the pulse wave velocity as:

$$c_o = \sqrt{\frac{Eh}{2\rho r}} \quad (4.5.10)$$

This is the well-known Moens-Korteweg formula for pulse wave velocity (Li, 2000). Moens in 1878 obtained this formula through experimentation and obtained

$$c_o = k_m \sqrt{\frac{Eh}{2\rho r}} \quad (4.5.11)$$

Where  $k_m$  is a constant. Korteweg, also in 1878, approached from a theoretical perspective by assuming a flat velocity profile, ignoring viscosity, fluid compressibility, and vessel wall constraints and obtained an identical formula (Noordergraaf, 1969; Li, 1987)

The flat velocity profile implies that the blood flow velocity across the artery is uniform. In a parabolic velocity profile, the centerline velocity is the highest and the velocity declines in a parabolic fashion

towards the vessel wall, such that at the arterial wall, the velocity is the lowest (Fig. 4.5.1). In the arterial system, the velocity profile is relatively flat or blunt at the entrance, or at the ascending aorta and becomes progressively parabolic when approaching smaller arteries.

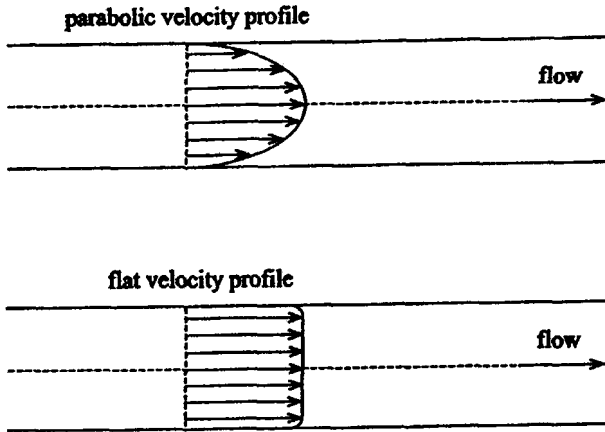


Fig. 4.5.1: Different velocity profiles. A blunt or flat velocity profile (bottom tracing) is when the blood velocity across the vessel is uniform, mostly find in large vessels, such as the proximal aorta. A parabolic velocity profile (top tracing) is when the centerline velocity is the highest with decreasing velocity towards the arterial wall, occurring largely in arteries, such as the femoral. A skewed velocity profile is when the blood velocity is high towards one wall than the opposite side.

Lamb (1898) later assumed an inviscid fluid contained within a thin-walled tube ( $h \ll r$ ) subject to small strains and arrived at equations of motion for the wall:

$$\rho_w \frac{\partial^2 u_z}{\partial t^2} = \frac{E}{1 - \sigma^2} \left( \frac{\partial^2 u_z}{\partial z^2} + \frac{\sigma}{r} \frac{\partial u_z}{\partial z} \right) \quad (4.5.12)$$

$$\rho_w \frac{\partial^2 u_r}{\partial t^2} = \frac{p}{h} \frac{E}{1 - \sigma^2} \left( \frac{\sigma}{r} \frac{\partial u_z}{\partial z} + \frac{u_r}{r^2} \right) \quad (4.5.13)$$

Where  $u_z$  and  $u_r$  are wall movement in the longitudinal and radial directions respectively. These equations were later incorporated by many investigators. Lamb obtained two roots for the wave velocity from a quadratic equation he derived. One is identical to the Moens-Korteweg formula, or Young's mode velocity of propagation, with the propagation wavelength much greater than the vessel lumen radius, or  $\lambda \gg r$  and Poisson ratio  $\sigma=0.5$ , or the incompressibility of fluid:

$$c_1 = \sqrt{\frac{Eh}{2\rho r}} \quad (4.5.14)$$

The other is now known as the Lamb mode velocity for wave propagating longitudinally in the arterial wall:

$$c_1 = \sqrt{\frac{Eh}{\rho(1-\sigma^2)}} \quad (4.5.15)$$

Velocities given in the longitudinal and radial directions are given by:

$$v_z = \left[ C_2 \frac{J_0(jr\sqrt{j\omega\rho/\eta})}{J_0(jr_i\sqrt{j\omega\rho/\eta})} + \frac{A_2}{\rho c} \right] e^{j\omega(t-z/c)} \quad (4.5.16)$$

$$v_r = \left[ \frac{\omega}{c} \sqrt{\frac{\eta}{j\omega\rho}} C_2 \frac{J_1(jr\sqrt{j\omega\rho/\eta})}{J_0(jr_i\sqrt{j\omega\rho/\eta})} + \frac{j\omega r}{2\rho c^2} A \right] e^{j\omega(t-z/c)} \quad (4.5.17)$$

#### 4.5.2 Linear Theories of Oscillatory Blood Flow in Arteries

In general, linear theories regarding blood flow begin with the fundamental Navier-Stokes equations for a Newtonian and incompressible fluid (Attinger, 1964) in cylindrical coordinates, and assuming irrotational flow. Pulsatile pressure and flow relations, as well as complex velocity of wave propagation can be obtained (Li, 1987).

Navier-Stokes equations for a Newtonian and incompressible fluid in cylindrical coordinates  $(r, \theta, z)$  and assuming irrotational flow, i.e. the angular  $\theta$  components are negligible, can be written as:

$$\begin{aligned} \frac{\partial v_z}{\partial t} + v_r \frac{\partial v_z}{\partial r} + v_z \frac{\partial v_z}{\partial z} &= -\frac{1}{\rho} \frac{\partial p}{\partial z} + \frac{\eta}{\rho} \left( \frac{\partial^2 v_z}{\partial r^2} + \frac{1}{r} \frac{\partial v_z}{\partial r} + \frac{\partial^2 v_z}{\partial z^2} \right) \\ \frac{\partial v_r}{\partial t} + v_r \frac{\partial v_r}{\partial r} + v_z \frac{\partial v_r}{\partial z} &= -\frac{1}{\rho} \frac{\partial p}{\partial r} + \frac{\eta}{\rho} \left( \frac{\partial^2 v_r}{\partial r^2} + \frac{1}{r} \frac{\partial v_r}{\partial r} + \frac{\partial^2 v_r}{\partial z^2} - \frac{v_r}{r^2} \right) \end{aligned} \tag{4.5.18}$$

where  $v_z$  = longitudinal velocity component  
 $v_r$  = radial velocity component  
 $\eta$  = viscosity of blood  
 and  $\eta/\rho$  = kinematic viscosity of blood

Notice that when the fluid is assumed to be ideal, i.e.  $\eta/\rho = 0$ , the equations reduce to:

$$\frac{1}{r} \frac{\partial}{\partial r} (rv_r) = -\frac{\partial v_z}{\partial z} \tag{4.5.19}$$

For linearized Navier-Stokes equations, the second and third terms of the left-hand side are negligible for small velocities. For long wavelength ( $\lambda \gg r$ ), one obtains solutions as follows, for a periodic sinusoidally varying function  $e^{j\omega(t-z/c)}$ :

$$p = -A\omega\rho e^{j\omega(t-z/c)} \tag{4.5.20}$$

$$v_z = \left[ -\frac{A_1\omega}{c} + C_1 \sqrt{\frac{j\omega\rho}{\eta}} J_0(jr \sqrt{\frac{j\omega\rho}{\eta}}) \right] e^{j\omega(t-z/c)} \tag{4.5.21}$$

$$v_r = -\left[ \frac{jA_1\omega^2 r}{2c^2} - \frac{C_1\omega}{c} J_1(jr \sqrt{\frac{j\omega\rho}{\eta}}) \right] e^{j\omega(t-z/c)} \tag{4.5.22}$$

where  $J_0$  and  $J_1$  are the zero and first order Bessel functions of the first kind, and  $A_1$  and  $C_1$  are constants.

By using Lamb's equations for the wall and applying the boundary condition that fluid and wall velocities are equal at the wall, i.e.

$$v_z(r = r_i) = \frac{\partial u_z}{\partial t} \quad (4.5.23)$$

and

$$v_r(r = r_i) = \frac{\partial u_r}{\partial t} \quad (4.5.24)$$

a complex velocity of propagation is obtained as

$$c_1 = k \sqrt{\frac{Eh}{2\rho r}} \quad (4.5.25)$$

where  $k$  contains Bessel functions  $J_0$  and  $J_1$ . For  $k = 1$ , as in the case when the fluid is ideal, i.e. the kinematic viscosity  $\eta/\rho = 0$ , this equation reduces to the familiar Moens-Korteweg formula for pulse wave velocity.

Differences in linearized theories are mostly in the description of arterial wall properties and arterial wall motion. More accurate descriptions of the blood-arterial wall interactions can be achieved by additions or improvements in the equations describing the wall and blood, or the so-called blood-wall interactions. These latter arise because of the fluid-tissue interface and the differences in mechanical behaviors. Indeed, modern clinical analysis has placed more emphasis on the blood-endothelial interface and on the blood flow and elastin-collagen interactions.

Morgan and Kiely (1954) added viscous fluid stress terms to the Lamb equations (4.5.12 and 4.5.13):

$$-\frac{\eta}{h} \left( \frac{\partial v_z}{\partial r} + \frac{\partial v_r}{\partial z} \right)_{r=r_i} \quad (4.5.26)$$

$$-\frac{2\eta}{h} \left( \frac{\partial v_z}{\partial r} \right)_{r=r_i} \quad (4.5.27)$$

a parameter, now known as the Womersley's parameter was introduced:

$$\alpha_w = r \sqrt{\frac{\omega \rho}{\eta}} \quad (4.5.28)$$

$$\omega = 2\pi f_h \quad (4.5.29)$$

$$f_h = \text{heart rate/sec} \quad (4.5.30)$$

$\rho$  (1.06 g/cm<sup>3</sup>) and  $\eta$  (0.03 poise or 3 centipoise) are the density and viscosity of blood, respectively and  $r$  is the inner radius of the artery. This parameter also represents the ratio of the relative contribution of inertia component to viscous component of blood flow. In other words, it describes the ratio of the movement of blood mass to the retardation of flow or flow resistance due to blood viscosity.  $\alpha_w$  is also dependent on arterial lumen radius, thus, the smaller the vessel, the smaller the value of  $\alpha_w$ .

Morgan and Kiely made assumptions to arrive at wave velocity and damping coefficient ( $\alpha$ ), for  $r = r_i$  and  $\alpha_w \gg 1$ :

$$c = \left[ 1 - \frac{1}{r} \left( 1 - \sigma + \frac{\sigma^2}{4} \right) \left( \frac{\eta}{2\omega\rho} \right)^{\frac{1}{2}} \right] \sqrt{\frac{Eh}{2r\rho}} \quad (4.5.31)$$

And for for  $\alpha_w \ll 1$

$$\alpha = \frac{\omega}{r} \left[ \frac{\eta(5-4\sigma)}{\omega\rho} \right]^{\frac{1}{2}} \sqrt{\frac{2r\rho}{Eh}} \quad (4.5.32)$$

For extremely low frequencies, or in the case of very small vessels, these equations can be compared to those derived earlier.

Many linear theories of oscillating blood flow in arteries have been proposed, but that of Womersley remains the most commonly used. A frequency dependent parameter not originally defined by him, but later known as the Womersley's parameter was introduced, as shown in eqn. (4.5.28). Womersley (1957) also utilized a linearized Navier-Stokes equation, and an equation of motion of a freely moving elastic tube with homogeneous and isotropic wall material. He also made assumptions that the pulse propagation wavelength is much greater than that of the arterial lumen radius, or  $\lambda \gg r$ , and that the propagating pressure pulse takes the form of

$$p = A e^{j\omega(t-z/c)} \quad (4.5.33)$$

where  $A$  is the amplitude of the pressure pulse ( $p$ ) and  $c$  is pulse wave velocity. He obtained

$$v_z = \left[ C_2 \frac{J_0(jr\sqrt{j\omega\rho/\eta})}{J_0(jr_i\sqrt{j\omega\rho/\eta})} + \frac{A_2}{\rho c} \right] e^{j\omega(t-z/c)} \quad (4.5.34)$$

$$v_r = \left[ \frac{\omega}{c} \sqrt{\frac{\eta}{j\omega\rho}} C_2 \frac{J_1(jr\sqrt{j\omega\rho/\eta})}{J_0(jr_i\sqrt{j\omega\rho/\eta})} + \frac{j\omega r}{2\rho c^2} A \right] e^{j\omega(t-z/c)} \quad (4.5.35)$$

An equation for the pulse wave velocity was derived, assuming arterial wall and blood densities are equal,

$$c = \sqrt{\frac{r\rho}{hE}} k_c \quad (4.5.36)$$

where  $k_c$  is a function of the Bessel function

$$F_{10} = \frac{2J_1(\alpha j^{3/2})}{\alpha j^{3/2} J_0(\alpha j^{3/2})} \quad (4.5.37)$$

where  $J_0$  and  $J_1$ , are zero and first order Bessel functions of the first kind. Solutions for  $J_0$  and  $J_1$ , are tabulated by Womersley and van

Brummelen (1961). Rewrite  $F_{10}$  in its complex form in terms of real and imaginary parts, we have:

$$F_{10} = X + jY \quad (4.5.38)$$

Womersley obtained an expression for complex wave velocity:

$$c = \frac{1}{X - jY} \sqrt{\frac{Eh}{2r\rho}} \quad (4.5.39)$$

From this, the phase velocity is:

$$c_1 = \frac{c_o}{X} \quad X = \frac{c_1}{c_o} \quad (4.5.40)$$

noting again that the Moens-Korteweg wave velocity is given by

$$c_o = \sqrt{\frac{Eh}{2r\rho}} \quad (4.5.41)$$

The attenuation expressed in terms of wavelength is given by:

$$\alpha_e = e^{-2\pi Y / X\lambda} \quad (4.5.42)$$

Attenuation represents the degree of damping of the propagating pulse.

Womersley later imposed longitudinal constraint of the wall due to vessel tethering. In the case of infinite longitudinal constraint,  $k_\infty$ , wave velocity takes the form:

$$\frac{c_o}{c} = \sqrt{\frac{1 - \sigma^2}{1 - F_{10}}} \quad (4.5.43)$$

When considering the arterial wall as viscoelastic, the above equation is modified by taking into account the viscous property of the wall,

$$\frac{c_o}{c} = (X - jY)(1 - jk_v \tan \phi) \quad (4.5.44)$$

It has been shown that the viscous component is relatively small in large arteries, such as the aorta. The viscous loss represented by the magnitude of  $\tan \phi$  is less than 10%.

Although inadequate, the Voigt model and the Maxwell model continues to be popular choices when taking into account of viscoelastic properties of the arterial wall. Womersley, as well as Morgan and Kiely (1954), and Jager et al. (1965) employed the Voigt model to describe the arterial wall properties. Jager et al. (1965) also assumed a thick-walled model, when the arterial wall thickness is a large fraction of the radius. A linearized Navier Stokes equation and dynamic deformation of the wall were also incorporated to arrive at a complex wave velocity:

$$c = \frac{Eh}{3\rho} \frac{2r + h}{(r + h)^2} (1 - F_{10}) \quad (4.5.45)$$

In general, pressure and flow are obtained as periodic solutions with spatial and temporal dependences as:

$$p(z, t) = Me^{j\omega(t-z/c)} \quad (4.5.46)$$

$$Q(z, t) = \frac{\pi r^2 M}{\rho c} (1 - F_{10}) e^{j\omega(t-z/c)} \quad (4.5.47)$$

Linear theories are based on certain assumptions as discussed in the previous section, they are mathematically tractable and allow solutions for pressure and flow to be expressed in closed forms.

#### ***4.5.3 The Lumped Model of the Arterial System: The Windkessel***

The idea of a lumped model of the arterial circulation was first described by Hales in 1733. Albeit largely qualitative, he did emphasize the storage properties of large arteries and the dissipative nature of small peripheral resistance vessels. In his description, the blood ejected by the

heart during systole into the arterial system distends the large arteries, primarily the aorta. During diastole, the elastic recoil of these same arteries propels blood to perfuse the smaller peripheral resistance vessels. This initiated the earlier conceptual understanding that the distensibility of large arteries are important in allowing the transformation of intermittent outflow of the heart to steady outflow throughout the peripheral vessels. In other words, the large overall "compliance" of the large arteries protects the stiff peripheral vessels of organ vascular beds from the large swing of blood pressure due to pulsations. This view is still held by many until this day. The significance of arterial pulsations remains a topic of debate.

The windkessel model is now credited to Frank (1899) whose original interest was in obtaining stroke volume from measured aortic pressure pulse contour. Methods to derive flow from pressure measurement or the so-termed pressure-derived flows (Li, 1983) have continued to attract considerable interest despite the advent of the electromagnetic blood flow and ultrasonic blood velocity measuring devices.

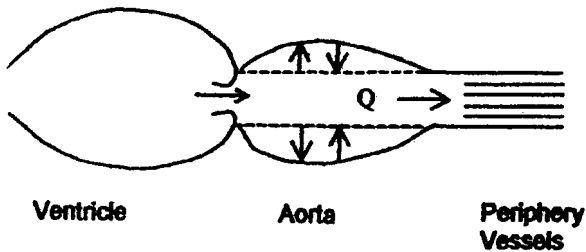


Fig. 4.5.2: Diagrammatic representation of the left ventricle and the arterial circulation based on the idea of the windkessel. The ventricle ejects into a compliant chamber representing the aorta, blood flow is stored in systole (solid line) and on elastic recoil in diastole (dotted line), the stiff peripheral vessels are perfused.

In the analysis of the windkessel model, the amount of blood flow,  $Q_s$ , stored during each contraction is the difference between inflow,  $Q_i$  to the large arteries and the outflow,  $Q_o$ , to the small peripheral vessel (Fig. 4.5.2),

$$Q_s = Q_i - Q_o \quad (4.5.48)$$

The amount of outflow is equivalent to the pressure drop from the arterial side ( $P$ ) to the venous side ( $P_v$ ) due to the peripheral resistance,  $R_s$

$$Q_o = (P - P_v)/R_s \quad (4.5.49)$$

At steady flow and assume that  $P_v$  is small, we obtain a familiar expression for estimating the peripheral resistance, and with the total inflow,  $Q = Q_i$ ,

$$R_s = \bar{P} / \bar{Q} \quad (4.5.50)$$

or mean arterial pressure to mean arterial flow.

The storage property can be described by the use of arterial compliance, which expresses the amount of change in blood volume ( $dV$ ) due to a change in distending pressure ( $dP$ ) in the artery. In this case, we have

$$C = dV/dP \quad (4.5.51)$$

The amount of blood flow stored, or  $Q_s$ , due to arterial compliance, is related to the rate of change in pressure distending the artery,

$$Q_s = C \, dP/dt \quad (4.5.52)$$

Substituting this equation and (3-2) into (3-1), we obtain from

$$Q_i = Q_s + Q_o \quad (4.5.53)$$

an expression relating the arterial pressure to flow incorporating the two windkessel parameters,  $C$  and  $R_s$ :

$$Q(t) = C \, dP/dt + P/R_s \quad (4.5.54)$$

In other words, the total arterial inflow is the sum of the flow stored and the flow going into the periphery.

In diastole, when inflow is zero, as in the case when diastolic aortic flow equals zero, then

$$0 = C \frac{dP}{dt} + P/R_s \quad (4.5.55)$$

or

$$dP/P = -dt/R_s C \quad (4.5.56)$$

This equation states that the rate of diastolic aortic pressure drop is dependent on both the compliance of the arterial system and the peripheral resistance. Both of which also determine the flow. Integration of both sides of equation (4.5.56) gives us

$$\ln P = t/R_s C \quad (4.5.57)$$

or

$$P = P_0 e^{-t/R_s C} \quad (4.5.58)$$

valid for the diastolic period, or  $t = t_d$ .

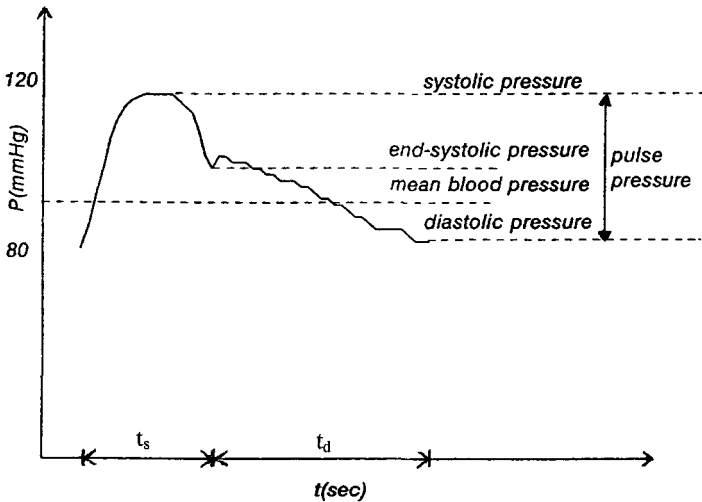


Fig. 4.5.3: Illustration of the measured aortic pressure pulse waveform. The systolic pressure, diastolic pressure, end-systolic pressure and mean blood pressure are also shown. The approximate exponential decay of diastolic pressure through the diastolic period ( $t_d$ ) from the end of the systolic period ( $t_s$ ) is seen.

This last equation is seen to be equivalent to

$$P_d = P_{es} e^{-t_d/\tau} \quad (4.5.59)$$

or that the diastolic aortic pressure decay (Fig. 4.5.3) from end-systolic pressure ( $P_{es}$ ) to end-diastolic pressure ( $P_d$ ) follows a mono-exponential manner with a time constant of  $\tau$ . The time constant of pressure decay  $\tau$ , is determined by the product of resistance and compliance, viz:

$$\tau = R_s C \quad (4.5.60)$$

or in terms of measured aortic pressure,

$$\tau = \frac{t_d}{\ln \frac{P_{es}}{P_d}} \quad (4.5.61)$$

and

$$C = \frac{t_d}{R_s \ln \frac{P_{es}}{P_d}} \quad (4.5.62)$$

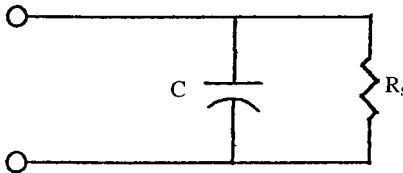


Fig. 4.5.4: The two-element resistance-capacitance electrical analog model of the windkessel. Compliance is represented by a capacitor and the peripheral resistance by a resistor.

Analysis utilizing simple electric analog, has given the windkessel a two-element representation. Arterial compliance is represented by a capacitor which has storage properties, in this case, electric charge. Peripheral resistance, with its viscous properties, is represented by a

resistor which dissipates energy. The electrical analog of the windkessel model of the arterial system is shown in Fig. 4.5.4.

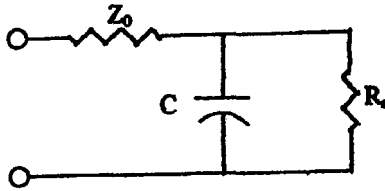


Fig. 4.5.5: An improved windkessel with three-elements.  $Z_0$ , represents the characteristic impedance of the proximal aorta.

A modified windkessel model (Fig. 4.5.5) that has three-elements were later proposed. This lumped model of the systemic arterial tree has been widely used. It consists, in addition to arterial compliance and peripheral resistance, a characteristic impedance of the proximal aorta.  $Z_0$ , as it is termed will be discussed in greater detail in a later section. Its hydraulic equivalent is illustrated in Fig. 4.5.6.

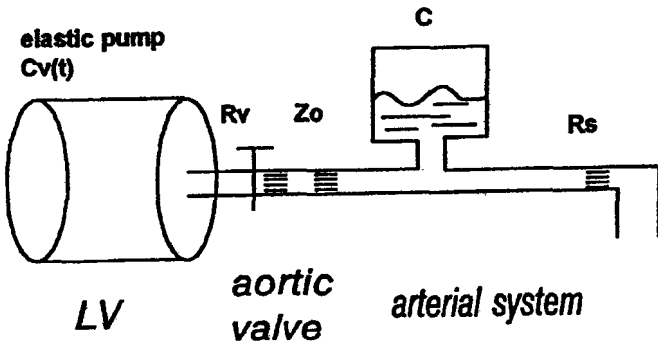


Fig. 4.5.6: The hydraulic equivalent of the three-element windkessel, popularly used to represent the arterial load to the heart. A bottle allowing volume displacement subjecting to pressure variations represents the arterial compliance. The peripheral resistance is represented by a needle valve whose partial opening and closing allows resistance to flow to be varied. The finite tube geometry and property represents the characteristic impedance of the aorta.

#### 4.5.4 Nonlinear Aspects and Pressure-Dependent Arterial Compliance

Although the Navier-Stokes equation in its complete form has recently been solved in closed form (Melbin and Noordergraaf, 1983), there are other kinds of nonlinearities. Thus, depending on the particular problem or application at hand, assumptions included in order to eliminate some or all of the nonlinearities may still be valid to provide a satisfactory solution. This is particularly true with regard to the use of Fourier analysis in studying pressure and flow waveforms and the derived input impedance analysis.

The general definition of arterial compliance is the ratio of an incremental change in volume due to an incremental change in distending pressure, i.e.

$$C = dV/dP \quad (4.5.63)$$

This is defined by the inverse of the slope of the pressure-volume (P-V) curve, with pressure plotted on the ordinate and volume on the abscissa (Fig. 4.5.7). Thus, compliance is the inverse of elastance.

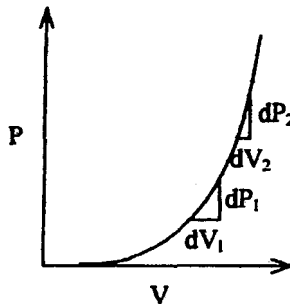


Fig. 4.5.7: Arterial pressure-volume diagram, defining compliance as the slope of the relation ( $C=dV/dP$ ). It is clear that the slope changes with increasing pressure ( $dV_1/dP_1$  vs.  $dV_2/dP_2$ ) and at higher pressures the volume change is smaller.

The pressure-volume curves of arteries have been found to be curvilinear. The slope changes along the P-V curve, steeper at higher pressures, signifying increased arterial stiffness or decreased compliance and distensibility. In other words, arteries stiffen when pressurized. This physiological phenomenon has been observed in many experiments.

This increased stiffness has been suggested to be related to the structure of the arterial wall. This implies that the compliance-pressure relation is not a constant one. The declining arterial compliance with increasing pressure has been observed in the central aorta and in individual arteries. The inverse exponential relation between compliance and pressure for the arterial system is shown in Fig. 4.5.8.

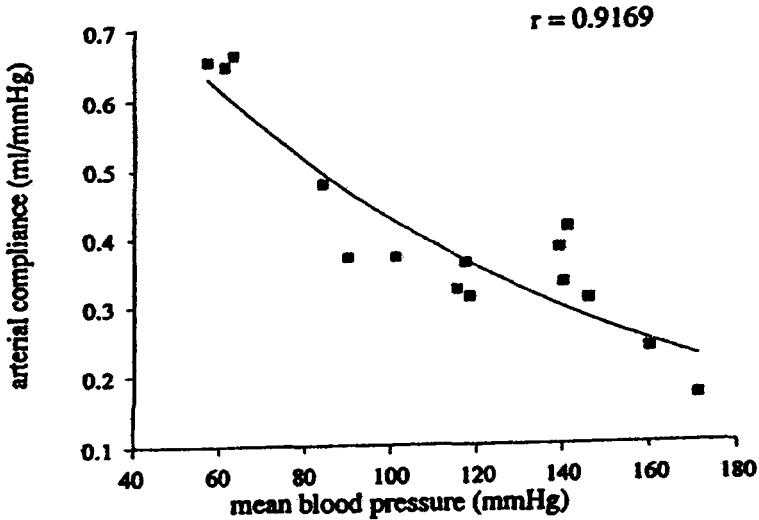


Fig. 4.5.8: Compliance plotted against mean arterial blood pressure reflecting the pressure-volume relation. The relationship is nonlinear, implying that at higher distending pressures the intraluminal volume change is smaller, resulting in a lower compliance. The decrease in arterial compliance with increasing blood pressure follows a negative exponential function.

A nonlinear model of the arterial system incorporating a pressure-dependent compliance element ( $C(P)$ ) is shown in Fig. 4.5.9 (Li et al., 1990). The model consists of the characteristic impedance of the proximal aorta ( $Z_0$ ), the peripheral resistance ( $R_S$ ), and  $C(P)$ . The compliance is exponentially related to pressure and is expressed as

$$C(P) = a \cdot e^{b(P(t))} \quad (4.5.64)$$

where  $a$  and  $b$  are constants. The exponent  $b$  is normally negative. Thus, an inverse relationship is established between arterial compliance and blood pressure; with increasing blood pressure arterial compliance decreases.

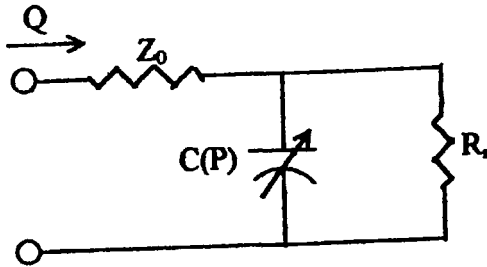


Fig. 4.5.9: Nonlinear arterial system model proposed by Li et al. (1990), incorporating a pressure-dependent compliance.  $Z_0$  is characteristic impedance of the ascending aorta,  $R_s$  is total peripheral resistance,  $C(P)$  is the pressure-dependent compliance, represented by a variable capacitor.  $Q$  is aortic flow.

Figure 4.5.9 shows that the flow through the compliance branch of the nonlinear model is given by

$$Q_c(t) = Q(t) - P(t)/R_s \quad (4.5.65)$$

where  $P(t)$  and  $Q(t)$  are the pressure and flow through the compliance branch, respectively. This flow can also be expressed as

$$Q_c(t) = C(P) \cdot dP(t)/dt \quad (4.5.66)$$

Equate these two equations, resulting in

$$dP/dt = (Q(t) - P(t)/R_s)/C(P) \quad (4.5.67)$$

This equation defines the dynamic relationship between pressure and flow for a nonlinear compliance element. Numerical methods can be employed to solve this equation.

Using difference representations, we have

$$\Delta t = t_{i+1} - t_i = dt \quad (4.5.68)$$

where  $\Delta t$  is the sampling interval, taken as 10 msec. The nonlinear model is then reduced to the following expression:

$$P(t_{i+1}) = P(t_i) + \Delta t \cdot (Q(t_i) - P(t_i)/R_s)/C(P) \quad (4.5.69)$$

With the measured aortic flow as the input, a numerical procedure can be programmed to solve  $P(t_i)$ ,  $C(P)$  and the aortic pressure

$$P_a(t_i) = Q(t_i) \cdot Z_o + P(t_i) \quad (4.5.70)$$

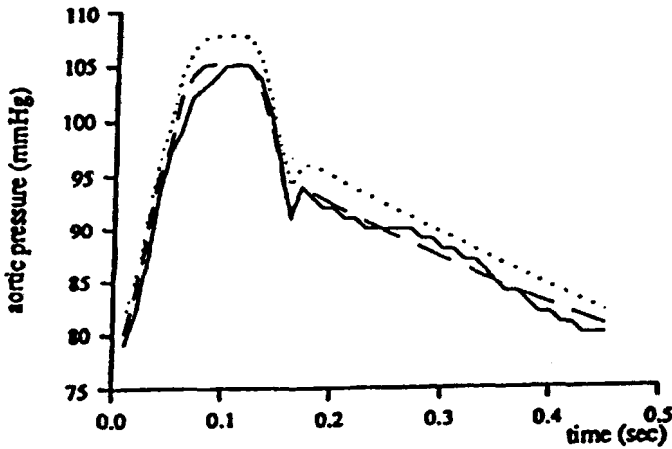


Fig. 4.5.10: The nonlinear and linear model predicted aortic pressure waveforms, compared to the measured aortic pressure. Dotted line: linear windkessel model; dashed line: nonlinear pressure-dependent compliance model.

This nonlinear model predicted aortic pressure accurately, as shown in Fig. 4.5.10. The linear three-element model predicted the measured aortic pressure with less accuracy, although the gross features are evident. The model-based arterial compliance plotted as a function of pressure for a complete cardiac cycle with a normal blood pressure level is shown in Fig. 4.5.11. It is clear from this figure that compliance is relatively independent of both pressure and flow in the early systole and maintains a value close to its maximum during this period. This

facilitates early rapid ventricular ejection. During mid-systole, arterial compliance begins to decline, this corresponds to increased aortic pressure and reduced ejection after peak ventricular outflow. In the late systolic phase, arterial compliance declines rapidly with a concurrent rapid decline of aortic flow, despite a falling aortic pressure. The compliance value is much higher at early systole than at late systole. Arterial system compliance reaches its minimum at the end of the ejection. For the diastolic period, when aortic flow is zero, compliance follows an exponential relation as given by equation (4.5.64). Its value increases throughout the diastole towards maximum, readying for the following ventricular ejection.

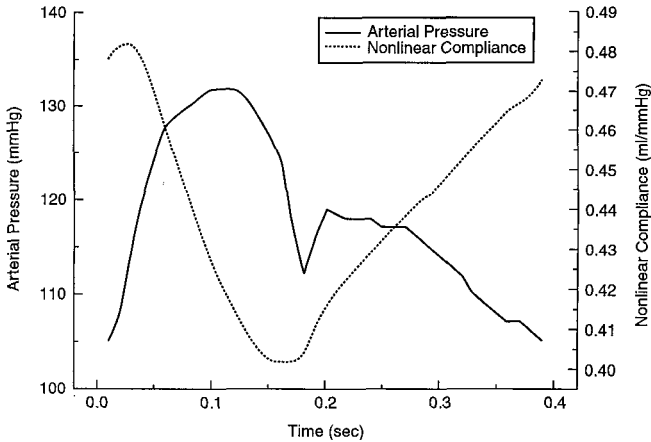


Fig. 4.5.11: Nonlinear pressure-dependent characteristics of arterial compliance as a function of time plotted for a complete cardiac cycle. Arterial compliance increases initially at the beginning of ejection and declines with increasing pressure. It reaches a minimum at about end-systole and increases steadily thence towards the end of diastole.

In describing fluid motions with a linearized Navier-Stokes equation, nonlinear terms are assumed to be small and are consequently neglected. Ling et al. (1973) Computed flows from an accurately measured pressure gradient (with a claimed resolution of 0.001 mmHg). They found that linear theory overestimated the steady flow term by several folds, while the pulsatile flow waveforms conformed rather well with

electromagnetically measured flow. Li et al. (1981) measured the propagation constant in arteries and found that the measured attenuation coefficients and phase velocities differed greatly from those predicted by linear theories. To explain the observed discrepancies, they evaluated and compared the nonlinear and linear theories for the femoral artery. For the nonlinear theory, the complete solution of the Navier-Stokes equation, the geometric taper, and pressure-dependent wall compliance were incorporated. Although varied nonlinearities have been incorporated in some nonlinear theories, in general vascular branching has not been included. Its effect is significant in pulse transmission. This will be discussed in the following chapter.

## Chapter 5

# Vascular Branching

### 5.1 Branching Geometry

#### *5.1.1 Complexity of Vascular Branching*

The branching geometry of the vascular network has intrigued investigators for centuries. Its complexity and precise arrangement of the large vessels and their connectivity to the vast number of small microcirculatory vessels have amazed scientists and clinicians alike. The intermingling of geometric architecture and the mechanical properties of the vascular structure at branching points is of particular interest here.

To perfuse organ vascular beds and meet specific tissue metabolic demands, the vascular system displays its utmost efficient network structure through branching of blood vessels. This allows prompt spatial and temporal distribution of oxygen and nutrients and removal of waste products. One would marvel the vascular system of the human heart, for instance, with its own well-meshed branching circulation, the coronary circulation, to supply its own blood according to its own energetics and mechanical performance. The lungs, with its branching pulmonary vascular system give another example of achieving the functional performance of ventilation-perfusion and on demand. The complex branching topology of the cerebral circulation to supply oxygen and blood flow to neuronal networks and the extensive network of vessels in the renal circulation, are just some of the examples one can marvel the branching structure of the vascular system.

The branching structure of blood vessels can be viewed as a simple consequence of the necessity in providing an efficient vascular network

for distribution of fluid flow, in this case, blood flow. The simplest form of branching is through bifurcation. A vascular structure of this form in which the mother or source vessel is bifurcating into two daughter or branching vessels, undergoes further bifurcation for generations. This is known as the “open tree” structure. In such simplistic and idealistic representation, each of the branching vessels are of the same lumen diameter and the same vessel length. In addition, the angle of bifurcation maintains the same. Thus, this uniform bifurcating structure represents a basic fractal-like tree network model of the vascular system. Theoretical studies based on bifurcation geometry have been numerous. The outcome from their predictions have been mixed. Good correlations have been found for the extent of bifurcation vessel lengths and diameters, much less for bifurcation angles (Zamir, 2000).

Vascular networks and branching geometry however are far more complex in the cardiovascular system. Although bifurcation is the most common form of vascular branching, trifurcation and multi-branching junctions also occur in the mammalian vascular systems. In addition, the uniformity in geometry is often not observed. That is, branching vessel diameters and lengths, as well as branching angles can vary considerably. Nevertheless, bifurcation predominates in vascular branching structure.

Examples of the vascular branching structure that do not obey the straight bifurcation scheme is readily visible by looking at the aorta and its branches. The aortic arch is curved and has many branches, none of which maintains the same vessel diameter and length in these branching arteries, such as the brachiocephalic and the subclavian. However, the two common carotid arteries represent a long, uniform, bifurcating structure. Taking the direction along the length of the thoracic aorta through abdominal aorta, we observe many branches that come off the aorta at almost right angles, far from those at the aortic arch or the aortoiliac junction. The aorta however, provides another kind of branching structure for efficient transport. For instance, the aorta itself, though tapered maintains a larger trunk diameter in comparison to its branching arteries and its mere length ensures fast delivery of blood to its branches. This represents another scheme of branching structure.

### 5.1.2 Nonuniform Branching and 3-D Branching Structure

The above considerations of branching structure are not limited to two-dimensional (2-D) vascular networks. In the 2-D structure, all blood vessels lie in the same plane. A three-dimensional (3-D) structure allows greater flexibility and expansion. Adding on the nonuniform scheme, the vascular tree has even greater flexibility in defining its structure.

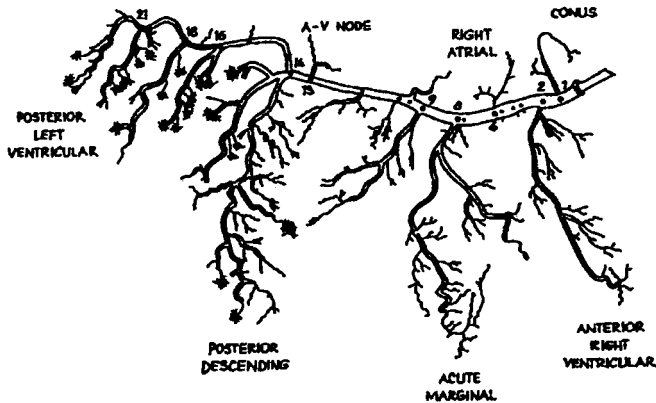


Fig. 5.1.1: A drawing of some of the main branches coming off from the right coronary artery as it circles the heart. Numbers refer to vascular junctions along the artery. From Zamir (2000).

Morphological structures of the branching vascular systems have been reported by numerous investigators. One such an example is shown in Fig. 5.1.1, given by Zamir (2000). The main vessel branches from the right coronary artery are shown, together with the numbers that identify branching junctions as they arise sequentially along the coronary artery. These numbers are related to the levels of the arterial tree as illustrated schematically in Fig. 5.1.2. This is used for mapping the branches arising at these junctions. This scheme clearly shows the tree structure that is nonuniform and incomplete in terms of the order of branching to terminations 5.1.3). Both the number of junctions and the level or the tree are clearly defined.

There are other differing branching structures found in the circulations. For instances, the morphometry in the pig coronary venous system by Kassab et al. (1994) and the network anatomy of arteries

feeding the spinotrapezius muscle in both normal and hypertensive rats by Schmid-Shonbein et al. (1986) differ considerably.

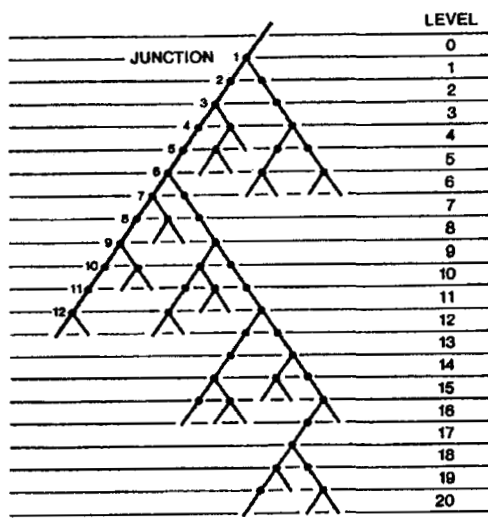


Fig. 5.1.2: Schematic drawing of the tree structure corresponding to the previous figure showing the number of junctions and levels.

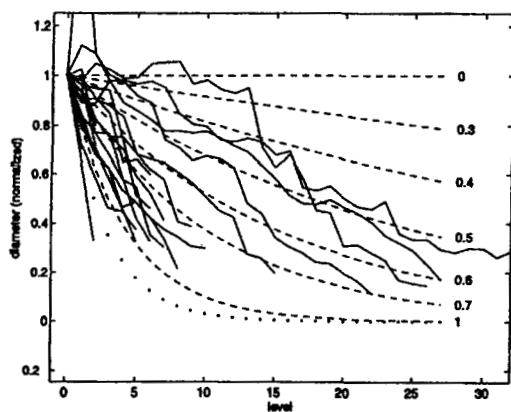


Fig. 5.1.3: Changes in normalized diameter along the right coronary artery and some of its main branches. The bifurcation index is shown on the right. Dotted line: square-law; dashed lines: cube-law. From Zamir (2000).

### 5.1.3 Space-Filling Properties and Modeling

It has been shown that the greater the body surface area, the greater the need for an expansion of vascular networks to perfuse the tissues. Many cardiac indices have therefore, been normalized to body surface area. With a given organ vascular bed, space-filling is then a property, whether in terms of area-expansion or volume-filling.

One approach takes into consideration of the space-filling problem is the structured tree model shown in Fig. 5.1.4. Here small arteries and arterioles exercise minimization principles to perfuse tissues with blood. Olufsen (2000) modeled branching small arteries and large arterioles with the termination reached when the arterioles reach a prescribed minimal radius. The determinants of the structured tree model are the scaling parameters  $\alpha$  ( $<1$ ) and  $\beta$  ( $<1$ ), the order of the tree and the geometric and elastic properties of the vessels. Results show the pressure and flow waveforms manifested in large arteries have similar forms to the measured data.

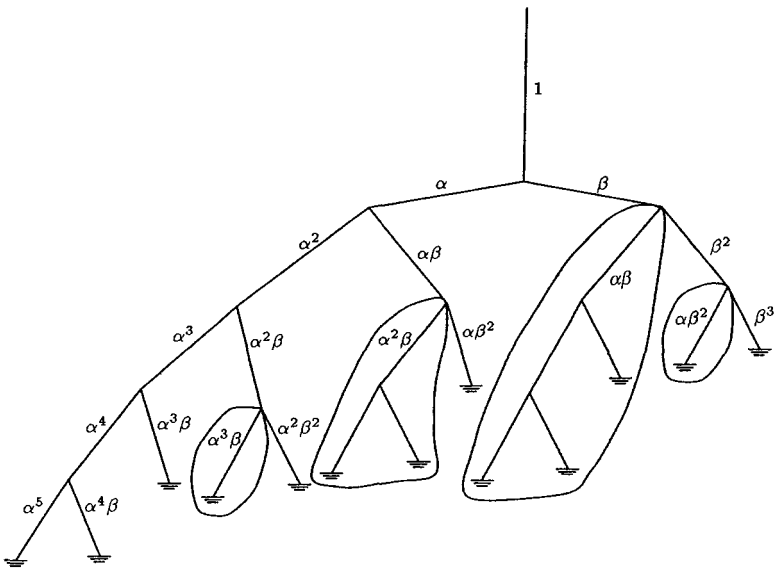


Fig. 5.1.4: A structured tree model in which at each bifurcation the radii of the daughter vessels are scaled linearly by factors  $\alpha$  and  $\beta$ , respectively. From Olufsen (2000).

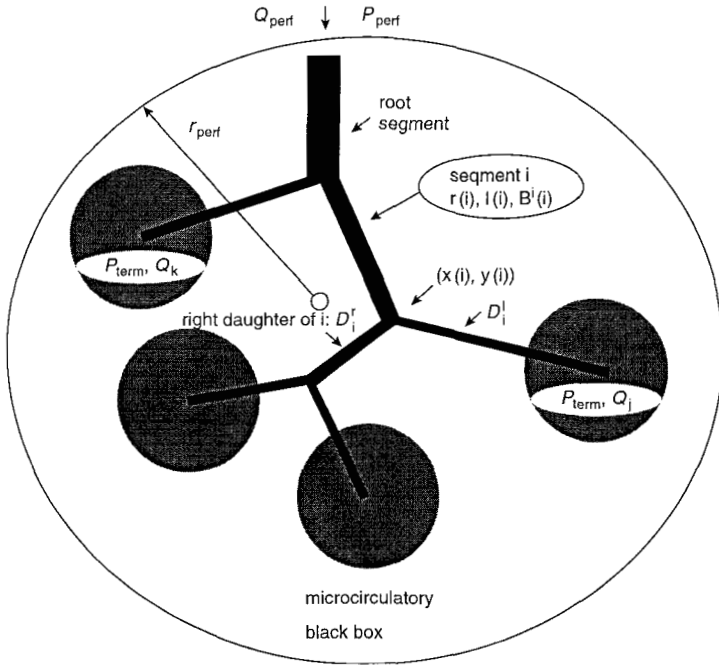


Fig. 5.1.5: A schematic drawing of the constrained constructive optimization, showing perfusion through the root segment and blood delivery by terminal segments at four randomly chosen locations within a given perfusion area. From Schreiner et al. (2000).

Another approach to examine the branching structure of blood vessels is through the constrained constructive optimization. This technique has been shown to be able to generate realistic models of arterial trees involving thousands of vascular segments. An example is given by Schreiner et al. (2000), shown in Fig. 5.1.5. Here, a drawing of the constrained constructive optimization scheme is displayed, showing perfusion through the root segment and blood delivery by terminal segments at four randomly chosen locations within a given perfusion area. Further, the bifurcation scheme is utilized where the radii of the mother and daughter vessels segments at each bifurcation follows:

$$r_m^k = r_{d1}^k + r_{d2}^k \quad (5.1.1)$$

It has been shown that  $2 \leq k \leq 3$  are physiologically relevant. Fig. 5.1.6 illustrates one such result after structural optimization is applied, assuming  $k=3$ .

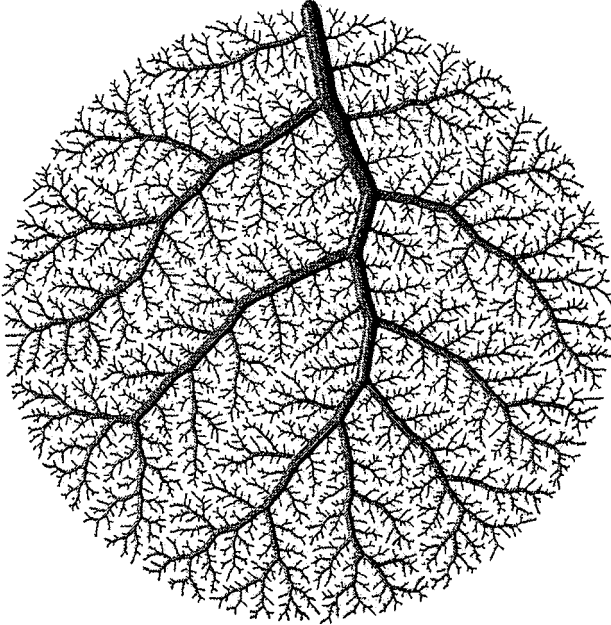


Fig. 5.1.6: Constrained constructive optimization obtained vascular tree network with 4,000 terminal segments generated in a 2-D perfusion area. Minimum intravascular volume is optimized at bifurcation exponent of  $k = 3$ . No minimum symmetry is assumed. From Schreiner et al. (2000).

## 5.2 Fluid Mechanics of Vascular Branching

### 5.2.1 Branching Geometry and Fluid Dynamic Considerations

There are numerous branching junctions in the vascular system. Bifurcations are the most common. Some of these are, for instances, aorta to left and right iliac arteries or aorto-iliac bifurcation, common carotid to internal and external carotid arteries or carotid artery

bifurcation, the femoral artery bifurcation, the celiac artery bifurcation, mesenteric bifurcation and coronary artery bifurcations.

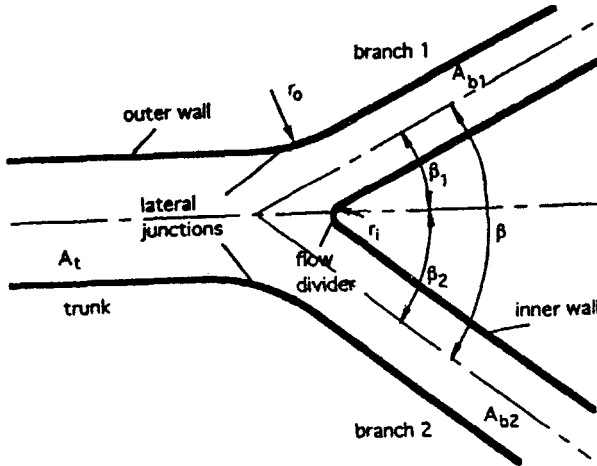


Fig. 5.2.1: Branching morphology with Y-shaped bifurcating tubes. The source or trunk vessel gives rise into two branches.  $A$  = cross sectional area,  $\beta$  = angle of branching or bifurcation angle,  $r$  = radius of curvature.

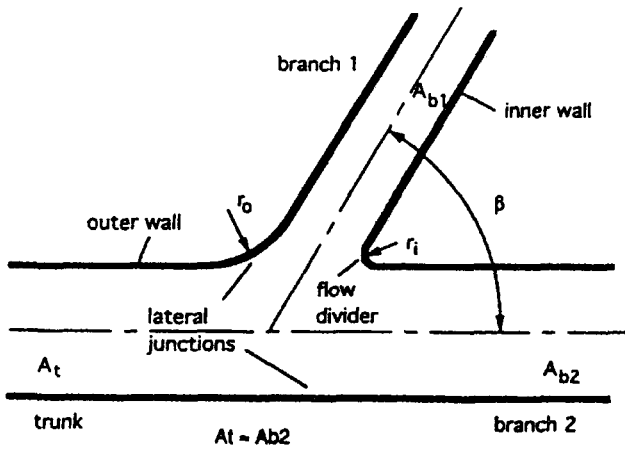


Fig. 5.2.2: Main vessel with a side branch or T-shaped bifurcation. One of the branching vessel has the same cross sectional area as the source vessel.

Bio-fluid dynamics for various arterial bifurcations have been intensively investigated. In the studies of bifurcations, two general shapes, such as T-shaped and Y-shaped branching morphology have been used (Lou and Yang, 1992). The aortic carotid iliac and coronary bifurcations are considered Y-shaped, while renal femoral, celiac and mesenteric branching are considered T-shaped in fluid mechanical studies. These are illustrated in Figs. 5.2.1 and 5.2.2.

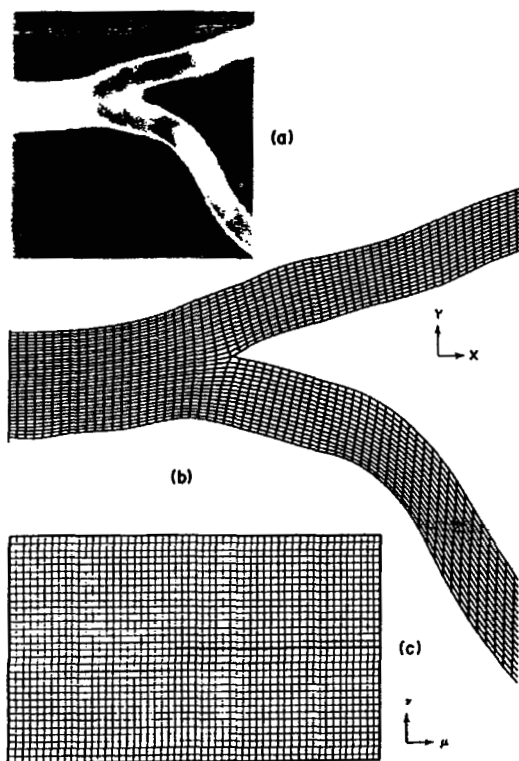


Fig. 5.2.3: Transformation of branch geometry to a rectangular mesh: (a) frontal-plane radiograph of the bifurcations, (b) the untransformed grid in the X-Y plane obtained from the radiograph, (c) the transformed grid in the u-v plane where the inner wall have been mapped onto the horizontal slit. From Friedman and Ehrlich (1984).

The importance of area ratios is dealt in the next section. Area ratios and curvatures of flow divider and lateral junctions are major geometric parameters considered in the formulation of many fluid mechanical

studies. Li (1985) has found that alteration of pressure and flow through vascular junctions is more significantly affected by geometry than by elastic factors.

The importance of area ratios is dealt in the next section. Area ratios and curvatures of flow divider and lateral junctions are major geometric parameters considered in the formulation of many fluid mechanical studies. Li (1985) has found that alteration of pressure and flow through vascular junctions is more significantly affected by geometry than by elastic factors.

The effect of flow divider curvature was studied in a numerical simulation model by Friedman and Ehrlich (1984). Two-dimensional steady flow calculation in computational regions obtained from radiographs of human aortic bifurcations have been shown to correlate well with unsteady measurements of wall shear in flow-through casts of the same vessels. Their results suggest that wall slope, hence curvature is an important factor affecting shear that contributes to atherogenesis. This approach is shown in Figs. 5.2.3 and 5.2.4.

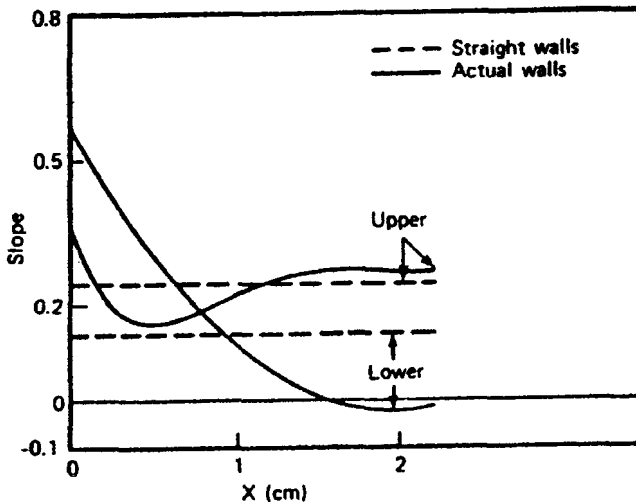


Fig. 5.2.4: Slope profile along the actual and straight inner walls. Since the end points of the straight walls are the same as those of the corresponding actual walls, the slopes of the straightened walls are equal to the mean slopes of the actual walls. From Friedman and Ehrlich (1984).

Many of fluid mechanical simulations and experiments in branching tubes have taken the assumption of rigid tubes. We have seen in earlier chapters that blood vessel compliance is of utmost importance in shaping the pressure and flow waveforms.

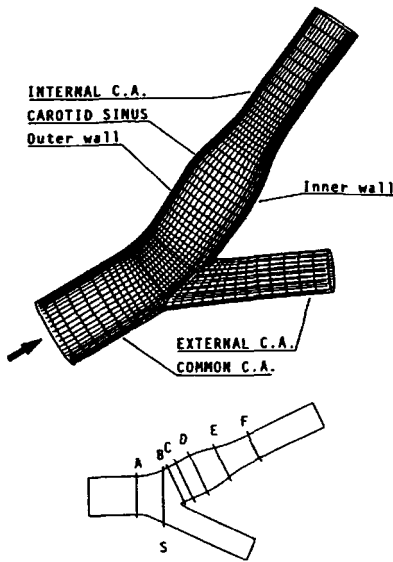


Fig. 5.2.5: Carotid bifurcation model. A, B, C, D, E, F, S indicate flow cross-section levels where numerical results are displayed. From Perktold and Rappitsch (1995).

One such study that addresses the importance of compliance is that of Perktold and Rappitsch (1995) who performed computer simulation of local blood flow and vessel mechanics in a compliant carotid artery bifurcation model. The flow analysis uses the time-dependent, three-dimensional, incompressible Navier-Stokes equations for non-Newtonian inelastic fluids. The wall displacement and stress analysis applies geometrically nonlinear shell theory where incrementally linear elastic wall property is assumed. Their comparison of rigid and compliant vessel models showed that wall shear stress magnitude decreased by 25% in the compliant model. In general, flow separation results in locally low

oscillating wall shear stress. These are illustrated in Figs. 5.2.5, 5.2.6 and 5.2.7. Carotid bifurcation has also been studied, for instances, by laser Doppler anemometer measurements of pulsatile flow in a model (Ku and Giddens, 1987) and in a three-dimensional analysis (Gilsen et al., 1999).

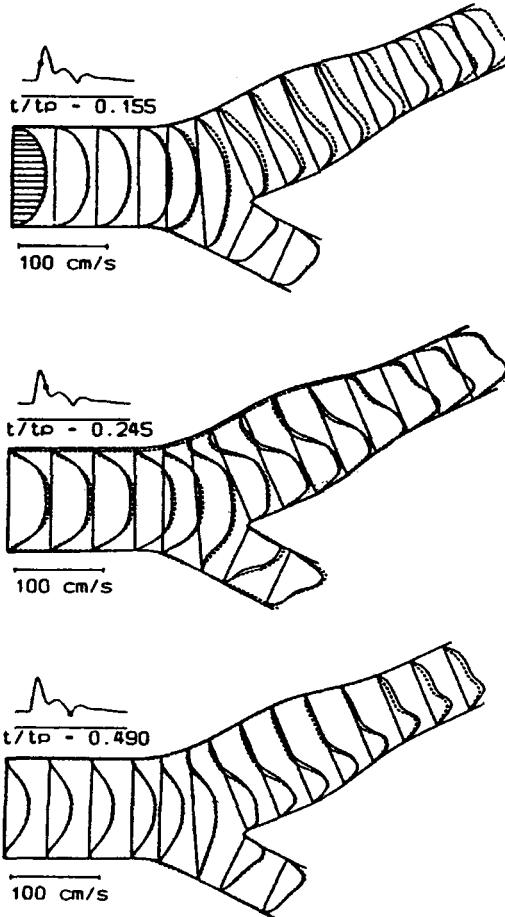


Fig. 5.2.6: Axial flow velocity profiles at the symmetry plane during systolic contraction phase (top), systolic deceleration phase (middle) and the pulse phase of minimum flow rate (bottom). Solid line: compliant model; dashed line: rigid model. From Perktold and Rappitsch (1995).

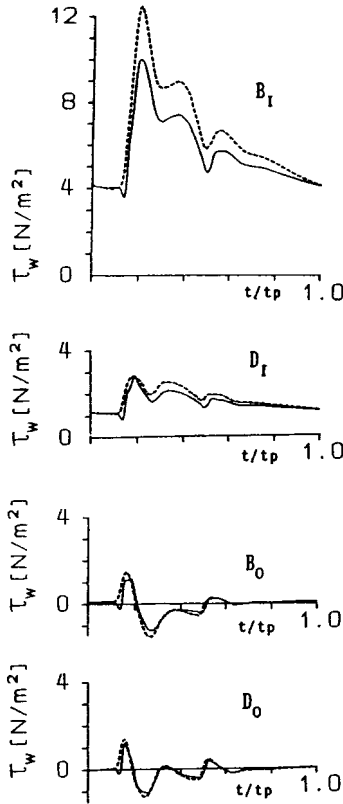


Fig. 5.2.7: Wall shear stress during the pulse cycle at the inner wall (internal divider wall)  $B_i$ ,  $D_i$  and at the outer internal wall  $B_o$ ,  $D_o$ . Solid line: compliant model; dashed line: rigid model. From Perktold and Rappitsch (1995).

### 5.2.2 Fluid Mechanics Associated with Atherosclerosis and Stenosis

The susceptibility of vascular branches to atherosclerosis is believed due in part to the unusual fluid dynamic environments that the vessel wall experiences in the regions. Fluid mechanical studies have shown that atherosclerosis may occur at branching points where the geometry is complex, a large Reynolds number and a lower than average wall shear stress. In general, the complex flow pattern is associated with a spatially nonuniform shear stress and wall curvature. The rate of change of shear

stress and shear rate have been shown to be important, as well as local turbulence and unsteady flow. In addition local disturbed flow patterns, recirculation zones, long particle residence times have been suggested to play significant roles in the onset and development of atherosclerosis.

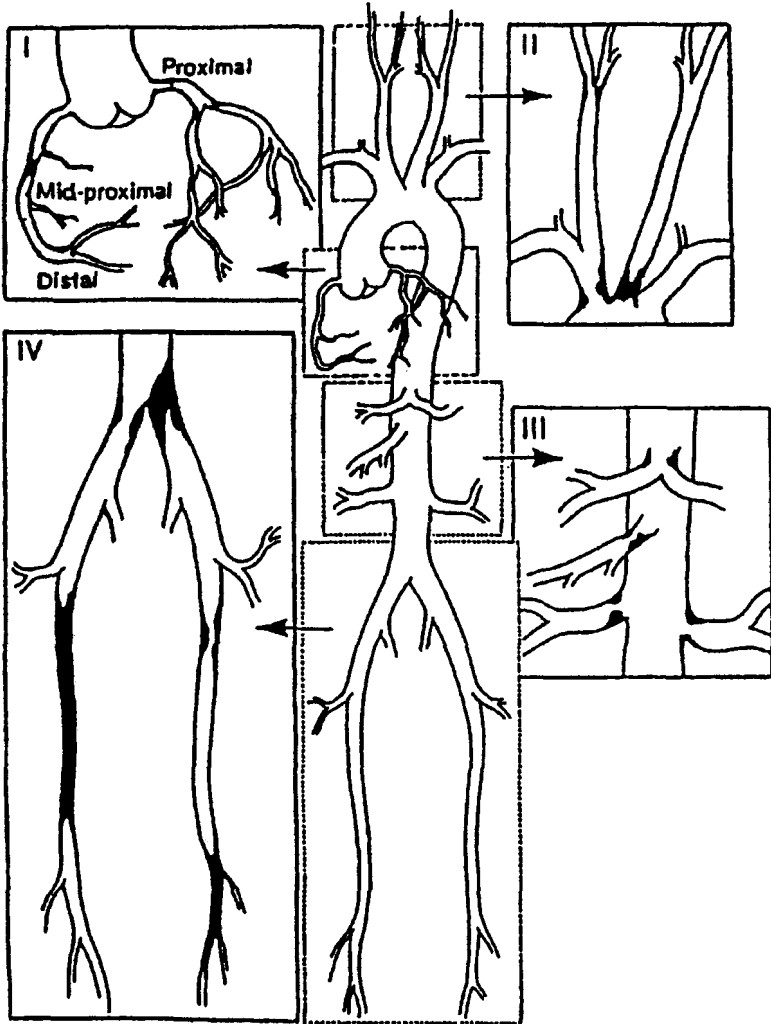


Fig. 5.2.8: Illustration of the distribution of atherosclerotic occlusive disease in humans. From DeBakey et al. (1985).

Numerous modeling and experimental studies have been proposed to investigate the fluid mechanical factors contributing to atherosclerosis. Caro et al. (1971) were earlier investigators to identify sites of atherogenesis as regions of reduced wall shear stress and suggested that the transport of lipoprotein within the arterial wall and across the endothelium is a major factor in atherosclerosis. These common atherosclerotic sites have been illustrated by DeBaakey et al. (1985) as shown in Fig. 5.2.8. Numerical simulation to predict some of these branching sites has been carried in a two-dimensional simulation (Lei et al., 1995). Friedman (1989) used a model to explain the thickening of arterial intima under shear. Thurbrigar and Robicsek (1995) suggested the importance of pressure-induced arterial wall stress as an important factor in atherosclerosis.

Stenosis, or the narrowing of the blood vessel, is associated with a serious hemodynamic consequence of pressure loss that develops across the stenosis. The pressure loss is primarily dependent on the flow rate and the geometry of the stenosis, since the fluid properties of density and apparent viscosity are relatively constant. The experimental equation for a pressure-drop was first introduced by means of an extensive series of in-vitro steady flow tests utilizing constrictions in the form of blunt-ended hollow plugs (Seely and Young, 1976).

Arteries with severe stenoses caused by atherosclerotic plaque growth may collapse under physiological conditions (Aorki and Ku, 1993). Artery collapse is a process where an artery buckles under certain pressure and stress conditions. The compression resulting from this collapse may lead to accelerated fatigue and rupture of the fibrous cap, which contains the plaque. The plaque rupture can lead directly to heart attack and stroke if occurring in coronary and cerebral vessels, respectively. It is known that local stenosis formed by an atherosclerotic lesion may cause mechanical conditions favorable for artery collapse. Plaque fatigue and distal embolization are also important considerations.

Blood flow must accelerate to high velocities in the narrowed stenosis. The high velocities in turn create a low or negative transmural pressure, which can result in collapse of the artery. Alternatively, the high velocities at the stenosis also generate high shear stresses, which may be related to plaque cap rupture and platelet activation (Tang et al.,

1999). It has been shown that the pulsatile blood flow characteristics, as we discussed in earlier chapters, cannot be neglected, particularly in the evolution of vortex structures downstream from the stenosis. It is essential to determine the wall shear stress temporal evolution downstream from a stenosis.

The close relation of atherosclerosis and stenosis and their morphological resemblance have indeed generated much interest in analyzing common fluid mechanical factors and consequences. In many instances, particularly in modeling studies, these two pathological conditions cannot be separated. Their importance in the manifestation of eventual diseases of the vascular system, however, is well recognized.

### 5.3 Pulse Transmission Characteristics at Vascular Branching

#### 5.3.1 Impedance Matching and Wave Reflections

One consequence of vascular branching is the pronounced changes in pressure and flow waveforms. To this end, analysis of pulse transmission characteristics at vascular branching has been limited. Pulse transmission at branching junction, unlike that along a single continuous vessel, depends on the mechanical and geometric properties of the source or mother vessel as well as on the branching or daughter vessels. Impedance is an effective means to embrace all these properties. If the combined impedances of the daughter vessel match that of the mother vessel, then, the transmission will simply be ideal and there will be no wave reflections, nor energetic losses at the branching junction.

The relations for the pressure and flow pulse waveforms expressed as magnitude and phase are, as defined previously, for the  $n$ th harmonic:

$$P_n = |P_n| e^{j(\omega t + \phi_n)} \quad (5.3.1)$$

$$Q_n = |Q_n| e^{j(\omega t + \phi_n)} \quad (5.3.2)$$

The vascular impedance obtained for the  $n$ th harmonic is therefore,

$$Z_n = |Z_n| e^{j\theta_n} \quad (5.3.3)$$

where the magnitude of impedance is simply the ratio of the pressure amplitude to the flow amplitude, and for the  $n$ th harmonic:

$$|Z_n| = \frac{|P_n|}{|Q_n|} \quad (5.3.4)$$

with the phase lag

$$\theta_n = \phi_n - \varphi_n \quad (5.3.5)$$

Characteristic impedance that reflect the vessel properties alone, irrespective of wave reflections can then be approximated from the high frequency average of the impedance modulus. Characteristic impedance, like input impedance, is complex, although its dependence on frequency is only weakly so in large vessels.

In order to isolate the contributions of vascular branching to overall pulse transmission characteristics, it is necessary to define local characteristic impedances that reflect the mechanical and geometric properties of the vessels at vascular junction.

A local reflection coefficient can be defined for vascular branching only:

$$\Gamma_l = \frac{Z_{od} - Z_{om}}{Z_{od} + Z_{om}} \quad (5.3.6)$$

where  $Z_{od}$  represents the resultant parallel combination of the characteristic impedance of branching daughter vessels, and  $Z_{om}$  is the mother vessel's characteristic impedance. For instance, for a bifurcation with daughter branch characteristic impedances of  $Z_{o1}$  and  $Z_{o2}$ , we have:

$$\frac{1}{Z_{od}} = \frac{1}{Z_{o1}} + \frac{1}{Z_{o2}} \quad (5.3.7)$$

For an equi-bifurcation (Fig. 5.3.1), one obtains:

$$\frac{1}{Z_{od}} = \frac{1}{Z_{o1}} + \frac{1}{Z_{o2}} = \frac{2}{Z_{o1}} \quad (5.3.8)$$

In terms of the mother or source vessel characteristic impedance,  $Z_{om}$ , and individual daughter or branch vessel characteristic impedance,  $Z_{o1}$ , we obtain for the local wave reflection due to equi-vascular branching only:

$$\Gamma_l = \frac{Z_{o1} - 2Z_{om}}{Z_{o1} + 2Z_{om}} \quad (5.3.9)$$

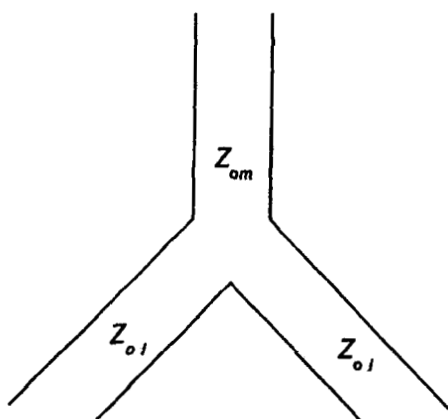


Fig. 5.3.1: Schematic representation of a branching vascular junction, An equi-bifurcation is illustrated with characteristic impedance of the mother ( $Z_{om}$ ) and daughter ( $Z_{o1}$ ) vessels respectively.

An alternative method that assumes frequency independence of characteristic impedance, is derived from the water-hammer formula (Li, 1985). In this formulation, the pressure and flow are expressed as:

$$P = \rho \cdot v \cdot c \quad (5.3.10)$$

$$Q = v \cdot \pi r^2 \quad (5.3.11)$$

The characteristic impedance is defined simply by the ratio of pressure to flow, i.e.

$$Z_o = \frac{\rho c}{\pi r^2} \quad (5.3.12)$$

This gives the characteristic impedance of a uniform cylindrical vessel that is independent of wave reflections. Of course, the blood flow is assumed to be Newtonian and that the viscosity of blood and the vessels wall are neglected in this formulation.

### 5.3.2 Area Ratio Concept

From a simple geometric perspective, the cross-sectional area of the adjoining vessels should provide some quantitative estimates of the mismatching characteristics of pulse transmission characteristics. Thus, the branching vessel lumen areas come into play. This concept of area ratio has been examined by several investigators. For instance, Karreman (1952) used area ratio in his mathematical formulation of wave reflection at an arterial junction. By assuming both the wall and fluid are non-viscous, and wall thickness remains the same for an infinitely long tube, he arrived at a value of area ratio (the ratio of the sum of the areas of daughter vessels to that of the mother vessel) for a reflectionless bifurcation of about 1.15,

With a modification by considering tethered elastic tubes containing viscous fluid, Womersley (1958) later arrived at a similar result with a correcting factor  $q$ , for a bifurcation, assuming the daughter vessels have identical characteristics ( $r_d, c_d$ ):

$$A_b = 2 \cdot \left( \frac{r_d}{r_m} \right)^2 \left( \frac{c_m}{c_d} \right) \cdot q \quad (5.3.13)$$

The local reflection coefficient due to the equi-bifurcation is then given by:

$$\Gamma_l = \frac{1 - A_b}{1 + A_b} \quad (5.3.14)$$

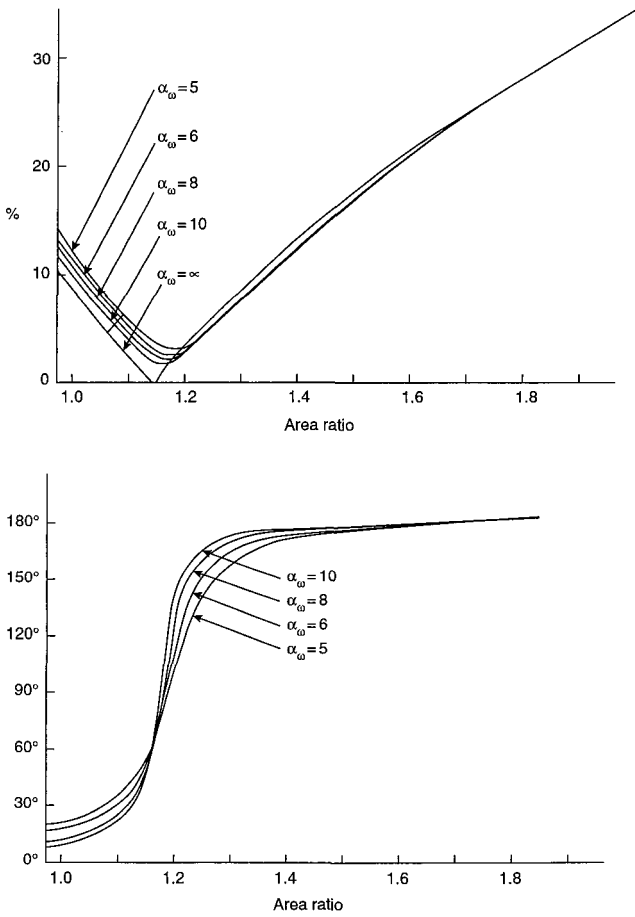


Fig. 5.3.2: Reflections at vascular branching. Magnitude and phase of local reflection coefficients computed for an equi-bifurcation are plotted against area ratios. From Womersley (1958).

Exact matching is not possible. Perfect matching is only obtained when the Womersley's number,

$$\alpha_\omega = r \sqrt{\frac{\omega \rho}{\eta}} \tag{5.3.15}$$

approaches infinity, or  $\alpha_w \rightarrow \infty$ , though the minimum reflection is only a few percent. This is shown in Fig. 5.3.2. The area ratios for the aortic junctions are usually between 1.15 and 1.25 (table 4.1), which represent a very small amount of reflections (Li et al., 1984). These same small amount of local reflections were found on the analog model of the systemic arterial tree by Westerhof et al. (1969). In terms of fluid dynamics, optimal energy transfer is achieved when the area ratio is close to one.

The relationship of local reflection coefficient, area ratio and junction vessel characteristic impedances can be easily appreciated from the following analysis. We first relate the characteristic impedance of the blood vessel to its geometric and elastic properties. From the water-hammer formula above for the characteristic impedance, we have

$$Z_o = \frac{\rho c}{\pi r^2} \quad (5.3.16)$$

Knowing the Moens-Korteweg relation and substituting for pulse wave velocity, we have:

$$Z_o = \frac{1}{A} \sqrt{\frac{Eh\rho}{2r}} \quad (5.3.17)$$

Now with a bifurcation, the resultant characteristic impedance of the daughter vessel branch impedances,  $Z_1$  and  $Z_2$ , is:

$$\frac{1}{Z_d} = \frac{1}{Z_1} + \frac{1}{Z_2} \quad (5.3.18)$$

For an equi-bifurcation, we have

$$\frac{1}{Z_d} = \frac{2}{Z_1} \quad (5.3.19)$$

or for n equal daughter branches:

$$\frac{1}{Z_d} = \frac{n}{Z_1} \quad (5.3.20)$$

The fraction of the pressure pulse that is reflected at the junction due to unmatched branching vessel characteristic impedances is

$$\Gamma_l = \frac{Z_d - Z_m}{Z_d + Z_m} = \frac{1 - Z_m / Z_d}{1 + Z_m / Z_d} \quad (5.3.21)$$

where  $Z_m$  and  $Z_d$  are the characteristic impedances of the mother and daughter vessels, respectively.

This latter leads to a junction reflection of

$$\Gamma_l = \frac{1 - nZ_m / Z_1}{1 + nZ_m / Z_1} \quad (5.3.22)$$

If we let

$$Z_m = \frac{\rho c_m}{A_m} \quad \text{and} \quad Z_1 = \frac{\rho c_1}{A_1} \quad (5.3.23)$$

then, for  $n$  equal branches, we obtain

$$\frac{Z_m}{Z_d} = n \cdot \frac{A_1}{A_m} \cdot \frac{c_m}{c_1} \quad (5.3.24)$$

where

$$A_r = n \cdot \frac{A_1}{A_m} \quad (5.3.25)$$

is the area ratio ( $A_r$ ) and  $c_m/c_1$  is the velocity ratio, related to the ratio of elastic properties of the branching vessels:

$$\frac{c_m}{c_1} = \sqrt{\frac{E_m}{E_1}} \quad (5.3.26)$$

This assumes that the wall thickness-to-radius ratio or  $h/r$  is relatively constant for the branching vessels.

Since

$$A_r = n \cdot \left( \frac{r_1}{r_m} \right)^2 \quad (5.3.27)$$

it is clear that alterations in branching vessel lumen radii could exert a more significant effect on wave reflections at vascular branching junction,  $\Gamma_l$ , than changes in their respective elastic moduli.

For constant elasticity for all vessels involved at vascular branching,, i.e.  $c_m/c_1=1$ , the wave reflections due to vascular branching becomes dependent only on area ratio, i.e.

$$\Gamma_l = \frac{1 - A_r}{1 + A_r} \quad (5.3.28)$$

### 5.3.3 Minimum Local Reflections at Vascular Branching Junctions

By examination of the characteristic impedances of mother and daughter vessels, that pulse wave reflection due to vascular branching is minimal (Li, 1984). Since reflection is energetically wasteful, this means little energy is lost due to pulse transmission through vascular branching junctions. This has been attributed to close to optimal area ratios and branching angles. Also geometric effect rather than elastic effect dominants pulse propagation through vascular branching junctions (Li, 1986).

The area ratio concept has received continued attention. Experimental results showed that minimum reflection is obtained when area ratio equals 1.23 for an equi-bifurcation. This correlates closely to that given by Womersley's theory (minimum reflection when area ratio equals 1.26). In small muscular vessels, viscous damping is appreciably more important than in large vessels. In these vessels, the point of

minimum reflection (in the reflection vs. area ratio plot) is shifted to a larger area ratio, accompanied by a larger phase change.

Table 5.3.1: Measured and Calculated Vascular Parameters

	A cm <sup>2</sup>	c cm/s	Z <sub>o</sub> dyn.s.cm <sup>-5</sup>	E 10 <sup>6</sup> dyn/cm <sup>2</sup>
Abdominal aorta	0.415	660	1686	5.54
Continuation branch	0.205	710	3671	6.41
Iliac artery	0.115	765	7051	7.44

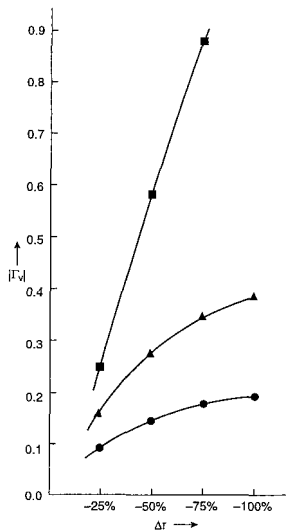


Fig. 5.3.3: Local reflection coefficient is plotted against the reduction in radius. Sharply increased reflection coefficient is associated with narrowing branching vessel lumen radius.

The importance of topological geometry and elastic properties at vascular branching junctions can be easily appreciated from the measurement of local reflection coefficients involving characteristic

impedances of junction vessels. By using measured and calculated vascular parameters (Table 5.3.1) obtained from measurements in dog aorto-iliac junction (a trifurcation with the abdominal aorta branching into its continuation branch and left and right iliac arteries), the local reflection was found to be just 0.07 (Li, 1984, 1986).

Fig. 5.3.3 shows that the local reflection coefficient is significantly increased when the vessel lumen radius is progressively decreased downstream from the junction (daughter vessels). But when the branching vessels become stiffer with increased elastic modulus, such changes in local reflection coefficient is rather moderate (Fig. 5.3.4). This indicates that junction geometry is more dominant in determining pulse transmission through vascular branching than elastic factors.

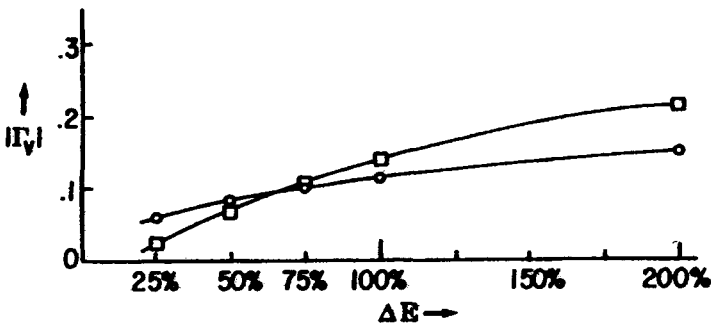


Fig. 5.3.4: Local reflection coefficient is plotted against the reduction in elastic modulus. Reflection is increased with increased branching vessel stiffness, but the increase is less pronounced as compared with corresponding percentage reduction in lumen radius.

## 5.4 Optimization Aspects Applicable to Vascular Branching

### 5.4.1 Optimizing Vessel Radius and the Cube Law

To overcome the resistance to blood flow, the power required will be inversely proportional to the fourth power of radius, or  $r^4$ , according to Poiseuille's law governing steady flow through a rigid cylindrical vessel:

$$P_1 = R_s Q^2 \quad (5.4.1)$$

where the Poiseuille resistance,  $R_s$ , to steady flow  $Q$ , is

$$R_s = \frac{8\eta l}{\pi r^4} \quad (5.4.2)$$

where  $l$  is the length of the vessel along which blood flows. Thus, a larger vessel radius is more advantageous. This is because the flowing blood encounters a smaller resistance. However, a greater volume of blood is required for perfusion through a vessel with a larger radius, hence a greater demand on metabolic energy:

$$V = \pi r^2 l \quad (5.4.3)$$

where  $V$  is the blood vessel volume.

The amount of volume flow,  $Q$ , is proportional to the square of the lumen radius,  $r^2$ , assuming the vessel is cylindrical:

$$Q = \pi r^2 v \quad (5.4.4)$$

where  $v$  is linear blood flow velocity.

The optimal radius is therefore the one that can minimize the resistance to blood flow, as well as the power of expenditure. This can be formulated as:

$$P_o = k_1 \frac{1}{r^4} + k_2 r^2 \quad (5.4.5)$$

where  $k_1$  and  $k_2$  are constants.

Differentiate  $P_o$  with respect to  $r$ , we have:

$$\frac{dP_o}{dr} = \frac{-4k_1}{r^5} + 2k_2 r = 0 \quad (5.4.6)$$

Substituting equations (5.4.1) and (5.4.2) into (5.4.6), we obtain:

$$Q^2 = \frac{k_2 \pi}{16 \eta l} r^6 \quad (5.4.7)$$

which gives an expression relating flow to the optimal vessel radius. We see that the flow is proportional to the cube of the vessel radius:

$$Q \propto r^3 \quad (5.4.8)$$

This relation is the well-known cube law. It is sometimes known as Murray's law. It states that in order to achieve a minimum amount of the rate of energy, the blood flow required to perfuse a blood vessel must be proportional to the cubic power of the radius. Controversy arises in the application of Murray's law. This stems from the fact that most of the resistance to blood flow are presented by small peripheral vessels (equation (5.4.1)), but that flow dominates in large vessels, such as the aorta. The applicability of the Murray's law therefore relies on where in the vasculature it is applied to.

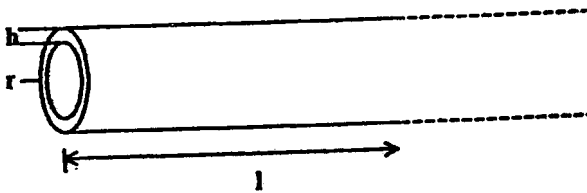


Fig. 5.4.1: A cylindrical blood vessel with radius  $r$  and length  $l$ .

Murray's (1926) minimum energy and Rosen's (1967) "Optimality Principles in Biology" have influenced earlier analysis of optimum branching. They both considered the use of a "cost function" which is commonly used in control systems engineering. The cost function considered is the sum of the rate of work done on the perfusing blood and the rate at which energy is utilized. This results in a cost function in terms of power associated with the flow-vessel interaction:

$$P_o = Q \Delta p + k(\pi r^2 l) \quad (5.4.9)$$

Where the first term is simply the rate of pressure-volume work and the second term is dependent on the volume of the vessel, assuming cylindrical in shape, with radius  $r$  and length,  $l$  (Fig. 5.4.1). Steady flow,  $Q$ , and pressure drop,  $\Delta p$  are considered here.

Power is the rate of energy use, i.e.

$$W = \int_0^T p(t)Q(t)dt \quad (5.4.10)$$

where  $p(t)$  and  $Q(t)$  are the pulsatile pressure and flow respectively and the instantaneous power is then

$$P_o = p(t)Q(t) \quad (5.4.11)$$

Equation (5.4.1) can be rewritten, employing Poiseuille's formula, as

$$P_v = \left(\frac{8\eta l}{\pi r^4}\right)Q^2 + k(\pi r^2 l) \quad (5.4.12)$$

The optimal vascular system in this concept is plausible only when individual vessel segments are optimized. Minimum rate of work is obtained, by differentiating  $P_o$  with respect to  $r$ ,

$$\frac{dP_v}{dr} = -\frac{32\eta l}{\pi r^5} Q^2 + 2k\pi r l \quad (5.4.13)$$

giving

$$r = \left(\frac{16\eta}{\pi^2 k}\right)^{1/6} Q^{1/3} \quad (5.4.14)$$

which is identical to eqn. (5.4.7), specifying the cube-law (eqn. (5.4.8)). For this radius, the corresponding minimum rate of energy is

$$P_v = \frac{3k}{2}\pi r^2 l \quad (5.4.15)$$

Thus, the optimal radius for a blood vessel when the minimum rate of energy is required for steady flow is proportional to the 1/3 power of flow,  $Q$ .

#### 5.4.2 Optimizing Branching Radii and Angles

Now consider a bifurcation with a mother vessel with length  $l_0$  and radius  $r_0$  that branches into two daughter vessels with lengths and radii of  $l_1$ ,  $l_2$  and  $r_1$  and  $r_2$ , respectively, as shown in Fig. 5.4.2. It is assumed that the vessels are lying in the same plane.

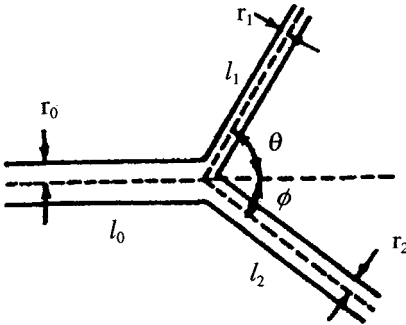


Fig. 5.4.2: Schematic drawing of a bifurcating vascular branching junction. A mother vessel branches into two daughter vessels. Lumen radius, length and bifurcation angles are shown.

We have for the cost function that assumes optimum rate of energy usage given by equation (5.4.15)

$$P_v = \frac{3k}{2} (\pi r_0^2 l_0 + \pi r_1^2 l_1 + \pi r_2^2) \quad (5.4.16)$$

The conservation of mass gives the equation of continuity of

$$Q_0 = Q_1 + Q_2 \quad (5.4.17)$$

which gives rise to the relation for the branching radii, from (5.4.6):

$$r_0^3 = r_1^3 + r_2^3 \quad (5.4.18)$$

which is again known as Murray's law or the cube law for bifurcation.

Defining an area ratio as the sum of the daughter vessel lumen areas over the mother vessel lumen area, we have:

$$A_r = \frac{r_1^2 + r_2^2}{r_0^2} \quad (5.4.19)$$

For an equi-bifurcation, or that  $r_1=r_2$ , we have

$$r_0^{3/2} = (2r_1^3)^{1/2} \quad (5.4.20)$$

Substitute, we have, for the area ratio:

$$A_r = 1.26 \quad (5.4.21)$$

When the angle of branching is involved, with half angles of branching of  $\theta$  and  $\varphi$ , the optimum rate of energy is obtained when

$$r_0^2 = r_1^2 \cos\theta + r_2^2 \cos\varphi \quad (5.4.22)$$

Extensive data of vascular branches have been obtained by several investigators for vascular branches in different vascular beds (e.g. Li et al., 1984; Schmidt-Shoenbein, 1986; Kassab et al., 1993; Kassab and Fung, 1995; Zamir, 2000). Data from pig coronary arteries by Kassab et al. (1993) show that Murray's law works very well in both control and hypertension hearts. A modified cost function that includes a metabolic constant  $k_m$  and takes into consideration the wall thickness of the vessel,  $h$

$$P_v = \left(\frac{8\eta l}{\pi r^4}\right)Q^2 + k(\pi r^2 l) + k_m(2\pi r h l) \quad (5.4.23)$$

This does not appear to differ significantly from Murray's formulation.

## Chapter 6

# The Venous System

### 6.1 The Reservoir Properties and Venous Return

#### *6.1.1 Venous Compliance and Reservoir Characteristics*

Veins are the principal conduits by which deoxygenated blood is returned to the heart, thus together with the arterial system, completing the closed-loop feature of the cardiovascular system. Blood from capillaries are returned through collecting venules to small veins and to large veins. Except the largest veins, i.e. vena cava, the great pulmonary veins and the smallest venules, veins have valves whose primary function is to facilitate the return of blood to the heart and prevent backflow.

The reservoir properties of the veins can be easily appreciated, since more than 70% of the total blood volume of the systemic vascular system are contained in veins under normal conditions, as we have seen in Fig. 2.1.2. Hemodynamically speaking, this is because of the large compliance, due to a large incremental volume ( $dV$ ) and small pulsatile change in pressure ( $dP$ ),

$$C = \frac{dV}{dP} \quad (6.1.1)$$

The reservoir property can also be easily appreciated in the case of blood loss. Under such condition, venous blood volume, not arterial blood volume, decreases in order to maintain sufficient arterial perfusion pressure. This is accomplished by the innervation of sympathetic fibers lining the venous walls, stimulation of which causes vasoconstriction,

and the narrowing of lumen diameters, hence a reduction in volume of the venous reservoir.

Veins return blood from organ vascular bed capillaries to the heart. The principal features of the venous system are its large volume and low pressure, hence greater compliance. Venous pressures are generally low, seldom exceed 12 mm Hg, or 10% of the systolic pressure in arteries, i.e. 120 mmHg. Veins have considerably smaller wall-thickness-to-radius ratio than corresponding arteries. This gives rise to the reservoir properties of the veins. In comparison, the walls of veins are much thinner, with less smooth muscle cells, and are less stiff than arterial walls. The large diameter and low pressure of veins permits the venous system to function as a storage reservoir for blood. But the relatively weak wall also means veins can be more easily suffering from tearing under greater shear stress or pressure.

During hemorrhage and blood loss events, venous blood volume, not arterial blood volume decreases in order to maintain vascular blood flow. This is accomplished by a reduction in total venous volume. This is achieved by vasoconstriction-induced reduction in vessel size of the vein whose walls have smooth muscle cells, as well as sympathetic adrenergic nerve fibers. Thus, the interplay of reflex action and the volume adjustment, allow venous pressure also to be maintained. The volume loss is normally restored through fluid retention and replenishment.

Veins acting as a storage reservoir of blood, also exhibit the function of blood distribution. Thus, they provide a critical element in blood volume control. For instance, in muscular parts of the body, such as upper and lower limbs, venous return is aided by the increase in venous tone ensures that the skeletal muscle pump increases venous pressure to ensure returning of blood to the heart. This is in addition to the peristaltic action of the veins and the one-way flow valves within the veins. The failure of the skeletal muscle contraction can lead to the common phenomenon of “venous pooling” of blood in the venous system of these limbs. Veins also play a major role in body organ temperature control through countercurrent exchanger mechanism. This latter is particularly effective in smaller vessels.

### ***6.1.2 Structural Properties of Veins***

Structurally speaking, veins and arteries have the same histological components as arteries, but with different contents and composition. The relatively thin wall of the veins, also contributes greatly to the large observed compliance. The collapsibility of the vein is due to several factors including: thin-walled vessel, large compliance, low transmural pressure. The latter is the principal controlling factor, as we shall see in the next section.

Despite the differences between arteries and veins, saphenous vein is the most commonly utilized vessel in coronary artery bypass surgery. The difference in elastic properties between arteries and veins is well appreciated from their differences in distending pressure and wall structure.

Venous walls are much thinner than those of correspondingly sized arteries, and are truly thin-walled vessels, i.e.  $h/r < 0.1$ . They contain much less smooth muscle and less elastic than arteries. Because of the collagen elastin composition, they exhibit less elastic recoil, but are easily stretched. Short-term venous blood redistribution can be accomplished by smooth muscle tone, or activation of sympathetic nerve fibers imbedded in the venous walls. Smooth muscle activation can alter the underlying elastic properties.

Veins are known to be non-circular in cross-section. Its collapsibility has been debated as to its inefficiency in metabolite transportation and blood flow. It has been shown that for an efficient fluid flow, the vessel needs to be cylindrical. This implies a circular cross-sectional area. Veins however, often exhibit an elliptical cross-sectional area. With an eccentricity ratio of 2 (major axis diameter/minor axis diameter), the power required to deliver the same amount of blood is almost twice ( $125/64$ ) that for a circular vessel lumen. In other words, for a given amount of power, the blood flow through an elliptical vessel lumen is about half ( $64/125$ ) that of a circular lumen. However, this inefficiency is well made up by the presence of venous valves. These valves serve as auxiliary one-way facilitators that reduce backflow which are energetically wasteful.

### 6.1.3 Venous Return

The heart fills with blood during diastole. Thus, the amount of venous return and filling pressure are both important governing factors of adequate filling and subsequent ejection. Superior and inferior vena cava are the principal large veins that return blood to the heart. Being in the thorax, the intrathoracic pressure is also an importance consideration. A positive filling pressure must be maintained in these veins to facilitate venous return. This is necessarily so independent of body position, magnitude and distribution of blood volume. Maintaining this proper central venous pressure requires the venous system to rapidly adjust to change in blood volume and its distribution. Since the vena cavae return blood to the right atrium, it is important that the venous pressure is slightly above the right atrial pressure. This is also necessary to prevent collapse when the difference of intravascular pressure and extravascular pressure becomes essentially zero or negative

$$\Delta P = P_i - P_e \quad (6.1.2)$$

Right atrial pressure is often considered as the “preload” to the pumping function of the heart. It is also often referred to as the filling pressure. Normal filling pressure is below 12 mmHg. Extremely high right atrial or filling pressure thus can hinder venous return. In coronary heart diseased subjects, it is not unusual to find filling pressure that exceeds 30 mmHg.

During exercise, the increased cardiac output depends also on an increased amount of venous return to the heart. Reduced filling due to lower venous return can result in reduced stroke volume, reflected in the Starling’s law. It is recognized that increased sympathetic smooth muscle activation in the venous walls or venous tone in conjunction with compression of veins by surrounding skeletal muscles are important, together with the unidirectional venous valves, in returning blood towards the heart.

## 6.2 Pressure and Flow Waveforms in Veins

### 6.2.1 *The Normal Pressure and Flow Waveforms in Veins*

Since veins are the major conduits that return blood to the heart, their pressure and flow waveforms must be intimately connected to cardiac function. This view has been deemed important particularly when considering large veins, such as the jugular vein, the main pulmonary vein and the vena cava. Veins are larger, but thinner, than their companion arteries. The relatively lower elastic modulus and greater compliance are reflected in the mechanical properties of the veins when stress-strain relations are examined. Since veins and arteries are normally structured in parallel and in close proximity to each other, there is usually cross-talk in pulsations, particularly the influence of arterial pressure oscillations on venous pulse waveform. This is seen in the jugular venous pulse, which is often compounded with the high pressure carotid artery pulse. The second major influence of the pulse waveform comes from cardiac chamber pressures, particularly that of the right and left atria. Thus, central venous pulses are important indicators of cardiac function.

Unlike arterial pressure and flow waveforms, those of veins can vary considerably, subjecting to its collapsibility and external factors. Several features can be identified, however, from a typical venous pulse. Figure 6.2.1 illustrates the jugular pressure and flow waveforms recorded in a normal subject (Kalmanson and Veyrat, 1978). The *a* wave reflects right atria contraction. This is followed by the *x* descent or valley, due to atrial relaxation. The *c* wave is attributed to the carotid artery cross-talk or the systolic bulging of the tricuspid valve during the onset of ventricular systole. The *v* wave occurs during ventricular relaxation. The *y* descent or valley is during the onset of the rapid filling phase. These *acxvy* landmarks in jugular venous pressure waveform can be easily altered with small perturbations, and significantly so in diseased conditions.

The jugular venous waveform reflects events occurring in the right atrium and right ventricle. Frequently, landmarks on the recording of the phasic waveform of the jugular venous pulse are often similar to the pressure waveforms of the jugular vein, superior vena cava, and the right atrium.

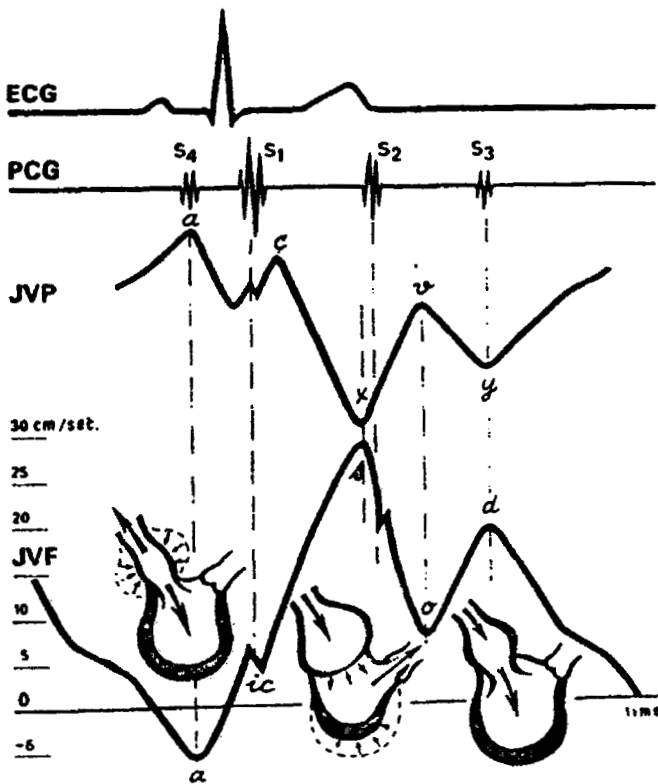


Fig. 6.2.1: Electrocardiogram (ECG), phonocardiogram (PCG), jugular venous pressure (JVP) and flow velocity (JVF) obtained from a normal subject. From Kalmanson and Veyrat (1978).

The relation of atrial function and venous flow has been studied by some investigators. Goto et al. (1988) used laser Doppler velocimeter and an optical fiber to measure blood flow velocity in the small vein and artery of the left atrium of a dog. The vein velocity was characterized by a prominent atrial systolic flow (Fig. 6.2.2). A considerable phase difference between arterial inflow and venous outflow was found and attributed to intravascular compliance properties.

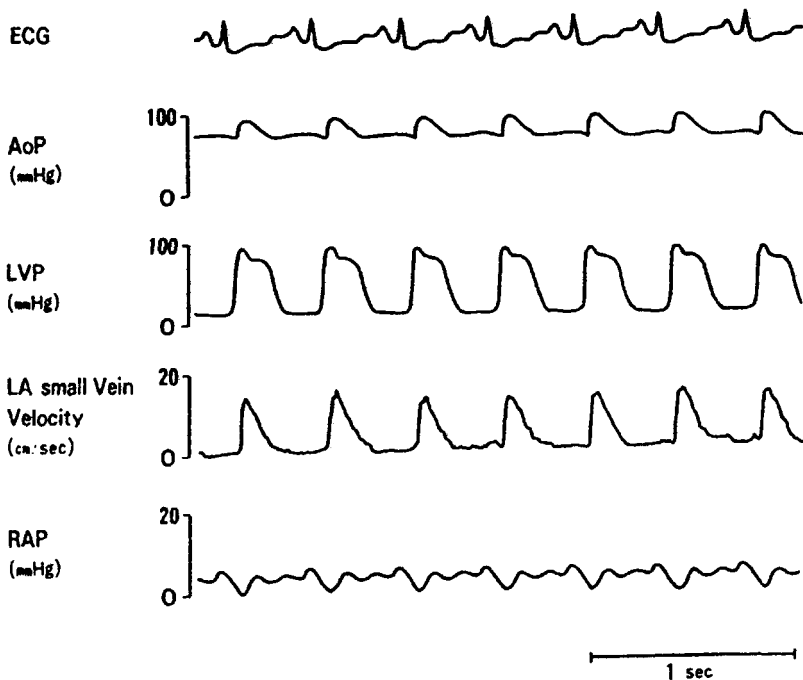


Fig. 6.2.2: Simultaneously recorded electrocardiogram, aortic pressure (AoP), left ventricular pressure (LVP), left atrial (LA) small vein velocity and right atrial pressure (RAP) in a dog heart. The venous flow velocity was measured by a laser Doppler velocimeter. From Goto et al (1988).

### 6.2.2 Respiration Effects on Venous Pressure and Flow Waveforms

Because the major central veins are within the thorax, respiration can have a profound influence on the central venous pressure and flow waveforms. In addition, they modify the venous return to the heart. Moreno (1978) provided recordings of venous pressure and flow waveforms subjected to such respiratory effects. Figure 6.2.3 shows how respiratory pressure changes can modulate the venous pressures measured in the thoracic and abdominal veins of an anesthetized dog. In an awake, instrumented dog, the respiratory effect is well illustrated when simultaneous measurements of pulmonary vein pressure and flow, vena caval flow, aortic and pulmonary aortic flows are recorded (Morgan et al., 1966). This group of investigators found that vena caval flow

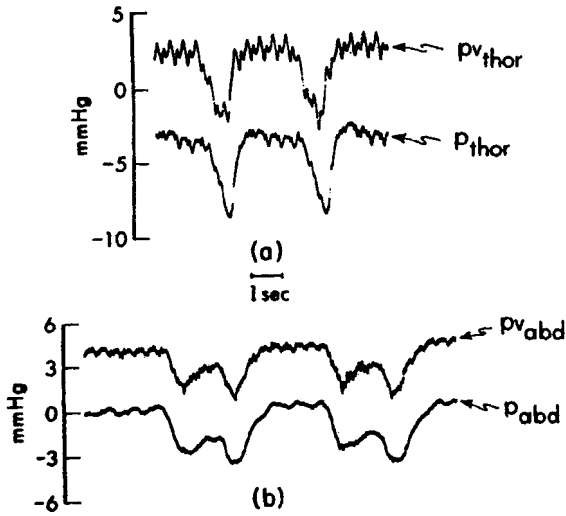


Fig. 6.2.3: Effects of respiratory pressure changes on venous pressure in the thoracic vein (a) and the abdominal vein (b). The modulating effect of respiration is clearly observed.  $p_{v_{thor}}$  = thoracic vena cava pressure,  $p_{thor}$  = intrapleural pressure,  $p_{v_{abd}}$  = abdominal vena cava pressure and  $p_{abd}$  = intraperitoneal pressure. From Moreno (1978).

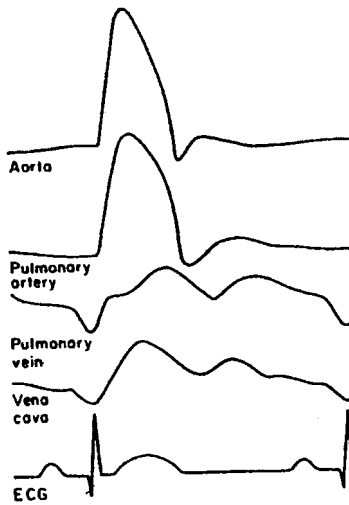


Fig. 6.2.4: Temporal relation of flow waveforms in the aorta, pulmonary artery, pulmonary vein and vena cava. From Morgan et al., (1966).

reverses during atrial contraction. Additionally, it can be seen from the figure that pulmonary vein pressure and flow peak in an almost out-of-phase manner. Figure 6.2.4 further illustrates the temporal relations of these flow waveforms.

### 6.2.3 Abnormal Venous Pressure and Flow Waveforms

As mentioned earlier that central venous pulse reflects the conditions of the heart. Fig. 6.2.5 illustrates the jugular venous pulse recorded in a subject with coronary arterial disease (Benchimol, 1981). This waveform will otherwise be interpreted as normal with identifiable acxvy landmarks. However, there is a prominent h wave, proceeding the atrial contraction and is normally associated with abnormal filling.

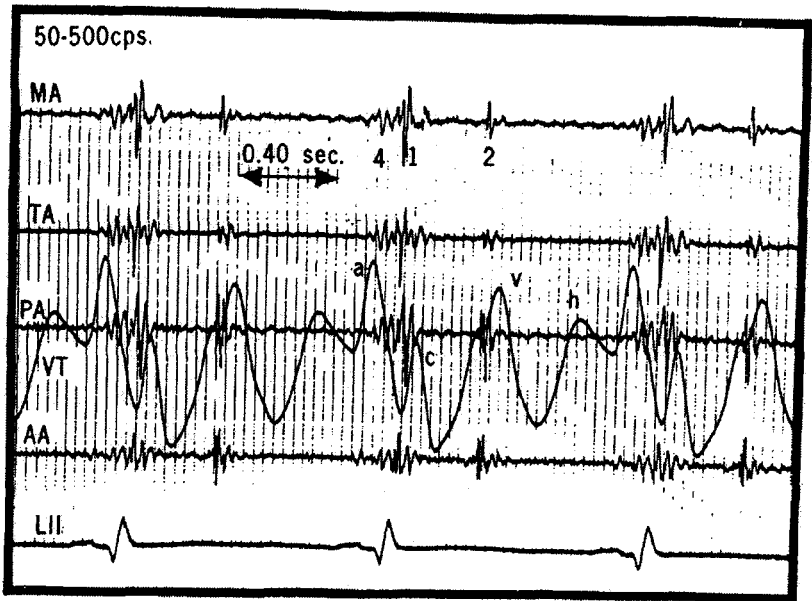


Fig. 6.2.5: Simultaneously recorded mitral (MA), tricuspid (TA), pulmonic (PA) and aortic (AA) phonocardiograms, together with the jugular venous pulse tracing (VT) in a subject with coronary arterial disease. *a*, *c*, *x*, *v*, *y* waves can be identified, together with an *h* wave. From Benchimol (1981).

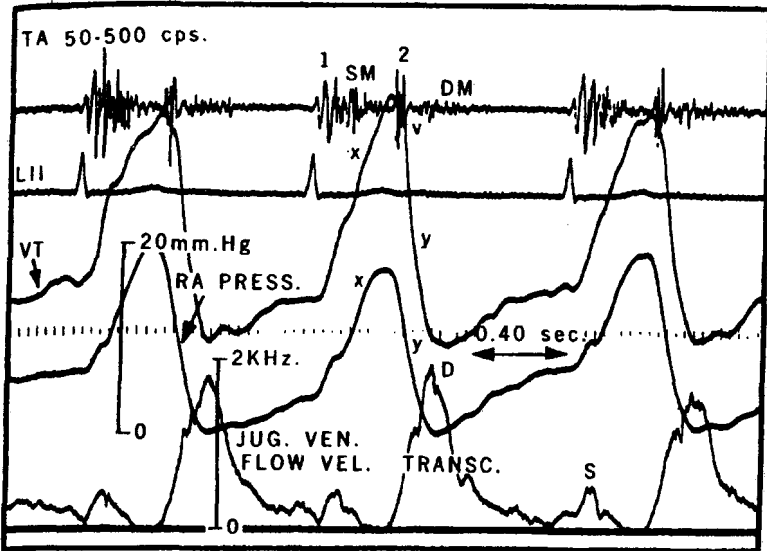


Fig. 6.2.6: Simultaneously recorded tricuspid (TA), lead II ECG (LII), jugular venous pulse tracing (VT), right atrial pressure (RA) and jugular venous flow velocity in a subject with mitral stenosis and mitral and tricuspid valve insufficiencies. Atrial fibrillation and murmur are also seen. Note the synchronous ascent and descent of the right atrial pulse with that of the jugular vein. From Benchimol (1981).

Abnormal filling is particularly relevant in the analysis of venous pressure and flow waveforms. Figure 6.2.6 illustrates simultaneously recorded jugular venous pressure and flow velocity waveforms together with right atrial pressure measured in a subject with mitral valve stenosis and mitral and tricuspid insufficiencies (Benchimol, 1981). A sustained systolic wave and a prominent *v* wave, followed by a rapid *y* descent are seen on the transcutaneous jugular pulse, as well as the right atrial pressure tracing. The jugular venous flow waveform also shows an augmented diastolic wave (D) during the filling phase. The synchronous ascent and descent of the right atrial pulse with that of the jugular vein can be observed.

Recordings of jugular pressure pulse often utilize tonometer, while the recording of jugular venous flow uses ultrasound Doppler velocity probe. The placements of these transducers and the applied pressure are

critical to the accuracy of the recorded signals. These are discussed in Chapter 8.

## 6.3 Modeling and Collapsible Vessel Properties

### 6.3.1 Steady Flow in Collapsible Tubes

That veins collapse is commonplace. The collapsibility is easily demonstrated by applying even a slight pressure over superficial veins, one can observe both venous pooling (bulging vein) and flow cessation due to occlusion. Transmural pressure is the difference between intravascular and extravascular or ambient pressure:

$$P_t = P_i - P_e \quad (6.3.1)$$

We have seen that the veins have low pulse pressure oscillating with  $P_t$  close to zero.

The collapsible tube with flow is connected by rigid connections to two reservoirs. The tube is enclosed in a chamber, containing, say water with an adjustable external pressure  $P_e$ . Such a resistor is first used by Starling in his heart-lung machine (Knowlton and Starling, 1912) in 1912. The flow in this tube is governed by the pressure differences,  $P_1 - P_e$  and  $P_2 - P_e$ . The amount of flow is dependent on the cross-section of the tube, and hence the transmural pressure. If the inlet pressure  $P_1$  and the external pressure  $P_e$  were fixed, i.e. a constant  $P_1 - P_e$ , then the flow velocity increases with decreasing  $P_2 - P_e$ . But with this, the cross-sectional area decreases, hence the volume flow which is the product of velocity and cross-sectional area first increases, then becomes limited. This flow-limiting phenomenon is well illustrated by Holt in 1941.

Assume laminar flow at a large Reynolds number so that Bernoulli's equation holds:

$$p_0 = p + \frac{1}{2} \rho v^2 \quad (6.3.2)$$

where  $p$  is the static pressure and  $p_0$  is the stagnation pressure and  $\rho$  is density of the fluid and  $v$  is flow velocity. The volume flow rate is obtained as the product of the cross-sectional area and the average velocity, i.e.

$$Q = Av = A \sqrt{\frac{2(p_0 - p)}{\rho}} = A \sqrt{\frac{2}{\rho} [(p_0 - p_e) - (p - p_e)]} \quad (6.3.3)$$

$A$  is the cross-sectional area which is a function of  $p-p_e$ . Conservation of mass states that  $Q$  remains constant along the tube, despite that  $p$  varies with distance down the tube. If  $p_0-p_e$  is fixed, then the flow rate changes with  $p-p_e$ :

$$\frac{dQ}{d(p - p_e)} = -\frac{A}{\rho v} + \left[ \frac{p}{A} \frac{dA}{d(p - p_e)} \right] \frac{A}{\rho} v \quad (6.3.4)$$

Pulse wave velocity can be derived with modification of the Moens-Korteweg formula. Area elasticity can be used instead of volume elasticity. Phase velocity of propagation in terms of pressure-cross-sectional area relation can be written as

$$c = \sqrt{\frac{A}{\rho} \frac{dp}{dA}} \quad (6.3.5)$$

or

$$c^2 = \frac{A}{\rho} \frac{d(p - p_e)}{dA} \quad (6.3.6)$$

Thus, equation (3) becomes:

$$\frac{dQ}{d(p - p_e)} = \frac{A}{\rho v} \left[ \left( \frac{v}{c} \right)^2 - 1 \right] \quad (6.3.7)$$

Thus, flow will increase with decreasing  $p-p_e$ , only if  $v < c$ . Flow reaches its maximum and limitation occurs when  $v=c$ . If  $v > c$ , then a further

decrease in  $p-p_e$  actually leads to a decrease in the flow. When the pulse wave velocity is low, as compared with flow velocity, the latter condition can occur. This  $v/c$  is known as the velocity fluctuation ratio or analogous to the Mach number.

Distensibility of the elastic tube is given as

$$D = \frac{1}{A} \frac{dA}{d(p - p_e)} \quad (6.3.8)$$

### 6.3.2 Flow Limitation and Model Experiments

Holt's first such investigation has set the milestone for researchers on collapsible tube behavior and veins. His set-up is shown in Fig. 6.3.1.

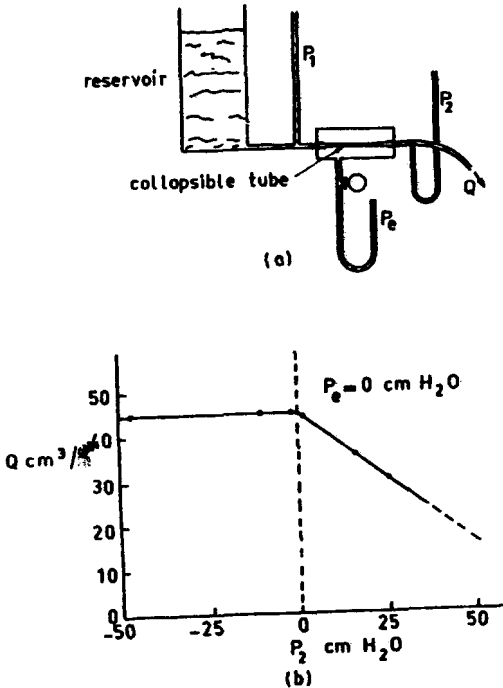


Fig. 6.3.1: (a) Flow in collapsible tube experimental set-up. The upstream and downstream pressures to the collapsible tube are  $p_1$  and  $p_2$ , respectively. The external pressure is denoted by  $p_e$ . (b) Flow ( $Q$ ) as a function of downstream pressure ( $p_2$ ), keeping  $p_e$  and reservoir head constant. From Holt (1969).

As above, flow  $Q$  through a segment of the collapsible tube is a function of the pressure just upstream to the collapsible segment,  $p_1$ , the pressure just downstream to it,  $p_2$ , and the external pressure within the enclosed chamber,  $p_e$ . The experimental results for the Penrose tube is shown also in Fig. 6.3.1. When the upstream pressure is greater than the downstream pressure ( $P_1 > P_2$ ) and the downstream pressure exceeds the external pressure,  $p_2 > p_e$ , the vessel is simply open over its entire length. The slope of the  $p_1 - p_2$  vs.  $Q$  is determined by the flow resistance of the cylindrical tube. The more interesting result occurs when  $p_2 < p_e$ , i.e. the tube no longer has a circular cross-section and is partially collapsed. Holt observed that flow to be constant in this range and described it as autoregulation, i.e. flow is now longer determined by the difference of upstream and downstream pressures,  $p_1 - p_2$ , but by  $p_1 - p_e$ . Flow limitation is said to be reached at this point.

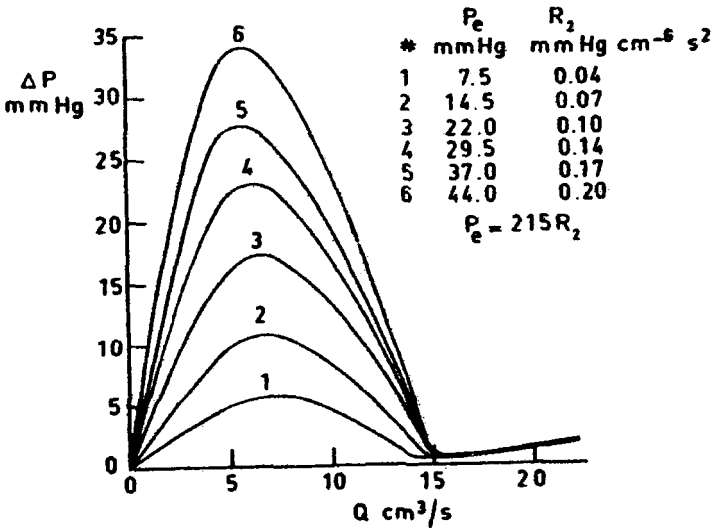


Fig. 6.3.2: Relationship of pressure gradient  $\Delta p$  ( $p_1 - p_2$ ) across the collapsible tube and flow ( $Q$ ) with increasing (1 to 6) external pressure  $p_e$  and nonlinear resistance,  $R_2$ . Notice the region when impedance is negative (decreasing  $\Delta p$  with increasing  $Q$ ). From Conrad (1969).

Several investigators have giving terms to the phenomenon observed that when there is constant flow with downstream pressure varying (Holt's experiment) as "flow regulator" (Robard, 1963; Holt, 1969). While Permutt et al. (1962) attribute it to the "vascular waterfall" suggesting flow may be independent of downstream pressure. Conrad's detailed account used the tunnel diode analogy and suggested "negative impedance" between pressure drop across the collapsible tube and flow (Fig. 6.3.2).

Brower and Noordergraaf (1973) chose to consider the pressure drop across the collapsible tube as a function of flow and the difference between external pressure and downstream pressure as the primary determinants of pressure-flow relationship in a collapsible vessel, viz:

$$p_1 - p_2 = f(Q, p_e - p_2) \quad (6.3.9)$$

They investigated this pressure drop ( $p_1-p_2$ ) to flow relation as a function of various parameters that are derived from the fluid and the tube, i.e. elastic property of the vessel and its geometric dimension and the properties of the fluid. The resulting simple relation shows flow,  $Q$ , as a function of the pressure drop,  $p_1-p_2$ , with  $p_e-p_2$  as a parameter that was gradedly varying (Fig 6.3.3). This figure resembles that of the transistor's voltage-current relationship. It can be seen here that the "negative impedance" concept suggested by Conrad does not exist here. Flow increases with pressure drop across the collapsible tube only within certain regime. At low pressure drop and low  $p_e-p_2$ , the relationship is more gradual and plateau is reached also gradually. At high pressure drop and high  $p_e-p_2$ , flow increases rapidly and reaching the plateau much faster. The plateau region reflects increases in flow that is independent of pressure drop  $\Delta p$ , across the collapsible vessel,  $p_1-p_2$ , and, the difference between external pressure and downstream pressure,  $p_e-p_2$ .

In order to explain previous observations, Brower and Noordergraaf (1973) expressed the relation in terms of all the governing factors:

$$p_1 - p_2 = k_Q(p_e - p_2) \quad (6.3.10)$$

This is true when

$$p_1 - p_2 = RQ \quad (6.3.11)$$

where  $k_Q$  is an empirical expression

$$k_Q = \frac{(Q/Q_c)}{[1 + (Q/Q_c)^6]^{-1/6}} \quad (6.3.12)$$

where  $Q_c$  is the critical flow when the plateau is reached. It is an empirically derived function and is dependent on the values of  $p_e - p_2$  only.

Otherwise, the whole relation reduce to that of a steady flow through the tube with circular cross-section:

$$p_1 - p_2 = RQ \quad (6.3.14)$$

An axially stretched Penrose tube showed no plateau (Brower and Noordergraaf, 1978) when  $\Delta p$  is plotted against flow.

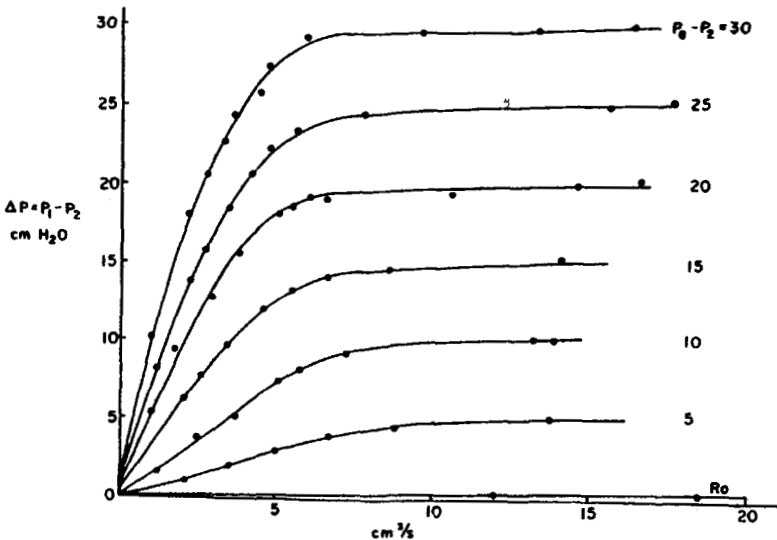


Fig 6.3.3: Pressure gradient ( $\Delta p = p_1 - p_2$ ) and flow ( $Q$ ) relation in a collapsible Penrose tube, while  $p_e - p_2$  is varied.  $R_o$  is the equivalent Poiseuille resistance when tube is open From Noordergraaf (1978).

Cross-sectional area in relation to transmural pressure in collapsible vessels has also been studied by several investigators. Kresch and Noordergraaf (1972) computed the shapes of the tube cross-sectional areas for different eccentricity for negative transmural pressures, beginning with an ellipse cross-section when the transmural pressure is zero. The resulting shapes are shown in Fig 6.3.4. Moreno et al.'s (1970) experimental findings seem to confirm these theoretically computed shapes.

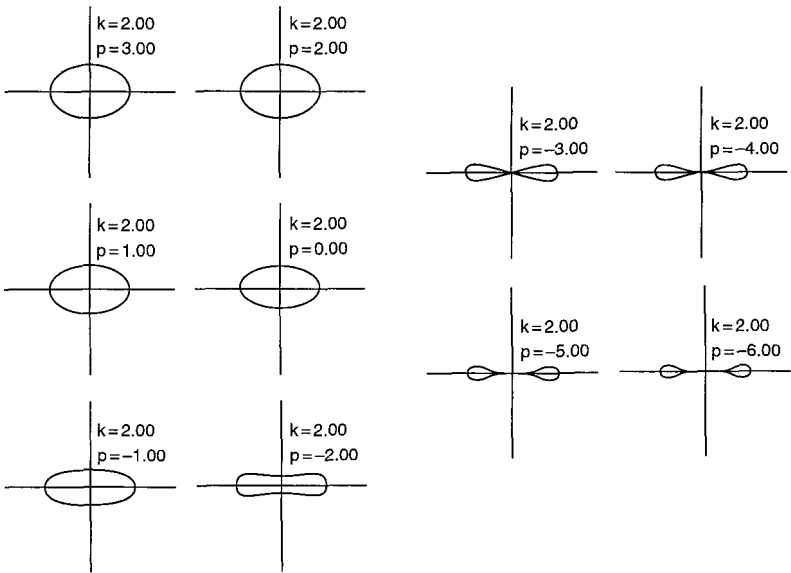


Fig 6.3.4: Computed cross-sectional area shapes for a collapsible vessel with varying transmural pressure ( $p$ ). Zero transmural pressure ( $p=0$ ) is assumed to be an ellipse with eccentricity  $k=2.0$ . From Noordergraaf (1978).

### 6.3.3 Pulse Wave Transmission Characteristics in Veins

The low pulse pressure and collapsible nature of veins make pulse transmission measurements difficult. There are thus few studies. Anliker et al. (1969) utilized a method that ensure system linearity and avoid wave reflection effects. This latter is because wave reflection effects

dominate at low frequencies (Chapter 4) and that the wave velocity is essentially constant, as is dynamic elastic modulus at high frequencies.

They generated high frequency small amplitude sinusoidal pressure waveforms which were introduced into the abdominal vena cava of anesthetized dog or by means of an electromagnetic impactor attached to the veins outer wall. A dual-sensor catheter-tip transducers were inserted into the vein to measure pulse wave velocity from transit time delays, i.e. foot-to-foot velocity. Their results are shown in Fig. 6.3.5. It is clear from our earlier analysis that the pressure-dependence of compliance and pulse wave velocity are clearly seen with increasing transmural pressure.

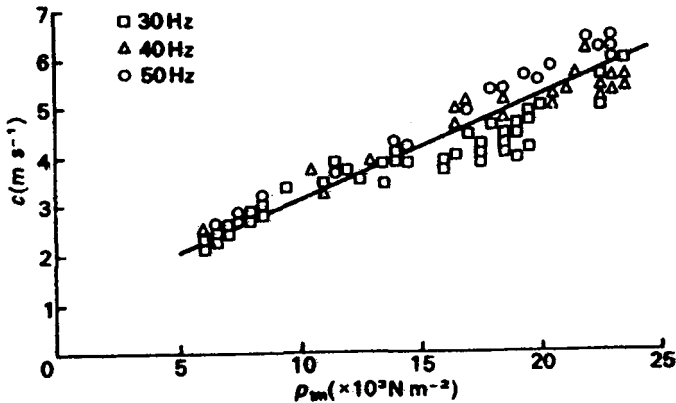


Fig. 6.3.5: Propagation velocity as a function of transmural pressure. Short trains of high frequency small amplitude sinusoidal pulse waves were imposed on the dog's abdominal vena cava. (Anliker et al., 1969).

Their results on attenuation showed that attenuation per wavelength is independent of frequency. Figure 6.3.6 shows that pulse wave amplitude declines with distance, described by:

$$a = a_0 e^{-kx / \lambda} \quad (6.3.15)$$

where  $x$  is distance along the vessel,  $\lambda$  is wavelength of propagation,  $a$  is the amplitude and  $a_0$  is the amplitude at  $x=0$ . The value of  $k$  for the vena cava of the dog is between 1.0 to 2.5, corresponding to attenuations of

63% to 92% per wavelength. This compares with 0.7 to 1.0 for the aorta. Thus, greater attenuation and slower pulse wave propagation velocity are found in the vena cava.

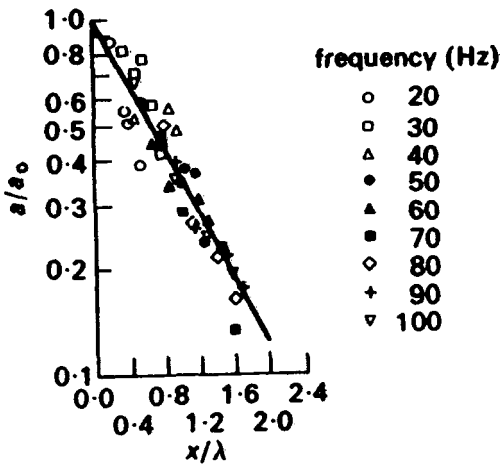


Fig. 6.3.6: Attenuation of short trains of high frequency small amplitude sinusoidal pulse waves were imposed on the dog's abdominal vena cava. Attenuation is represented by the amplitude ratio ( $a/a_0$ ) as a function of changes in propagating distance as a fraction of wavelength ( $x/\lambda$ ). From Anliker et al. (1969)

The attenuation was attributed to the viscosity of blood, the radial transmission to surrounding tissues and the viscoelastic properties of the walls. This latter is the predominating factor, as have been found for the systemic arteries by Li et al. (1981). That the attenuation per wavelength is practically independent of frequency suggest that the energy dissipation is independent of strain rate. This study uses frequencies of 20-100 Hz, much higher than the highest significant component of natural pulse pressure and flow waveforms.

Pulse wave velocity as seen from the above experimental measurements, is significantly lower in veins than in corresponding size arteries. This can be measured as foot-to-foot velocity or can be readily estimated from the Moens-Korteweg formula.

But with the changing cross-sectional area and the transmural pressure, pulse wave velocity is seen to be dependent on both vessel

compliance and frequency. Brower and Scholten (1975) demonstrated this latter in a collapsible Penrose, while Anliker et al. (1969) measured this in dog veins. The former was analytically derived by Kresch and Noordergraaf (1969) for the case of uniform collapse tube:

$$c = \sqrt{\frac{A}{\rho(dA/dp)}} k_v \quad (6.3.16)$$

where

$$k_v = \left[ 1 - \frac{2J_1(\sqrt{j\omega k_A})}{j\omega k_A J_0(\sqrt{j\omega k_A})} \right] \quad (6.3.17)$$

and

$$k_A = \frac{\rho A}{\pi \eta k} \quad (6.3.18)$$

Where  $J_0$  and  $J_1$  are Bessel function of the zeroth and first order and  $A$  is the cross-sectional area,  $dA/dp$  is the distensibility of a circular tube with the same cross-sectional area,  $\kappa$  is the shape factor which equals 1.0 for a circular vessel and 2.0 for a collapsed vessel,  $\rho$  and  $\eta$  are the density and viscosity of the fluid. Wave velocity is dependent on shape is observed by Bailie (1972). Thus, in this formulation the phase velocity is frequency dependent and cross-sectional area dependent.

## Chapter 7

# The Microcirculation

### 7.1 Structure of the Microcirculation

#### *7.1.1 Functional Organization of the Microvasculature*

The function of the cardiovascular system is to provide a homeostatic environment for the cells of the organism. The exchange of the essential nutrients and gaseous materials occurs in the microcirculation at the level of the capillaries. These microvessels are of extreme importance for the maintenance of a balanced constant cellular environment. Capillaries and venules are known as exchange vessels where the interchange between the contents in these walls and the interstitial space occur across their walls.

The microcirculation can be described in terms of a network such as that shown in Fig.7.1.1. It consists of an arteriole and its major branches, the metarterioles. The metarterioles lead to the true capillaries via a precapillary sphincter. The capillaries gather to form small venules, which in turn become the collecting venules. There can be vessels going directly from the metarterioles to the venules without supplying capillary beds. These vessels form arteriovenous (A-V) shunts and are called arteriovenous capillaries. The thickness of the wall and endothelium of these structures and the proportionate amounts of the various vascular wall components have been shown in Chapter 2. The capillary and venule have very thin walls. The capillary as mentioned before, lacks smooth muscle and only has a layer of endothelium. The smooth muscle and elastic tissue are present in greater amounts in vessels having vasoactive capabilities, such as arterioles. This is also the site of greatest drop in mean blood pressure. For this reason, arterioles are the principal

contributors to peripheral vascular resistance that can effectively alter cardiac output.

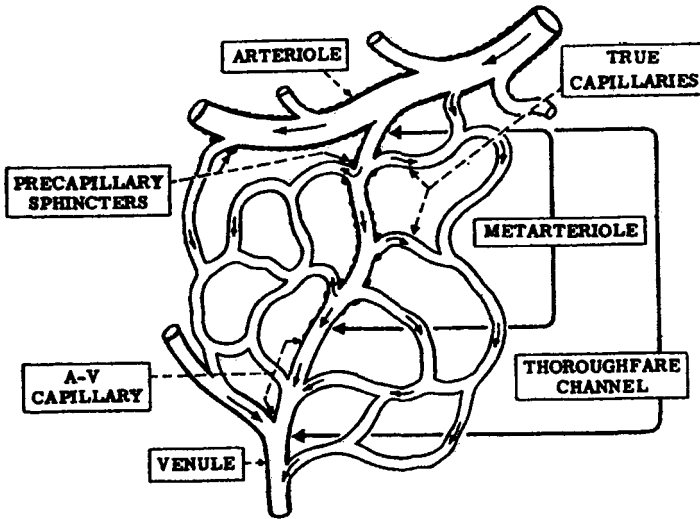


Fig.7.1.1: A network of microcirculatory unit, illustrating the constituent components.

The structural components of the microcirculation are classified into resistance, exchange, shunt, and capacitance vessels. The resistance vessels, comprising the arterioles, metarterioles, and precapillary sphincters, serve primarily to decrease the arterial pressure to the levels of the capillaries to facilitate effective exchange.

Differences in microvascular behavior are attributed to the differences in the overall function of the body organ in which these microvessels exist. Thus, flow in the microvessels of the brain differs from that in the heart or the lungs. Some capillaries are fed by the arterioles and collected by the venules, but others can bypass the capillaries and connected directly to either small artery to a small vein. These latter are known as anastomoses which serve to control flow and certain transport processes. As well known in the countercurrent mechanism for the body temperature control, the small arteries and veins run parallel and frequently adjacent to each other, while branching

arteioles and venules are close to  $90^\circ$ . Capillaries, in general, are running parallel next to perfusing muscle or tissues. These are well illustrated by the photomicrographs of Smaje et al. (1970) in the cremaster muscle of the rat (Fig. 7.1.2) and also by Zweifach et al. (1974) in the cat omentum (Fig. 7.1.3).

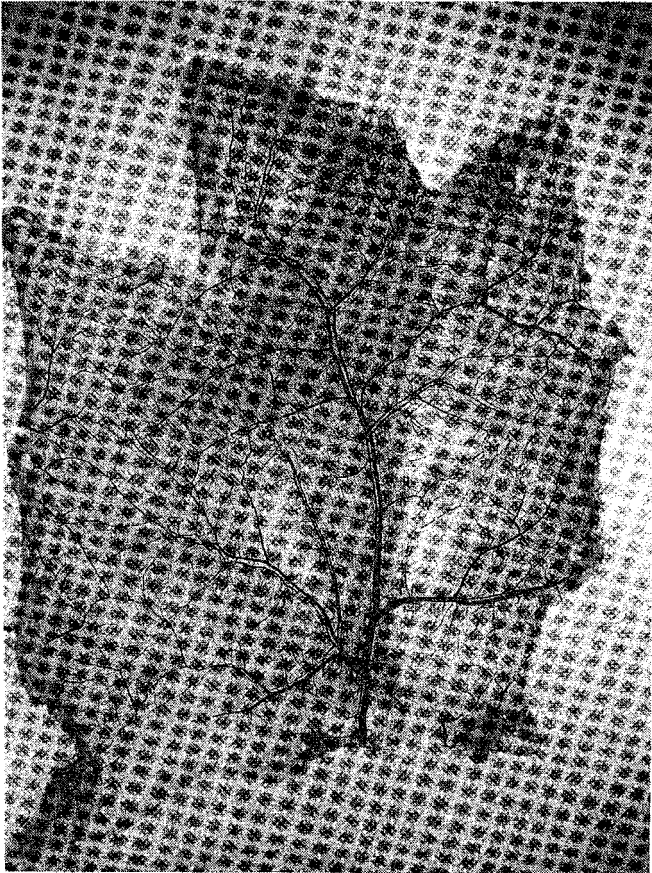


Fig. 7.1.2: Photomicrograph of rat cremaster muscle showing pattern of vascular structure. Y-shaped and T-shaped branching junctions are common, in addition to cross-connections of the vessels. From Smaje et al. (1970).

A bat (a flying mammal) wing and the mesenteric bed of a small mammal are popular preparations for studying blood flow in the microcirculation. The flow into the capillaries has been shown to remain

pulsatile or intermittent in nature (e.g. Zweifach, 1974). It has also been shown that the rhythmic vasomotor activity of the precapillary sphincters is responsible for the observed intermittency. The sphincters may also exhibit constriction and dilation in response to changes in local metabolites, chemicals, or sympathetic stimuli. Together with the arterioles, the precapillary sphincters serve to adjust the amount of blood flow to meet the demands in tissues.

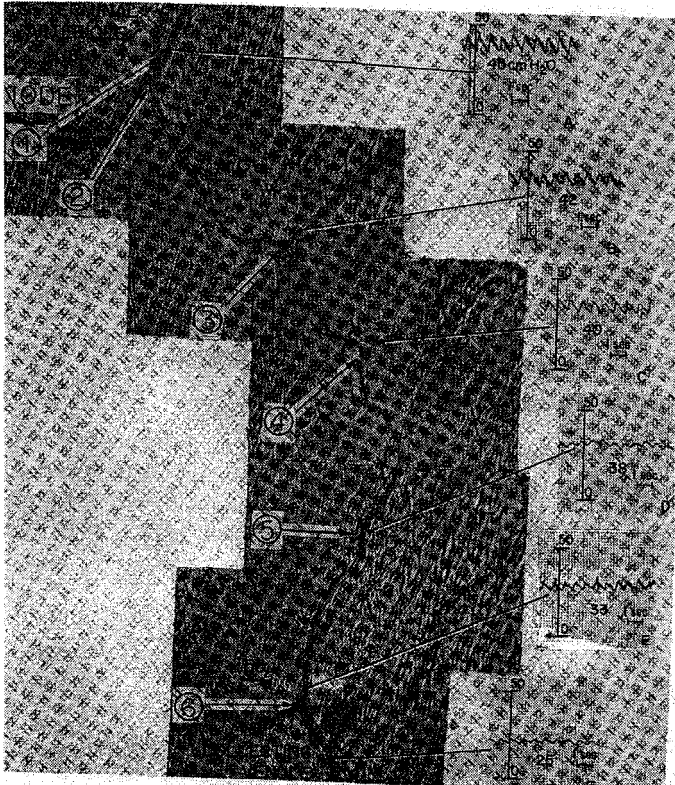


Fig. 7.1.3: Photomicrographic reconstruction of the microcirculation from a terminal arteriole through capillaries to a collecting venule. The flow into the capillaries remains pulsatile or intermittent. Direct pulsatile pressure recordings are shown. From Zweifach (1974).

If we compare the size of red cells from various mammals, we find the perhaps surprising fact that their diameters seem to be rather uniform and independent of mammalian body size (Li, 1996). This is summarized

in Table 7.1. Data from more than one hundred mammalian species show that the red blood cells are of similar size and that there is no single mammal has a red cell diameter over 10  $\mu\text{m}$ . This suggests the structural sizes of the capillaries are in the same order of magnitude in these mammals. It should be noted however, that the structures and functions of the endothelial cells lining the capillaries may differ, depending on the microvascular bed of a particular organ they serve. In addition, the topological branching structures of the different microvascular beds are unique for each organ. For instance, the pulmonary microcirculation has an entirely different vascular tree structure as compared to the coronary microcirculation, or that of the cerebral microcirculation.

Table 7.1.1: Diameters of red blood cells (RBC) of some mammalian species.

Species	Body weight (kg)	RBC Dismeter ( $\mu\text{m}$ )
Shrew	.01	7.5
Mouse	.20	6.6
Rat	.50	6.8
Dog	20	7.1
Man	70	7.5
Cattle	300	5.9
Horse	400	5.5
Elephant	2000	9.2

The arteriole (10-125  $\mu\text{m}$ ) has smooth muscle cell layers in its wall with the nerve connection to its outermost layer. Even the terminal arteriole still has a single layer of smooth muscle cells. A meta-arteriole has a discontinuous layer of smooth muscle cells. Pre-capillary sphincter is the last smooth muscle cell at the end of terminal arterioles. Similarly, there are post-capillary venules, and collecting venules (10-50  $\mu\text{m}$ ) and small collecting veins which already has intima endothelial layer, the media with smooth muscle layers.

### 7.1.2. The Capillary Circulation

The extensiveness of the organizational structure of the network of capillaries is necessary for efficient cellular transport and diffusion

processes to take place. These processes are slow in comparison to blood perfusion. For this reason, a capillary is normally in the neighborhood and within reach to any single cell at a distance of about three to four cells apart. A given capillary can have a length of about 1 mm and a diameter of 4-10  $\mu\text{m}$ .

Two principal types of capillaries are found. The true capillaries have no vascular smooth muscle and form network with other capillaries. The arterio-venous or A-V capillaries have some amount of smooth muscle and are directly connected to muscular arterioles and small venules. Phasic flow patterns are determined by the vasomotion, attributed to the small arterioles, the A-V capillaries, the pre-capillary sphincters. These latter give rise to the constant dilation and constriction that modulate the flowing blood. Local control dominates, as the pre-capillary sphincters do not have nerve connections. The true capillary walls are without connective tissue and smooth muscle and consist of a single layer of endothelial cells surrounded by a basement membrane of collagen and mucopolysaccharides.

Differences in capillary endothelium structure give rise to different capillary function in different tissues. This is well illustrated in Fig. 7.1.4, where a continuous capillary, a fenestrated capillary and a sinusoid capillary are shown. In a continuous capillary (Fig. 7.1.4 (A)), 4 nm clefts, a complete basement membrane and numerous vesicles are seen. (Fig. 7.1.4 (B)) shows the fenestrated capillary with pores through a thin portion of the wall, few vesicles and a complete basement membrane. (Fig. 7.1.4 (C)) shows a sinusoidal capillary with large para-cellular gaps extending through the discontinuous basement membrane. Because of the structural differences, the continuous capillary has been found to be the least permeable, while the sinusoidal capillary, the most permeable. Continuous capillaries are found, for instances, in muscle, nervous tissue and the lungs. The fenestrated capillaries are found, for example, in intestines. The sinusoidal capillaries are located, for instances, in the liver, adrenal cortex and bone marrow.

Nutrients and formed substances can move across the wall of continuous capillaries either through or between the endothelial cells. Lipid-soluble substances diffuse through the cell membrane. Water and ions diffuse through the water-filled clefts between cells. There are

transport mechanisms that allow glucose, some amino acids and macromolecules to move across some capillary walls. Some of these mechanisms have not been elucidated. One such mechanism is through vesicle-mediated transport process.

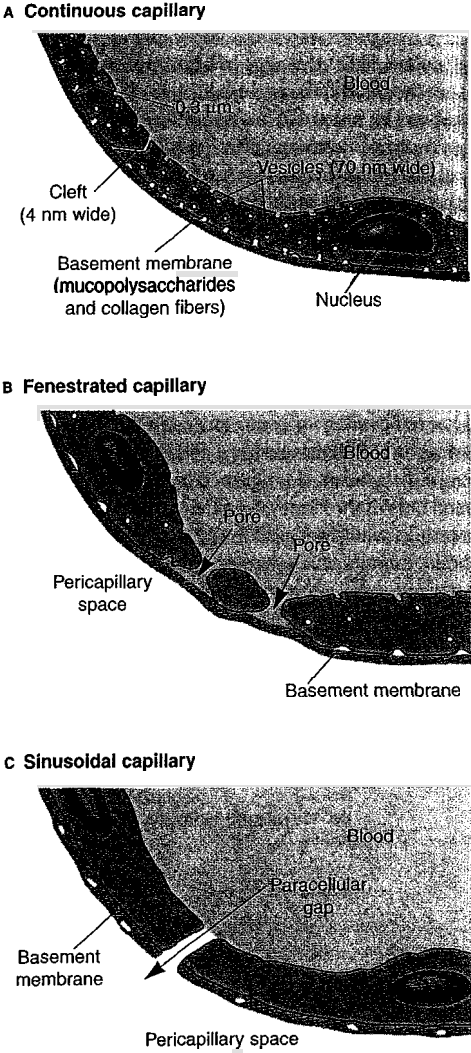


Fig. 7.1.4: Structure of portions of the endothelial wall in (A) a continuous capillary, (B) a fenestrated capillary, and (C) a sinusoidal capillary. From Randall et al. (1997).

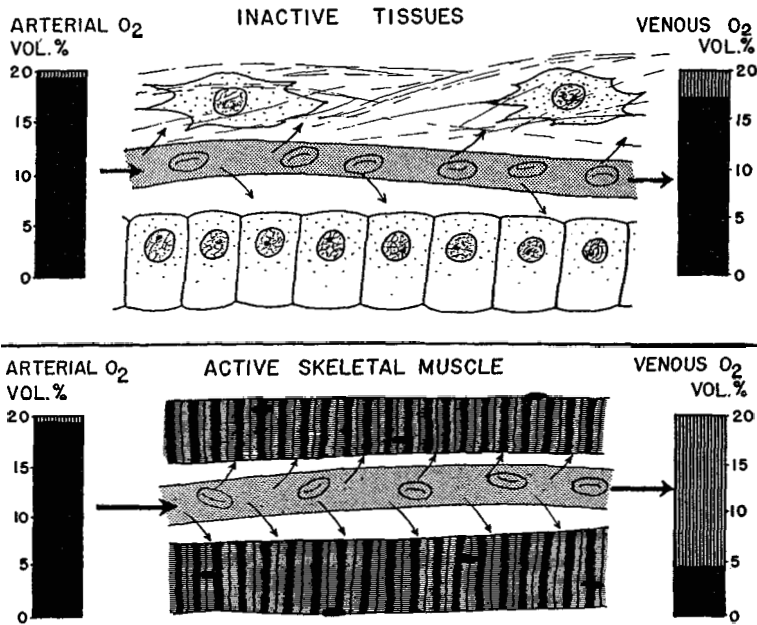


Fig. 7.1.5: Oxygen extraction in inactive skin tissue (top) and active skeletal muscle tissue (bottom). From Rushmore (1972).

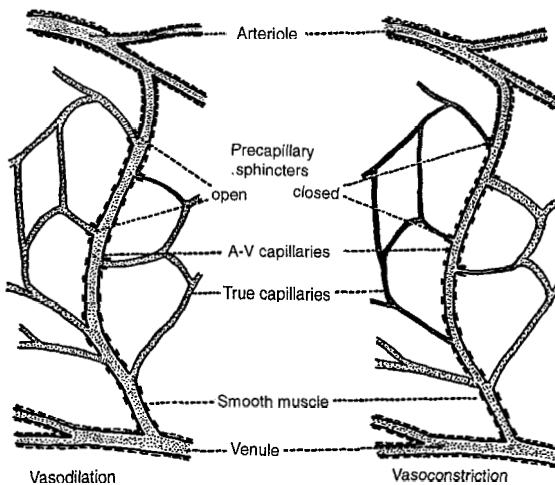


Fig. 7.1.6: Illustration of the vasomotion in a capillary network. From Rushmore (1972).

The primary role that the capillaries play is in the oxygen exchange. The quantity of oxygen extracted from the blood during its flow through capillaries is determined by the relationship between the rate of oxygen utilization and the blood flow. This is illustrated in Fig. 7.1.5. The top figure shows slight oxygen extraction and small arterio-venous oxygen differences occur in tissues with relatively small oxygen requirements and active blood, such as skin. The bottom figure shows tissues which release energy at rapid rates, such as contracting muscle, extract a major portion of the oxygen from the blood.

As we mentioned earlier, capillaries in some tissues may consist of arterio-venous (A-V) capillaries known as thoroughfare channels and true capillaries. The blood flow through different portions of the capillary bed is affected by contraction and relaxation of smooth muscle in the arterioles, A-V capillaries and precapillary sphincters. Phasic changes in these regions produce cyclic alterations in the amount and distribution of blood flow through the various capillaries. This is known as the vascular vasomotion (Fig. 7.1.6).

## 7.2. Pressure-Flow Relation and Microcirculatory Mechanics

### 7.2.1 Flow-Related Mechanical Characteristics of the Microcirculation

Pressure, flow and forces are drastically smaller in the microcirculation as opposed to the macro-circulation. We know that the Reynolds number as defined by

$$R_e = \frac{\rho v d}{\eta} \quad (7.2.1)$$

is very small as compared an artery. For instance, the Reynolds number may be 0.03 for a 100  $\mu\text{m}$  arteriole. With even smaller diameter and blood velocity, the Reynolds number is at least an order smaller in the capillary.

Steady flow is assumed in many hemodynamic and rheological studies. This is because the Womersley's number, defined as

$$\alpha_w = r \sqrt{\frac{\omega \rho}{\eta}} \quad (7.2.2)$$

is very small. Womersley's number can be viewed as the ratio of oscillatory flow to steady flow. When  $\alpha_w$  approaches zero, the approximation of a steady flow is a reasonable one.

In relation to entry length, it is now small compared with the diameter of the microvessels. Thus, the flow becomes fully developed towards a parabolic profile, despite the relatively short length of the vessels.

The Newtonian fluid aspect needs to be carefully addressed. The blood and its formed elements now contribute more to the abnormality of the viscosity. The well-known Fahraeus-Lindqvist effect explains the decreasing blood viscosity in very small vessels. Nevertheless, the Poiseuille's equation has been viewed as important in the microcirculation, in that the flow is determined by the driving force of the pressure gradient and the resisting force of viscosity.

$$Q = \frac{8\eta l}{\pi r^4} \Delta p \quad (7.2.3)$$

Although remaining pulsatile, the flow in the capillaries is intermittent at best. A single arteriole branches into several and sometimes 15 or so capillaries. The branching phenomena and optimization aspect we discussed in Chapter 5, now needs to incorporate considerably more local control aspects, in terms of exchange between the capillaries and its surrounding tissues, as well as the vasomotion due to smooth muscle tone in the arterioles.

The flow into the capillaries has been shown to remain pulsatile or intermittent in nature. It has also been shown that the rhythmic vasomotor activity of the precapillary sphincters is responsible for the observed intermittency. The sphincters may also exhibit constriction and dilation in response to changes in local metabolites, chemicals, or sympathetic stimuli. Together with the arterioles, the precapillary

sphincters serve to adjust the amount of blood flow to meet the demands in tissues.

Starling's hypothesis describes the filtration and absorption of fluid across capillary walls. The capillary wall is known to consist of endothelium with a basement membrane that is highly permeable to allow fluid exchange. Several factors govern such exchange: (1) hydrostatic capillary blood pressure,  $p_c$ , (2) osmotic pressure of plasma proteins,  $\pi_c$ , (3) hydrostatic interstitial fluid pressure,  $p_i$  and (4) osmotic pressure,  $\pi_i$ , of the proteins in the interstitial fluid. These define the Starling's hypothesis:

$$p_c - p_i = \pi_c - \pi_i \quad (7.2.4)$$

under equilibrium. In other words, the difference in fluid pressure in the capillary and the surrounding interstitial tissue equals the difference in osmotic pressure between the capillary blood and the extravascular fluid.

Depending on the physiological demand, the microcirculatory system adjusts itself rapidly and efficiently. For this reason, the trans-capillary flow is given by a modification of eqn. (7.2.4) to:

$$Q = k_c S (p_c - p_i - \pi_c + \pi_i) \quad (7.2.5)$$

where  $k_c$  is capillary permeability and  $S$  is the cross-sectional area available for the exchange. Capillary permeability is in the order of  $10 \cdot 3^9 \text{ g}^{-1} \text{ cm}^2 \text{ s}$ . Several methods are available to measure this flow, including the micro-occlusion and electro-optical techniques and the use of optical dye.

### ***7.2.2 Some Pressure-Related Mechanical Characteristics of the Microcirculation***

Pressure measurement techniques in the microvessels were mostly based on the method originally designed by Wiederhielm et al. (1964). Zweifach and colleagues have refined the technique and performed extensive measurements (e.g. Zweifach, 1974 and Zweifach and Lipowsky, 1977). Fig. 7.2.1 illustrates such an intravascular

measurement of pressure and velocity in a cat mesentery microvascular bed. Arterial to venous distribution of the pressure and velocity is shown. Pressure dropped rapidly in small arterioles, but more gradually in the capillaries. The velocity drop parallels the velocity in the arterioles, not so in the venous side.

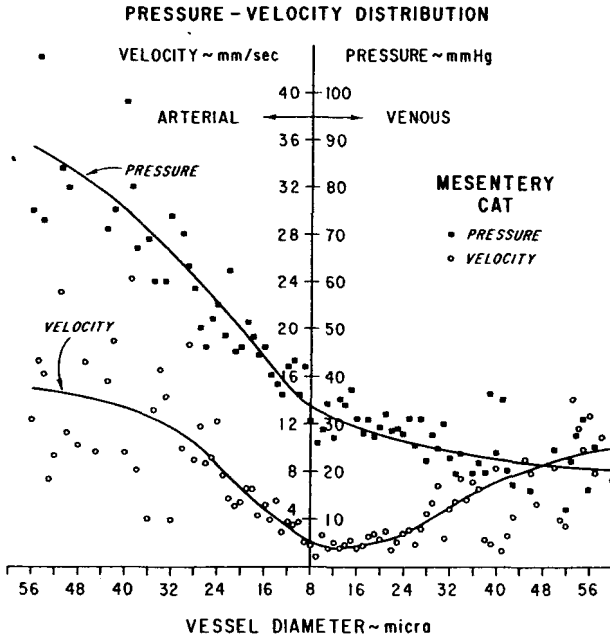


Fig. 7.2.1: Illustration of arterial to venous distribution of intravascular pressure and velocity in the cat mesentery as a function of microvessel diameters. Solid lines are fitted curves. From Zweifach and Lipowsky (1977).

The pressure gradient,  $\Delta p/\Delta z$  or  $dp/dL$  can be measured by the micro-occlusion technique. Here, two pressure probes are inserted into two side branches of a given vessel and flow is occluded in these side branches. The two pressure readings divided by the distance between the two measurement sites gives the pressure gradient.

Lee and Schmid-Shonbein (1995) have estimated distensibility of capillaries in skeletal muscles based on the pressure-area relation (see Chapter 2). They made a comparison of capillary distensibility when the

fascia of the skeletal muscle is tact or removed (Fig. 7.2.2). It is interesting to note that the capillary distensibility is retained even when the fascia is intact. However, the greater distensibility when fascia is removed case suggests that skeletal muscle contraction can influence capillary distensibility. The consequence is a reduction of the distensibility during contraction.

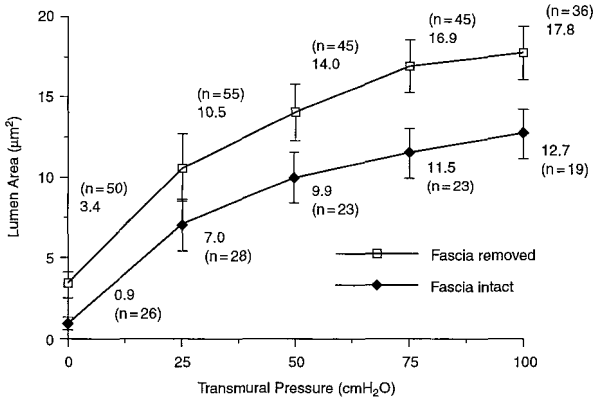


Fig. 7.2.2: Measurement of capillary distensibility in terms of lumen area and transmural pressure when fascia is either left intact or removed. From Lee and Schmid-Schonbein, (1995).

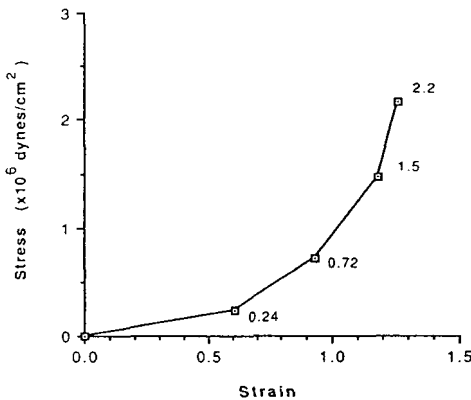


Fig. 7.2.3: Circumferential stress-strain relation of isolated capillary blood vessels. From Lee and Schmid-Schonbein (1995).

The circumferential stress-strain relation of microvessels follow the curvilinear relations found arteries and veins, though to a greatly different extent. The circumferential stress-strain relation of isolated capillary blood vessels in gracilis muscle of Sprague-Dawley rats with fascia removed is shown in Fig. 7.2.3. Here, the capillary wall is not in contact with muscle fibers. The assumption is made that all the circumferential tension is carried by the basement membrane.

It should be noted here that the diameters of microvascular vessels change continuously throughout the cardiac cycle. Thus, the compliance change must follow the nonlinear behavior as we have shown earlier for the arteries. In other words, the compliance is pressure-dependent (Chapter 4), thus time-varying. The measurements of diameters of subendocardial arterioles and subendocardial venules by Kajiya and his colleagues (Yada et al., 1993) support this conclusion (Fig. 7.2.4).

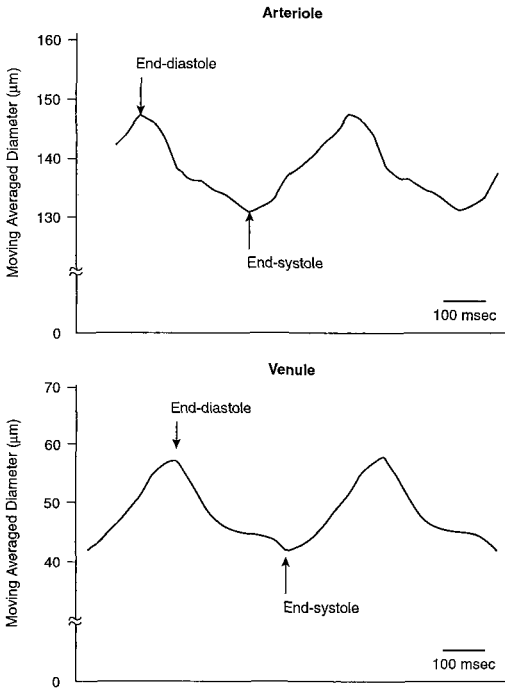


Fig. 7.2.4: Continuous variations of the diameters of a subendocardial arteriole and a subendocardial venule throughout the cardiac cycle. From Yada et al. (1993)

### 7.3. Pulse Transmission and Modeling Aspects

#### 7.3.1 Pressure and Flow Waveforms in Arterioles and Capillaries

Pulses, originating at the left ventricle, are modified as they propagate toward the periphery. This is attributed to the effects of blood viscosity, to arterial viscoelasticity resulting in frequency dispersion and selective attenuation, and to site dependent summation of incident and reflected pulses. Pulsations, however, persist even in the microcirculation.

Quantification of peripheral resistance has long been an interest to both researchers and clinicians. Since the largest mean pressure drop occur in the arteriolar beds. These latter have been suggested to contribute mostly to the peripheral resistance.

It has been presumed for decades that flow in the microcirculation, particularly in the arterioles and capillaries, is entirely steady flow. Consequently, Poiseuille's formula has been applied. Poiseuille in 1841 arrived at an empirical relationship relating pressure drop  $\Delta P$  to steady flow  $\bar{Q}$  in a cylindrical vessel with diameter  $D$  and length  $l$ .

Thus, the amount of steady flow through a blood vessel is proportional to the pressure drop and the fourth power of the diameter. Independently, at about the same time in 1939, Hagen had performed numerous experiments and, at about the same time, arrived at a similar expression. This formula was later modified to the presently known Hagen-Poiseuille equation, or simply, the Poiseuille's law:

$$\bar{Q} = \frac{\pi r^4}{8\eta l} \Delta p \quad (7.3.1)$$

Although credit has been given fully to Poiseuille, it was Hagenbach (1860) who came up with an exact relation relating steady flow to the fluid viscosity  $\eta$ , and the pressure gradient,

$$Q = -\frac{\pi r^4}{8\eta} \frac{dp}{dz} \quad (7.3.2)$$

Pressure gradient in the Poiseuille's law is simply  $\Delta P/l$ . Poiseuille resistance to steady flow is therefore:

$$R_s = \frac{8\eta l}{\pi r^4} \quad (7.3.3)$$

Steady flow was assumed because of the belief that small peripheral vessels are resistance vessels, preventing pulsations occurring.

As mentioned above, the largest mean pressure drop occurs in small arterioles. Referring back to Chapter 2 regarding the structure of the vascular walls, we see that this is also where smooth muscle tends to exert its influence. Thus, accompanying the smooth muscle (Somlyo and Somlyo, 1968) activation, is a change in vessel lumen radius. Since flow varies by the fourth power of radius, a small change in radius can amount to a large alteration in flow. Thus, the peripheral resistance can alter central arterial flow and hence, cardiac output.

It is now known that pulsatile ejection by the ventricle requires only about 10% additional energy for the same stroke volume compared to constant outflow. This minimal additional energy associated with pulsatile ventricular ejection indicates the compliant properties of the receiving arterial tree.

An appreciable fraction of the energy in the pressure and flow pulses generated by the heart reaches the capillaries in pulsatile form. This has been demonstrated experimentally by, for instance, Wiederhelm et al. (1964), in frog's mesentery, Intaglietta et al. (1970, 1971) in cat omentum, Zweifach (1974), Zweifach and Lipowsky (1977) and Smaje et al. (1980). It has been postulated that pulsations are necessary to attain optimal organ function. Steady perfusion could impair organ function (Wilkins et al., 1967; Jacobs et al., 1969; Arzelius, 1976). Direct recording of pressure obtained by Zweifach (1974) suggests that in the terminal arteriole, the pulse pressure is still large, about 15 mmHg, with a mean pressure of about 60 mmHg. Intaglietta et al. (1970) provided pulsatile velocity data. Mean velocities in the microcirculation are in the centimeters per second range, as measured by electro-optical methods.

### 7.3.2 Pulse Transmission Characteristics in the Microcirculation

The steady flow concept assumed for the microcirculation is in accordance with the windkessel theory that peripheral vessels act as stiff tubes. This would protect the small vessels against sudden surges in flow and rapid changes in pressure.

With the advent of new technology, particularly the servo-controlled micropipette device for pressure measurement and electro-optical methods for velocity recording, studies of the pulse transmission in arterioles and capillaries became feasible. Although significantly damped, pressure and flow pulses generated by the heart persist into these vessels.

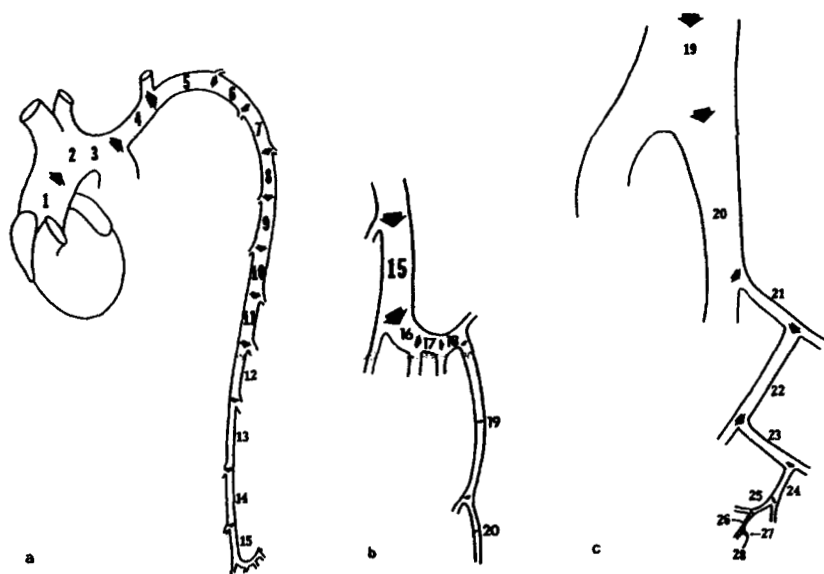


Fig. 7.3.1: Schematic illustration of the pulse transmission path from the ascending aorta to the index finger artery.

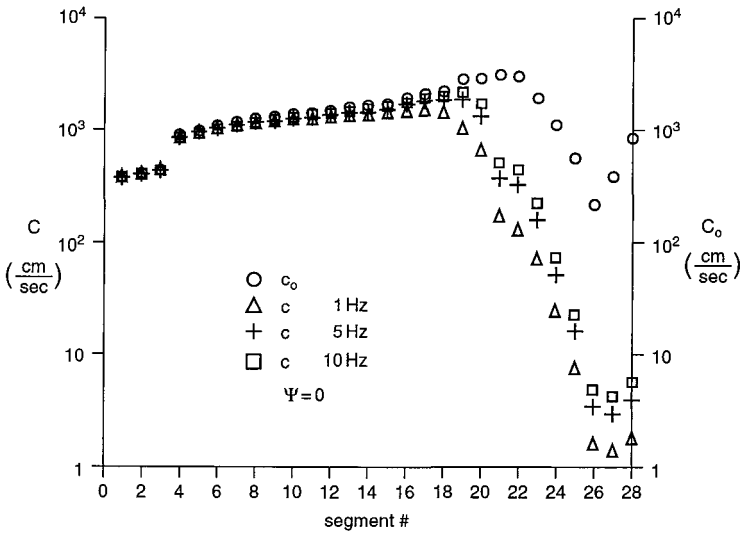


Fig. 7.3.2: Pulse wave velocity at different frequencies shown plotted as a function of transmission site from the ascending aorta to the index finger artery.

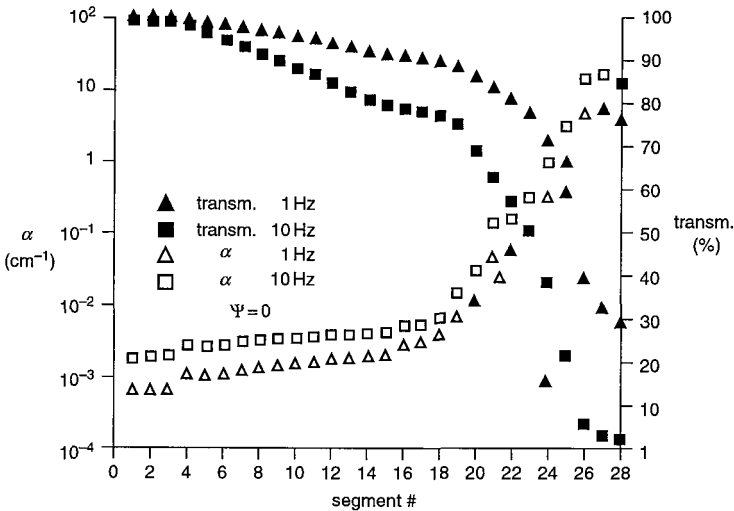


Fig. 7.3.3: Attenuation coefficient and percentage transmission at different frequencies shown plotted as a function of transmission site from the ascending aorta to the index finger artery.

Li et al. (1980) first provided analytical expressions to predict pulse wave velocity and attenuation in the microcirculation. Linearized pulse transmission theory was utilized. Subsequently, the same group computed the pulse transmission from the left ventricle to the human index finger vessel (Salotto et al., 1986 Fig. 7.3.1). Their computation was based on Westerhof's viscoelastic tube theory, with complex elastic modulus.

The results show wave velocity of a few centimeters per second and attenuation of about 30 percent at 1 Hz in large arterioles. With increasing frequencies, the attenuation become substantial and pulse transmission is greatly reduced at 10 Hz. These are shown in Fig. 7.3.2 and Fig. 7.3.3. This explains in parts why the observed pressure and flow waveforms, though pulsatile, are becoming more sinusoidal in the microcirculation.

A wave speed of 7.2 cm/s in the capillary with an exponential attenuation of 83%/cm was calculated by Caro et al. (1978). Estimated phase velocity from Intaglietta et al.'s (1971) data would give 7-10 cm/s, in general agreement. They also gave an analytical expression for the propagation speed in the case of a sinusoidal pulse propagating through an elastic vessel, assuming blood is Newtonian:

$$c = \frac{1}{4} d \sqrt{\frac{\omega}{\eta D}} \quad (7.3.4)$$

where  $d$  is capillary diameter and  $D$  is the distensibility. Since blood viscosity appears to decrease when measured in capillary tubes of decreasing diameter, blood, in fact, is non-Newtonian. This is known as the Fahraeus-Lindqvist effect.

### ***7.3.3 Modeling Aspects of the Microcirculation***

Modeling of any microvascular bed is a challenge, particularly when validation of predicted phenomena is necessary. A complete study requires not only the stringent measurement techniques, but also the understanding of the complexity of the underlying system properties.

Mayrovitz (1975, 1976) and Noordergraaf (1978) provided an analysis of a model of the microcirculatory dynamics. The bat wing was selected for the ease of accessibility and measurements of the microvascular bed parameters. A distributed model was developed based on the wing's vascular anatomy. The topology of this model is shown in Fig. 7.3.4 which includes a perfusing artery, arterioles and collecting venules and a vein, as well as capillaries, precapillary sphincter. Geometric dimensions of the branching structure are also shown in the table. Poiseuille formula was utilized for describing small vessel pressure-flow relationship. Pressure distribution along the vascular bed and its change due to diameter alteration of fourth order branching vessels are shown in Fig. 7.3.5 during control, simulated contraction and vasodilation. Experimental results provide a validation that the model predicted pressure distributions are reasonably accurate.

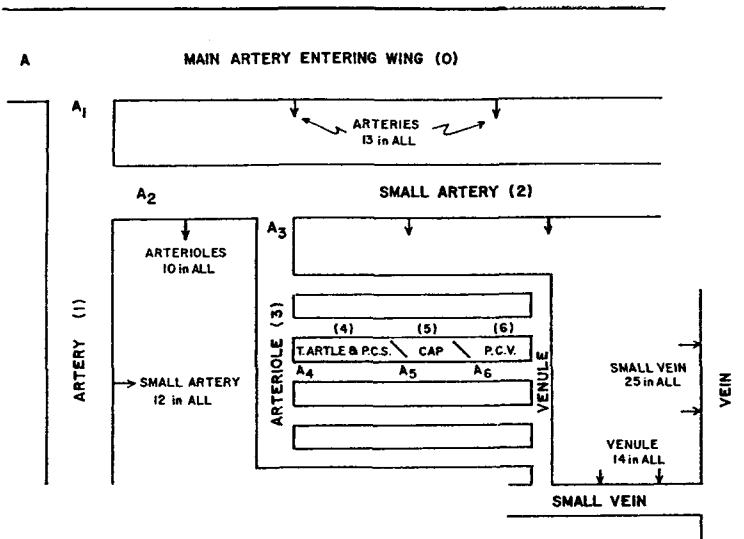


Fig. 7.3.4: Topological model of the microvascular bed of the bat wing. One pathway for a main artery to a vein is displayed. The branching order is numbered and the particular sites are denoted by A<sub>1</sub>-A<sub>6</sub>. Terminal arteriole (T. ARTLE), precapillary sphincter (P.C.S.), CAP (capillary) and post-capillary venule (P.C.V.) are also marked. Corresponding geometric dimensions are also shown in the table. From Mayrovitz (1976).

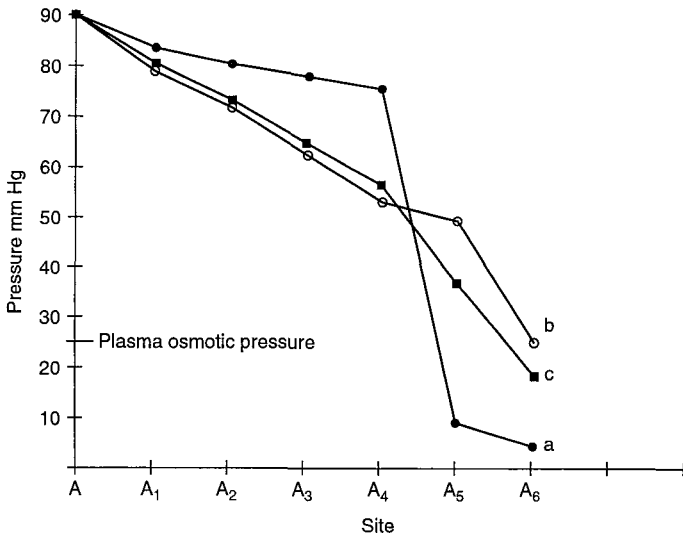
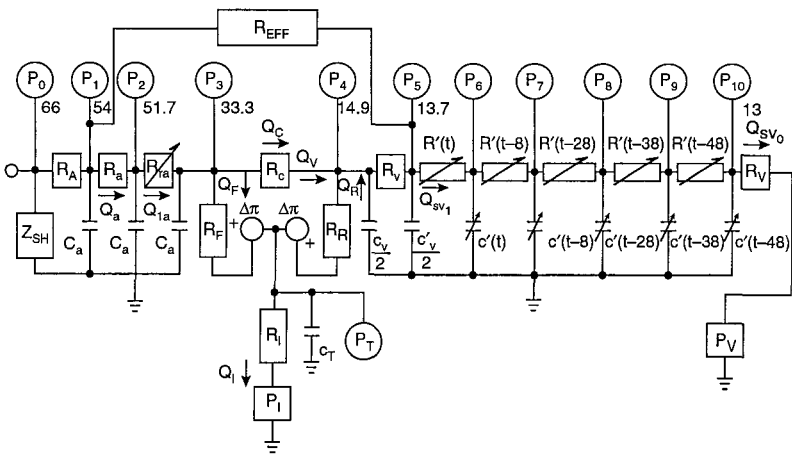


Fig. 7.3.5: (A) Pressure distribution along the vascular bed and its change due to diameter alteration of fourth order branching vessels during control (c), simulated contraction (a) and dilation (b). Corresponding experimental results are shown in (B).



DETAILED MICROVASCULAR MODEL

Fig. 7.3.6: A dynamic microcirculatory model. P=pressure, Q=flow, R=resistance, C=compliance,  $\Delta\pi$ =osmotic pressure difference across the capillary wall.

A dynamic model was later developed by the same group that included resistance and capacitance, as well as time-varying compliance properties. The model also provided description of vasomotion, capillary filtration and re-absorption processes. This is illustrated in Fig. 7.3.6.

## Chapter 8

# Hemodynamic Measurements and Dynamics of the Assisted Circulation

### 8.1 Pressure, Flow and Dimension Measurements

#### *8.1.1 Invasive Blood Pressure Measurements*

##### 8.1.1.1 The Needle-Pressure Transducer System

The combination of a fluid-filled catheter and a pressure transducer continues to be the most commonly used measurement system for in-vivo recording of pulsatile blood pressure waveforms. This blood pressure measurement system can be applied to cardiac chambers, major arteries and veins, as well as smaller (~1 mm) vessels of the circulation. This is because of the long, well-established and improved catheterization techniques in combination with angiographic imaging modalities in clinical catheterization laboratories. The catheter system has the added advantage of the ease of injecting radio-opaque dyes for visualization of the vasculature, as well as administering therapeutic drugs. Balloon catheter for angioplasty applications and micro-pore catheter for local intravascular drug delivery have also become popular. The more recent multi-lumen, multi-functional catheters include thermodilution, as well as the addition of electrodes for either atrial or ventricular pacing capabilities. These technological advances have promoted the popularity of interventional cardiology.

Forssmann and Cournand, who shared the 1956 Nobel prize in Medicine with Richards, are the original inventors who decades earlier first recorded blood pressure waveforms in peripheral arteries and cardiac chambers. The catheter has the flexibility and maneuverability

that allows accessibility to different parts of the circulation. There are instances, where a combination of a hyperdermic needle and a pressure transducer suffices, particularly when the blood vessel is superficial or under intra-operative conditions. Brachial, radial or femoral arteries are common superficial sites for pressure measurements with needle-transducer systems. Left ventricular chamber pressure measurement with direct apex insertion of a needle is also common under open chest conditions.

The performance of a needle-pressure transducer system can be evaluated through basic mechanical and electrical modeling. The simplest representation of the system is an undamped spring-mass system of natural frequency:

$$f_n = \frac{1}{2\pi} \sqrt{\frac{\pi r^2}{\rho l} \cdot \frac{dp}{dV}} \quad (8.1.1)$$

where  $r$  is the internal lumen radius of the needle,  $l$  is the length of the needle and  $\rho$  is the fluid density. Typically the needle and pressure transducer dome are filled with saline. This provides the required fluid coupling that is necessary when the needle is inserted into an artery which is filled with blood. Heparine is often added to prevent blood clotting in the catheter. Blood pressure pulsation is transmitted via fluid coupling resulting in the movement of the pressure transducer diaphragm (stainless steel). The greater the amount of fluid, the greater is the fluid movement or inertia. Thus, the inertia is represented by

$$L = \frac{\rho l}{\pi r^2} \quad (8.1.2)$$

The compliance of the pressure transducer is determined by the movement of the stainless steel diaphragm within the fluid-filled transducer dome. Compliance which is defined as volume displacement per unit distending pressure, is the inverse of stiffness:

$$C = \frac{dV}{dp} \quad (8.1.3)$$

$$\text{Compliance} = \frac{1}{dp/dV} = \frac{1}{\text{stiffness}} \quad (8.1.4)$$

Thus, a more compliant the pressure transducer means that volume displacement ( $dV$ ) of its diaphragm is greater when subjecting to the same amount of applied pressure ( $dp$ ). The consequence of this in the accuracy of blood pressure recording is explained below. The compliance of the needle (typically made of stainless steel with high Young's modulus of elasticity and therefore, very stiff) is negligible. Equation (8.1.1) can be re-written as:

$$f_n = \frac{1}{2\pi} \sqrt{\frac{1}{LC}} \quad (8.1.5)$$

When the needle is narrow, the Poiseuille resistance,  $R$ , becomes important in the determination of the frequency response. A second-order RLC system representation is necessary.

As we have seen in earlier chapters that blood pressure waveform is periodic and can be represented by a Fourier series as the sum of a mean pressure and a number of sine waves of fundamental frequency  $f$  (heart rate/sec) and harmonics,  $nf$  ( $n = 1, 2, \dots, N$ ):

$$p(t) = \bar{p} + \sum_{n=1}^N p_n \sin(n\omega t + \phi_n) \quad \omega = 2\pi f \quad (8.1.6)$$

which, when substituted into the second order differential equation describing the fluid motion, results in the amplitude ratio for the  $n$ th harmonic:

$$\frac{P_{mn}}{P_{on}} = \sqrt{\frac{1}{1 - (n\omega)^2 LC + (n\omega RC)^2}} \quad (8.1.7)$$

its corresponding phase angle:

$$\phi_n = \tan^{-1} \frac{n\omega RC}{1 - n\omega LC} \quad (8.1.8)$$

where  $P_{mn}$  = measured pressure for the  $n$ th harmonic and  $P_{on}$  = actual pressure of the  $n$ th harmonic component. For a distortion-free blood pressure measurement system, or one with a flat frequency response, it is necessary that the amplitude ratio  $P_{mn}/P_{on}=1.0$ , or there is no difference between the measured pressure and the actual pressure. Under this condition, the phase angle  $\phi_n = 0$ , i.e., there is no phase shift between the two.

For the pressure measurement system to record the arterial blood pressure waveform faithfully, it must have sufficient dynamic frequency response (Li et al., 1976). This often results in changing the needle size or length of the needle, especially when an additional pressure transducer of different compliance specification is unavailable.

### 8.1.1.2 The Catheter-Pressure Transducer Systems

For a catheter-pressure transducer system, frequently an underdamped system, compliance as well as geometric factors are important. Figure 8.1.1 provides a lumped approximation of the system. The above second-order representation can be applied to evaluate dynamic frequency response of the system.

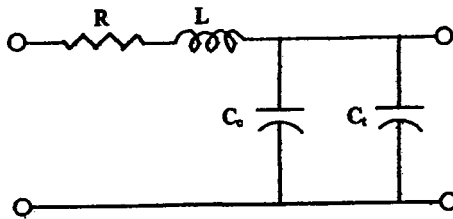


Fig. 8.1.1: Lumped model representation of the catheter-manometer system.  $R$ = Poiseuille resistance of the fluid in the catheter.  $C$  = compliance combination of the catheter and the manometer ( $C=C_c+C_t$ ;  $C_c$ =compliance of the catheter and  $C_t$ = compliance of the transducer).  $L$  = inertia of fluid.

Either a sinusoidal pressure generator or a step-response "pop-test" are common methods to evaluate dynamic frequency response of the catheter system.. Commonly, a step increase in pressure is applied against the catheter-transducer system and the balloon which is connected to the same chamber as the catheter is inflated. The balloon

is then rapidly “popped” (thus, pop-test) with a sharp needle. The pressure in the chamber thus falls to atmospheric pressure, completing the step decrease in pressure. If the catheter system had a perfect dynamic response, then its response would follow exactly the step decline in pressure. However, clinically and experimentally used catheter-transducer combinations are usually underdamped, resulting in oscillations in amplitudes.

The damped natural resonance frequency,  $f_d$  is obtained as the inverse of the period of oscillation:

$$f_d = \frac{1}{T} \quad (8.1.9)$$

where T is the period of oscillation. This can be obtained from the interval of the peak-to-peak or trough-to-trough oscillations. The exponential damping,  $\alpha_e$  is determined from the peak amplitudes  $A_1$  and  $A_2$ ,

$$\frac{A_1}{A_2} = e^{-\alpha_e t} \quad (8.1.10)$$

or in terms of amplitude ratio,  $A_p$ ,

$$A_p = \ln \frac{A_2}{A_1} \quad (8.1.11)$$

The relative damping factor,  $\alpha_d$ , is obtained from the following expression:

$$\alpha_d = \frac{A_p}{\sqrt{4\pi^2 + A_p^2}} \quad (8.1.12)$$

Most catheter-manometer systems exhibit underdamped responses, where the damping factors are typically of 0.1-0.3. The useful frequency range can be estimated by multiplying the resonant frequency by the damping factor. For instance, if the resonant frequency is 45 Hz and the damping factor is 0.2, then the “useful flat frequency range” is  $35 \times 0.2$  or 9 Hz. The flat frequency response refers to an amplitude ratio (equation

(8.1.7)) within  $\pm 5\%$  of unity, or 1. In other words, the measured pressure is within  $\pm 5\%$  of the actual pressure. Thus, higher resonant frequencies and greater damping factors (up to critical damping) offer better dynamic frequency response.

The step response or pop-test has its advantages of simplicity and rapid tracking of system response. This “pop test” or step response method is shown in Fig. 8.1.2. One can apply either a positive step (step increment in pressure) or a negative step (step decrement in pressure). An ideal blood pressure measurement system follows the step exactly, with no overshoot or undershoot, and no time delay. In practice, however, overshoot and oscillations are common. Fig. 8.1.2 also illustrates the underdamped response of a fluid-filled catheter-manometer system. The dynamic frequency response in terms of relative amplitude ratio vs. frequency for the step response of Fig. 8.1.2 is shown in Fig. 8.1.3. The single resonance peak occurs as the underdamped catheter-manometer system was approximated by the second order system.

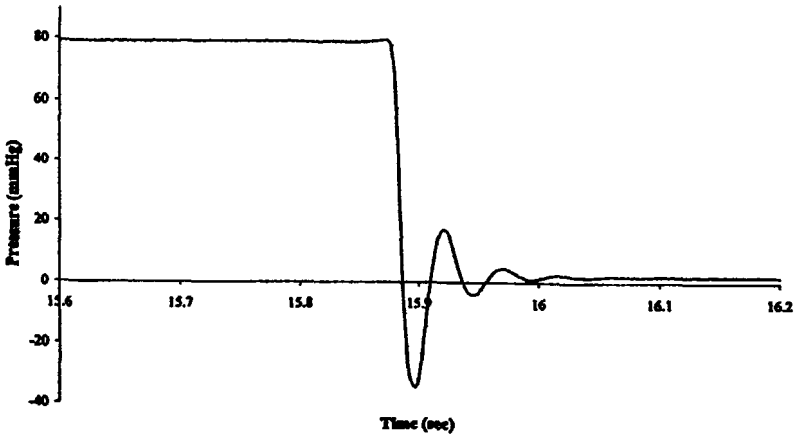


Fig. 8.1.2: The pop-test (step response) for the dynamic testing of transducer system performance,  $f = 1/T =$  resonant frequency. The catheter transducer system is seen to be an underdamped system.

In general, linearity, hysteresis, and dynamic system response are necessary considerations in fluid-filled blood pressure measurement systems. Linearity refers to the output response vs. input applied

pressure, obtained from static calibrations. This is not generally a problem, since most combinations have static calibrations that are linear to within  $\pm 1\%$  or better, over the range of 0-200 mmHg. Hysteresis refers to the differences in outputs with increasing and decreasing blood pressure within the blood pressure range of interest. This is also typically small. Thus, dynamic frequency response is of the major importance.

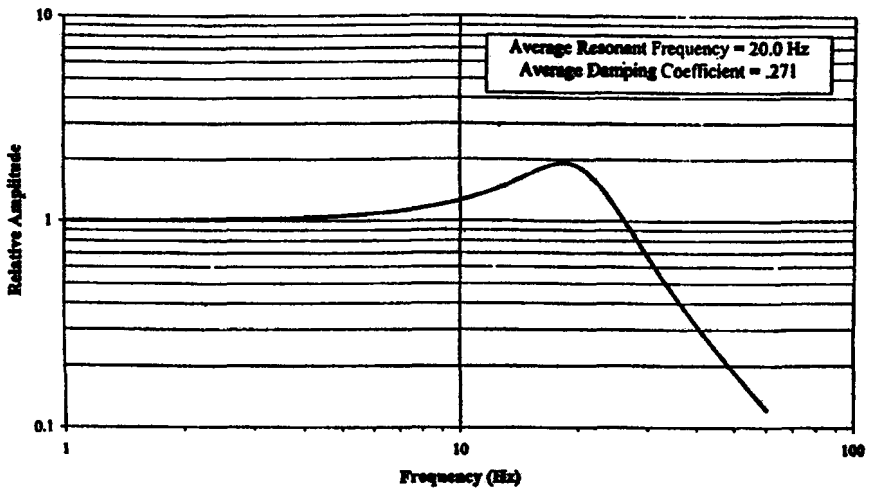


Fig. 8.1.3: Dynamic frequency response shown as the relative amplitude ratio vs. frequency. The resonance frequency in this example is 20 Hz.

Blood pressure waveforms that are closer to sinusoidal waveforms require less harmonic components to resynthesize the original waveform and thus place less stringent demand on the frequency response. For instance, the femoral artery can be recorded with a lower dynamic frequency response than either central aortic pressure or left ventricular pressure. This is because the femoral arterial pressure is generally smoother and with rounded dicrotic notch. Blood pressure waveforms that are closer to rectangular waveform require much higher frequency response to resynthesize the waveforms accurately. This is because rectangular and square waves contain an infinite number of sinusoidal or cosinusoidal components. Normal left ventricular pressure, for instance

contains much higher frequency components than the femoral arterial pressure. The first derivatives of pressure, such as LV  $dp/dt$ , also requires higher frequency response for accurate recording.

When the blood pressure waveform is recorded with a low resonant frequency and low damping ratio fluid-filled blood pressure measurement system, erroneous phase shifts and large oscillations can be observed. Fig. 8.1.4 illustrates this point with the aortic pressure waveform measured simultaneously by a high fidelity catheter-tip pressure transducer and a low fidelity fluid-filled catheter-pressure transducer system. The two waveforms are calibrated and superimposed. Overestimation of systolic pressure and underestimation of diastolic pressure can be observed. In addition, end-systolic pressure at aortic valve closure, systolic, diastolic and ejection periods cannot be accurately determined.

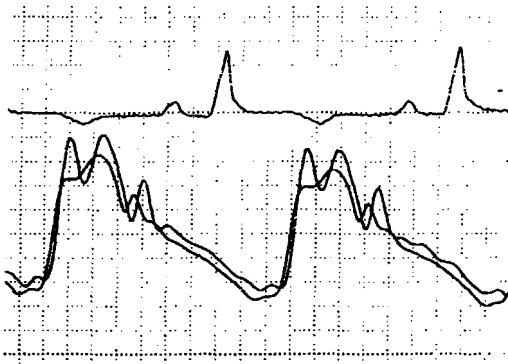


Fig. 8.1.4: Aortic blood pressure waveform measured with an underdamped catheter-manometer system and a high-fidelity catheter-tip pressure transducer. Overshoot and oscillations are clearly seen.

Li and Noordergraaf (1977) have analyzed responses of differential manometer systems. For these systems, the individual frequency response, as well as static and dynamic imbalances are important factors to be considered. Catheter-tip pressure transducers offer superior frequency response, sufficient even for cardiac sound recording. They, however, suffer from fragility, temperature-sensitivity, and the need to be calibrated against known manometric systems. The efficacy of

catheterization in the diagnostic setting has been discussed by Li and Kostis (1984).

### **8.1.2 Noninvasive Blood Pressure Measurements**

#### **8.1.2.1 Auscultatory Measurement of Blood Pressure**

The auscultatory Korotkoff sound method remains the most popular form of noninvasive blood pressure measurement in the clinical setting. This method however, lacks accuracy when compared to invasive catheter technique. Errors of 5-10 mmHg error is common. This technique, however, is simple to employ and has surprisingly high repeatability. It allows both systolic and diastolic pressures to be determined.

Figure 8.1.5 illustrates the modern auscultatory method. The cuff is inflated to a pressure exceeding the expected systolic arterial pressure ( $P_s$ ). During the inflation of the cuff with cuff pressure exceeding that of the systolic pressure, the segment of the artery under the cuff is forced to collapse, either partially or completely. The cuff is then allowed to deflate slowly at a few mmHg per second. This is accomplished through a needle valve which allows air to escape, hence dropping the cuff pressure. During deflation, the initial arterial lumen opening that is detected is the systolic pressure. The first vascular sounds that emerge is generally referred to as phase 1, define  $P_s$ . When either the vascular sounds become muffled (phase IV) or disappear completely (phase V), the diastolic pressure ( $P_d$ ) is obtained. This technique has an estimated accuracy of 5-10 mmHg. There remains debate as to whether phase IV or V is a better indicator of diastolic pressure. Figure 8.1.6 illustrates the Korotkoff vascular sounds recorded in a brachial artery. When vascular reactivity is altered with hand-grip, the spectral content is shifted, such that the Korotkoff sound intensity is increased, together with a higher observed blood pressure (Fig. 8.1.6; Matonick and Li, 1999).

The width and length of the cuff are important considerations in the application of the auscultatory method, typically a width to circumference ratio of 0.4 is used. There is an optimum width of the cuff, narrower than optimum cuffs tend to impose an arterial stress below that of cuff pressure and can result in an overestimation of blood pressure. A

wider cuff than optimum provide accurate recording only at the center of the cuff and can cause error in detection as stress declines away from the center, giving a lower estimation of pressure.

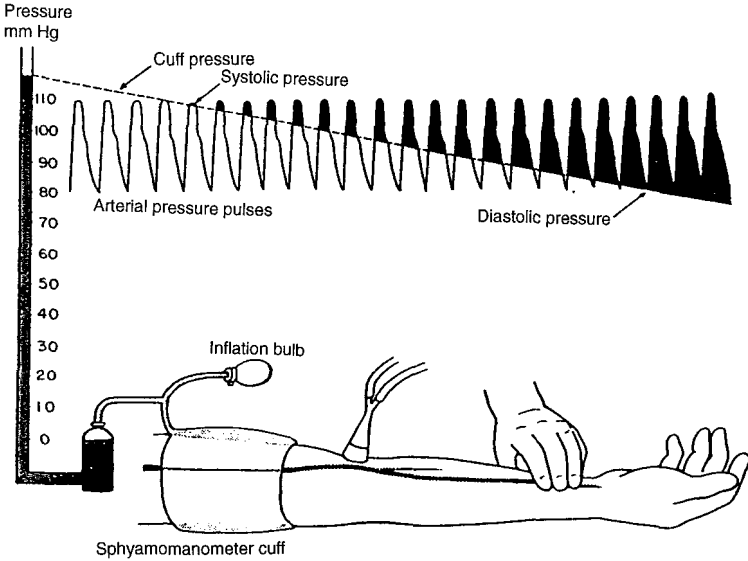


Fig. 8.1.5: Illustration of the auscultatory method for recording blood pressure. From Rushmer (1972).

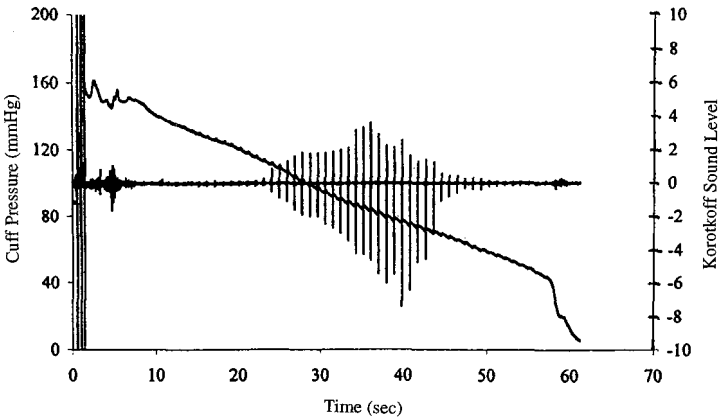


Fig. 8.1.6: Korotkoff vascular sounds recorded in a brachial artery.

Numerous theories have been proposed as to the generation of the Korotkoff sounds. Their origins have been a controversial subject of research. Some have suggested that they are pressure-related rather than flow-related (Drzewiecki et al., 1987).

### 8.1.2.2 Blood Pressure Measurement with the Oscillometric Method

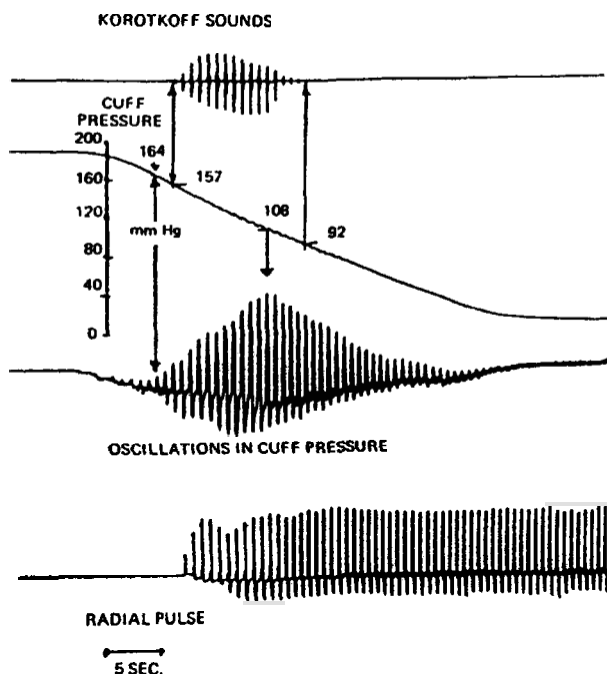


Fig. 8.1.7: Korotkoff sounds recorded concurrently with cuff pressure. Maximum oscillation in cuff pressure corresponds to mean blood pressure as shown. Radial arterial pulse distal to the brachial artery measurement site is also shown. From Geddes (1984).

Alternative to the use of the stethoscope is the oscillometric method. Marey in 1885 found that cuff pressure oscillated over a considerable range of mean cuff pressures. He suggested that the oscillation is maximal when the arterial wall is not stressed circumferentially. Removal of this circumferential stress, provides a basis for noninvasive

tonometry. This is "vascular unloading", as Marey termed it. The tension within the wall of the artery under such circumstance is zero when the transmural pressure is zero. The maximal oscillation was found to correspond to mean arterial pressure. The oscillometric method continued to gain popularity, although this technique is rather accurate for systolic and mean blood pressure detection, its accuracy is much less so for diastolic pressure measurement.

Geddes (1984) has provided a detailed analysis and comparison of the cuff technique and oscillometry. Fig. 8.1.7 shows the corresponding appearance and disappearance of the Korotkoff sounds and the oscillations in cuff pressure. Maximum oscillation in cuff pressure corresponds to mean blood pressure as shown. Thus, in addition to systolic and diastolic pressures, mean blood pressure can be obtained. The radial pulse distal to brachial artery measurement site is also shown.

### 8.1.2.3 Noninvasive Blood Pressure Monitoring with Tonometer

There are several methods for noninvasive recording of blood pressure waveforms, including the volume pulse method, the pressure pulse method, the cantilever and optical deflection methods.

In the volume pulse method (Fig. 8.1.8), the successful recording hinges on the relationship between intravascular pressure distension and radial displacement. The pressure pulse method (Fig. 8.1.8), such as the tonometer, is dependent on the interplays of contact stress, the deformation stress and arterial pressure. Arterial pressure is actually a fraction of the contact stress. Drzewiecki et al. (1983) have shown that in arterial tonometry, with arterial flattening, shear stress becomes negligible compared with the normal stress in the arterial wall and skin, and uniform contact stress is developed over the transducer-skin interface. This is the ideal state for pulse recording with tonometry. Arterial tonometry for measuring blood pressure is based on the principle that when a pressurized blood vessel is partially collapsed by an external object, the circumferential stresses in the vessel wall are removed and the internal and external pressures are equal. Since tonometers are basically force transducers, they are useful only when applied to superficial arteries with solid bone backing.

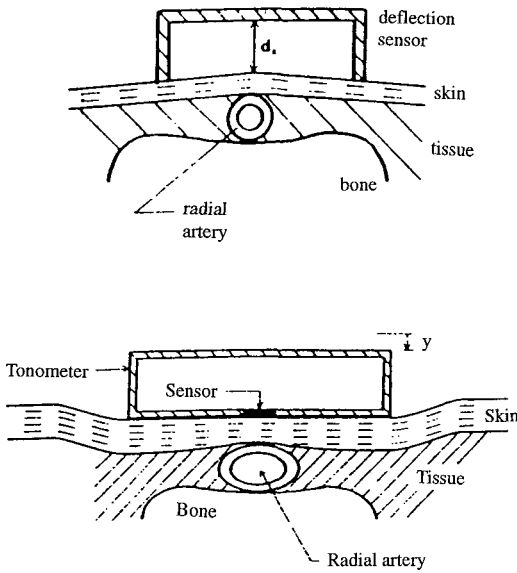


Fig. 8.1.8: Illustration of the volume pulse method (top) and the pressure pulse method (bottom). Notice the difference in the sensor placement.

### 8.1.3 Blood Flow Measurement

#### 8.1.3.1 Electromagnetic Flowmeter

In-vivo accurate measurement of blood flow lagged behind that of pressure for decades. The electromagnetic flowmeter is based on Faraday's law of induction:

$$e = v \times B - J / \sigma_c \quad (8.1.13)$$

where the induced electric field is  $E$ , in a conductor moving with a velocity  $v$  in a magnetic field intensity  $B$ .  $J$  is the current density and  $\sigma_c$  is the conductivity (of blood). Figure 8.1.9 illustrates the principle. Bevir's (1971) virtual current theory, however, presents a more practical analysis.

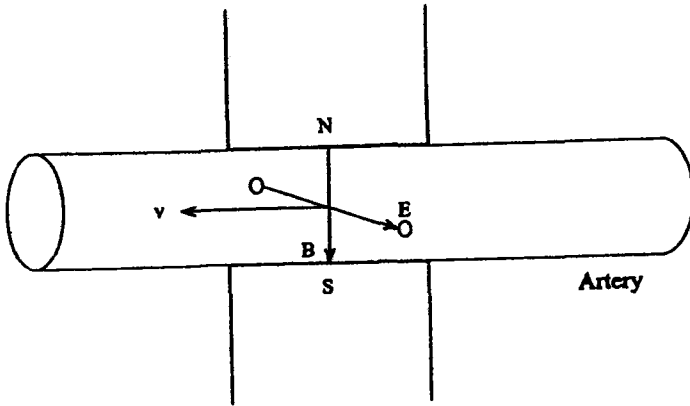


Fig. 8.1.9: Illustration of the electromagnetic blood flow measurement principles. The moving conductor (blood with velocity,  $v$ ) in a magnetic field ( $B$ ) induces an electric motive force and the potential ( $E$ ) is picked up by the electrodes.

Wyatt (1984) has recently reviewed blood flow and velocity measurement by electromagnetic induction. The cannular flowmeters with uniform field and point electrodes have the defect of a high degree of dependence on velocity distribution when they are not symmetric. The perivascular flowmeters have two defects: in addition to their sensitivity to velocity distribution, they are also sensitive to wall conductivity effects. The former can be reduced by using insulated- or multiple-electrodes, which improve the signal-to-noise ratio. Mills' (1966) catheter-tip flowmeter has the advantage that it is unaffected by the vessel wall. Boccalon et al. (1978) has devised a noninvasive electromagnetic flowmeter which provides useful clinical applications.

### 8.1.3.2 Ultrasound Doppler Velocimeters

Ultrasonic methods of measuring blood flow velocity are based on either the transmission or the reflection of ultrasound. Ultrasound propagation velocity through biological tissue is about 1560 m/s. Its associated wavelength can be easily calculated from

$$\lambda = \frac{c}{f} \quad (8.1.14)$$

Typical diagnostic ultrasound utilizes frequencies in the range of 1 MHz to 15 MHz. Thus, the corresponding wavelengths are 0.78 mm and 0.156 mm, respectively.

The transit-time ultrasound measurement of blood velocity utilizes two crystal transducers placed at two different locations, serving as transmitter and receiver. With known ultrasound velocity,  $c$ , and the transit time  $\Delta t = t_1 - t_2$ , we have:

$$\Delta t = \frac{2vD}{c^2 \cos \theta} \quad (8.1.15)$$

where  $D/\cos\theta$  is the distance between the transceiver and  $\theta$  is the angle between the axial blood velocity and the transceiver.

A more common approach is the ultrasound Doppler technique, based on the back scattering of ultrasound by red blood cells. Turbulence, therefore, increases the scattering. Two commonly used types are continuous wave Doppler (CWD) and pulsed wave Doppler (PWD). In the CW mode, the Doppler shifted frequency,  $f_d$ , of the back scattered ultrasound is:

$$f_d = \frac{2v \cos \theta}{c} \cdot f_0 \quad (8.1.16)$$

where  $v$  is the blood velocity,  $\theta$  is the angle between the ultrasound beam and the centerline, and  $f_0$  is the transmitted ultrasound frequency. In the PW mode, a velocity profile across the vessel can be obtained. Signal from cells scatters in a range at a depth of:

$$z = \frac{ct_d}{2} \quad (8.1.17)$$

By pulsing the ultrasound beam, one can obtain range resolution along the beam. Generally, a short burst of ultrasound is transmitted with a repetition frequency  $f$ . The backscattered signal is received and sampled after a time delay  $t_d$ .

Velocity profiles can also be obtained by the use of thermal-convection velocity sensors, such as hot-wire anemometers. Thermistors

have been popular thermal velocity probes mounting on either a catheter or a needle. These sensors have been applied to clinical settings (Roberts, 1972).

In general, Doppler measured blood flow velocity (Fig. 8.1.10; Yao and Pearce, 1991) compares well with that obtained by electromagnetic method.

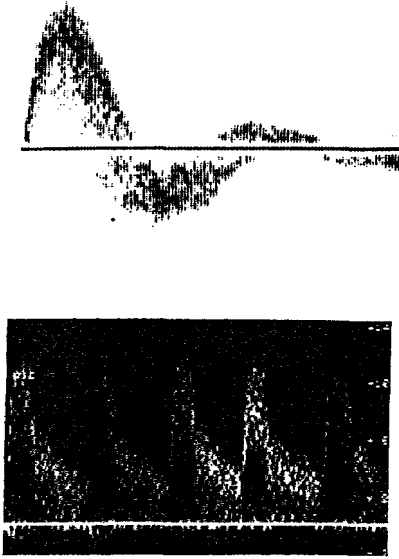


Fig. 8.1.10: Doppler ultrasound measured spectral blood flow velocity.

### 8.1.3.3 Indicator Dilution Methods and Thermodilution

Quantification of blood flow, even in the microcirculation by the introduction of indicators to the circulatory system has been exercised for quite some time. Dye dilution has been used for many decades. The indicator dilution method for measurement of blood flow is well illustrated in Fig. 8.1.11 (Geddes, 1984) in which an indicator of known mass is injected upstream. With the velocity of blood flow, the indicator is diluted and its concentration is detected and sampled downstream. The amount of flow,  $Q$ , is calculated from the following relation:

$$Q = \frac{m}{C_c \times t} \quad (8.1.18)$$

where  $m$  is the mass of the injectate,  $C_c$  is the concentration, and  $t$  is time.

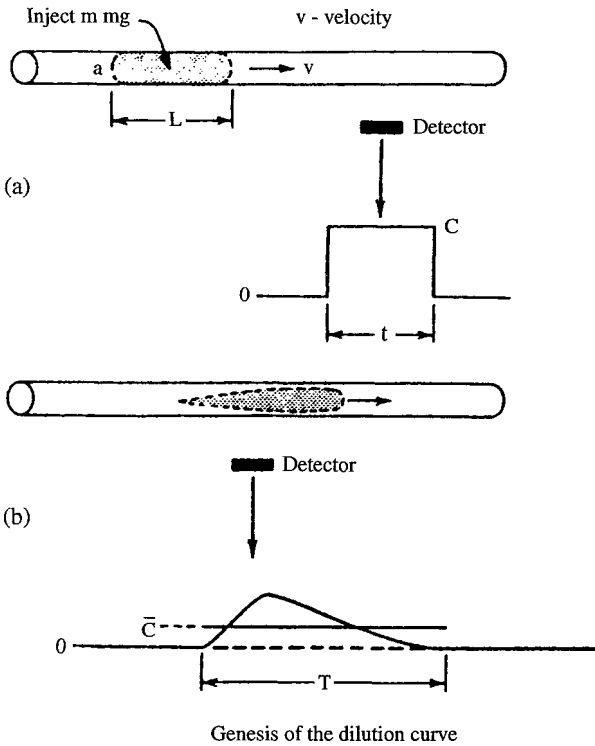


Fig. 8.1.11: Principle of the dye dilution technique and the genesis of the dye dilution curve of concentration vs. time. From Geddes (1984).

The Stewart-Hamilton principle states that if a known concentration of indicator is introduced into a flow stream and its temporal concentration is measured at a downstream site, then the volume flow can be calculated. The Stuart-Hamilton principle relates the flow ( $Q$ ) to the mass ( $m$ ) of indicator injected and the concentration ( $c(t)$ ) of the indicator measured downstream at time  $t$ :

$$Q = \frac{m}{\int_0^{\infty} c(t) dt} \tag{8.1.19}$$

Thus, if the area under the concentration vs. time curve is found, flow can be easily obtained. For measurement of blood flow in a single vessel, the above formulation works well. When applied to measuring cardiac output, however, the continuous pumping of the heart introduces the problem of recirculation. To overcome this, an exponential extrapolation of the concentration-time curve's descending limb is imposed such that an approximation of the integral with the area under the curve is achieved.

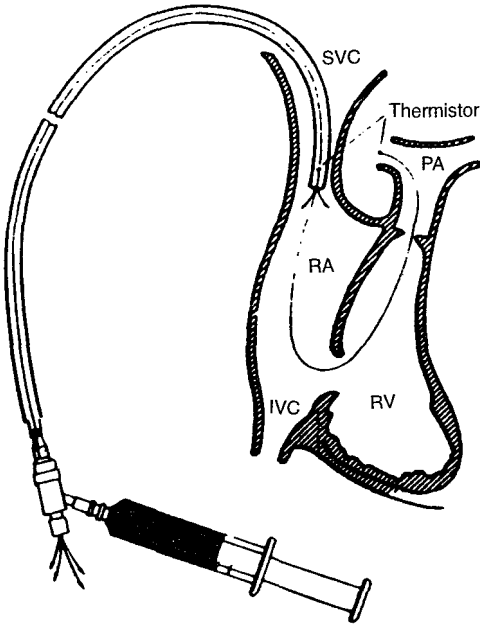


Fig. 8.1.12: Thermodilution method in man. The injection catheter is in the superior vena cava (SVC). The thermistor for measurement of indicator temperature is inside the injection catheter 1 to 2 cm from the tip. The thermistor for measurement of blood temperature is in a main branch of the pulmonary artery (PA). RA and RV are right atrium and right ventricle, respectively.

Indicators that have commonly been used include Evans blue dye, Indocyanine green and some radioactive isotopes, such as Albumin Iodide<sup>131</sup>. The advantage of the non-toxicity and affordability of repeated determinations within a short time span makes cold solutions

excellent choices as indicators. This was demonstrated by Fronck and Ganz (1960) in the measurement of flow in single vessels including cardiac output by local thermodilution. The advent of thermodilution has made cold saline and dextrose popular indicators.

In thermodilution, normal saline or isotonic dextrose (5%) in water is used as the injectate, either at 0°C or at room temperature. The most popular site of injection is the right atrium and the sampling site is the pulmonary artery. By this choice of the sites, the effect of recirculation is minimized. In this approach, a flow-directed balloon-tipped catheter can be introduced into a vein and upon inflation of the balloon, the catheter is guided with the flow into the right atrium, the right ventricle or the pulmonary artery. The thermodilution catheter typically has a thermistor near the tip of the catheter to monitor sampling site temperature. The faster the flow, the greater is the temperature increase.

Ganz et al. (1971) demonstrated this method (Fig. 8.1.12) by injecting a 10 ml of cold (0.5-5°C) isotonic dextrose solution into the superior vena cava of a patient with normal circulation. The injectate was delivered in 1-2 seconds. The area under the thermal curve was found by planimetry which is now substituted with an analog integrator or with a digital computer.

For the thermodilution technique (Li, 2000), the standard cardiac output (CO) determination in-vivo is normally calculated from the following formula:

$$CO = \frac{V_i(T_b - T_i)S_iC_i}{S_bC_b \int \Delta T_b(t) dt} 60 F_c \quad (8.1.20)$$

where

$V_i$  = volume of the injectate in ml

$T_b, T_i$  = temperature of the blood and injectate, respectively

$S_b, S_i$  = specific gravity of the blood and injectate, respectively

$C_b, C_i$  = specific heat of blood and injectate, respectively

The ratio of  $(S_iC_i)/(S_bC_b)$  is 1.08 when 5% dextrose in water is used as an indicator. This ratio is 1.10 when normal saline is used.

The indicator heat loss along the catheter between the site of injection and the delivery site is accounted for by a correction factor,  $F_c$ :

$$F_c = \frac{T_b - T_{id}}{T_b - T_i} \quad (8.1.21)$$

where  $T_{id}$  is the temperature of the injectate through the catheter at the delivery site.  $F_c$  has been reported to be between 0.8 and 0.9.

#### 8.1.4 Measurement of Vascular Dimensions

Measurements of geometric dimensions of blood vessels, such as length, diameter and wall thickness, are of considerable importance in quantifying dynamic behavior. Strain gages are popular for length measurements. Mercury-in-silastic rubber, constantan, silicon, and germanium transducers are examples. They are based either on dimensional change or resistivity change. Change in resistance ( $\Delta R$ ) is derived from:

$$R = \frac{\rho_r l}{A} \quad (8.1.22)$$

where  $A$  is the cross-sectional area and  $l$  is the length of the strain gage wire. The fractional change in resistance is given by:

$$\frac{\Delta R}{R} = (1 + 2\sigma) \frac{\Delta l}{l} + \frac{\Delta \rho_r}{\rho_r} \quad (8.1.23)$$

where  $\sigma$  is the Poisson ratio (ratio of radial strain to longitudinal strain). The first term on the right-hand side is due to dimensional effect, the second term to piezoresistive effect. Strain gage transducers can be applied to measure length as well as pressure. In both cases, the resultant change in resistance is detected by a Wheatstone bridge circuitry. Superior resolution with high gage factors can be obtained with semiconductors.

High-resolution dimension measurement can also be obtained with ultrasonic dimension gages. The disadvantage is more complex circuitry. The method requires a pair of piezoelectric transducers (1-15 MHz) either sutured or glued on to the opposite sides of a vessel for pulsatile diameter measurement or for wall thickness measurement. It is operated

in the PW mode at  $f = 1$  KHz. Figure 4.1.1 gave an example of dimensional measurement (cardiac muscle segment length) with the ultrasonic dimension gages. The small size of piezoelectric crystal ultrasonic dimension transducers allows their implantation for chronic and conscious animal studies. Dynamic measurements of large vessel diameter and wall thickness can be simultaneously recorded with ultrasound operating in M-mode. However, its limitation lies in boundary identification and resolution. Similar problem is encountered with angiographic recording. Magnetic resonance imaging affords high resolution, but the disadvantage of the inability to provide real time recording. Recent advance in intravascular ultrasound (IVUS) provides structural detail, as well as dimension measurements.

## **8.2 The Assisted Circulation and the Intra-Aortic Balloon Pump**

### ***8.2.1 Mechanical Assist Devices and the Assisted Circulation***

The heart is generally viewed as an energetic mechanical pump. As such, a means to assist its function under adverse conditions need to be mechanical in nature. With limited donors for heart transplants and the limited success with long term use of artificial hearts (although the most recent patient survived about 4 months), other avenues of cardiac assistance for a failing heart take center-stage. Mechanical assistance and replacements for damaged hearts have grown in application in recent years and is expected to grow in the near future. While many problems have developed during clinical studies of total artificial hearts, artificial heart assist devices appear to operate without such extensive difficulties. The versatility of such devices are in their varied designs to be either temporary or permanent, internal or external and can operate in a number of modes relative to the natural heart. The most common mode for implantable heart assist devices is to operate in parallel with the left ventricle with blood pumped from the left atrium to the ascending aorta. In this mode (parallel to the left ventricle) the assist device can take over varying percentages of the pumping work and blood flow. The most common mode of operation for temporary assist devices, for example, the intra aortic balloon pump (IABP), is in-series with the left ventricle. The IABP is surgically inserted into the descending aorta below the

aortic arch and is operated in a counterpulsation mode (Fig. 8.2.1). In this type of operation the balloon is inflated during diastole and deflated during systole. Timing of inflation and deflation is considered the most important determinant of efficacy.

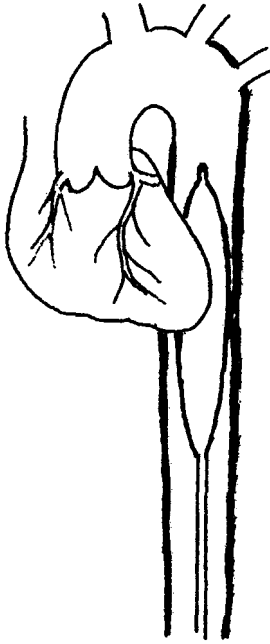


Fig. 8.2.1: illustration of the placement of intra-aortic balloon pump in the descending aorta. Inflation in diastole and deflation in systole constitutes the basis of counterpulsation in-series cardiac assistance.

Some of the bypass devices have been utilized as temporary assist devices and in-series devices have been utilized as permanent assist devices. In all of the applications, the control of the device timing relative to the natural heart is quite critical. While for temporary devices manual controls are, in many cases, acceptable, it is clear that for permanent implanted devices, automatic, and preferably implantable, controls are essential. Many of the attempts at automatic control of heart assist devices were studied in conjunction with IABP since the balloon pumps are widely used in the clinical setting.

Intra-aortic balloon pump and its control reflect an excellent example of the dynamic interaction of the heart and the vascular system. The heart pumps blood into the arterial system only during systole, while diastole occupies the remaining period. Many investigators recognized that the possibility of providing additional flow to vital organ vascular beds, including the coronaries, exists during diastole. This observation enables mechanical assistance designed to improve blood flow supplied by a failing ventricle through proper timing. The intra aortic balloon pump (IABP) was introduced to modify aortic pressure in a pulsatile manner, first in dogs and later in humans in the 1960's. An elongated balloon is inserted via the superficial femoral artery and advanced to the descending aorta. Deflation in systole and inflation in diastole produces in-series assistance. A variation is a device that directs blood from the failing ventricle to the aorta, thus producing parallel assistance. IABP has most widely been used in patients with either cardiogenic shock (Pierce et al., 1981; Waksman et al., 1993) after acute myocardial infarction (Muller, 1994; Ohman et al., 1994; Ishihara et al., 1994) or left ventricular failure after cardiac surgery. The beneficial aspects in terms of hemodynamics are the decreased systolic afterload, augmented diastolic aortic pressure, increased cardiac output, reduced left ventricular size, and improved myocardial metabolism.

Some of the direct and immediate beneficial effects of IABP have been the reduction of epicardial segment elevation and limitation of the spread of myocardial infarct, reduced S-T segment elevation and reduced infarcted zone area. In addition, mortality and morbidity associated with acute myocardial infarction might also be decreased by IABP. However, when IABP is initiated in a delayed fashion, i.e. six hours after the onset of symptoms of transmural myocardial infarction accompanied by acute heart failure, IABP does not seem to alter myocardial infarct size, nor to alter morbidity or mortality in patients. Thus, the hemodynamic and cardiac electrophysiological beneficial effects and success rate of mechanical assistance are higher, the earlier the application of such devices.

Li et al. (1984) and others have examined the hemodynamic effects of IABP in terms of ultrasonic dimension gauges recorded cardiac muscle shortening. These miniature piezoelectric crystals were implanted

typically in the subendocardium of the left ventricle in the normal, border, and ischemic zones. Pumping was initiated at various times after the onset of coronary artery occlusion. Contraction, assessed by segmental muscle shortening was significantly improved in the border zone, but unchanged either in the central ischemic zone, or in the normal zone. This was attributed to the border zone regional increase in myocardial blood flow and in the availability of oxygen due to augmented diastolic perfusion pressure.

There are disputes as to which appropriate hemodynamic variables are suitable as controls to optimize the efficacy of cardiac assist devices (CADs) either in-series or in-parallel. Two such variables utilized are the aortic pressure and the cardiac output. Their use as input control signals has been found to be inadequate from both experimental and model studies.

Apart from IABP, left ventricular assist devices (LVADs) exist in several types. They may be either pulsatile or non-pulsatile, synchronous or non-synchronous to the pumping of the natural heart. These may be the sac type, the diaphragm type, the pusher-plate type, the roller pump, or the centrifugal pump type.

The LVADs are used in patients with either reversible or nonreversible cardiac failure and can be used for temporary or permanent assistance. These types of cardiac assist devices are sometimes referred to as parallel assist devices or bypass devices because they direct blood from either the left atrium or the left ventricle to the aorta, hence acting in parallel with the natural heart pump. As with all cardiac assist devices, the primary aim of the LVAD is to provide adequate perfusion to vital organ vascular beds. Of secondary concern is to unload the heart, or to reduce afterload and hence myocardial oxygen consumption.

Blood pressure is often higher when the LVAD is on rather than off. This tends to increase the load on the left ventricle, which is already in failure with reduced external work capability. The counterpulsation mode allows the reduction of afterload however, if properly synchronized. Synchronous actuation, with left ventricular apical cannulation, provides the greatest amount of ventricular unloading. Nevertheless, synchronization does not appear to be a priority of many of

the designs of cardiac assist devices, whose primary use are to maintain adequate cardiac output.

### ***8.2.2 Optimization of Intra-Aortic Balloon Pumping: Physiological Considerations***

The major hemodynamic aims and consequently the benefits of IABP are the increase in coronary perfusion and the reduction of ventricular afterload, hence an increase in cardiac efficiency. The extent of these benefits is dependent upon a number of physical and physiological parameters. These include the position of the balloon in the aorta, the volume displacement and its geometric size relative to the aorta, the driving gas, the rates and timing of balloon inflation and deflation, the heart rate, the viscoelastic properties of the aorta, neural-humoral influences, and the severity of the heart failure. Theoretically speaking, the optimal position for the intra aortic balloon should be as close to the aortic valve as possible, in order to generate the augmentation of mean arterial diastolic pressure ( $P_d$ ) to enhance coronary perfusion. But this positioning obstructs flow to the aortic arch vessels. Thus, the ideal position chosen is normally along the descending thoracic aorta just distal to the arch. Balloon volume determines the absolute magnitude of changes in hemodynamic parameters. Experimental studies indicate that diastolic pressure augmentation through volume displacement also enables one to effectively lower peak ventricular pressure and myocardial oxygen consumption due to the rapid balloon collapse prior to the following ventricular systole.

The effects of balloon geometry indicate that the greatest augmentation of diastolic aortic pressure occurs at complete occlusion. This condition however is not desirable, from the point of view of afterload reduction, although there have been cases where occlusion up to 95 percent have been shown to give good hemodynamic results. Balloon configuration and its properties are also important. Nonuniform inflation characteristics can cause preferential inflation at the terminal segments of the balloon and this results in ineffective volume displacement and pressure augmentation. Multiple segment chamber balloons have been designed to eliminate this by causing inflation to proceed from the distal end to the proximal end (closer to the heart).

This increases mean diastolic pressure in the region of the coronary arteries and augments coronary perfusion.

The rates of rise and fall of balloon inflation and deflation have been shown both theoretically and experimentally to be crucial determinants of IABP performance (Li et al., 1984). They result from the density and viscosity of the driving gas, and the pressure of the gas source. The three primary driving gases commonly that have been used are helium (He), nitrogen (N<sub>2</sub>), and carbon dioxide (CO<sub>2</sub>). The effects on global and regional ventricular function have also been investigated. The use of nitrogen has been commonplace until its replacement by helium. Carbon dioxide was used because of its greater solubility and reduced risk of gas embolism in the event of leakage. Helium use leads to faster rise and fall times. The timing of IABP relative to the diastolic phase of the cardiac cycle is also very important. Experiments performed on dogs verified theoretical predictions on these timing effects (Li et al., 1984; Zelano et al., 1985). It appears that the optimal inflation time is a time period just prior to the aortic valve closure or the dicrotic notch on the pressure tracing. A short delay is necessary to take into account the balloon rise time and the finite propagation time of the pressure pulse in the aorta. Enhancement of cardiac output and mean diastolic pressure at greatly reduced systolic loading and tension time index values can be achieved. Regional contractile properties in the normal and ischemic border zones are also improved (Fig. 8.2.2). Early inflation will decrease cardiac output and increase myocardial oxygen consumption through an increase in tension-time index. Late inflation will result in a lowering of mean diastolic pressure and a decrease in cardiac output.

Since mean diastolic pressure is proportional to coronary blood flow, coronary perfusion can be seriously compromised by improper timing of balloon inflation. The time of deflation may vary depending upon the desired hemodynamic effects. To minimize end diastolic aortic pressure, it is necessary to deflate the balloon prior to ventricular ejection taking into account the fall time of the gas in the balloon. Ideally, deflation should be timed such that the minimum of the diastolic pressure coincides with the onset of ventricular ejection. This will also minimize ventricular afterload.

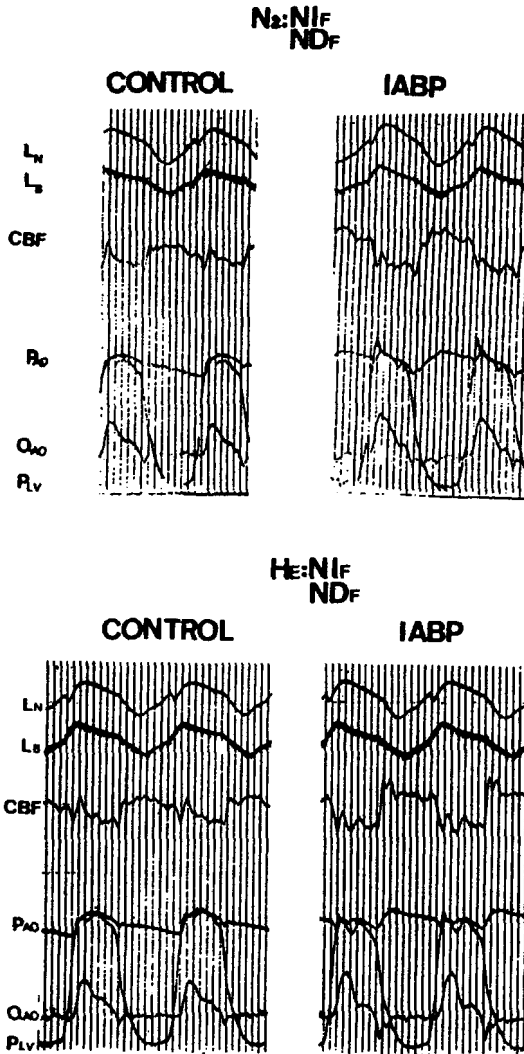


Fig. 8.2.2: Intra-aortic balloon pumping (IABP) efficacy on segmental cardiac muscle shortening, coronary blood flow (CBF) and aortic flow. Top: normal inflation ( $NI_F$ ) and normal deflation ( $ND_F$ ) of the balloon when nitrogen ( $N_2$ ) is used as the driving gas. Bottom: same, except helium ( $He$ ) is used as the driving gas. It is clear that in both cases, IABP greatly improved coronary blood flow, muscle shortening and aortic flow through proper timing of diastolic aortic pressure augmentation.  $L_N$  and  $L_B$  are segment lengths.  $P_{aO}$ =aortic pressure,  $Q_{aO}$ =aortic flow,  $P_{LV}$ =left ventricular pressure.

Both theoretical and experimental studies have shown that late deflation can increase coronary blood flow and stroke volume substantially. This is particularly beneficial to a failing heart with low cardiac output. But late deflation will also increase the load on the heart during ejection, hence increasing myocardial oxygen consumption. An appropriate compromise would be to produce the maximum increase in mean diastolic pressure and coronary perfusion from systolic augmentation (late deflation) and at the same time keep afterload low. Deflation bordering on isovolumetric systole seems to be the best choice. This choice tends to maximize the oxygen supply to demand ratio as well as cardiac efficiency, which is defined as the ratio of external work (stroke volume  $\times$  mean arterial pressure) to myocardial oxygen consumption. It is clear that the duration of the inflation-deflation interval is critical to the ability of an IABP to maximize coronary perfusion and to reduce the work requirements of the failing left ventricle. While timing and inflation-deflation rates are important determinants of IABP performance, other hemodynamic factors can also exert their influences. These include the pressure-diameter relationship of the aorta, peripheral resistance, heart rate, the severity of heart failure and neural-humoral interactions. For instance, a pressure increase will signal the baroreceptor reflexes to alter heart rate. The combined effects of increased balloon occlusion and heart rate at lower pressure enhance augmentation of mean diastolic pressure. The IABP cannot physically pump blood like a cardiac bypass device, and must rely on the heart to perform the necessary work. Thus the severity of heart failure is also a critical determinant of the beneficial effects of IABP.

### ***8.2.3: Optimization of Intra-Aortic Balloon Pumping: Modeling Aspects***

Modeling studies are useful in providing detailed parameter analyses and to obtain specific predictions which yield quantitative information regarding the interaction of IABP with the cardiovascular system. Some investigators have employed a windkessel model of the vascular system, with a flow source model of the left ventricle, to explain observed changes in left ventricular pressure and aortic flow during IABP using

derived mathematical relationships. Others have calculated the relative ventricular work and aortic input impedance as a function of device phasing for the fundamental frequency components and showed that these parameters were minimized when the fundamental components of aortic pressure and flow had a phase difference of  $180^\circ$  (Jaron et al., 1983). Changes in the timing were shown to increase impedance and ventricular work which could limit cardiac output and overload an already weakened heart.

Several investigators have studied the ability of IABP to augment hemodynamic performance dependence on cardiac state. No single combination of device timing variables can simultaneously achieve the best improvement for all hemodynamic parameters considered. Nerz et al. (1979) and Cui et al. (1990) using a time-varying compliance model of the left ventricle and an arterial system model, studied timing, pumping rate, balloon placement in the aorta, and device stroke volume. They indicated that increasing device pumping rate or rise and fall time of the pumping pulse caused a greater increase in coronary blood flow and cardiac output with a greater decrease in aortic end diastolic pressure. Additional increases in coronary and aortic flows could be obtained when termination of the device pulse occurred past end diastole. The overall improvement in hemodynamic parameters was greater for larger balloon volumes. Balloon inflation at the beginning of end systole was most effective in enhancing hemodynamic parameters. Others have shown that additional increases in coronary and aortic flows can be obtained at the expense of systolic loading with balloon deflation later than end diastole. Some of these model predictions have been verified in experimental animal studies by Li et al. (1984). Model studies generally can adequately predict short-term effects of IABP on the cardiovascular system (Dai and Li, 1995). But the long-term effects on the cardiovascular system will have to include physiological control aspects.

#### ***8.2.4: Optimization of Intra-Aortic Balloon Pumping: Control Aspects***

A real-time closed loop control scheme for IABP is necessary because of the heart rate changes and the changes in the physiological state of the cardiovascular system. Dynamic timing adjustments are therefore

essential. Dynamic control of the assisted circulation can be performed by, for instance, the utilization of state variable analysis and a conjugate gradient optimization method. The chosen state variables can be the fundamental components and phases of aortic pressure and flow with a constraint for pressure and flow to return to normal. It is obvious that the constraint necessity is for the fundamental components of aortic pressure and flow to be 180 degrees out of phase. This allows maximal coronary perfusion due to aortic diastolic pressure augmentation. A performance index of normalized left ventricular power can then be used to assess the efficacy of counterpulsation.

IABP efficacy is dependent on selected performance indices that are implemented based on the control algorithms. These also need to operate in real-time for practical purposes. These indices should be evaluated on a beat to beat basis and attempts made to either minimize or maximize each index by adjusting balloon timing. Clark et al. (1973) developed a closed-loop control scheme to maximize a weighted performance index comprised of mean systolic pressure, mean diastolic pressure, and end diastolic pressure to optimize IABP performance. The algorithm was implemented on both mini- and microcomputers. Timing was controlled using a regression equation to predict the systolic time interval (STI) from the measured heart rate. The algorithm gave reasonable results. Other schemes and computer-based controller have also been applied, based on weighted indices, such as coronary blood flow, tension time index, end diastolic pressure, left ventricular stroke work, and cardiac output, as well as left ventricular viability ratio and endocardial viability ratio, to assess pumping efficacy.

Earlier, we developed a closed loop model of the cardiovascular system in order to evaluate the most suitable control variables for mechanical assistance (Puri et al., 1982). The model assumes that the heart operates on the Frank-Starling mechanism and includes the carotid sinus baroreceptor control. Their results showed that heart rate and left atrial pressure (LAP) were the most sensitive parameters for the control of assistance, and that the extent of assistance is dependent on the severity of heart failure. The choice of the performance index, as well as the weighting factors, is critical in determining IABP efficacy. There is no totally automated system that presently exists clinically for closed-

loop control of cardiac assistance. To arrive at this goal it was shown that model studies are important, because they predict either the open-loop or closed-loop quantitative behavior of hemodynamic parameters.

A microprocessor-based controller to implement real-time automation of pump time using an IABP was developed by Zelano et al. (1985, 1990). The system sensed atrial P-waves, R-waves, and second heart sounds, and operated in an open loop mode. The results of experiments on dogs with this device indicate that automatic control of IABP in an open loop mode yields equivalent increases in cardiac output, coronary blood flow, with reduced resistance, and decreases in end diastolic pressure and ventricular oxygen consumption when compared to normal control adjustment by a certified balloon pump technician. A closed-loop control algorithm however would be more desirable.

Improvement in the dynamics of the assisted circulation can be valuable once the design of assist devices is refined and the control strategies are better defined. To this end, the understanding of the dynamics of the natural vascular system is a necessary step to the appreciation of the overall function of the circulation.

# BIBLIOGRAPHY

- Altman P.L. and D.S. Dittmer. *Biology Data Book*. FASEB, Bethesda, 1961.
- Anliker M., Histan, M.B., and Ogden, E. Dispersion and attenuation of small artificial pressure waves in the canine aorta. *Circ. Res.* 23: 539-551, 1968.
- Anliker M., M.K. Wells, and E. Ogden. The transmission characteristics of large and small pressure waves in the abdominal vena cava. *IEEE Trans. Biomed. Eng.* BME-16:262-273, 1969.
- Arntzenius A.C. The Importance of Pulsations. *Proc. Cardiovasc. System Dynam. Soc Conf.*, Philadelphia, 1976.
- Attinger E.O. *Pulsatile Blood Flow*. McGraw-Hill, New York, 1964.
- Bailie J.A. On the dispersion of waves in fluid-filled cylinders of slightly elliptical cross-section. *J. Biomech.* 5:165, 1972.
- Benchimol A. *Noninvasive Diagnostic Techniques in Cardiology*. Williams & Wilkins, Baltimore, 1981
- Berger D., J. K-J. Li, W. K. Laskey and A. Noordergraaf. Repeated reflection of waves in the systemic arterial system. *Am. J. Physiol. (Heart & Circ. Physiol.* 33) 264:H269-281, 1993.
- Berger DS, Li J K-J: Temporal relationship between left ventricular and arterial system elastances. *IEEE Trans Biomed Eng* BME-39: 404-410, 1992.
- Bevir M. Sensitivity of electromagnetic velocity probes. *Phys. Med. Biol.* 16: 229-232, 1971.
- Boccalon H., Candelon, B., Puel, P., Enjalbert, A., and Doll, H. Assessment of pulsatile blood flow by a noninvasive electromagnetic device. In *Noninvasive Cardiovascular Diagnosis*, ed. E.B. Dietlrich, pp. 231-240. Univ. Park Press, Baltimore, 1978.
- Brower R.W. and A. Noordergraaf. Pressure-flow characteristics of collapsible tubes; a reconciliation of seemingly contradictory results. *Ann. Biomed. Eng.* 1:333, 1973.
- Brower R.W. and C. Scholten Experimental evidence on the mechanism for the instability of flow in collapsible vessels. *Med. Biol. Eng.* 13:839, 1975.
- Brutsaert D.L. *The force-velocity-time interrelation of cardiac muscle*. In: *The Physical Basis of Starling's Law of the Heart*, pp. 155-175. Eds. R. Porter and D.W. Fitzsimons, Elsevier, Amsterdam, 1974.

- Caro C.G., Pedley, T.J., Schroter, R.C., and Secd, W.A. *The Mechanics of the Circulation*. Oxford Univ. Press, Oxford, 1978.
- Chaveau A. and Marey, E. Appareils et experiences cardiographiques. Demonstration nouvelle de mechanisms des mouvements du coeur par l'emploi des instruments enregistreurs a indications continues. *Mem. Acad. Med.* 26: 268, 1863.
- Clark J.W., G. R. Kane, and H. M. Bourland. On the feasibility of closed loop control of intra aortic balloon pumping. *IEEE Trans. Biomed. Eng.*, BME-20:404, 1973.
- Cox R.H. and Pace, J.B. Pressure-flow relations in the vessels of the canine aortic arch. *Am. J. Physiol.* 228: 1-10, 1975.
- Cox R.H. Pressure dependence of the mechanical properties of arteries in vivo. *Am. J. Physiol.* 229:1371-1375, 1975.
- Cui T., W. Welkowitz, J. K-J. Li, S. Petrucelli and A. Spotnitz. A novel mechanical cardiac assist device for reversing left ventricular failure. *Trans. Am. Soc. Artif. Internal Organs*, 36:401-404, 1990.
- Dai J.-W., and J. K-J. Li. Aortic impedance alteration on the response of single segment intra-aortic balloon pumping: a model-based analysis. *Annals Biomed. Eng.*, 23:S40, 1995.
- Drzewiecki G., S. Field, I. Mubarak, and J.K-J. Li. Effect of Vascular Growth Pattern on Lumen Area and Compliance Using a Novel Pressure-Area Model for Collapsible Vessels. *Am. J. Physiol. (Heart & Circ. Physiol.)*, 273:H2030-2043, 1997.
- Drzewiecki G.M., J. Melbin and A. Noordergraaf. Noninvasive blood pressure recording and the genesis of Korotkoff sound. Ch.8, *Handbook of Bioengineering*, Eds.: R. Skalak and S. Chien. New York: McGraw-Hill, 1987.
- Drzewiecki G.M., Melbin, J., and Noordergraaf, A. Arterial tonometry: review and analysis. *J. Biomech.* 16: 141-152, 1983.
- Fawcett D.W. *A Textbook of Histology*. Chapman & Hill, New York, 1994.
- Frank O. Die Grundform des arteriellen pulses. *Z. Biol.* vol. 37:483-526, 1899.
- Fronck A. and V. Ganz. Measurement of flow in single vessels including cardiac output by local thermodilution. *Circ. Res.* 8:175, 1960.
- Fung Y.C. *Biomechanics: Circulation*. Springer-Verlag, New York, 1997.
- Galilei G. *Dialogues Concerning Two New Sciences*. 1637. Translated version (H. Crew and A. DeSalvio): Macmillan, New York, 1914.
- Ganz W. R. Donoso, H.S. Marcus, J.S. Forrester, H.J.C. Swan. A new technique for measurement of cardiac output by thermodilution. *Am. J. Cardiol.* 27:392-396, 1971.
- Geddes L.A. *Cardiovascular Devices and Their Applications*. Wiley, New York, 1984.
- Goto M., M. Yanaka, W. Yosifumi, O. Hiramatsu, Y. Ogasawara, K. Tsujioka and F. Kajiya. Analysis of phasic blood flow velocity in atrial coronary arteries and veins by laser Doppler method. *Proc. 9<sup>th</sup> Cardiovasc System Dynam Conf.*, pp.125-128, 1988.

- Green H.D. Circulatory system: physical principles. In: *Medical Physics 2*, ed. O. Glasser, Year Book Publishers, New York, 1950.
- Hagenbach E. Uber die Bestimmung der Sahigkeit einer Flussigkeit durch den Ausfluss aus Rohren. *Ann. Der Physik* 109:385-426, 1860.
- Hales S. *Statcal Essays Containing Haemostaticks*. London, 1733.
- Harvey W. *De Motu Cordis*. London, 1628.
- Holt J.P. Flow through collapsible tubes and through in situ veins. *IEEE Trans. Biomed. Eng.* BME-16: 274-283, 1969.
- Intaglietta M., Parvula, R.F., and Thompkins, W.R. Pressure measurements in the Mammalian microvasculature. *Microvasc. Res.* 2: 212-220, 1970.
- Intaglietta M., Richardson, D.R., and Thompkins, W.R. Blood pressure, flow, and elastic properties in microvessels of cat omentum. *Am. J. Physiol.* 221: 922-928, 1971.
- Ishihara M, Sato H, Tateishi H, Uchida T, Dote K. Intraaortic balloon pumping as the postangioplasty strategy in acute myocardial infarction. *Am. Heart J.* 122:385-389, 1991.
- Jacobs L.A., Klopp, E.H., Seamore, W., Topaz, S.R., and Gott, V.L. Improved organ functions during cardiac bypass with a roller pump modified to deliver pulsatile flow. *J. Thorac. Cardio. Surg.* 58: 703-712, 1969.
- Jager G.N., Westerhof, N., and Noordergraaf, A. Oscillatory flow impedance in electrical analog of arterial system. *Circ. Res.* 16: 121-133, 1965.
- Jaron D., T. Moore, and P. He. Theoretical considerations regarding the optimization of cardiac assistance by intraaortic balloon pumping. *IEEE Trans. Biomed. Eng.*, BME-30:117, 1983.
- Kalmanson D. and C. Veyrat. Clinical aspects of venous return: a velocimetric approach to a new system dynamic concept. In: *Cardiovascular System Dynamics*, eds. J. Baan, A. Noordergraaf, J. Raines, pp. 297, MIT Press, 1978.
- Kelly R.P., Tang C-T., T-M. Yang, C-P. Liu, W.L. Maughan, M-S. Chang and D. Kass. Effective arterial elastance as index of arterial vascular load in humans. *Circ.* 86:513-521, 1992.
- Knowlton F.P. and E.H. Starling. The influence of variations in temperature and blood pressure on the performance of the isolated mammalian heart. *J. Physiol.* 44: 206-219, 1912.
- Korteweg D.J. Uber die Fortpflanzungsgeschwindigkeit des Schalles in elastischen Rohren. *Ann. Phys. Chem.* 5: 525-537, 1878.
- Kresch E. and A. Noordergraaf. A mathematical model for the pressure-flow relationships in a segment of veins. *IEEE Trans. Biomed. Eng.* 16:296, 1969.
- Kresch E. and A. Noordergraaf. Cross-sectional shape of collapsible tubes. *Biophys. J.* 12:274, 1972.
- Lamb H. On the velocity of sound in a tube as affected by the elasticity of the walls. *Manchester Mem.* 42: 1-16, 1898.
- Lberall A.S. Anatomy and steady flow characteristics of the arterial system with an introduction to its pulsatile characteristics. *Math. Biosci.* 1: 375-395, 1967.

- Lee J.S. and T.C. Skalak. *Microvascular Mechanics*. Springer-Verlag, New York, 1989.
- Lee J.S. and G.W. Schmid-Schonbein. Biomechanics of skeletal muscle capillaries: hemodynamic resistance, endothelial distensibility, and pseudopod formulation. *Ann. Biomed. Eng.* 23:226-246, 1995.
- Lee J.S., E.P. Salathe, and G.W. Schmid-Schonbein. Fluid exchange in skeletal muscle with viscoelastic blood vessels. *AM. J. Physiol.* 253:H1548-H1566, 1987.
- Li J. K-J. *Arterial System Dynamics*. New York Univ. Press, 1987.
- Li J. K-J. *Comparative Cardiovascular Dynamics of Mammals*. CRC Press, New York, 1996.
- Li J. K-J. Scaling and invariants in cardiovascular biology. In: *Scaling in Biology*, pp. 113-128, eds. J.H. Brown and G.B. West, Oxford Univ. Press, 2000.
- Li J. K-J. *The Arterial Circulation: Physical Principles and Clinical Applications*. Human Press, Totowa, New Jersey, 2000.
- Li J. K-J., Comparative cardiac mechanics: Laplace's law. *J. Theor. Biol.*, 118, 339-343, 1986.
- Li J. K-J., J. Melbin and A. Noordergraaf. Directional disparity of pulse wave reflections in dog arteries. *Am. J. Physiol. (Heart & Circ. Physiol.)*, 247:H95-99, 1984.
- Li J. K-J., Van Brummelen, A.G.W., and Noordergraaf, A. Fluid-filled blood pressure measurement systems. *J. Appl. Physiol.* 40: 839-843, 1976.
- Li J. K-J. Laminar and turbulent flow in the mammalian aorta: Reynolds number. *J. Theor. Biol.*, 135:409-414, 1988.
- Li J. K-J and Zhu Y. Arterial compliance and its pressure dependence in hypertension and vasodilation. *Angiology, J. Vasc. Diseases.* 45:113-117, 1994
- Li J. K-J. and Kostis, J.B. Aspects determining accurate diagnosis and efficacy of catheterization. *Proc. Ist Int. Congr. Med. Instrument.* A07, 1984.
- Li J. K-J. and Noordergraaf, A. Evaluation of needle-manometer and needle differential-manometer systems in the measurement of pressure differences. *Proc. 3rd NE Bioeng. Conf.* 5: 275-277, 1977.
- Li J. K-J. Pressure-derived flow: a new method. *IEEE Trans. Biomed. Eng.*, BME-30, 244-246, 1983.
- Li J. K-J. Regional left ventricular mechanics during myocardial ischemia. In: *Simulation and Modeling of the Cardiac System*. pp. 451-462, Ed. S. Sideman, Martinus Nijhoff Publishers, 1987.
- Li J. K-J. Time domain resolution of forward and reflected waves in the aorta. *IEEE Trans. Biomed. Eng.*, BME-33:783-785, 1986.
- Li J. K-J., Hemodynamic significance of metabolic turnover rate. *J. Theor. Biol.*, 103:333-338, 1983.
- Li J. K-J., J. Melbin, K. Campbell and A. Noordergraaf. Evaluation of a three-point pressure method for the determination of arterial transmission characteristics. *J. Biomechanics*, 13, 1023-1029, 1980.

- Li J. K-J., J. Melbin, R. A. Riffle and A. Noordergraaf. Pulse wave propagation. *Circ. Res.* 49, 442-452, 1981.
- Li J. K-J., T. Cui and G. Drzewiecki. A nonlinear model of the arterial system incorporating a pressure-dependent compliance. *IEEE Trans. Biomed. Eng.*, BME-37:673-678, 1990.
- Li J. K-J., W. Welkowitz, J. Zelano, D. A. Molony, J. B. Kostis and J.W. Mackenzie. Effects of balloon inflation and deflation rates on global and regional ventricular performance. *Progr. Artif. Organs*, 137- 140, 1983.
- Li J. K-J., W. Welkowitz, J. Zelano, D. A. Molony, J. B. Kostis and J. W. Mackenzie. Intraortic balloon counterpulsation: blood flow increment dependence on inflation interval. *Proc. 6th. Internat. Cardiovascular System Dynamics*, 6:72-75, 1984.
- Li J.K-J. , R. McMahon, M. Singh, Y. Zhu, D. Amory, G. Drzewiecki, and D. O'Hara. Noninvasive pulse wave velocity and apparent phase velocity in normal and hypertensive subjects. *J. Cardiovas. Diagn. Procedures*, 13:31-36, 1996.
- Li J.K-J., Melbin, J., and Noordergraaf, A. Pulse transmission to vascular beds. *Proc. 33rd ACEMB* 22: 109, 1980.
- Ling S.C. Atabek, H.B., Letzing, W.G. and Patel, D.J. Nonlinear analysis of aortic flow in living dogs. *Circ. Res.* 33: 198-212, 1973.
- Matonick J.P., and J. K-J. Li. Noninvasive monitoring of blood pressure during hand-grip stress induced vascular reactivity. *Proc. 34th. Assoc. Adv. Med. Instrum.*, 1999.
- Maughan W.L., K. Sunagawa, D. Burkhoff and K. Sagawa. Effect of arterial impedance changes on the end-systolic pressure-volume relation. *Circ. Res.* 54:595-602, 1984.
- Mayrovetz H.N., M.P. Wiedeman and A. Noordergraaf. Analytical characterization of microvascular resistance distribution. *Bull. Math. Biol.* 38:71, 1976.
- Mayrovetz H.N., M.P. Wiedeman and A. Noordergraaf. Microvascular hemodynamic variations accompanying microvessel dimensional changes. *Microvasc. Res.* 10:322, 1975.
- Mayrovitz H.N. Assessment of human Microvascular Function. In: *Analysis and Assessment of Cardiovascular Function*. pp. 248-273. Eds: G. Drzewiecki and J. K-J. Li, Springer-Verlag, New York, 1998.
- McDonald D.A. *Blood Flow in Arteries*. Arnold, London, 1960, 1974.
- Mills C.J. A catheter-tip electromagnetic flow probe. *Phys. Med. Biol.* 11: 323-324, 1966.
- Moens A.I. *Die Pulskurve*. Leiden, 1878.
- Moreno A.H. Dynamics of pressure in central veins. In: *Cardiovascular System Dynamics*, eds. J. Baan, A. Noordergraaf, J. Raines, pp. 266, MIT Press, 1978.
- Moreno A.H., A.I. Katz, L.D. Gold and R.V. Reddy. Mechanical distension of dog veins and other very thin-walled tubular structures. *Circ. Res.* 27:1069-1079, 1970.

- Morgan B.C., F.L. Abel, G.L. Mullins, and W.G. Guntheroth. Flow patterns in the caeae, pulmonary artery, pulmonary vein and aorta in intact dogs. *Am. J. Physiol.* 210:903, 1966.
- Morgan G.W. and Kiely, J.P. Wave propagation in a viscous liquid contained in a flexible tube. *J. Acoust. Soc. Am.* 26: 323-328, 1954.
- Muller HS. Role of intra-aortic counterpulsation in cardiogenic shock and acute myocardial infarction. *Cardiology* 84:168-174, 1994.
- Nerz R., P. D. Myerowitz, and P. I. Blackshear. A simulation of the dynamics of counterpulsation. *J. Biomech. Eng.*, 101:105, 1979.
- Nichols W.W. and M.F. O'Rourke. *McDonald's Blood Flow in Arteries*. 4th. edition, Arnold, London, 1998.
- Nichols W.W. Conti, C.R., Walker, W.E., and Milnor, W.R. Input impedance of the systematic circulation in man. *Circ. Res.* 40: 451-458, 1977.
- Nichols W.W., and McDonald, D.A. Wave velocity in the proximal aorta. *Med. Biol. Eng.* 10: 327-335, 1972.
- Noordergraaf A. *Circulatory System Dynamics*. Academic Press, New York, 1978.
- Noordergraaf A. Hemodynamics. In: *Biological Engineering*. Ed: H.P. Schwan. McGraw-Hill, New York, 1969.
- Ohman EM, Goeroge BS, White CJ, Kern MJ, Gurbel PA, Freeman RJ, et al. Use of aortic counterpulsation to improve sustained coronary artery patency during acute myocardial infarction: results of a randomized trial. *Circulation* 90:792-299, 1994.
- Oka S. *Cardiovascular Hemorheology*. Cambridge Univ. Press, London, 1981.
- Permutt S., B. Bromberger-Barnea, and H.N. Bane. Alveolar pressure, pulmonary venous pressure, and the vascular waterfall. *Med. Thorac.* 19:239-260, 1962.
- Pierce W.S. et al. Ventricular-assist pumping in patient with cardiogenic shock after cardiac operations. *N. Engl. J. Med.*, 305: 1606-1610, 1981.
- Puri N. N., J. K-J. Li, S. Fich and W. Welkowitz. Control system for circulatory assist devices: determination of suitable control variables. *Trans. Am. Soc. Artif. Intern. Organs*, 28, 127-132, 1982.
- Randall D., W. Burggren and K. French. *Animal Physiology: Mechanisms and Adaptations*. W.H. Freeman, New York, 1997.
- Robard S. Autoregulation in encapsulated, passive, soft-walled vessels. *Am. Heart J.* 65:648, 1963.
- Roberts V.C. *Blood Flow Measurements*. Williams and Wilkins, Baltimore, 1972.
- Rosen R. *Optimality Principles in Biology*. Butterworth, London, 1967..
- Rushmer R.F. *Structure and Function of the Cardiovascular System*. Saunders, Philadelphia, 1972.
- Salotto A., Muscarella, L.F., Melbin, J., Li, J.K-J., and Noordergraaf, A. Pressure pulse transmission into vascular beds. *Microvasc. Res.* 32: 152-163, 1986.
- Smaje L., B.W. Zweifach and M. Intaglietta. Micropressures and capillary filtration coefficients in single vessels of the cremaster muscle of the rat. *Microvasc. Res.* 2:96-110, 1970.

- Somlyo A.P. and Somlyo, A.V. Vascular smooth muscle, 1. Normal structure, pathology, biochemistry and biophysics. *Pharm. Rev.* 20: 197-272, 1968.
- Stahl W.R. Similarity analysis of biological systems. *Persp. Biol. Med.*, 6:291, 1963.
- Starling M.R. Left ventricular-arterial coupling relations in the normal human heart. *Am. Heart J.* 125:1659-1666, 1993.
- Suga H, Sagawa K and Shoukas A: Load independence of the instantaneous pressure-volume ratio of the canine left ventricle and effects of epinephrine and heart rate on the ratio, *Circ. Res.* 32:314-322, 1973.
- Sunagawa K., W.L. Maughan, D. Burkhoff and K. Sagawa. Left ventricular interaction with arterial load studied in isolated canine left ventricle. *Am. J. Physiol.* 265:H773-780, 1983.
- Van Brummelen A.G.W., Some digital computer applications to hemodynamics. Ph.D. dissertation, Univ. of Utrecht, The Netherlands, 1961.
- Van den Bos G.C., N. Westerhof and O.S. Randall. Pulse wave reflection: can it explain the differences between systemic and pulmonary pressure and flow waves? *Circ. Res.* 51:470-485, 1982.
- Waksman R, Weiss AT, Gotsman MS, Hasin Y. Intra-aortic balloon counterpulsation improves survival in cardiogenic shock complicating acute myocardial infarction. *Eur. Heart J.* 14:71-74, 1993.
- Weizsacker H.W. and K. Pascal. Anisotropic passive properties of blood vessel walls. In: *Cardiovascular System Dynamics: Models and Measurements*, pp. 347-362. Eds. T. Kenner, R. Busse, H. Hinghofer-Szalkay, Plenum, 1982.
- Wells S.M., B.L. Langeille, and S.L. Adamson. In vivo and in vitro mechanical properties of the sheep in thoracic aorta in the perinatal period and adulthood. *Am. J. Physiol.* 274:H1749-H1760, 1998.
- Westerhof N. and Noordergraaf, A. Arterial viscoelasticity: a generalized model. *J. Biomech.* 3: 357-379, 1970.
- Westerhof N., Bosman, F., DeVries, C.J., and Noordergraaf, A. Analog studies of the human systemic arterial tree. *J. Biomech.* 2: 121-143, 1969.
- Wiederhielm C.A., J.W. Woodbury, S. Kirk and R.F. Rushmer. Pulsatile pressure in microcirculation of the frog's mesentery. *Am. J. Physiol.* 207:173-176, 1964.
- Wilkins H., Regdson, W., and Hoffmeister, F.S. The physiological importance of pulsatile blood flow. *New Engl. J. Med.* 267: 443-445, 1967.
- Womersley J.R. The mathematical analysis of the arterial circulation in a state of oscillatory motion. *WADC Tech. Rept.* WADC-TR56-614, 1957.
- Wyatt D.G. Blood flow and blood velocity measurement in vivo by electromagnetic induction. *Med. Biol. Eng. Comput.* 22:193-211, 1984.
- Yada T., O. Hiramatsu, A. Kimura, M. goto, Y. Ogasawaray, K. Tsujioka, S. Yamamori, K. Ohno, H. Hosaka and F. Kajiya. In vivo observation of subendocardial microvessels of the beating porcine heart using a needle-probe videomicroscope with a CCD camera. *Circ. Res.* 72:939-946, 1993.

- Yao S.T. and W.H. Pearce. The use of noninvasive tests in peripheral vascular disease: current status. In: *Modern Vascular Surgery*, ed. J.B. Chang, Vol. 4, pp. 49-65, PMA Publishing, California, 1991.
- Zamir M. *The Physics of Pulsatile Flow*. Springer-Verlag, New York, 2000
- Zelano J., J. K-J. Li, W. Welkowitz, D. A. Molony, J. Kostis and J. Mackenzie. Real-time automation of intra-aortic balloon pumping. *Progr. Artif. Organs*, 85:491-499, 1985.
- Zelano J.A., J. K-J. Li and W. Welkowitz. A closed loop control scheme for intra-aortic balloon pumping. *IEEE Trans. Biomed. Eng.* BME-37:182-192, 1990.
- Zhu Y. *Computer Based Analysis of Systolic/Diastolic Left Ventricular Function and Pressure-Dependent Arterial Compliance*. Ph.D. dissertation, Rutgers University, NJ, 1996.
- Zweifach B.W. and H.H. Lipowsky. Quantitative studies of microcirculatory structure and function. III. Microvascular hemodynamics of cat mesentery and rabbit omentum. *Circ. Res.* 41:380-390, 1977.
- Zweifach B.W. Quantitative studies of microcirculatory structure and functions. I. Analysis of pressure distribution in the terminal vascular bed. *Circ. Res.* 34: 858-866, 1974.

# Index

- activation, 23, 29, 36, 38, 156, 174, 175, 207
- angioplasty, 9, 214
- anisotropy, 28
- aorta, 5, 6, 9, 10, 14, 16, 18, 21, 22, 23, 26, 29, 39, 45, 46, 50, 52, 74, 76, 77, 83, 85, 91, 92, 93, 94, 96, 97, 99, 100, 102, 103, 108, 109, 110, 118, 119, 123, 130, 131, 135, 137, 138, 143, 148, 165, 166, 168, 179, 190, 208, 209, 234, 235, 236, 237, 238, 239, 241, 242
- aortic arch, 18, 22, 36, 37, 98, 99, 119, 143, 235, 238
- aorto-iliac junction, 18, 21, 22, 143, 166
- apparent phase velocity, 104, 105, 106
- area ratio, 20, 150, 151, 160, 161, 162, 163, 164, 171
- arterial compliance, 83, 87, 88, 89, 113, 132, 135, 136, 137, 138, 139, 140
- arterial stiffness, 136
- arteriole, 19, 192, 195, 196, 200, 201, 205, 207, 211
- assisted circulation, 13, 243, 244
- atherosclerosis, 9, 154, 156, 157
- attenuation coefficient, 100, 104, 109, 141
- augmentation index, 119
- auscultatory, 13, 222, 223
- autonomic nervous system, 36
- autoregulation, 185
- baroreceptor, 38, 39, 241, 243
- beta adrenergic blockers, 8
- bifurcation, 18, 143, 145, 146, 147, 148, 149, 152, 158, 159, 160, 161, 162, 164, 170, 171
- blood flow, 2, 3, 5, 6, 7, 8, 10, 11, 15, 19, 35, 42, 43, 44, 45, 46, 63, 73, 76, 120, 121, 122, 124, 126, 127, 131, 132, 142, 143, 152, 157, 160, 166, 167, 168, 173, 174, 177, 194, 200, 202, 226, 227, 229, 231, 234, 236, 237, 239, 240, 241, 242, 243, 244
- blood pressure, 3, 5, 6, 8, 10, 12, 13, 18, 20, 26, 27, 35, 36, 37, 38, 39, 42, 43, 47, 50, 54, 59, 90, 92, 93, 94, 106, 131, 133, 137, 138, 139, 192, 202, 214, 216, 217, 219, 221, 222, 223, 224, 225
- blood volume, 16, 19, 34, 132, 172, 173, 175
- brachial artery, 222, 223, 224, 225
- branching, 3, 9, 12, 17, 18, 20, 21, 22, 76, 93, 103, 119, 141, 142, 143, 144, 146, 147, 148, 149, 150, 152, 154, 156, 157, 158, 159, 160, 161, 163, 164, 165, 166, 168, 170, 171, 193, 194, 196, 201, 211, 212
- bypass, 174, 193, 235, 237, 241
- capillaries, 2, 3, 9, 10, 19, 20, 73, 172, 173, 192, 193, 194, 195, 196, 197, 200, 201, 203, 206, 207, 208, 211

- carbon dioxide, 5, 30, 33, 35, 239
- cardiac assistance, 234, 235, 244
- cardiac cycle, 46, 87, 139, 140, 205, 239
- cardiac indices, 146
- cardiac muscle, 76, 77, 79, 87, 234, 236, 240
- cardiac output, 12, 13, 19, 20, 39, 81, 82, 84, 175, 193, 207, 231, 232, 236, 237, 238, 239, 241, 242, 243, 244
- carotid artery, 109, 110, 148, 152, 176
- carotid sinus, 36, 37, 38, 39, 243
- catheter, 6, 9, 13, 91, 92, 98, 101, 189, 214, 215, 217, 218, 219, 221, 222, 227, 229, 231, 232, 233
- catheter-manometer system, 6, 217, 218, 219, 221
- catheter-tip transducer, 189
- characteristic impedance, 83, 85, 88, 96, 97, 98, 111, 117, 135, 137, 138, 158, 159, 160, 162, 163, 164, 166
- circumferential stress, 205, 224, 225
- closed-loop control, 243, 244
- collagen, 9, 10, 23, 28, 29, 39, 109, 126, 174, 197
- collapsible tube, 182, 184, 185, 186
- contact stress, 225
- contractility, 3, 82, 85, 87
- coronary artery, 144, 145, 149, 174, 237
- coronary blood flow, 239, 240, 241, 242, 243, 244
- coupling, 83, 86, 87, 215
- creep, 10, 48, 49, 53
- cube law, 168, 171
- damping, 51, 94, 100, 104, 127, 129, 164, 218, 221
- diameter, 13, 18, 20, 22, 25, 26, 27, 28, 29, 43, 44, 46, 47, 49, 50, 51, 52, 73, 74, 75, 82, 99, 108, 121, 143, 145, 173, 174, 196, 197, 200, 201, 206, 210, 211, 212, 233, 241
- diastole, 2, 46, 77, 91, 131, 133, 140, 175, 235, 236, 242
- dimensional analysis, 41, 44, 153
- distensibility, 10, 76, 131, 136, 191, 203, 204, 210
- distributed model, 211
- Doppler ultrasound, 229
- dynamic elastic modulus, 51, 189
- echocardiography, 13
- ejection, 10, 46, 76, 77, 79, 81, 82, 83, 88, 91, 92, 97, 99, 114, 140, 175, 207, 221, 239, 241
- elastance, 81, 83, 84, 85, 86, 87, 88, 89, 136
- elastic modulus, 28, 51, 52, 53, 103, 166, 176, 189, 210
- elastin, 9, 10, 23, 28, 39, 109, 126, 174
- electric analog, 134
- electromagnetic flowmeter, 6, 13, 226, 227
- end-diastolic volume, 79, 81
- endothelium, 20, 23, 24, 156, 192, 197, 202
- end-systole, 77, 81, 85, 88, 91, 140
- entry length, 75, 201
- equation of continuity, 11, 121, 170
- equation of motion, 128
- external work, 83, 237, 241
- Fahraeus-Lindqvist effect, 201, 210
- femoral artery, 18, 21, 51, 94, 102, 109, 110, 117, 141, 149, 220, 236
- flow acceleration, 71, 120
- flowmeter, 5, 6, 13, 226, 227
- foot-to-foot velocity, 101, 102, 103, 189, 190
- forward wave, 114, 116
- Fourier, 10, 41, 54, 55, 56, 58, 60, 94, 136, 216
- fractal, 9, 143
- Frank-Starling mechanism, 81
- frequency domain, 10, 52, 94, 116
- frequency response, 13, 216, 217, 218, 219, 220, 221
- gas law, 30
- geometry, 7, 12, 63, 75, 102, 135, 142, 143, 150, 151, 154, 156, 165, 166, 238

- Gorlin equation, 69  
harmonic content, 94  
heart rate, 1, 38, 39, 43, 46, 82, 84, 127, 216, 238, 241, 242, 243  
heart sounds, 244  
heart valves, 3, 16  
helium, 239, 240  
hematocrit, 34  
hemoglobin, 5, 10, 31, 32, 33, 34  
hypertension, 5, 9, 171  
hysteresis, 10, 48, 49, 50, 219  
impedance, 11, 12, 59, 62, 83, 85, 88, 94, 95, 96, 97, 98, 99, 104, 105, 108, 111, 117, 119, 120, 135, 136, 137, 138, 157, 158, 159, 160, 162, 185, 186, 242  
incompressible, 27, 28, 41, 45, 48, 68, 124, 125, 152  
incremental elastic modulus, 51  
*indicator dilution*, 229  
inflation-deflation, 241  
inotropic, 82  
interstitial fluid pressure, 202  
intra-aortic balloon pump, 13, 235  
intravascular, 9, 13, 148, 175, 177, 182, 202, 203, 214, 225, 234  
jugular pressure pulse, 181  
jugular vein, 176, 181  
Korotkoff sounds, 224, 225  
laminar flow, 64, 74, 182  
linearity, 45, 55, 188, 219  
local reflection, 158, 160, 161, 162, 165, 166  
longitudinal constraint, 129  
lumped model, 11, 130, 135  
Mach number, 45, 74, 184  
magnetic resonance imaging, 9  
mammal, 46, 194, 196  
mathematical modeling, 8  
maximum elastance, 81, 85  
Maxwell model, 53, 130  
mean arterial pressure, 5, 22, 84, 132, 225, 241  
mechanoreceptors, 36  
microcirculation, 3, 7, 8, 9, 12, 13, 19, 20, 192, 193, 194, 195, 196, 200, 201, 206, 207, 208, 210, 229  
minimum reflection, 162, 164  
model, 6, 10, 11, 20, 46, 53, 80, 83, 87, 88, 99, 108, 119, 130, 131, 134, 135, 137, 138, 139, 143, 146, 151, 152, 153, 154, 156, 162, 211, 212, 213, 217, 237, 241, 242, 243  
myocardial oxygen consumption, 1, 237, 238, 239, 241  
natural frequency, 215  
Navier-Stokes equations, 11, 41, 63, 124, 125, 152  
near-infrared spectroscopy, 32  
Newtonian fluid, 72, 73, 201  
noninvasive, 8, 13, 18, 106, 107, 222, 224, 225, 227  
nonlinear, 11, 28, 46, 88, 137, 138, 139, 140, 152, 185, 205  
nonuniformities, 9, 89, 93, 110, 119  
Nyquist criterion, 61  
optimal, 12, 162, 164, 167, 168, 169, 170, 207, 238, 239  
optimization, 147, 148, 201, 243  
orifice flow, 69  
oxygen, 1, 5, 7, 14, 18, 30, 31, 32, 33, 35, 142, 200, 237, 238, 239, 241, 244  
parabolic velocity profile, 66, 122, 123  
parallel assist, 236, 237  
peak-to-peak velocity, 102  
periodic, 54, 55, 56, 60, 61, 125, 130, 216  
peripheral resistance, 8, 11, 12, 38, 83, 85, 87, 88, 130, 132, 133, 134, 135, 137, 138, 206, 207, 241  
permanent assist device, 235  
phase velocity, 100, 104, 105, 106, 109, 129, 191, 210  
piezoelectric transducer, 233  
Pi-numbers, 42  
Poiseuille's formula, 169  
Poisson ratio, 27, 28, 45, 48, 124, 233  
pop test, 219

- preload, 79, 81, 82, 175
- pressure gradient, 41, 63, 64, 65, 120, 140, 185, 201, 203, 206
- pressure transducer, 13, 92, 101, 214, 215, 216, 217, 221
- pressure-diameter relation, 50, 51, 241
- pressure-volume relation, 81, 83, 85, 87, 137
- propagation constant, 100, 103, 104, 105, 106, 107, 108, 109, 141
- pulmonary circulation, 5, 7, 15, 19
- pulse transit time, 101
- pulse transmission, 12, 13, 18, 91, 141, 157, 158, 160, 164, 166, 188, 208, 210
- P-wave, 244
- radial artery, 1
- radial strain, 26, 27, 28, 48, 233
- receptors, 35, 36, 37, 38
- red blood cell, 9, 10, 33, 34, 35, 73, 196, 228
- reflected wave, 97, 101, 102, 103, 105, 106, 110, 111, 115, 116, 118, 119
- reflection coefficient, 105, 116, 117, 118, 119, 158, 160, 161, 162, 165, 166
- reflection site, 99, 110, 119, 120
- resonance frequency, 218, 220
- Reynolds number, 10, 45, 46, 73, 74, 75, 154, 200
- R-wave, 244
- scaling laws, 44
- shear stress, 12, 72, 73, 152, 154, 156, 173, 225
- similarity, 44, 45, 115
- smooth muscle, 3, 9, 10, 20, 23, 24, 28, 29, 36, 39, 173, 174, 175, 192, 196, 197, 200, 201, 207
- sphere, 14
- spring-mass system, 215
- Starling's law, 175
- steady flow, 7, 46, 63, 64, 132, 140, 151, 156, 166, 167, 170, 187, 201, 206, 207, 208
- stenosis, 9, 67, 156, 157, 181
- step response, 219
- storage reservoir, 6, 19, 173
- strain, 25, 26, 27, 28, 46, 47, 48, 49, 52, 122, 176, 190, 204, 205, 233
- stress, 10, 11, 25, 46, 47, 48, 49, 52, 53, 72, 73, 122, 126, 152, 154, 156, 157, 173, 176, 204, 205, 222, 224, 225
- stroke volume, 6, 81, 82, 83, 84, 92, 131, 175, 207, 241, 242
- sympathetic nervous system, 36
- systolic pressure, 81, 84, 86, 87, 92, 119, 133, 134, 173, 221, 222, 243
- taper, 18, 21, 22, 23, 141
- temporary assist device, 234, 235
- thermodilution, 13, 214, 232
- thick-walled, 11, 130
- thin-walled, 18, 123, 174
- time constant, 49, 53, 84, 134
- time domain, 10, 94, 97, 111, 118
- time-dependent, 70, 152
- time-varying compliance, 85, 88, 89, 213, 242
- tonometer, 181, 225
- Torricelli's equation, 69
- T-shaped, 149, 150, 194
- turbulence, 46, 74, 155
- ultrasound, 98, 181, 227, 228, 229, 234
- underdamped, 217, 218, 219, 221
- uniform collapse, 191
- uniform vessel, 18, 108
- vascular branching, 12, 22, 93, 141, 143, 157, 158, 159, 161, 164, 165, 166, 170
- vascular hypertrophy, 9
- vascular sounds, 222, 223
- vascular stiffness, 12
- vascular tree, 3, 4, 9, 14, 18, 20, 89, 94, 144, 148, 196
- vasoactivity, 39, 40
- vasoconstriction, 3, 36, 39, 40, 99, 112, 113, 114, 115, 116, 117, 118, 172, 173
- vasodilation, 38, 99, 112, 113, 115, 116, 117, 118, 211

- velocity gradient, 63, 64, 65, 72, 73, 121
- velocity profile, 64, 66, 75, 122, 123, 153, 228
- venous return, 173, 175, 178
- ventilation-perfusion, 5, 39, 142
- venule, 20, 192, 195, 205, 211
- viscoelastic, 8, 10, 11, 48, 49, 50, 53, 80, 105, 106, 109, 129, 130, 190, 210, 238
- viscosity, 8, 30, 44, 51, 63, 64, 72, 73, 100, 108, 122, 125, 126, 127, 156, 160, 190, 191, 201, 206, 210, 239
- viscous modulus, 51, 52
- Voigt model, 53, 130
- wall stress, 156
- wall thickness, 7, 23, 25, 27, 29, 39, 40, 48, 51, 103, 130, 160, 164, 171, 233
- waterfall, 12, 186
- water-hammer, 97, 111, 159, 162
- wave reflections, 12, 92, 93, 94, 99, 100, 103, 104, 105, 106, 107, 111, 157, 158, 160, 164
- windkessel, 6, 10, 46, 83, 87, 91, 99, 131, 132, 134, 135, 139, 208, 241
- Womersley's parameter, 127
- Young's modulus, 7, 25, 47, 121
- Y-shaped, 149, 150, 194